Doctoral theses at NTNU, 2021:278

Haoran Li

Nonlinear Wave Loads, and Resulting Global Response Statistics of a Semi-Submersible Wind Turbine Platform with Heave Plates

Doctoral thesis

NTNU
Norwegian University of
Science and Technology
Thesis for the degree of
Philosophiae Doctor
Faculty of Engineering
Department of Marine Technology

NTNU
Norwegian University of
Science and Technology

Haoran Li

Doctoral theses at NTNU, 2021:278

NTNU

ISBN 978-82-326-5499-4 (printed ver.)
ISBN 978-82-326-6193-0 (electronic ver.)
ISSN 1503-8181 (printed ver.)
ISSN 2703-8084 (electronic ver.)

NTNU
Norwegian University of
Science and Technology

Haoran Li

Nonlinear Wave Loads, and Resulting Global Response Statistics of a Semi-Submersible Wind Turbine Platform with Heave Plates

Thesis for the degree of Philosophiae Doctor

Trondheim, August 2021

Norwegian University of Science and Technology
Faculty of Engineering
Department of Marine Technology

NTNU
Norwegian University of
Science and Technology

NTNU
Norwegian University of Science and Technology

Thesis for the degree of Philosophiae Doctor

Faculty of Engineering
Department of Marine Technology

ISBN 978-82-326-5499-4 (printed ver.)
ISBN 978-82-326-6193-0 (electronic ver.)
ISSN 1503-8181 (printed ver.)
ISSN 2703-8084 (electronic ver.)

Doctoral theses at NTNU, 2021:278

PRINTED IN
NORWAY
NO - 1598

NORDIC SWAN ECOLABEL
Printed matter
2041 0731

Printed by Skipnes Kommunikasjon AS

Abstract

Floating wind turbines (FWTs) are considered to be a promising way to harness the energy from winds over deep water and farther offshore. However, there are some challenges to bring this technology to full maturity. In deep water, FWTs may be exposed to harsh environments and steep waves which induce highly nonlinear wave loads. Given that the natural frequencies of FWTs are designed to be outside the wave frequency range, these nonlinear wave loads can excite eigenfrequencies of FWTs, leading to larger dynamic responses that strain the mooring system or to structural vibrations. However, engineering tools limit hydrodynamic modeling to linear and weakly nonlinear models, and underpredict the dynamic responses of FWTs, especially at the low- and high-frequency regions. Therefore, well-validated modelling tools are needed to capture these nonlinear wave loads and resulting global responses more accurately while keeping the computational efficiency at a reasonable level. The focus is on semi-submersible FWTs due to their wide applicability across a range of water depths.

In this thesis, a computational fluid dynamics (CFD) model (OpenFOAM) and an engineering model based on potential-flow theory with Morison-type drag (SIMA) are developed to investigate nonlinear wave diffraction and radiation loads on the DeepCwind semi-submersible FWT. Then, the estimated second-order difference-frequency wave load quadratic transfer functions (QTFs) and frequency-dependent added mass and linearized damping from the CFD simulations with turbulence model are used to improve the engineering model. The nonlinear wave loads and resulting global responses estimated from the CFD model, the original and modified engineering models are validated against experimental measurements.

Compared to the experimental measurements in regular waves, the CFD model gives better estimations for the higher order wave diffraction loads, especially for the CFD with turbulence model. The SIMA model has large discrepancies in predcition of amplitude of higher order wave diffraction loads. For the difference-frequency wave diffraction loads, CFD and SIMA agree well at the lower frequencies, while CFD predicts larger wave loads at higher wave frequencies. Additionally, large discrepancies in the phases are found for both high order and difference-frequency wave diffraction loads. The modified engineering model reduces the underprediction of low-frequency wave diffraction loads compared to the original engineering model and CFD with a laminar flow model.

The low-frequency added mass derived from the CFD simulation is generally around 12% larger than that estimated by the potential flow theory. This additional added mass in the CFD simulation is due to viscous effects. The linearized damping shows a small dependence on the oscillation period and a larger dependence on the oscillation amplitude near resonant frequencies of the DeepCwind semi-submersible FWT. At these frequencies, radiation damping is completely negligible compared to the viscous damping, and the accuracy of Morison's drag forces in capturing the viscous damping is sensitive to the drag coefficient.

In the free decay tests, the modified engineering model predicts natural periods close to the experimental results, and the underprediction of the damping is reduced compared to the original engineering model. The low-frequency motions, mooring line tensions and tower-base loads response to an irregular wave are underestimated using the original engineering model. The additional linear damping estimated by matching the decay motions from the CFD simulations increases this underestimation, while the modified QTFs based on CFD simulations result in larger low-frequency responses. The overestimation is reduced by modifying the frequency-dependent damping at the same time and the best agreement with the experimental measurements is achieved. Meanwhile, the combined modifications give improved agreement with experimental data in terms of damage equivalent loads for the mooring lines and tower base.

Preface

This thesis is submitted to the Norwegian University of Science and Technology (NTNU) for partial fulfilment of the requirements for the degree of philosophiae doctor.

This doctoral work has been performed at Department of Marine Technology, NTNU, Trondheim. Professor Erin E. Bachynski-Polić from Department of Marine Technology, NTNU is the main supervisor. Professor Trygve Kristiansen from Department of Marine Technology, NTNU is the co-supervisor.

The work is financially supported by a scholarship from China Scholarship Council (CSC) from August 2017 to July 2021 and a scholarship from Department of Marine Technology, NTNU from June 2018 to January 2021, which are greatly appreciated. The financial support from the Norwegian Ship-owners' Association Fund to attend academic conferences is also acknowledged. Computing resources are granted by the Norwegian Research Council (Program for Supercomputing, under project nn9676k).

Acknowledgment

First and foremost, I would like to express my sincere gratitude to my main supervisor Professor Erin E. Bachynski-Polić. She not only gave me the opportunity to pursue my PhD at NTNU but also provided me excellent guidance and positive support to overcome scientific problems I encountered. Discussions on weekly meeting made me learn how to systematically solve problems and analyze results, which is crucial for me to be an independent researcher. Her remarkable experience and knowledge on my research work have truly been inspiring.

I would like to extend my gratitude to my co-supervisor Professor Trygve Kristiansen. His valuable suggestions in my PhD mid-term evaluation helped me a lot when I was struggling.

The early discussions with Irene Rivera-Arreba about her experiences on OpenFOAM were greatly helpful for the start of PhD work. I also greatly appreciate the technical support from Dr. Jianxun Zhu and Dr. Cai Tian for the OpenFOAM and use of HPC. I am also grateful to Dr. Shi Deng and Dr. Kun Xu for discussions on the work.

I would like to appreciate the time and work of my thesis committee members: Prof. Antonio Souto-Iglesias, Dr. Qing Xiao and Assoc. Prof. Amir R. Nejad.

Many thanks to my friends and colleagues at the Department of Marine Technology for making this four years journey a fun and pleasant experience. I cherished the get-togethers, cross-country skiing trips and cabin trips. All the support and memory have become the highlights of my life.

Finally, I want to express my deepest gratitude to my parents. Your love, support and understanding means everything to me.

Haoran Li
August 2021
Trondheim, Norway

Publications

This thesis consists of an introductory part and a collection of papers, which are appended.

List of Appended Papers

Paper 1:
Haoran Li and Erin E. Bachynski (2021). Experimental and numerical investigation of nonlinear diffraction wave loads on a semi-submersible wind turbine. *Renewable Energy, Volume 171, 709-721.*

Paper 2:
Haoran Li and Erin E. Bachynski-Polić (2021). Analysis of difference-frequency wave loads and quadratic transfer functions on a restrained semi-submersible floating wind turbine. *Ocean Engineering, Volume 232, 109165.*

Paper 3:
Haoran Li and Erin E. Bachynski-Polić (2021). Experimental and numerically obtained low-frequency radiation characteristics of the OC5-DeepCwind semisubmersible. *Ocean Engineering, Volume 232, 109130.*

Paper 4:
Haoran Li and Erin E. Bachynski-Polić (2021). Validation and application of nonlinear hydrodynamics from CFD in an engineering model of a semi-submersible floating wind turbine. *Marine Structures Volume 79, 103054.*

The following papers are not regarded as part of the thesis, either due to the scope or because they were part of a large international collaboration:

List of Additional Papers

Paper 5:

Haoran Li and Erin E. Bachynski (2019). Numerical Simulation of Fully Nonlinear Interaction Between Regular and Irregular Waves and a 2D Floating Body. *Proceedings of the ASME 2019 38th International Conference on Ocean, Offshore and Arctic Engineering (OMAE2019), Glasgow, Scotland*

Paper 6:

Amy Robertson, Sébastien Gueydon, Erin E. Bachynski, Lu Wang, Jason Jonkman, D Alarcón, E Amet, A Beardsell, P Bonnet, B Boudet, C Brun, Z Chen, M Féron, D Forbush, C Galinos, J Galvan, P Gilbert, J Gómez, V Harnois, F Haudin, Z Hu, J Le Dreff, M Leimeister, F Lemmer, Haoran Li, G McKinnon, I Mendikoa, A Moghtadaei, S Netzband, S Oh, A Pegalajar-Jurado, M Q Nguyen, K Ruehl, P Schünemann, Wei Shi, H Shin, Y Si, F Surmont, P Trubat, J Qwist, S Wohlfahrt-Laymann (2020). OC6 Phase I: Investigating the underprediction of low-frequency hydrodynamic loads and responses of a floating wind turbine. *Journal of Physics: Conference Series. IOP Publishing, 2020, 1618(3): 032033.*

Paper 7:

Lu Wang, Amy Robertson, Jason Jonkman, Yi-Hsiang Yu, Arjen Koop , Adrià Borràs Nadal, Haoran Li, Wei Shi, Romain Pinguet, Yang Zhou, Qing Xiao, Rupesh Kumar, Hamid Sarlak (2021). Investigation of nonlinear difference-frequency wave excitation on a semisubmersible offshore-wind platform with bichromatic-wave CFD simulations. *3rd International Offshore Wind Technical Conference, 2021, American Society of Mechanical Engineers.*

Declaration of authorship

In all of the papers included in the thesis, Haoran Li was responsible for initiating ideas, developing the numerical models, performing all calculations and analysis, providing the results and writing the manuscripts. Professor Erin E. Bachynski-Polić contributed to all the papers with valuable discussions, suggestions and corrections to increase the scientific quality of the publications.

Abbreviations

BFWT	Bottom-Fixed Wind Turbine
CFD	Computational Fluid Dynamics
CM	Center of Mass
DOF	Degree of Freedom
DTU	Technical University of Denmark
EU	European Union
FWT	Floating Wind Turbine
GE	General Electric
GWEC	Global Wind Energy Council
IEA	International Energy Agency
KC	Keulegan-Carpenter
MARIN	Maritime Research Institute Netherlands
NREL	National Renewable Energy Laboratory
NTNU	Norwegian University of Science and Technology
OC3	Offshore Code Comparison Collaboration
OC4	Offshore Code Comparison Collaboration Continuation

OC5	Offshore Code Comparison Collaboration Continued, with Correlation
OC6	Offshore Code Comparison Collaboration, Continued with Correlation and unCertainty
OWT	Offshore Wind Turbine
PSD	Power Spectral Density
QTF	Quadratic Transfer Function
RAO	Response Amplitude Operator
SWL	Still Water Line
TLB	Tension Leg Buoy
TLP	Tension Leg Platform
VOF	Volume of Fluid

Contents

List of Figures

List of Tables

Chapter 1

Introduction

1.1 Background and motivation

Due to energy shortages and stringent regulations on environmental pollution, a huge development in the exploitation of renewable and clean energy sources such as wind, wave, tidal and solar across the world has been seen in recent decades. Among these potential energy sources, wind energy will be a major contributor to the increase of renewable energy production as this technology is highly suitable for wide implementation. Compared with onshore wind, offshore wind offers higher wind speeds with less turbulence, great area availability, and little visual and acoustic pollution, etc. According to the annual report of the Global Wind Energy Council (GWEC), the total installed wind power capacity across the world reached 650 GW by the end of 2019 and the offshore wind market accounts for 5% [1, 2]. The global installed wind power capacity over last ten years is given in Fig. 1.1, showing rapid growth in offshore wind. In Europe, the largest offshore market, a net addition of 502 grid-connected offshore wind turbines across 10 wind farms was added in 2019 and the average rated capacity of turbines doubled in one decade [3].

The majority of offshore wind turbines (OWTs) are installed in shallow water with bottom-fixed foundations. The economically limiting water depth for installing bottom-fixed structures is around 50 m [4]. However, over 80% of the offshore wind resources are located at water depths over 60 m [5] where bottom-fixed wind turbines (BFWTs) become excessively expensive. Floating wind turbines (FWTs) provide a promising solution in deep water. The foundation steel costs for three different kinds of OWTs are compared in Fig. 1.2 [6]. As the technology matures, the cost of FWTs is expected to decrease, thus enabling commercial-scale deployment [7]. On

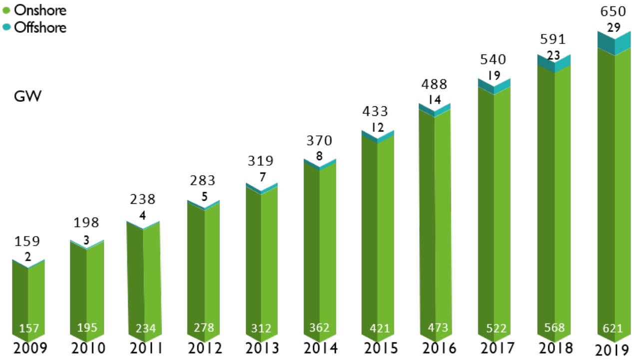

Figure 1.1: Global installed onshore and offshore wind power capacity [1].

the other hand, the environmental conditions in deep water may be more severe than those in shallow water. Table 1.1 compares the 50-year extreme significant wave height (H_s) and lifetime mean spectral peak period (T_P) of waves at 14 chosen European offshore sites due to their harsh wind and wave conditions [8]. The steep waves in deep water induce highly nonlinear wave loads, placing more stringent demands on the fidelity of simulation tools in accurately capturing these nonlinear wave loads.

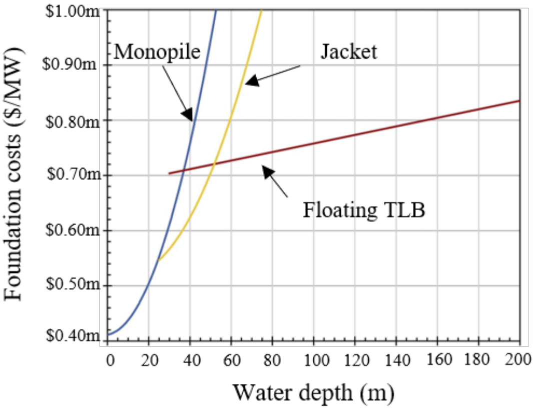

Figure 1.2: Model of foundation costs as a function of water depth [6]

The largest driver of cost reduction of OWTs is the increase in the capacity of individual wind turbines [5], allowing the same amount of wind energy to be captured with fewer machines. According to the annual report of WindEurope [3], the average rated capacity of installed OWTs in Europe

Table 1.1: Environmental conditions of 14 chosen European offshore sites [8], T_p represents lifetime mean spectral peak period

Area	Name	Water depth (m)	50-year H_s (m)	T_p (s)
Atlantic	Sem Rev	33	8.15	11.06
Atlantic	Buoy Estaca de Bares	694	10.67	11.66
Atlantic	Buoy Cabo Silleiro	449	10.19	11.84
Atlantic	Sao Pedro Pilot Zone	60	8.32	11.73
Atlantic	Sybil Head, Co. Kerry	103	13.37	11.77
English Channel	Marwick Head	68	9.32	11.17
Mediterranean	Mediterranean	2558	12.45	5.87
North Sea	Horn Sea West	42	7.02	6.81
North Sea	Belwind 1	31	6.54	5.55
North Sea	Norway 5	202	10.96	11.06
North Sea	North Sea Center	29	8.66	6.93
North Sea	Utsira II	277	10.11	10.05
North Sea	FINO 3	22	8.62	6.70
North Sea	Moray Firth	46	5.94	6.77

is 7.8 MW in 2019 is more than twice as large as the capacity (3 MW) in 2009, as shown in Fig. 1.3. In 2013, a 10MW reference wind turbine was proposed by DTU [9]. In 2018, GE Renewable Energy proposed a 12 MW wind turbine design [10]. A 15 MW reference wind turbine was proposed in IEA wind task 37 [11] and the offshore wind is targeting even larger 15-20 MW turbines for 2030 [12]. The increase of individual turbine capacity is closely linked with the increasing of rotor size, hub height and structural mass, as indicated by comparing the structural properties of four representative reference wind turbines in Table 1.2, i.e. NREL-5 MW [13], LW-8 MW [14], DTU-10 MW [9] and IEA-15 MW [11]. The increasing turbine size and capacity also introduce new challenges and opportunities for the design of supporting structures, tower and mooring line system.

The floating wind industry has experienced rapid development in recent years. Europe hosts 70% of the worldwide floating wind fleet [3]. The world's first operational floating wind farm was Hywind Scotland, which consists of five 6 MW Hywind spars and was commissioned in October 2017. The WindFloat Atlantic wind farm in Portugal was the world's second commercial floating wind farm, consisting of three 8.4 MW WindFloat semi-

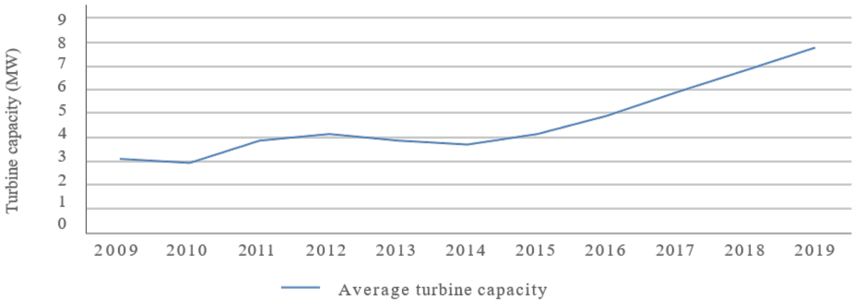

Figure 1.3: Average size of commercial offshore wind farm projects in the year (MW) [3]

submersibles [15], and started to supply power to Portuguese grid at the end of 2019. In the next three years, the capacity will significantly increase with the new installation of projects in the UK, France, Norway and Portugal which are shown in Table 1.3. The individual turbine sizes of floating wind farms have reached the same capacities as those of bottom-fixed wind farms.

Table 1.2: Offshore wind turbine capacity and structural properties

Turbine	NREL	LW	DTU	IEA
Capacity (MW)	5	8	10	15
Rotor diameter (m)	126	164	178	240
Hub height (m)	90	110	119	150
Blade mass (t)	18	35	42	65
Hub mass (t)	57	90	106	190
Nacelle mass (t)	240	285	446	630
Tower mass (t)	347	558	605	860

From Table 1.3, it can be seen that there are mainly four floating supporting structures for wind turbines in the current industry: barge, semi-submersible, spar-buoy and tension leg platform (TLP) as shown in Fig. 1.4. They have different ways to achieve stability. The barge and semi-submersible obtain their stability from a large water-plane area moment of inertia. The spar-buoy is gravity-based, with its center of gravity as low as possible, and a large separation between the center of gravity and center of buoyancy. The TLP is kept upright through the external force from stiff vertical tethers which counteract the excess buoyancy. Although the long-term survivability of these floating support structures has been demonstrated in the oil and gas industry, significant differences exist. With a smaller payload

Table 1.3: Floating wind farm in Europe [3]

Wind farm	Country	Capacity (MW)	Floater type	Turbines number and model
Windfloat Atlantic Phase 1	Portugal	25	Semi-sub	3×V164-8.4 MW (MHI Vestas)
EolMed	France	24	Barge	4×6.1M152 (Senvion)
Provence Grand Large	France	28.5	TLP	3×V164-9.5 MW (MHI Vestas)
EFGL	France	30	Semi-sub	3×V164-10.0 MW (MHI Vestas)
Eoliennes Flottantes de Groix	France	28.5	TLP	3×V164-9.5 MW (MHI Vestas)
Kincardine	UK	50	Semi-sub	5×V164-9.5 MW (MHI Vestas)
Hywind Tampen	Norway	88	Spar-buoy	11×SG 8.0-167DD (SGRE)

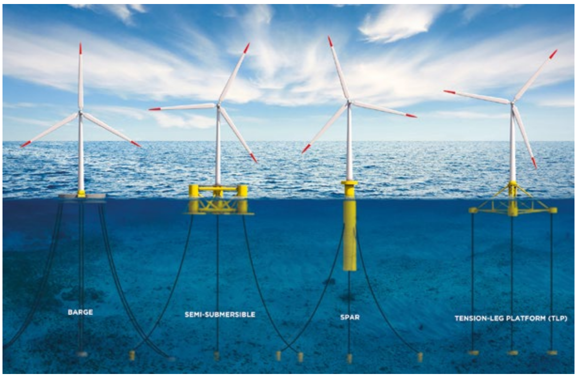

Figure 1.4: Floating supporting structures for wind turbines [16] (from left to right: barge, semi-sub,spar,TLP)

and no permanent residences for personnel, FWTs are significantly smaller than oil and gas platforms [17]. Another main difference is a mean pitch angle for the floating wind platforms during operation due to the aerodynamic thrust force. The investigations and implementations of semi-submersible and spar-buoy are in the leading positions compared to the barge and the TLP concepts [16]. Furthermore, the spar-buoy is constrained to deep water due to the large draft while the semi-submersible is applicable to a wider range of water depth due to its small draft. Hence, the semi-submersible becomes the focus in this thesis.

Various forms of semi-submersible FWTs have been commissioned or are being studied. The concepts consisting of three or four columns connected by pontoons or braces have been widely applied, such as WindFloat in Portugal [15], Dutch Tri-floater in Netherlands [18], Compact Semi-Sub in Japan [19], WindSea Semi-Sub in Norway [20], V-shaped Semi-Sub in Japan [19], LIFES50+ in EU [21], OO-Star in EU [21], CSC in Norway [22] and OC4, OC5, OC6 DeepCwind Semi-Sub in US [23–25]. In this thesis, the OC5 and OC6 DeepCwind semi-submersible platforms are used for different studies, as shown in Fig. 1.5.

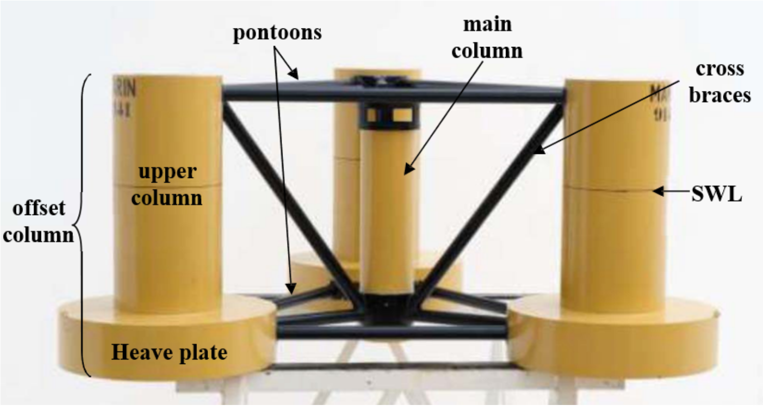

Figure 1.5: DeepCWind floating semi-submersible platform [23]

The DeepCwind semi-submersible platform consists of a main column attached to the tower and three offset columns that are connected to the main column through a series of pontoons and cross braces. At the base of each offset column is a larger diameter cylinder, or heave plate, which helps to reduce the amplitude of the heave resonance and moves the heave resonance periods outside the wave frequency range. The heave plates provide additional added mass and enhance the flow separation and vortex shedding processes that provide viscous damping [26]. This also poses new challenges to accurately simulate these nonlinear wave loads in the modelling tools. The engineering tools (potential flow theory with Morison drag) were found to severely underestimate the low-frequency nonlinear wave loads and dynamic responses for this semi-submersible FWT [25, 27].

1.2 Research objectives

The overall objective of this thesis is to investigate the nonlinear wave loads on a semi-submersible FWT through engineering tools and higher-fidelity numerical models such as CFD, and to develop methodologies to improve the engineering tools for investigating the global responses of a semi-submersible FWT. This is addressed by defining two sub-objectives.

The harsh environments and steep waves in deep water where the FWTs are installed and the complex flow around the heave plate induce highly nonlinear wave loads on the FWTs. These nonlinear wave loads are important for capturing the global responses of FWTs. However, engineering tools limit hydrodynamic modeling to linear and weakly nonlinear models. By solving the governing equations (nonlinear Navier-Stokes equations), CFD methods can apply higher order wave models and better model highly nonlinear effects. Furthermore, the solutions in the CFD methods are based on the geometry and mass properties of the floating structure, without predetermining coefficients like engineering tools. However, the accuracy of predictions, such as the effect of different length/time scales on resolutions, numerical convergence and computational efficiency should be considered when using CFD methods in the design of FWTs.

The first sub-objective of this thesis is related to the comparisons of the estimated nonlinear wave loads among different methods and is formulated as:

O1 Quantify the differences of estimated nonlinear wave loads on a semi-submersible FWT between engineering tool and CFD method against the experiments

Although the nonlinear wave loads are small, they can excite eigenfrequencies of a semi-submersible floating system, leading to larger oscillations that strain the mooring system or vibrations that cause fatigue damage to the structure. Hence, the global responses of FWTs induced by nonlinear wave loads are another focus in this thesis. Simulating the FWT in CFD directly may be the best approach, but the substantial computational time it takes to capture the low-frequency responses counteracts its advantage of high computing precision, especially when enormous amounts of simulations are needed in the design of FWTs. The computational efficiency of traditional engineering tools can meet the requirement of massive simulations. However, the engineering tools cannot reach the required accuracy. A hybrid numerical model can be developed by modifying the hydrodynamics in the engineering tools based on the estimated nonlinear wave loads in the CFD simulations, which can improve the accuracy of engineering tools while keeping the computational efficiency at a reasonable level.

The second sub-objective of this thesis is to develop and validate this hybrid numerical model and use it to investigate the resulting global responses of FWTs induced by the nonlinear wave loads, and is formulated as:

O2 Develop and validate a hybrid numerical model between engineering tool and CFD method which is used to investigate the global responses of FWTs.

The two sub-objectives are connected because the estimated nonlinear wave load by the CFD method in **O1** can be used to modify the hydrodynamics and improve the accuracy of engineering tools in **O2**.

1.3 Main contributions

Based on the research objectives defined in Section 1.2, several contributions to the scientific community have been made. The main contributions are further discussed in Chapter 4, and briefly summarized in the following. The relations among objectives, contributions and appended papers are illustrated in Fig. 1.6.

C1 Assessment of the higher order wave loads on a constrained semi-submersible FWT under regular waves, considering upright and trimmed conditions, and an evaluation of wave loads on each column of semi-submersible platform.

C2 Quantification of the low-frequency wave loads on a constrained upright and trimmed semi-submersible FWT under irregular and bichromatic waves, including the loads on the whole floater and each column.

C3 A method to modify the difference-frequency wave-excitation load quadratic transfer functions (QTFs) from potential flow solutions based on CFD simulations under the constrained and floating conditions, which is extensively validated against the experimentally measured wave loads.

C4 Estimation of the added mass and damping on a whole floater and each column around the natural periods of surge, heave and pitch motion through simulations with forced oscillation motions.

C5 A methodology to modify the frequency-dependent added mass and damping estimated by potential flow theory based on the CFD results, extensively validated against the free decay motions in surge, heave, and pitch from both CFD simulations and experiments.

C6 A hybrid numerical model that implements the nonlinear hydrodynamics from CFD simulations in engineering tools for the investigation of the global responses of a semi-submersible FWT induced by the nonlinear wave loads.

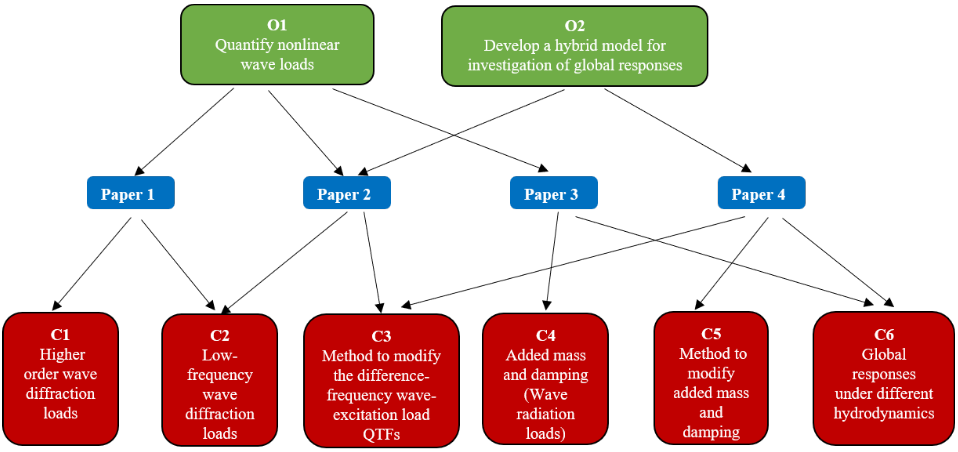

Figure 1.6: Relations among objectives, contributions and papers

1.4 Thesis organization

The thesis consists of five chapters. A brief description of each chapter is provided as follows:

Chapter 1: Introduction
This chapter gives an overview of the background and motivation for this thesis, and states the objective of the research. The main contributions to the scientific community, together with their relations to the objectives are also presented.

Chapter 2: Literature Survey and Review of Experiments for Validation
This chapter summarizes previous work related to investigation of nonlinear

wave loads and global responses of FWTs using engineering tools and CFD methods. The experimental setups related to the OC5 and OC6 projects are described.

Chapter 3: Numerical Modelling and Response Metrics
The theoretical background about engineering model and Navier-Stokes/VOF solver (CFD) used in this thesis is described in this chapter. The approaches for estimating QTF values and added mass and damping from time series of nonlinear hydrodynamic loads are described. Meanwhile, the methodology of implementation of CFD results into the engineering tool is also provided. In addition, some metrics used in the analysis are defined in this chapter.

Chapter 4: Research Findings
This chapter mainly presents the results and outcomes of this thesis. The nonlinear wave loads on an upright and trimmed restrained semi-submersible floater, the estimated added mass and damping from the forced oscillations, and global responses of FWTs are discussed, including results from engineering tool, CFD method and experiments.

Chapter 5: Conclusions and Recommendations for Future Work
This chapter presents the conclusions, together with the recommendations for future work based on the limitations identified in the current work.

Chapter 2

Literature Survey and Review of Experiments for Validation

As discussed in Chapter 1, FWTs in deep water may be exposed to harsh environments and steep waves which induce highly nonlinear wave loads. These nonlinear wave loads are important for the local and global responses of FWTs. In order to reduce uncertainties in design and cost margins, an accurate description of the hydrodynamic loads on floating platforms and the resulting dynamic responses is of particular interest for the design of FWTs. In general, there are three different approaches to predict the hydrodynamic loads/responses of FWTs: engineering tools, more general numerical solutions (such as CFD methods) and model- and full-scale experiments. The advantages and disadvantages of all approaches are summarized in Table 2.1. In the following sections, the previous work relevant for estimation of nonlinear wave loads and global responses analyses of FWT using these approaches is described. A brief introduction to the experiments used to validate the numerical simulations in this thesis, is also given.

2.1 Engineering tools

To preform the analysis of FWTs, engineering tools have been developed to represent the dynamics of the rotor, floater and mooring system in a fully coupled way. That means a fully coupled aero-hydro-servo-elastic model is required to take the aerodynamics, hydrodynamics, structural dynamics, control systems and mooring lines into account. The design load cases

Table 2.1: Comparisons of different approaches to predict hydrodynamic loads/responses of FWTs

Tool	Advantages	Disadvantages
Engineering tools	Relatively cheap computational cost. Well recognized accuracy.	Flexible, but low-fidelity models. Relatively simple geometries.
CFD methods	Complex models. Complex geometries. Visualization. Local and global quantities.	High computational cost. Uncertainty. Requirement for expert knowledge.
Experiments	Complex geometries. Local and global quantities.	Expensive. Uncertainty. Scaling (model-scale).

(DLCs) should cover the most significant conditions that a FWT may experiences, which are described by the wind, marine, electrical and other extreme conditions. The detailed information can be found in International Electrotechnical Commission (IEC) standards [28].

In the current work, the focuses are the nonlinear hydrodynamic loads and resulting global dynamic responses of FWTs. First-/Second- order potential flow theory is widely used to compute the hydrodynamic loads on the large volume structures of the FWTs. It assumes the fluid to be incompressible, irrotational and inviscid. Therefore, viscous effects are considered through empirical models, such as Morison-type drag. The wave loads on the slender structures of the FWTs with small diameter compared to the wave length are estimated by using Morison's equation based on the instantaneous position of FWTs.

In the early history of the simulations of FWTs, frequency-domain methods based on linear potential flow models are commonly used to analyze the responses of FWTs. Bulder et al. [29] used a linearized potential flow panel program called DIFFRAC [30] developed by MARIN to find response amplitude operators (RAOs) of a triple-floater concept. Lee [31] used a linear frequency-domain method to analyze the responses of a TLP FWT in random seas. Vijfhuizen et al. [32] used a frequency-domain tool, known as WAMIT [33], to carry out a hydrodynamic analysis of barge floater with moonpool for 5 MW wind turbine. Wayman [34] performed coupled dynamic analysis for various TLP and barge floaters in the frequency domain. Sclavounous et al. [35] presented a fully coupled dynamic analysis by coupling LINES, WAMIT and FAST codes to carry out a parametric design study of FWT concepts and mooring systems in the frequency domain.

Analysis in the frequency domain (FD) is computationally efficient and can give an intuitive understanding of the qualitative behavior of the system, such as the natural frequencies of FWTs which can be placed away from the wave-energy range to minimize the dynamic responses. Therefore, frequency-domain methods are widely used in the initial design of FWT. However, FD calculations have some limitations. For instance, in terms of which nonlinearities can be included, an iterative approach is limited. However, these nonlinearities are important for the analysis of FWTs. For example, without consideration of coupling between motions and flexibility of tower and blade, the FD analysis could wrongly predict the natural frequencies of system [36].

In recent years, a series of numerical tools have been developed to model FWTs in a coupled time-domain analysis, such as OpenFAST developed by National Renewable Energy Laboratory (NREL) [37], SIMA (SIMO [38]/RIFLEX [39]) developed by SINTEF Ocean, HAWC2 developed by DTU [40], ADAMS developed by MSC Software Corporation [41], Bladed developed by GL Garrad Hassan [42] and some commercial tools like SIMPACK and ANSYS which are also used in modeling FWTs [43, 44]. The calculation of hydrodynamic loads in the first three numerical tools and related research work are discussed in the following paragraphs.

The hydrodynamic loads in OpenFAST include the linear hydrostatic restoring, nonlinear viscous drag from Morison's equation, added mass and damping from linear wave radiation (including free-surface memory effects) and incident wave excitation from linear and second-order wave diffraction. The radiation and diffraction problems are solved in the frequency domain using WAMIT [33]. Coulling et al. [45] used FAST to simulate a semi-submersible FWT and found that the second-order difference-frequency wave forces were quite important in capturing the global responses. Bayati et al. [46] assessed the effect of second-order hydrodynamics on a semi-submersible FWT using FAST and WAMIT and the responses were overpredicted in the WAMIT due to lack of viscous drag forces and the second-order difference-frequency loads cannot be neglected in the time-domain dynamic analysis (FAST). Cao et al. [47] found the full quadratic transfer function (QTF) instead of Newman's approximation was known to better simulate the dynamic responses of a conceptual semi-submersible platform for carrying the DTU 10 MW reference wind turbine. Gueydon et al. [48] compared two different numerical tools, FAST and aNySIM developed by Maritime Research Institute Netherlands (MARIN) in simulating the effect of second-order wave loads on the OC4 semi-submersible platform and underlined the importance of resonance phenomena in response to the second-order wave loads and suspected that the lack of damping played a major role in the amplification of the motions.

SIMO is used in SIMA to take the hydrodynamic loads into account. Linear Airy wave theory, higher order Stokes regular wave theory and second-order irregular wave theory are used to calculate wave kinematics. The frequency-dependent hydrodynamic properties, such as first-order wave force transfer functions, second-order wave force QTFs and radiation added mass and damping, are estimated based on potential flow theory (WAMIT). Viscous drag forces from Morison's equation and body-to-body hydrodynamic coupling forces are also taken into account. Luan [22] used SIMA to design a braceless semi-submersible wind turbine and found the predictions of low-frequency motions were very sensitive to the viscous drag coefficients on the columns and pontoons. Kvittem et al. [49] examined the dynamic responses of a single semi-submersible wind turbine based on different hydrodynamic theories in SIMA and the study showed that the Morison model with forces integrated up to wave elevation gave a good prediction of the motions compared to the potential flow model with quadratic drag forces and motions were sensitive to the added mass coefficients. Berthelsen et al. [50] and Karimirad et al. [51] built a numerical model of a braceless semisubmersible FWT in SIMA and calibrated it against model-scale experimental data. A combination of higher horizontal drag coefficients in the splash zone with a lower value further below gave a better agreement with the measured surge motion compared to a uniform drag coefficient.

The hydrodynamic forces acting on the floater and mooring lines in HAWC2 are calculated using Morison's equation based on the instantaneous position of the body. Larsen et al. [52] compared three different HAWC2 versions where one is based on Morison's approach (HAWC2-standalone) and another two are coupled together with a potential flow solution WAMSIM [53] and WAMIT respectively in dynamic analysis of a floating 5 MW semi-submersible wind turbine. A drift force could cause a different response in especially the mooring lines, where the tension in the upstream line was higher for the HAWC2-standalone than for the coupled versions. The advanced hydrodynamic codes in WAMIT and WAMSIM were linear, rather simple with respect to viscous drag force modeling, and not capable of handling flexible structures. Karimirad et al. [54] compared DeepC [55] and HAWC2 tools in modeling a spar-type FWT and the results showed the nonlinear hydrodynamics had strong effects around natural frequencies and weak effects in the range of the wave frequency.

Although many engineering tools based on different theories have been developed to model FWTs, the accuracy and reliability of results obtained from these engineering tools must be assured by comprehensive testing and validation. A series of international collaboration projects conducted by the IEA focused on the validation of these engineering tools in design of OWTs through code-to-code and code-to-data comparisons. In OC3 Phase IV, the spar-buoy FWT called “Hywind,” was imitated [56, 57]. Most engineering tools could predict equivalent hydrodynamic loading on the spar in conditions where radiation damping is negligible. The hydrodynamic damping was underestimated in the engineering tools, even when including the linear radiation damping from potential flow theory and the nonlinear viscous drag from Morison-type drag. Therefore, additional linear hydrodynamic damping found by matching modeled still-water free-decay responses with experimental data was included. From the comparisons of the surge free decay simulations in the OC3 project [57] of Fig. 2.1, all codes with additional linear damping agreed on the surge displacement except POSTECH’s result which is shown in the red line of Fig. 2.1. The less damping was caused by missing the additional linear damping.

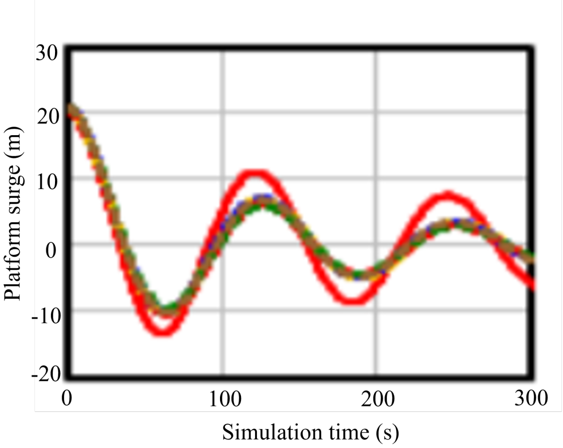

Figure 2.1: Surge decay motions in the OC3 project [57]

The second phase of OC4 [23] and OC5 [24] projects concentrated on further development and validation of engineering tools using a semi-submersible FWT. The OC4 project [58] found differences in numerical predictions of second-order mean drift loads on the semi-submersible platform, and significant underprediction of the low-frequency, nonlinear wave excitation loads and responses of the semi-submersible FWT compared to a 1:50 scaled experiment was found in the OC5 [27] and OC6 [25] projects.

In conclusion, engineering tools can provide relatively accurate results when nonlinear phenomena are not significant. In extreme weather conditions, the waves become strongly nonlinear and induce nonlinear wave loads. The frequencies of these nonlinear wave loads are often larger or smaller than the incident wave frequency. FWTs are normally designed to have their eigenfrequencies outside the excitation range of the incident waves. These nonlinear wave loads may potentially excite the eigenfrequencies of the FWTs and result in the large, slow oscillations for semi-submersible platforms [45] or high-frequency vibrations for TLP platforms [59–62]. Although these nonlinear wave loads are much smaller than the linear wave excitation loads, the accurate prediction of nonlinear wave excitation and the resulting responses is quite crucial to guarantee the safety and reliability of the FWTs. Due to the limitations of linear or weakly nonlinear hydrodynamic modeling, these mid-fidelity engineering tools may be less reliable for analysis of FWTs under the conditions where nonlinear phenomena are dominant, such as estimations of the low-frequency responses of the semi-submersible FWTs.

2.2 CFD methods

Higher order numerical tools, like CFD methods, have been successfully used in many areas of engineering. They can more precisely simulate all physical effects if resolved, including flow viscosity, hydrostatic forces, wave diffraction and radiation forces, wave run-up, slamming forces and motions of floating structures. Hence, CFD method could be an alternative tool for modeling of FWTs.

The hydrodynamic loads on a fixed structure were investigated firstly. Benitz et al. [63, 64] compared the hydrodynamic loads on the constrained OC4-DeepCwind semi-submersible wind turbine under current-only and wave-only conditions between CFD and engineering tool and found the CFD simulations could capture shadowing effects and transverse forces from vortex shedding which were not found in the engineering tool. Wang et al. [65] used STAR-CCM+ [66] to investigate the wave excitation loads on the OC5-DeepCwind semi-submersible platform. A preliminary comparison to second-order potential-flow theory showed that the CFD model predicted significantly higher difference-frequency wave excitation loads, especially for the surge force.

Added mass and damping play a significant role in accurate prediction of FWT motions. Some forced oscillations of FWTs were carried out in CFD models to quantify the added mass and damping. For a platform with heave plates, the estimated added mass from CFD models (ANSYS CFX [67] or OpenFOAM [68]) was found to be larger than the one predicted by the potential flow theory [69, 70], specially for the larger Keulegan-Carpenter(KC) numbers, and viscous effects were predominant in the damping term [70]. That was due to the occurrence of flow separation around the sharp edges of the heave plates. An accurate simulation of this unsteady flow separation was found to be essential for accurately predicting the hydrodynamic coefficients [71]. Additionally, Wang et al. [72] investigated the influence of different shapes of heave plates on hydrodynamic coefficients in Fluent [73] and found the added mass coefficient increased whereas the damping coefficient decreased with KC number for all types of heave plates.

Alternatively, the damping around the natural periods of FWTs can also be determined from simulations of free-decay motions. Burmester et al. [74–76] investigated the surge decay of a moored semi-submersible FWT using CFD. The damping owing to wave radiation was a linear damping and simulations with free surface increased the linear damping. The 3-Degree of Freedom (DOF) simulations slightly increased linear and quadratic damping compared to 1-DOF simulation. Dunbar et al. [77] compared the discrepancy of heave and pitch decay of a semi-submersible FWT between the CFD method and engineering tool and found the discrepancy was associated with Reynolds-number-dependent viscous effects. The pitch decay of the OC5-DeepCwind FWT was simulated in a CFD code ReFRESCO [78] by Wang et al. [79]. The damping in pitch decay mainly came from the contribution of heave plates, which was nonlinear damping.

Some other researches implemented CFD to investigate the responses of FWTs, especially under the regular waves. Rivera-Arreba et al. [80] used a CFD method (OpenFOAM) and an engineering tool (SIMA) to investigate the responses of the OC5 semi-submersible platform under non-steep regular waves. The heave response under waves with a period close to heave resonance in the potential flow model was 40% lower than in the CFD model. The mesh in the CFD model was adapted to comply with motion of floater based on the dynamic mesh deformation approach which allows the mesh to deform while the number of mesh remains constant. There is another approaches for the mesh adjustment in OpenFOAM by allowing for topological changes, which means that the number of mesh is allowed to change, named as overset mesh method. The capacity of overset mesh method in modelling FWTs were investigated by Pinguet et al. [81, 82]. The numerical results, such as decay motions and motions under regular wave conditions, showed good agreement with the experimental data and a more refined mesh could reduce the discrepancies with experimental measurements. Bruinsma et al. [83] evaluated two different methods, under-relaxation and predictor-corrector, to address the instability of the Navier-Stokes/6-DOF solver in the OpenFOAM for simulating the OC5 semi-submersible FWT. The numerical results compared well with the physical model experiments. Both methods significantly improved the stability of the numerical solutions, however the predictor-corrector method seemed to be more effective at eliminating the oscillations in the forces. Tran and Kim [84] compared the regular wave-induced motions of the OC5 semi-submersible FWT using the CFD method based on the Chimera overlap grid method and a potential flow linear diffraction model extended with and without Morison drag forces. The CFD method that did not use any tuning parameters could predict the motion well whereas the potential flow model needed to take the Morison drag forces or the quadratic damping matrix into account for better prediction. Similar conclusions were also found in the research work of Ferrandis et al. [85]. Wang et al. [86] computed the surge, heave, and pitch RAOs of OC5 semi-submersible FWT by simulating the motions under two regular waves in the CFD code ReFRESCO [78] and compared it with experimental data. It was proved that the CFD had the capability to reasonably predict the surge RAO. Poor predictions of heave and pitch RAOs were expected to be improved by considering the nonlinear effect of mooring lines. Hu et al. [87] and Liu et al. [88] used their own in-house code based on the constrained interpolation profile method [89] and a simple algorithm for capturing the free surface (THINC scheme [90]) to analyze hydrodynamic loads on a semi-submersible wind turbine and found that the numerical model could simulate the nonlinear phenomena in large-amplitude wave conditions.

In addition to semi-submersible FWTs, investigations of other types of FWTs using CFD methods were also carried out. Beyer et al. [91] used a coupled multi-body system (MBS) software SIMPACK and CFD (ANSYS CFX) to simulate a surge free-decay test of a flexible spar-type wind turbine in still water and found the difference of pitch motion between MBS with CFD and MBS with linear hydrodynamics was due to vortex-induced forces on the platform predicted by CFD. Nematbakhsh et al. [92, 93] proposed a CFD model where the Navier–Stokes equations were solved on a regular structured grid using a level set method for the free surface and an immersed boundary method for the turbine platform to simulate a TLP wind turbine, which were compared with simulations from potential flow theory [94]. A higher mean surge motion was noticed in CFD simulations due to better representation of nonlinear effects. The chance of strong vortex shedding behind TLP was small due to the large diameter of the TLP and the small KC number.

The above research work investigated the hydrodynamic loads and motion responses of FWTs ignoring the aerodynamic loading. In addition, some other researches focus on a fully coupled CFD method for analysis of FWT, considering aero-hydro-servo-elastic problems [95–99].

By solving the governing equations, nonlinear Navier-Stokes equations, CFD methods can apply higher order wave models and better model highly nonlinear effects. One major benefit is that the solutions are based on the geometry and mass properties of the floating structure, without predetermined coefficients. However, the choice of turbulence model is also quite crucial for the simulation results, especially for the conditions where the KC number is sufficiently high and vortices are expected. Another benefit is that CFD methods can measure the flow velocity and pressure at any given point in space and time, which is quite important for our better understanding of the differences with experiments. However, the accuracy of predictions, numerical convergence and computational efficiency need to be validated to increase the confidence in the predictions. Furthermore, the prohibitive computational cost of CFD methods makes it unfeasible to perform extensive parametric studies and optimization of FWTs. To reduce the computational cost, most numerical simulations by the CFD methods are carried out at model scale, which introduces scaling problems considering the significant difference of Reynolds numbers at model scale and full scale. With rapid improvement of computing power, the limitation of substantial computational cost is expected to weaken.

2.3 Experiments

An efficient and reliable way of investigating the hydrodynamic loads and dynamics of FWTs is through physical tests. However, limited sources of data exist from full-scale tests of FWTs in the natural environment. The Hywind spar-buoy FWT was instrumented in Norway to capture key performance data by Equinor (formerly Statoil) in 2009 [100]. The WindFloat concept was tested off the coast of Portugal to obtain the coupled aero-hydro-servo-elastic data by Principle Power Inc. [101] in 2011. In addition, the Blue H two-bladed concept of TLP FWT was tested at a small scale off the coast of Southern Italy in 2008 [101].

A wind/wave basin model test requires less time, resources and risk than a full-scale test which is difficult to perform under controlled conditions, which makes it suitable for the model validation. In 2006, a 1:47 scaled model test of the OC3-Hywind spar FWT was conducted at SINTEF Ocean (formerly MARINTEK) [102], with Froude scaling applied. DC motors were used to control the rotational speed of the rotor and the blade pitch anlge. It was found that the natural frequencies of the six rigid-body modes of the Hywind system were strongly influenced by hydrodynamic added mass. Other experiments about Hywind [103] revealed that the dynamic responses in terms of displacements, accelerations and tower and mooring line forces had a large component at second or third harmonic wave frequency and low-frequency (such as surge or pitch natural frequency).

In comparison with the Hywind spar-buoy, a 1:100 scaled model test of a Tension-Leg-Buoy (TLB) wind turbine was carried out in the Marine Cybernetics Laboratory (MCLab) at NTNU in 2011 [44]. From the results, TLB motions were significantly smaller than those of the spar-buoy. The hydrodynamic loads on the TLB tower were lower than on the spar-buoy. However, the anchor loads for the TLB were significantly higher than for the spar-buoy. In addition, the TLB indicated a significant cost savings potential due to the smaller steel mass of the floater.

Principle Power Inc. tested a 1:105 scaled semi-submersible FWT [104] and results were used to develop the first full-scale WindFloat in 2011. Due to the mean aerodynamic loads on the turbines, mean surge motion was found in the experiment. The heave plates on each column had minor effect on the first- and second-order yaw motion. The experiments about a braceless semi-submersible FWT [105] suggested that for the floater, the interaction between the aerodynamic and hydrodynamic loads was observed primarily at low frequencies. A 1:19 small-scale constrained model of the HiPRWind floater in bichromatic waves was performed to make direct measurements of the low-frequency loads at the Canal de Ensayos Hidrodinamicos de El Pardo (CEHIPAR), in Madrid, Spain [106]. At the same time, numerical modeling with frequency domain solver WAMIT has been carried by Simos et al. [107]. The comparisons showed that the Newman's approximation underestimated the second-order responses. A comprehensive 1:50 scaled model test of the NREL 5 MW reference wind turbine atop a semi-submersible platform was conducted by Goupee et al. [108]. The second-order difference-frequency surge motion was reduced as wind speeds increased. The pitch motion trends had similar trends with unaltered wave energy frequency response as the surge motion and decreasing difference-frequency response as wind speeds increased.

In addition, some other model tests focused on the influence of heave plates on the added mass and damping. Cozijn et al. [109] performed experiments with a buoy with a skirt to investigate the heave, roll and pitch damping and found that the heave and pitch damping contained linear and quadratic components. Moreno et al. [110], Philip et al. [111] and Nallayarasu et al. [112] experimentally investigated the hydrodynamic coefficients of heave plates on a spar platform. The added mass and damping increased with KC number, independent of frequency except for the increasing damping coefficients towards larger frequency at higher frequencies. For the hydrodynamic coefficients of heave plates of a semi-submersible FWT, Lopez-Pavon et al. [69] also confirmed there was a relatively weak dependence on oscillation frequencies, and a large dependence on KC number.

The main disadvantage with model-scale tests is the difficulty of scaling results to the full-scale results, considering the big difference in Reynolds numbers. Furthermore, due to the limitations of the test conditions and accuracy of the test equipment, different model experiments could obtain different results. For example, the conclusions of Chua et al. [113] were not completely consistent with the results of Tao and Dray [114] when investigating the effect of oscillation frequency on the damping of heave plates under similar KC number and oscillating periods.

2.3.1 Review of experiments for validation in this thesis

In the present work, two sets of experimental data are considered to validate the numerical simulations: Phase I of the Offshore Code Comparison Collaboration, Continued, with Correlation, and unCertainty (OC6) project [25] and Phase II of the Offshore Code Comparison Collaboration, Continued, with Correlation (OC5) project [27]. All data and experimental results are given at full scale, except when explicitly mentioned.

E1: Phase I of OC6 project

In Phase I of OC6 project, the main focus is on understanding the reasons for the previously documented underprediction of the wave-induced loads and motion responses of a floating semi-submersible FWT at its surge and pitch natural frequencies in engineering tools [27]. Two new wave-tank validation campaigns with the 1:50 scaled model of the OC5-DeepCwind semi-submersible platform were carried out at the concept basin at MARIN together with the equipment needed to measure the loads and responses of the structure.

The first validation campaign focused on the estimation of the diffraction and radiation hydrodynamic loads on the constrained platform separately.

The tower of the wind turbine was removed and the platform was attached to the carriage through a frame as shown in Figs 2.2 and 2.3. The platform can be held fixed under wave excitation (one regular wave and one irregular wave based on the JONSWAP spectrum, given in Table 2.2) to investigate the wave diffraction loads. Meanwhile, the platform can be forced to oscillate only in the surge direction (x direction) to estimate the wave radiation loads. The details of the forced oscillation tests are provided in Table 2.3. Assuming the frequency of the radiated wave is the oscillation frequency, the length of the radiated wave can be obtained by the dispersion relation. The ratios between oscillation amplitudes (A) and radiated wave lengths (L) are also given in Table 2.3. The wave loads on the entire structure were measured using a six-component gauge connecting the platform and the frame. The right-handed coordinate system used in this research originates at the center of the main column at the still water line, with positive x being in the direction of propagating waves, and z being up, as shown in Fig. 2.3.

Figure 2.2: The constrained semi-submersible platform attached to a carriage in the OC6 project [25]

In the second campaign, since hydrodynamic loads were of primary interest in the OC6 project, the floating system was simplified by removing the wind turbine and changing the tower to a stout, rigid one, shown in Fig. 2.4. The inertial properties of the floater with tower corresponded to the total inertial properties of system in the OC5 Project. The mooring system in the OC6 project was replaced with 3 taut-spring-lines to reproduce the angle at the fairlead and the equivalent linear stiffness of the catenary

Table 2.2: Parameters of waves in the constrained condition

Type	Spectrum	Wave height/Significant wave height (m)	Period/ Peak period (s)
Regular wave	-	7.1	12.1
Irregular wave	JONSWAP, γ=3.3	7.4	12.0

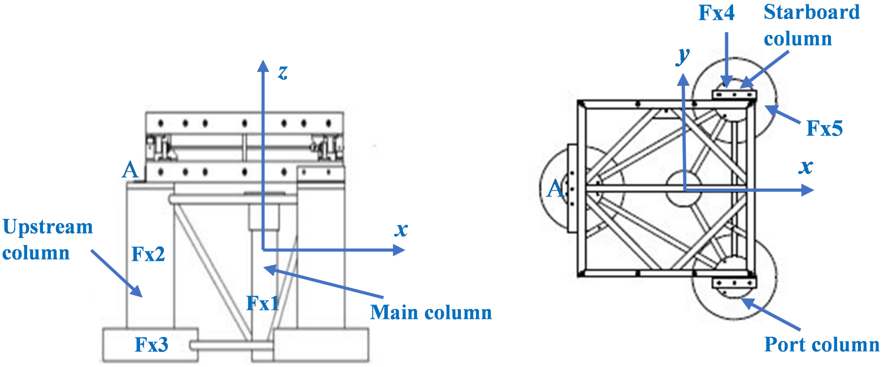

(a) Side view *(b) Top view*

Figure 2.3: Side and top view of the constrained model

Table 2.3: Specifications for surge forced oscillation in the OC6 project

Amplitude (m)	Period (s)	A/L
30.07	104.5	1.75E-3
9.54	31.2	6.21E-3
3.37	21.0	4.93E-3

system in the OC5 project. The mooring system configuration is shown in Fig. 2.5. The same coordinate system as the one used in the first validation campaign was defined in this part (shown in Fig. 2.5). The global motions, such as surge (x-displacement), heave (z-displacement) and pitch (y-rotation), the mooring line tensions at each fairlead were measured. For this configuration, the decay motions in still water and responses to the irregular wave (Table 2.2) were investigated. The initial offsets for the surge, heave and pitch decay are given in Table 2.4.

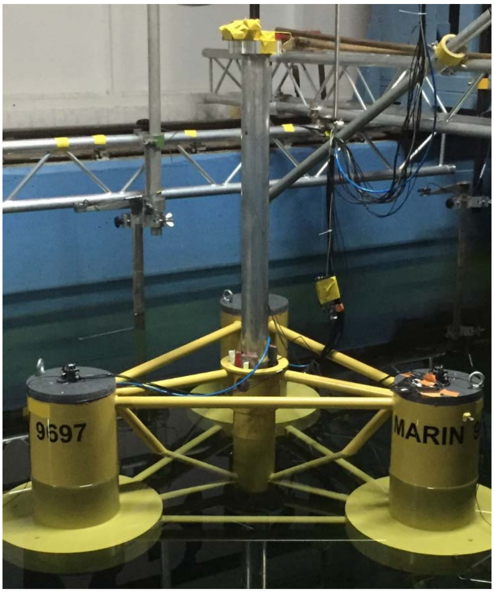

Figure 2.4: The floating semi-submersible platform with rigid tower [25]

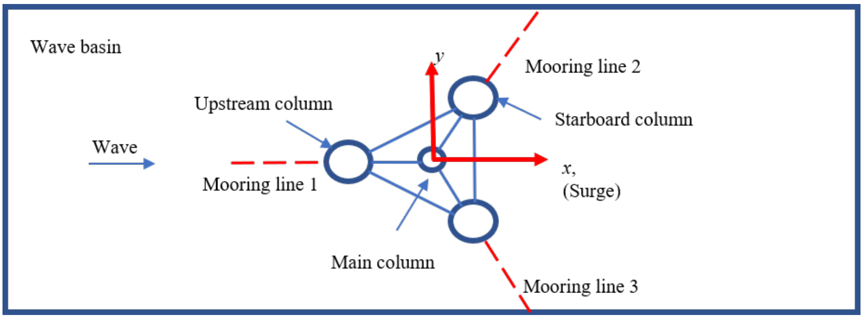

Figure 2.5: Top view of mooring system in the OC6 project

More information about the experiment setup and definition of semi-

Table 2.4: Specifications for free decay tests in the OC6 project

Mode	Initial offset
Surge	-1.86 m
Heave	-1.06 m
Pitch	-2.21°

submersible platform can be found in the definitions of the OC6 [25] and OC5 [24] projects. The total experimental uncertainty analysis was carried out by Robertson et al. [115]. The uncertainty in the measured wave elevation is estimated as 0.03 m. The uncertainty of wave loads on the constrained platform is about 2% for the measured force and 5% for the measured moments [25].

E2: Phase II of OC5 project

As a connection between superstructures and supporting structures of FWTs, the tower base is important for the safety and reliability of the FWTs. In Phase I of the OC6 project, the tower base loads were not measured. The experimentally measured tower base loads from Phase II of the OC5 project were used to validate the numerical simulations in the current research.

In Phase II of the OC5 project, the turbine was a 1:50 scaled horizontal-axis model of the NREL 5 MW reference wind turbine with a flexible tower affixed atop a semi-submersible platform which had the same geometry as the platform in the OC6 project, as shown in Fig. 2.6. The system was moored using brass chain in a catenary mooring system. The azimuth angles of mooring line were the same as they were in the OC6 project, as shown in Fig. 2.5. The tower base loads in response to an irregular wave (Table 2.5) were measured. The same coordinate system as the one used in the OC6 project was defined in this part. More information on the experiment setup can be found in Goupee et al. [116] and Wendt et al. [117]. The uncertainty analysis of experiment were given in Robertson et al. [118]. The main properties of the system and the parameters of the selected irregular wave following the JONSWAP wave spectrum in the OC5 and OC6 projects are compared in Table 2.5.

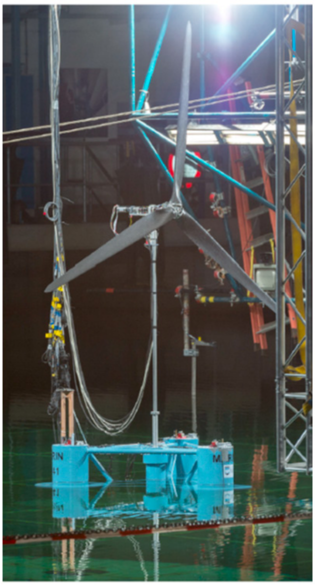

Figure 2.6: Instrumented OC5-DeepCwind model in the MARIN offshore basin [27]

Table 2.5: Comparisons of the moored semi-submersible FWT between OC5 and OC6 project

	OC5 project	OC6 project
Water depth (m)	200	180
Mass (kg)	1.3958E+7	1.419625E+7
Draft (m)	20	20
CM location below SWL (m)	8.07	7.53
Roll inertia about system CM (kg-m^2)	1.3947E+10	1.2898E+10
Pitch inertia about system CM (kg-m^2)	1.5552E+10	1.28518E+10
Yaw inertia about system CM (kg-m^2)	1.3692E+10	1.4189E+10
Mooring line pretension (N)	1.112E+6	1.11225E+6
Significant wave height (m)	7.1	7.4
Peak period (s)	12.1	12
Peak enhancement factor (-)	2.2	3.3

Chapter 3

Numerical Modelling and Response Metrics

This chapter describes the numerical models that are utilised in this research, including the engineering model based on potential flow theory and the fully nonlinear Navier-Stokes/VOF model (CFD method). The approaches to estimate the QTF values and added mass and damping from the time-domain simulations (or experiments) are also given together with the methodology of applying the nonlinear hydrodynamics from the CFD simulations in an engineering tool. Finally, a set of response metrics used to represent the important physical quantities of interest is summarized.

3.1 Engineering model

An engineering model based on potential flow theory has been built using the software SIMA, developed by SINTEF Ocean. For the time-domain analysis of FWTs in the current research, two main built-in modules are engaged: SIMO [38] and RIFLEX [39]. Generally, SIMO can take various kinds of hydrodynamic loads into account while RIFLEX is a non-linear finite element solver which can use beam and bar elements to model the system based on small strain theory. In the current simulations, the model is built based on the set-up of experiments (Section 2.3.1), rather than the full scale FWT. Hence, the floater and the rotor-nacelle-assembly (RNA) are modelled as rigid bodies, while the mooring lines and tower are represented as nonlinear bar or beam elements, respectively. The hydrodynamic loads on the mooring lines can be calculated by the Morison's equation.

The hydrodynamic loads on the floater are estimated using different theories depending on the size of the components. For large-volume structures, such as columns and heave plates shown in Fig. 1.5, diffraction and radiation are relatively important and potential flow theory is used. For slender structures with small diameters compared with the wave length, such as pontoons and cross braces shown in Fig. 1.5, Morison's equation is used.

The semi-submersible floater is represented by a 6-DOF rigid body. The time-domain equations of motions can be represented as:

$$[\boldsymbol{M}+\boldsymbol{A}(\infty)]\ddot{\boldsymbol{x}}(t)+\int_{-\infty}^{\infty}\boldsymbol{K}(t-\tau)\dot{\boldsymbol{x}}(\tau)d\tau+\boldsymbol{C}\boldsymbol{x}(t)=\boldsymbol{F}^{(\boldsymbol{1})}+\boldsymbol{F}^{(\boldsymbol{2})}+\boldsymbol{F}^{(\boldsymbol{D})}+\boldsymbol{F}^{(\boldsymbol{R})}, \tag{3.1}$$

where $\boldsymbol{M}$ is the mass matrix of the floater, $\boldsymbol{A}(\infty)$ is the infinite-frequency added mass matrix, $\ddot{\boldsymbol{x}}$, $\dot{\boldsymbol{x}}$, $\boldsymbol{x}$ are acceleration, velocity and displacement vectors of the floater, respectively. $\boldsymbol{K}(t-\tau)$ is a matrix of retardation functions which represent the fluid memory and can be calculated from the frequency-dependent damping. $\boldsymbol{C}$ is the linear hydrostatic restoring matrix, $\boldsymbol{F}^{(\boldsymbol{1})}$ is a vector of first-order wave excitation forces, $\boldsymbol{F}^{(\boldsymbol{2})}$ contains the second-order mean, rapidly and slowly varying wave drift forces, $\boldsymbol{F}^{(\boldsymbol{D})}$ represents the forces and moments due to Morison-type viscous drag and $\boldsymbol{F}^{(\boldsymbol{R})}$ are the forces from RIFLEX elements, such as mooring lines and tower.

For the columns/heave plates of floater, the first-order ($\boldsymbol{F}^{(\boldsymbol{1})}$ in Eq. 3.1) and second-order ($\boldsymbol{F}^{(\boldsymbol{2})}$ in Eq. 3.1) wave-excitation forces are estimated based on the wave force transfer functions from potential flow solvers, such as WAMIT [33] or WADAM [119], which also provide the frequency-dependent potential added mass and damping. The pontoons/cross braces contribute to the added mass through the inertia term of Morison's equation (added mass coefficient is 1.0), which is frequency-independent. The retardation functions in Eq. 3.1 are calculated based on the frequency-dependent potential damping ($\boldsymbol{b}(\boldsymbol{\omega})$)

$$\boldsymbol{K}(\tau)=\frac{2}{\pi}\int_{0}^{\infty}\boldsymbol{b}(\omega)\cos\omega\tau d\tau. \tag{3.2}$$

The infinite-frequency added mass ($\boldsymbol{A}(\infty)$ in Eq. 3.1) is then determined to give the best match between the added mass calculated from the retardation function (after truncation) and the frequency-dependent potential added mass together with the contributions of pontoons/cross braces.

In addition, viscous effects are considered by applying drag forces from Morison's equation. A constant transverse drag coefficient (0.774, based on towing tests [25]) is applied for each component of the floater while the axial drag coefficient ($C_{da}=2.48$, based on previous comparisons of a similar engineering tool with experimental data from the DeepCwind test campaign [23]) is applied for the heave plates of the floater. The axial drag force on the heave plate (F_{DA}) is calculated based on Eq. 3.3. D is the diameter of the heave plate. U is the water particle velocity along the axial direction.

$$F_{DA} = \frac{1}{2}\rho_{water}C_{da}\frac{\pi D^2}{4}U|U| \tag{3.3}$$

When external waves, such as the experimental measured waves or the calculated waves in CFD methods, are input into SIMA, they are treated as a superposition of linear regular waves at different frequencies. The wave potential of each regular wave (Φ_i) is, according to Airy's theory, expressed by

$$\Phi_i = \frac{\zeta_{ai} g}{\omega_i}\frac{\cosh k_i(z+d)}{\cosh k_i d}\cos(\omega_i t - k_i x + \phi_{\zeta i}), i = 1...N, \tag{3.4}$$

where ζ_{ai} is wave amplitude of each component, ω_i is wave circular frequency, d is water depth, k_i is wave number and $\phi_{\zeta i}$ is wave component phase angle. Then the wave velocity ($\boldsymbol{U}$) is calculated by

$$\boldsymbol{U} = \nabla\boldsymbol{\Phi} = \nabla\left(\sum_{N}\Phi_i\right). \tag{3.5}$$

This linear approach considers the wave steepness as a small quantity, which may not be a realistic assumption in all conditions.

3.1.1 Potential flow theory

The solver (WAMIT [33] or WADAM [119]) calculates wave loads on the offshore structures based on the potential flow theory which assumes the flow to be incompressible, inviscid, irrotational and solves Laplace's equation subjected to appropriate boundary conditions [120].

Based on the first-order potential flow theory, the first-order wave loads can be solved at the mean position of the body with linearized boundary conditions and the resulting loads oscillate with the incident wave frequency. The first-order problem is split in two sub-problems: small-amplitude harmonic waves on a stationary rigid body (diffraction problem), and small rigid body motions in still water (radiation problem). By the Haskind relations, only one of these two sub-problems must be solved. Using, for example, a source distribution technique, the first-order velocity potential $\Phi^{(1)}$ solving the wave-body interaction problem can be obtained.

The solution for the first-order velocity potential includes the incident wave and the diffraction velocity potential estimated from diffraction problem and the radiation velocity potential calculated from radiation problem. Then the first-order wave loads ($\boldsymbol{F}^{(I)}$) are obtained by integrating the linear hydrodynamic pressure along the mean wetted surface of the structure (S_{B0}):

$$\boldsymbol{F}^{(I)} = \int_{S_{B0}} -\rho \Phi_t^{(1)}(x,t) \boldsymbol{n} dS. \tag{3.6}$$

The solution consists of the first-order wave excitation forces ($\boldsymbol{F}^{(\mathbf{1})}$), frequency-dependent potential added mass ($\boldsymbol{A}(\omega)$) and damping ($\boldsymbol{B}(\omega)$) which are required for the time-domain simulations described in Eq. 3.1. Different wetted surfaces where the linear hydrodynamic pressures are integrated gives the first-order wave loads on different components of floater.

For the semi-submersible FWTs with natural frequencies outside of the wave excitation range, second-order wave loads may also be important. The second-order wave loads are obtained by integration of all product of pressure and normal vector to the surface which gives second-order force contributions over the mean wetted surface (S_{B0}) and by integration of first-order pressure along the instantaneous wetted surface (S_B):

$$\boldsymbol{F}^{(II)} = \int_{S_{B0}} \{p^{(1)}(\boldsymbol{\alpha}^{(\mathbf{1})} \times \boldsymbol{n}) + p^{(2)}\boldsymbol{n} + p^{(0)}(\boldsymbol{\alpha}^{(\mathbf{2})} \times \boldsymbol{n})\} dS + \int_{S_B} p^{(1)} \boldsymbol{n} dS, \tag{3.7}$$

where $p^{(0)}$, $p^{(1)}$, $p^{(2)}$ refer to the hydrostatic, first-order and second-order pressure, respectively, $\boldsymbol{\alpha}^{(\mathbf{1})}$ and $\boldsymbol{\alpha}^{(\mathbf{2})}$ represent the oscillatory first-order and second-order angular motion vector and $\boldsymbol{n}$ is the normal vector to the body boundary.

The pressure up to the second-order can be expressed as:

$$p = -\rho g z - \rho \Phi_t^{(1)} - \rho \Phi_t^{(2)} - \frac{1}{2} \rho \nabla \Phi^{(1)} \cdot \nabla \Phi^{(1)}, \tag{3.8}$$

where $\Phi^{(2)}$ represents the second-order velocity potential includes both sum-frequency and difference-frequency components. According to the research work by Pinkster [30], the second-order wave loads ($\boldsymbol{F}^{(II)}$) can be decomposed into five components:

$$\begin{aligned}\boldsymbol{F}^{(II)} = &-\int_{WL}\frac{1}{2}\rho g(\zeta_r^{(1)})^2\boldsymbol{n}dl + \boldsymbol{\alpha^{(1)}}\times(\boldsymbol{M}\ddot{\boldsymbol{X}}_{\boldsymbol{G}}^{(\boldsymbol{1})})\\ &-\int_{S_{B0}}\{-\frac{1}{2}\rho(\nabla\Phi^{(1)})^2-\rho(\boldsymbol{X}^{(\boldsymbol{1})}\nabla\Phi_t^{(1)}-\rho\Phi_t^{(2)})\}\boldsymbol{n}dS.\end{aligned} \tag{3.9}$$

The first term represents the contribution of the first-order wave elevation ($\zeta_r^{(1)}$), the second term represents the contribution of the first-order force due to body rotations ($\boldsymbol{\alpha}^{(\boldsymbol{1})}$), the third term comes from the quadratic term of fluid velocity, the fourth term is due to the coupling of the first-order pressure gradient and first-order motion, and the last term comes from the contribution of second-order velocity potential. Here, WL represents the waterline.

The slowly-varying wave drift force is calculated based on the difference-frequency velocity potential while the rapidly-varying force is estimated based on the sum-frequency component. Considering the natural frequencies of the semi-submersible FWT used in the current research, the slowly-varying wave drift force is of greater interest than the rapidly-varying term. For a seastate with N wave components of frequency ω_i, amplitude A_i and phase ϵ_i, the slowly varying wave drift forces due to potential flow $\boldsymbol{F}^{(d)}$ can be written as:

$$\begin{aligned}\boldsymbol{F}^{(d)}(t) = \sum_{i=1}^{N}\sum_{j=1}^{N}A_iA_j[&\boldsymbol{T}_{ij}^{(c)}\cos\{(\omega_i-\omega_j)t+(\epsilon_i-\epsilon_j)\}+\\ &\boldsymbol{T}_{ij}^{(s)}\sin\{(\omega_i-\omega_j)t+(\epsilon_i-\epsilon_j)\}].\end{aligned} \tag{3.10}$$

The coefficients $\boldsymbol{T}_{ij}^{(c)}$ and $\boldsymbol{T}_{ij}^{(s)}$ are the quadratic transfer functions (QTFs) for the difference-frequency wave loads. The computation of the full QTF requires an additional mesh of the free surface as shown in Fig. 3.1. The mesh size of the free surface is smaller near the floater. The radius of free surface is about three times larger than the center-center distance between offset columns. The diagonal values of the full QTF matrix represent the mean wave drift forces which only depend on the first-order potential flow solutions.

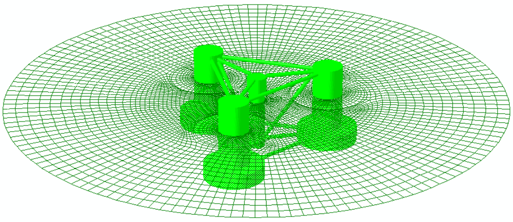

Figure 3.1: Mesh of floater and free surface in HydroD/WADAM

3.2 Navier-Stokes/VOF model

In order to more accurately predict the hydrodynamic loads and motions of FWTs, we should solve the Navier-Stokes equations. Although a direct solution is not feasible, CFD methods assuming incompressible flow and with proper turbulence modelling are considered as higher-fidelity numerical methods to account for relevant linear and nonlinear hydrodynamic effects including viscous effects. A well-known open-source CFD-toolbox is OpenFOAM [68]. Throughout this work, the waveFoam solver is used when structure is considered fixed and rigid, while the waveDyMFoam solver is utilised when rigid body motions are considered. The waveFoam or waveDyMFoam solver is based on the interFoam or interDyMFoam solver provided by OpenFOAM, respectively, which is extended with the wave generation and absorption toolbox, waves2Foam, developed by Jacobsen et al. [121]. The two solvers use the two-phase incompressible Navier-Stokes equations in combination with a volume of fluid (VOF)-surface capturing scheme [122] to compute the fluid flow around the semi-submersible. In order to simulate the flow-dependent motion of a floating structure, the Navier-Stokes/VOF solver is coupled with a 6-degree of freedom (DOF) motion solver in the waveDyMFoam solver together with the implementation of a dynamic mesh and motion restraints. Furthermore, a fully nonlinear potential flow solver, Oceanwave3D [123], is coupled with the waveFoam solver to minimize numerical diffusion and reduce the computational time for the irregular wave case [124].

3.2.1 Governing equations

The governing equations in the Navier-Stokes/VOF solver consist of mass conservation and momentum conservation for an incompressible flow of air and water:

$$\frac{\partial u_i}{\partial x_i} = 0, \tag{3.11}$$

$$\frac{\partial \rho u_i}{\partial t} + \frac{\partial \rho u_j u_i}{\partial x_j} = -\frac{\partial p^*}{\partial x_i} + F_{b,i} + \frac{\partial}{\partial x_j}[\mu_{eff}\frac{\partial u_i}{\partial x_j}], \tag{3.12}$$

where $u_i(i = x, y, z)$ are the fluid velocities in Cartesian coordinates, ρ is the fluid density, p^* is pressure in excess of the hydrostatic pressure, F_b is an external body force including gravity and μ_{eff} is the effective dynamic viscosity. For laminar flow, μ_{eff} is equal to the laminar dynamic viscosity. For turbulent flow, it should include the turbulent dynamic viscosity $\rho \upsilon_t$.

The local density ρ and the effective dynamic viscosity μ_{eff} are defined by the volume fraction α which is bounded between 0 (air) and 1 (water). The turbulent dynamic viscosity $\rho \upsilon_t$ is neglected in laminar flow model in *Paper 1*.

$$\rho = \alpha \rho_{water} + (1 - \alpha)\rho_{air} \tag{3.13}$$

$$\mu_{eff} = \alpha \mu_{water} + (1 - \alpha)\mu_{air} + \rho \upsilon_t \tag{3.14}$$

The air-water interface is tracked by the VOF method [122] in OpenFOAM. The volume fraction is advanced in time once the velocity is known, following the scalar advection equation:

$$\frac{\partial \alpha}{\partial t} + \frac{\partial u_i \alpha}{\partial x_i} + \frac{\partial u_{r,i}\alpha(1 - \alpha)}{\partial x_i} = 0. \tag{3.15}$$

Using a standard finite-volume approximation for solving Eq. 3.15 will lead to significant smearing of the interface which is vastly reduced by the introduction of the artificial velocity u_r. It is only active in the vicinity of the interface where $0 < \alpha < 1$. This is thoroughly discussed in Berberović et al. [125]. To ensure the boundedness of the solution, a multi-dimensional flux limited scheme (MULES) is used.

Despite the existence of the interface compression term, the air-water interface can be smeared over several cells. That means there is no specific location of the interface. The wave gauge functionality in waves2Foam is used to identify the location of free-surface. One or more wave gauge positions are defined in the numerical domain. The free surface elevation ζ, relative to the still water level, is given by:

$$\zeta = \int_{x_0}^{x_1} \alpha dz - d, \tag{3.16}$$

where x_0 and x_1 are user-defined start and end points in the vertical line over which the α field is integrated. d is the water depth of the still water level.

3.2.2 Turbulence modelling

Turbulent effects are incorporated in the governing equations by using different transport equations to calculate the turbulent kinematic viscosity v_t. The $k-\omega$ SST turbulence model [126], a blending of the $k-\omega$ [127] and the $k-\epsilon$ [128] models, has shown good performance in simulating two-phase flow and wave elevation [129–131] and is implemented in the current research. The equations for the incompressible $k-\omega$ SST turbulence model for a single fluid in OpenFOAM are given as:

$$\frac{\partial k}{\partial t} + \frac{\partial u_j k}{\partial x_j} - \frac{\partial}{\partial x_j}[(\nu + \sigma_k \nu_t)\frac{\partial k}{\partial x_j}] = P_k - \beta^* \omega k, \tag{3.17}$$

$$\frac{\partial \omega}{\partial k} + \frac{\partial u_j \omega}{\partial x_j} - \frac{\partial}{\partial x_j}[(\nu + \sigma_\omega \nu_t)\frac{\partial \omega}{\partial x_j}] = \frac{\gamma}{\nu_t} G - \beta \omega^2 + 2(1 - F_1)\frac{\sigma_{\omega 2}}{\omega}\frac{\partial k}{\partial x_j}\frac{\partial \omega}{\partial x_j}, \tag{3.18}$$

where k is the turbulent kinetic energy, P_k is the production term of k, ν is kinematic viscosity, ν_t is the turbulent kinematic viscosity and ω is the specific dissipation rate. This is thoroughly described by Menter et al. [126].

For the two-phase fluid, the original $k-\omega$ SST turbulence model causes significant wave damping which is triggered by the increasing turbulent viscosity around the air-water interface [132]. This increase is induced by the large production of turbulent kinetic energy P_k, in that zone which is linked to the large velocity gradient around the air-water interface due to the large density ratio (around 1000/1). None of the incompressible two-phase solvers implemented in OpenFOAM includes the density explicitly. Only the turbulent kinematic viscosity ν_t is modelled instead of the turbulence dynamic viscosity $\mu_t = \rho \nu_t$. In a two-phase flow, the density is variable around the air-water interface and should be included in the turbulence equations. Therefore, a modified solver is built to explicitly consider the density in the incompressible $k-\omega$ SST model based on the work by Fan and Anglart [133].

All CFD simulations are run at model scale. For the regular wave in Table 2.2 (*Paper 1*), the KC and Reynolds numbers (Re) on the constrained floater are shown in Table 3.1. The KC number is around 1 for most of components and weak vortices are expected in the CFD simulations. Although the Reynolds numbers are on the order of $10^4 - 10^5$, previous studies considering the same geometry suggest that the turbulence model is not essential for the CFD simulations due to the low KC number of upper column and heave plate [84]. Therefore, for the investigation of nonlinear wave loads under the regular wave, a laminar flow model and the turbulence model are compared (*Paper 1*). The CFD with turbulence model shows better performance and is implemented for the rest of study in this thesis.

Table 3.1: KC and Reynolds numbers for different parts of the constrained floater under the regular wave [134] (model scale)

	Main column	Upper column	Heave plate	Cross brace
KC(-)	2.89-3.43	1.86	0.93	13.94
Re($\times 10^5$)	0.33-0.40	0.62	1.23	0.08

3.2.3 Boundary conditions

To solve the governing equations of the Navier-Stokes/VOF solver, boundary conditions are imposed to all the surfaces in the numerical domain, including the surface of a semi-submersible floater. The general denomination of boundary surfaces is given in Fig. 3.2. These conditions inherently depend on the type of problem to be solved. The inlet and outlet boundary conditions in the coupling of OceanWave3D are given in Section 3.2.6.

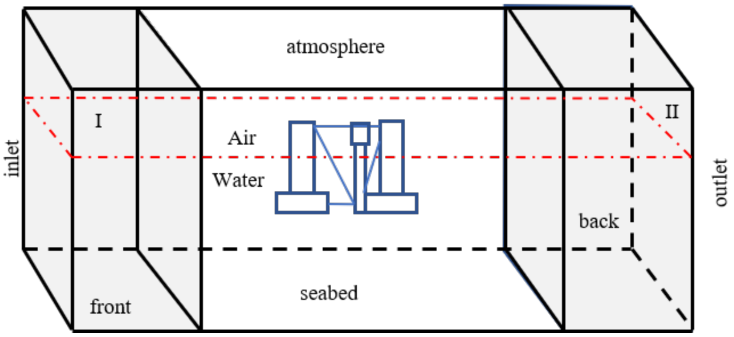

Figure 3.2: Schematic representation of computational domain in the CFD simulations

- The velocity and the α field at the inlet are given by the applied wave theory (stream function wave theory for *Paper 1* and second order bichromatic wave theory [135] for *Paper 2*) if needed or are specified as zero normal gradient (*Paper 3*). The pressure is specified as zero normal gradient. For the cases with waves (*Paper 1* and *2*), k is fixed at zero and ω is set as 0.001 $1/s$ whereas both are set as zero normal gradient if no wave (*Paper 3*).

- At the outlet, front, back and seabed, all the boundaries are specified as zero normal gradient.

- For the atmosphere, the total pressure is set as zero and an atmospheric boundary condition is set for the velocity and the α field. This means that air and water are allowed to leave the numerical domain, while only air is allowed to flow back in. k is fixed at zero and ω is specified as zero normal gradient.

- On the floater surface, the pressure is set as zero normal gradient. For the laminar flow model, a slip condition is applied, which means the effect of viscosity and turbulence generation are neglected. For the turbulent flow model, a no-slip boundary condition (zero velocity) is specified, and k is fixed at $1e^{-5}$ m^2/s^2 and ω is set as 1.0 $1/s$.

- A continuous wall function based on Spadling's law [136] switching between low and high Reynolds numbers is implemented for the turbulent viscosity. Hence, it requires that the non-dimensional wall distance y^+ should be between 10 and 300.

- In *Paper 3*, for the free decay, the displacement of the floater is calculated based on the total forces, while a prescribed sinusoidal displacement is applied for the forced oscillation. The displacements of other boundaries are set to zero.

Even though the density is explicitly considered in the turbulence model of the modified solver, the turbulence viscosity around air-water interface increases at the end of longer simulations if a uniform turbulent viscosity is implemented. Therefore, different values of the turbulent kinetic energy (k) and specific dissipation rate (ω) at the floater and other boundaries shown in this section are applied to accurately simulate the flow around the floater and reduce the influences of increasing turbulence viscosity around air-water interface.

3.2.4 Relaxation zones

The relaxation zones (Region I and II in Fig. 3.2) in the waves2Foam toolbox are implemented to avoid wave reflection from outlet boundary (II) and also to prevent internally reflected waves (I). An arbitrary shape can be defined. In the present work, the relaxation zone is rectangular. In the relaxation zones, the velocity and the α field are updated each time step according to

$$\psi = \chi\psi_{target} + (1-\chi)\psi_{computed}, \tag{3.19}$$

where ψ_{target} are the target solution at the inlet or outlet boundary condition and $\psi_{computed}$ are the computed solution obtained from the Navier-Stokes/VOF solver. The weighting factor for each of the two solution (χ) is determined by

$$\chi(\xi) = 1 - \frac{\exp(\xi^{\beta}) - 1}{\exp(1) - 1}, \tag{3.20}$$

where ξ is the local coordinate in the relaxation zone, which, as Fig. 3.3 indicates, is zero at the outer part of the relaxation zone and one at the inner edge. β is the shape factor and the default value, $\beta = 3.5$ is used in the present work.

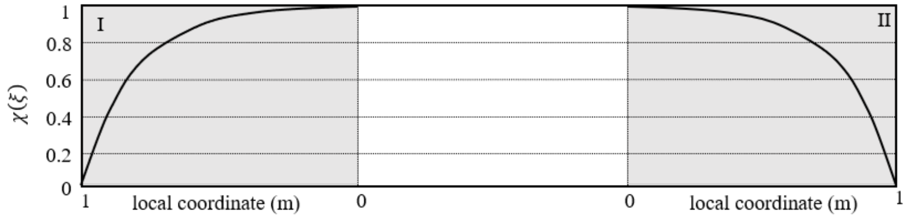

Figure 3.3: Schematic representation of the spatial weighting factor in the relaxation zone of CFD numerical domain

3.2.5 Coupling of Navier-Stokes/6-DOF solver

In *Paper 3*, a coupled fluid-structure model is applied to simulate the flow-dependent motion of a floating structure in Navier-Stokes/VOF solver. Total forces on the body are calculated by solving the Navier-Stokes equations for fluid and 6-DOF motion equations are used to obtain the rigid body motions. The implementation of a tighter coupling between fluid and motion solver can solve the instabilities of solutions caused by the discrete time integration [137]. OpenFOAM provides two different methods:

an under-relaxation and a predictor-corrector method [138]. The under-relaxation method applies an under-relaxation factor to the acceleration of the structure when updating the displacement in the 6-DOF loop. The applied under-relaxation factor acts as a low-pass filter to remove the high frequency oscillations of acceleration from the time integration. By doing so, the solver is more stable. However, this method also introduces a diffusive term to the numerical model which has a negative effect on the convergence rate of the solution. The predictor-corrector method implements a subiteration loop around the Navier-Stokes and 6-DOF solvers. The subiteration loop allows the numerical model to make an initial 'predictor' step and one or more 'corrector' steps for update the pressure fields. At the last subiteration loop, the under-relaxation factor shold be reset to 1 to ensure time consistency. Based on Bruinsma's work [83], the predictor-corrector method is more effective at eliminating the oscillations in the force profile. In order to reduce the computational time, the fixed number of subiteration loops to correct pressure in the predictor-corrector method is replaced with a quite small tolerance ($10^{-8}\ Pa$) when solving for the pressure. No significant oscillation is seen in the results of force profiles.

A deforming mesh technique is employed to conform to the moving boundary of the floater. For the free decay, the solver allows for specification of an innerDistance and an outerDistance. The mesh nodes within innerDistance move with the floater, while the mesh nodes between innerDistance and outerDistance morph. No morphing occurs for the mesh nodes outside the outerDistance. The solver of the forced oscillation uses a diffusivity function to control how the mesh morphing is distributed: farther away from the floater, there is less mesh morphing. The diffusivity function is the square of the inverse distance between the floater and mesh position.

The restraints for the floater are implemented by a linear spring without considering interaction with the fluid. The spring is given a simple constant stiffness and a rest length in the free decay. The force in the spring follows Hooke's law. When the length of spring is equal to the rest length, the force in the spring is zero.

3.2.6 Coupling of Navier-Stokes/OceanWave3D

In *Paper 1*, for the irregular wave case, an efficient domain decomposition strategy is implemented. As illustrated in Fig. 3.4, the smaller CFD domain Γ where the Navier-Stokes/VOF equations are solved is coupled with a larger potential flow (OceanWave3D [123]) domain Ω, where a larger mesh size can be applied. The coupling zones are the relaxation zones (I and II) in the waves2Foam toolbox. The coupling strategy is based on one-way coupling, where the information only propagates from outer domain to inner domain. No target solution for the air velocity is provided in the potential flow solver, and zero air velocity is strongly imposed on the coupling domain boundaries. Domains A and B are the relaxation zones in the potential flow solver. More details regarding the coupling method can be found in the work of Paulsen et al [124].

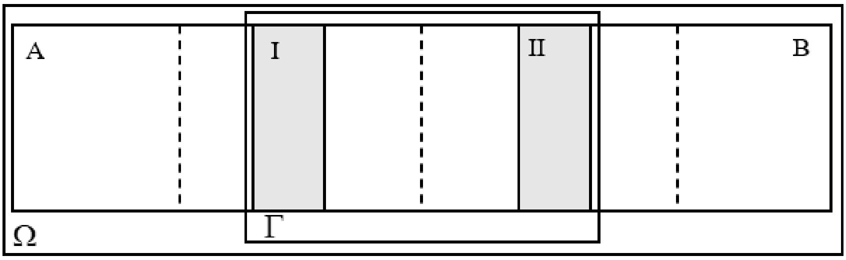

Figure 3.4: Schematic representation of the coupled potential and Navier-Stokes/VOF solver domains

As the wave maker motion is not measured in the experiment, the measured irregular wave at the center of body is used to generate a time series of wave elevation at the wave maker as an input signal at the inlet of potential flow domain, following the procedure shown by Bachynski et al. [139]. The outlet boundary of the potential flow domain is defined by setting a constant current with zero velocity. The cell size in the potential flow domain is 10 times larger than the one in the CFD domain. The center of the two computational domains is co-located with the center of the floater.

3.2.7 Computational domain

The floater at scale 1:50 was built in the CFD numerical wave tank, mimicking the experimental set-up (OC6 Phase I). The same coordinate system is also used in the CFD model, as shown in Fig. 3.5. The width (3.72 m, model scale) and water depth (3.6 m, model scale) of the numerical wave flume are equal to those of the experimental facility. The length of the numerical wave tank should be long enough to dissipate the reflected waves from the boundaries and varies based on the type of problem being investigated. In addition, the height of the air regime is set to 1 m (model scale). Fig. 3.5 shows a plan view of the numerical wave tank with floater which is placed at the origin of the numerical domain.

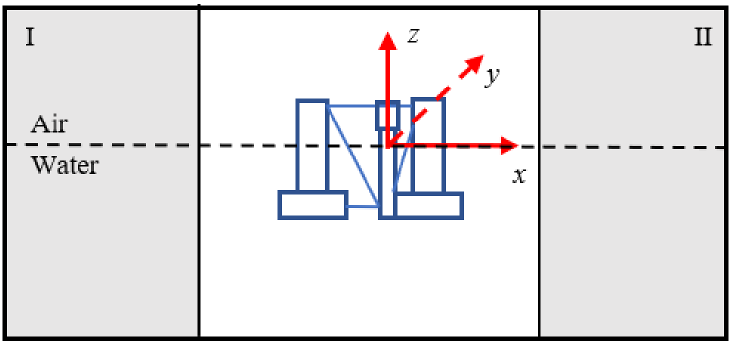

Figure 3.5: Overview of the CFD numerical wave tank with a semi-submersible FWT

3.2.8 Spatial and temporal discretization

In OpenFOAM, based on finite volume method, the computational domain is discretized into finite regions in space known as cells where the conservation principles are applied. After an initial discretization, the size of a background cell in all the directions is the same. Thereafter, the mesh needs to be refined towards the floater surface and air-water interfaces. In addition, some viscous layer cells adjacent to the floater surface are generated when the turbulence model is implemented. An example of the mesh topology is shown in Fig. 3.6. This local refinement allows for a high-resolution interface while keeping the total number of computational cells relatively low. The initial discretization and refinement vary among the papers in Appendix B. In each case, three different mesh topologies are chosen to carry out the mesh convergence study. The results are presented in the *Paper 1, 2* and *3* in Appendix B.

The Courant-Friedrichs-Lewy (CFL) condition is implemented to determine the time step. The fixed time step is used for the constrained condition and four different time steps are chosen to carry out the time step convergence study. The results can be found in *Paper 1* and *2* in Appendix B. The adjusted time step is implemented for the case with dynamic mesh (*Paper 3*). To ensure numerical stability, the maximum Courant number should have a value between zero and one, such that a fluid particle cannot move further than the length of a computational cell within a single time step. A maximum Courant number of 0.5 is utilised throughout the simulations in *Paper 3*.

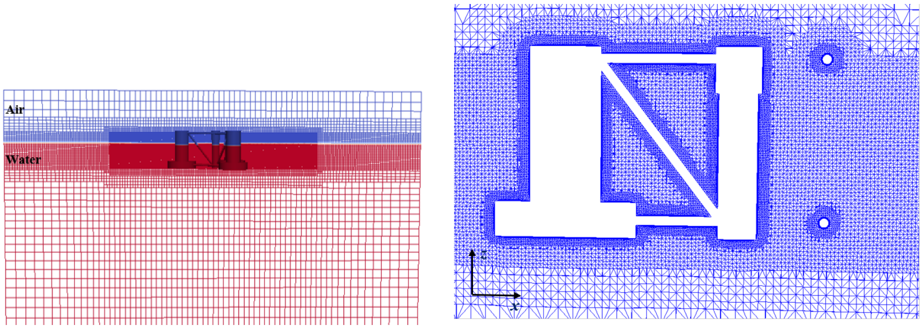

(a) Side view *(b) Cross section at $y = 0$*

Figure 3.6: Refined mesh towards the floater and the free surface

3.3 Estimation of QTF values

Ideally, one would like to carry out irregular wave simulations to investigate the difference-frequency wave loads. However, the substantial computational time of the CFD method makes it difficult to carry out long simulations of irregular waves. Additionally, CFD simulations of irregular waves may suffer from significant wave damping triggered by an increase in the viscosity around the air-water interface [132]. Therefore, bichromatic waves are applied to estimate the difference-frequency wave loads and QTF values [140, 141].

Bichromatic waves are generated by adding together two regular waves with different wave frequencies. In the current research, the first order components of the bichromatic waves are close to the peak period of the irregular wave in Table 2.5 while the difference frequency aligns with either the surge or pitch natural frequency of the FWT where the largest wave-induced responses can be excited in irregular waves [142]. The wave amplitudes (around 1.75 m) of wave components are determined by making the calculated maximum wave height when two waves are added linearly close to the significant wave height of the irregular-wave (7.1 m). As the wave period decreases, the wave steepness increases when keeping the wave amplitude constant, and the generated wave elevation in the CFD simulation attenuates over time. Hence, smaller wave amplitudes are applied for shorter wave periods. The parameters of the bichromatic waves are described in *Paper 2* in Appendix B.

The harmonic components (mean values and all first- and second- order harmonics) of wave elevation and wave loads are identified by fitting a second order expansion model to the steady-state part of the numerical time signal with a least squares procedure. In bichromatic waves, the wave elevations and wave loads on a fixed floater are approximated by Eq. 3.21. Components above the second order are found to be negligible.

$$\begin{aligned} I(t) = \bar{I} &+ I_1^{c(1)}\cos(\omega_1 t) + I_1^{s(1)}\sin(\omega_1 t) + I_1^{c(1)}\cos(\omega_2 t) + I_1^{s(1)}\sin(\omega_2 t) \\ &+ I_2^{c(2)}\cos(2\omega_1 t) + I_2^{s(2)}\sin(2\omega_1 t) + I_2^{c(2)}\cos(2\omega_2 t) + I_2^{s(2)}\sin(2\omega_2 t) \\ &+ I^{c(+)}\cos\{(\omega_1+\omega_2)t\} + I^{s(+)}\sin\{(\omega_1+\omega_2)t\} \\ &+ I^{c(-)}\cos\{(\omega_1-\omega_2)t\} + I^{s(-)}\sin\{(\omega_1-\omega_2)t\}, \end{aligned} \tag{3.21}$$

where I is the measured quantity of interest (the wave elevation η or wave loads F), and ω_1, ω_2 are the two incident wave frequencies. Each harmonic component is represented by a sum of cosine and sine parts, thus allowing the identification of the phase. The first-order harmonics at the incident wave frequencies I_1, I_2 and the second-order difference-frequency component $I^{(-)}$ are all computed in this way. An example is shown in Fig. 3.7.

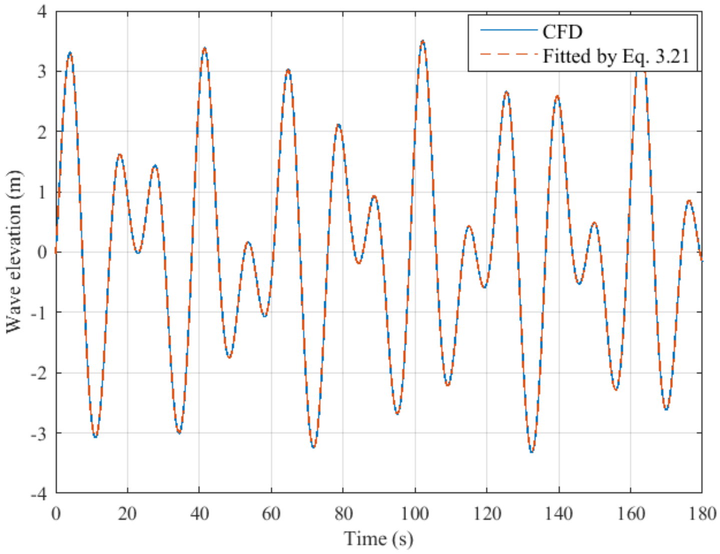

Figure 3.7: Bichromatic wave elevations

The QTF values can be represented by a series of complex numbers ($a+bi$ for $\omega_1 > \omega_2$ and $a-bi$ for $\omega_1 \leqslant \omega_2$). Hence, the difference-frequency wave loads on a fixed floater ($\boldsymbol{F}^{(2)}$ in Eq. 3.1) in bichromatic waves are approximated by

$$\begin{aligned}
\boldsymbol{F}^{(2)}(t) &= \boldsymbol{F}_{12}(t) + \boldsymbol{F}_{21}(t) \\
&= \mathrm{Re}[(A_1 A_2\{(a+bi)e^{-i((\omega_1 t-\epsilon_1)-(\omega_2 t-\epsilon_2))} \\
&+ (a-bi)e^{-i((\omega_2 t-\epsilon_2)-(\omega_1 t-\epsilon_1))}\}] \\
&= 2A_1A_2\{[a\cos(\epsilon_1-\epsilon_2)+b\sin(\epsilon_1-\epsilon_2)]\cos(\omega_1 t-\omega_2 t) \\
&+ [-a\sin(\epsilon_1-\epsilon_2)+b\cos(\epsilon_1-\epsilon_2)]\sin(\omega_1 t-\omega_2 t)\},
\end{aligned} \tag{3.22}$$

where A_1, A_2, ω_1, ω_2, ϵ_1, ϵ_2 are the two incident wave amplitudes, frequencies and phases which can be calculated by Eq. 3.21. Given the cosine (F_d^c) and sine (F_d^s) parts of second-order difference-frequency wave loads from Eq. 3.21, the real (a) and imaginary (b) parts of the QTF value can be found by solving Eq. 3.23.

$$\begin{cases} 2A_1A_2[a\cos(\epsilon_1-\epsilon_2)+b\sin(\epsilon_1-\epsilon_2)] = F_d^c \\ 2A_1A_2[-a\sin(\epsilon_1-\epsilon_2)+b\cos(\epsilon_1-\epsilon_2)] = F_d^s \end{cases} \tag{3.23}$$

3.4 Estimation of added mass and linearized damping

Added mass and damping play a significant role in accurate prediction of FWT motions, especially near the resonance frequencies. They are characterized by two parameters: the motion amplitude (A) and period (T). The nondimensional parameters are then the KC ($KC = 2\pi A/D$) number and the Stokes number $\beta = D^2/\nu T$ with D being the diameter of column and ν being the kinematic viscosity of water. Alternatively, one of the control parameters can be replaced by the Reynolds number ($Re = KC \cdot \beta$). In the current research, several forced oscillations with different motion amplitudes around the natural periods of surge, heave and pitch motion are performed using CFD to identify the added mass and linearized damping coefficients for a semi-submersible FWT. Meanwhile, the numerical results are validated against experimental measurements including forced oscillations in surge.

In the forced oscillations, harmonic motion is imposed on the floater. The position of the floater is:

$$X(t) = A\sin(\omega t), \tag{3.24}$$

where $X(t)$ represents surge motion along the x axis, $x(t)$, heave motion along the z axis, $z(t)$, or pitch motion around y axis, $\theta(t)$. For pitch, the center of rotation is located at the origin of the coordinate system (Fig. 3.5). A is the oscillation amplitude and ω is the oscillation frequency.

The hydrodynamic force on the floater, $F_H(t)$, is obtained by subtracting the inertial force, $F_I(t)$, and the linear hydrostatic restoring force, $F_K(t)$, from the measured or simulated total force, $F_T(t)$. That is:

$$F_H(t) = F_T(t) - F_I(t) - F_K(t). \tag{3.25}$$

Expressions for the inertial force and linear hydrostatic restoring force in the experimental and numerical results are given in Table 3.2. In the CFD simulations, the estimated total force is the integral of the pressure along the surface of the floater and it does not include inertial forces. The linear hydrostatic restoring coefficient can be obtained from the variation of buoyancy loads due to small displacements in still water. Hence, the linear restoring coefficient in surge is zero and the linear restoring coefficient in heave, K_{33}, and in pitch, K_{55}, can be written as:

$$K_{33} = \rho g A_{wp}, \tag{3.26}$$

$$K_{55} = \rho g V Z_B + \rho g \int_{A_{wp}} x^2 ds, \tag{3.27}$$

where ρ is water density, g is the acceleration due to gravity, A_{wp} is the waterplane area, V is the volume of the floater, Z_B is the vertical coordinate of the center of buoyancy and the integral of Eq. 3.27 represents the waterplane area moment of inertia about y axis. In Eq. 3.27, the effect of weight is not included, because the estimated total force in the CFD simulation does not include the weight. The diameter of the main column of the floater has a sudden increase from 6.5 m to 7.7 m at 4.25 m above the still water line (see the ledge in Fig. 3.6). When the heave oscillation amplitude exceeds the distance between the ledge and the still water line, varying waterplane area is used in K_{33}.

The first harmonic component of the hydrodynamic force, $F_H^{(1)}(t)$, or moment $M_H^{(1)}(t)$, with the same frequency as the motion, ω, is extracted and decomposed into in-phase and out-of-phase components:

$$F_H^{(1)}(t) = F_{H,cos}^{(1)} \cos(\omega t) + F_{H,sin}^{(1)} \sin(\omega t), \tag{3.28}$$

$$M_H^{(1)}(t) = M_{H,cos}^{(1)} \cos(\omega t) + M_{H,sin}^{(1)} \sin(\omega t). \tag{3.29}$$

Table 3.2: Motion, inertial force and linear restoring force in the experimental and CFD simulations. In the experiments, forced oscillations were only carried out in surge.

	$X(t)$		$F_I(t)$		$F_K(t)$	
Motion	Experiment	CFD	Experiment	CFD	Experiment	CFD
Surge	$x(t)$	$x(t)$	$-m\cdot\ddot{x}(t)$	0	0	0
Heave	N/A	$z(t)$	N/A	0	N/A	$K_{33}\cdot z(t)$
Pitch	N/A	$\theta(t)$	N/A	0	N/A	$K_{55}\cdot\theta(t)$

The first-order hydrodynamic force or moment on the floater can be expressed based on the added mass (C_a) and linearized damping coefficients (C_{dx}, C_{dz}, C_ϕ) as

$$F_H^{(1)}(t) = -\rho C_a V\ddot{X}(t) - \frac{1}{2}\rho C_{dx,dz}A_s\frac{8}{3\pi}\omega A\dot{X}(t), \tag{3.30}$$

$$M_H^{(1)}(t) = -C_a I\ddot{X}(t) - \frac{1}{2}\rho C_\phi A_s R\frac{8}{3\pi}\omega A\dot{X}(t), \tag{3.31}$$

where A_s is the project area of the whole floater along x or z direction, I is the mass of moment inertia about the y axis and R is distance between the center of wetted part of the whole floater and the origin of coordinate system.

Then, the added mass and linearized damping coefficients are found:

$$C_a = \frac{F_{H,sin}^{(1)}}{\rho V\omega^2 A} \quad \text{or} \quad C_a = \frac{M_{H,sin}^{(1)}}{I\omega^2 A}, \tag{3.32}$$

$$C_{dx,dz} = \frac{F_{H,cos}^{(1)}}{4/3\pi\rho A_s\omega^2 A^2} \text{ or } C_\phi = \frac{M_{H,cos}^{(1)}}{4/3\pi\rho A_s R\omega^2 A^2}. \tag{3.33}$$

The projected area for the pitch damping coefficient (C_ϕ) is the same as the surge damping coefficient (C_{dx}). The estimated linearized damping coefficient from the CFD simulations includes both radiation damping and viscous damping.

In engineering tools, the viscous contributions of the columns/heave plates and pontoons/cross braces to the damping are taken into account by including the drag term from Morison's equation separately. Based on Morison's equation, the total viscous surge, heave force $F_{x,z-Mori}(t)$ and pitch moment $M_{y-Mori}(t)$ on the floater are evaluated by adding the viscous contributions of each part of floater.

$$F_{x,z-Mori}(t) = \sum_i \frac{1}{2}\rho C_d A_{s,i} v_i(t)|v_i(t)|, \tag{3.34}$$

$$M_{y-Mori}(t) = \sum_i \frac{1}{2}\rho C_d A_{s,i} (R_i \theta_i(t))|(R_i \theta_i(t))| R_i, \tag{3.35}$$

where C_d is the transverse and axial quadratic drag coefficients in Morison's equation (Section 3.1), $A_{s,i}$ is the projected area of each column or brace along x or z direction, $v_i(t)$ is the horizontal (surge force) or vertical (heave force) velocity and $\theta_i(t)$ is the angular (pitch moment) velocity at the center of wetted part of each part of floater and R_i is the distance between the center of the each wetted part of floater and the origin of coordinate system.

Then, the frequency-dependent linearized equivalent damping coefficients from the contribution of Morison's drag are obtained for surge (C_{dx}), heave (C_{dz}) and pitch (C_{ϕ}) damping coefficients by fitting the time series of total viscous surge, heave force and pitch moment, minimizing the error, i.e. $|F_{x,z-Mori}(t) - 1/2\rho C_{dx,dz} A_s v(t)|$ and $|M_{x,z-Mori}(t) - 1/2\rho C_{\phi} A_s t R\theta(t)|$. An example is shown in Fig. 3.8.

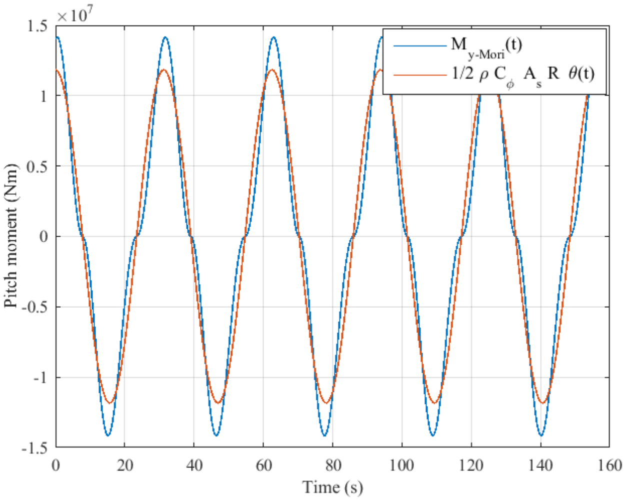

Figure 3.8: Linearized total pitch moment

3.5 Development of the engineering model

Contributions C3 and C5 in Section 1.3 are related to modifying the engineering model based on computed quantities from CFD. The difference-frequency surge force and pitch moment QTFs from potential flow solutions are modified based on the estimated difference-frequency wave loads on a restrained floater subjected to bichromatic waves in the CFD simulations (Section 3.3). The frequency-dependent added mass and damping coefficients from the first-order potential flow theory are modified based on the calculated added mass and linearized damping coefficients from CFD simulations of forced oscillations around the surge, heave and pitch natural periods (Section 3.4). The following subsections describe the procedures for these modifications.

3.5.1 Modification of QTF values

When modifying the QTF values used in the engineering model, it is important to consider which effects are included. In the second-order potential flow solutions, the second-order wave loads consist of quadratic contributions from the first-order solutions, and contributions given by the second-order velocity potential (Eq. 3.9).

The computational cost for the CFD simulations with dynamic mesh increases sharply compared to the cost for the static mesh, especially considering longer simulations for capturing the low-frequency responses. Hence, when estimating the QTF values from CFD simulations, the floater is restrained. The Morison drag forces on the floater are calculated separately in the engineering model. Hence, the QTFs for the fixed condition from CFD simulations ($QTF_{CFD,fixed}$) are estimated by subtracting the contributions of the Morison drag and the difference-frequency wave components. However, the contributions due to the first-order motions are not included in the CFD results. Because the first-order motion is predicted well by first-order potential solutions, it is assumed that the contribution due to the first-order motion can be accurately estimated by the difference between the QTFs for the fixed and floating floater in potential flow solutions (WAMIT). The fixed and floating surge force and pitch moment QTFs from potential flow solutions are compared in *Paper 2* and *3*. The differences are the contributions due to the first-order motions. Then, the QTF values for the floating condition based on CFD simulations in the fixed condition are expressed as:

$$QTF_{CFD,floating} = QTF_{CFD,fixed} + (QTF_{WAMIT,floating} - QTF_{WAMIT,fixed}). \tag{3.36}$$

Taking advantage of symmetry relations, we consider the upper-left-half ($f_2 \geqslant f_1$ in the left subplot of Fig. 3.9) when discussing how the QTF from potential flow is modified based on bichromatic wave simulations using CFD. The diagonal of the difference-frequency QTF matrix ($f_2 = f_1$) represents the mean drift force, which only depends on first order information and is not modified. First, based on the CFD simulations, the surge force and pitch moment QTF values along the surge and pitch natural frequencies (dashed line in the left subplot of Fig. 3.9) are obtained. Next, the magnitudes and phases of these QTFs and the QTFs estimated by potential flow theory (WAMIT) are separately interpolated to obtain values at denser sets of frequencies (using an interval of 0.001 Hz).

Then, the interpolated results from WAMIT along the surge and pitch natural frequencies are replaced with the interpolated results from CFD simulations. To propagate the correction to other parts of the QTF, the WAMIT magnitudes or phases with the same f_2 are extracted and corrected based on the results from CFD model. There are two different cases: in case (1), regions with only one value from CFD model, the gradient is maintained to be the same before and after modification; in case (2), regions with two values from CFD model or one value from CFD and one value from WAMIT, the gradient varies linearly between CFD values or CFD and WAMIT values. An example is shown in the right subplot of Fig. 3.9. Finally, this modified QTF matrix is downsampled to an interval of 0.05 Hz and implemented in the engineering model.

In addition to this approach, two other approaches are considered to modify the QTF values. The details of approaches and the comparisons of the low-frequency wave loads on a restrained floater under the irregular wave are described in Appendix A.

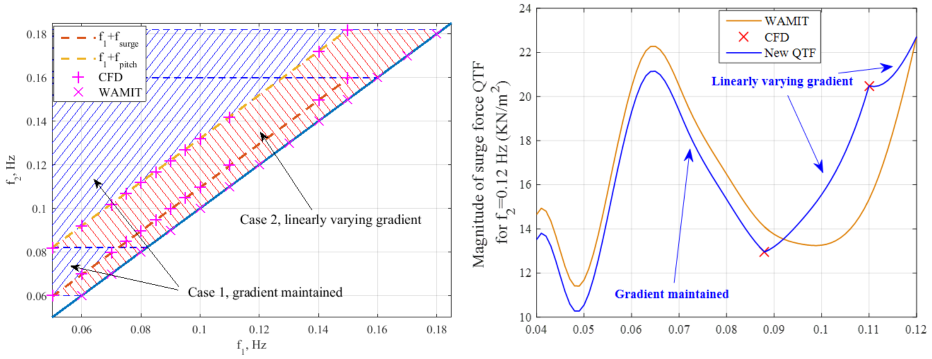

Figure 3.9: Different regions of the QTF for modification

3.5.2 Modification of added mass and damping

In the CFD simulations, the hydrodynamic added mass and linearized damping around the surge, heave and pitch natural periods are estimated through the forced oscillation simulations in surge, heave and pitch (Section 3.4). The pitch moments from forced oscillations in surge and the surge forces from forced oscillations in pitch are used to calculate cross terms (pitch-surge/surge-pitch).

The first-order radiation solutions are used to calculate the added mass and damping in potential flow theory. However, the assumption of inviscid flow limits the amount of damping, requiring the potential flow solutions to be augmented with viscous effects by including Morison-type drag. In WAMIT, a panel model is used for the columns/heave plates and a Morison model is implemented for each part of floater. The results consist of the frequency-dependent added mass and damping from the panel model, the frequency-independent added mass of the pontoons/cross braces calculated by applying the inertial term of Morison's equation (the added mass coefficient is 1.0) and linearized damping of each part of floater obtained from the drag term of Morison's equation applying the Fourier-averaged approach (Section 3.4).

Because Morison drag forces on each part of the floater are calculated separately in the time domain analysis, the linearized damping from Morison-type drag should be deducted from the damping of CFD simulations when modifying the damping from WAMIT. The added mass and linearized damping coefficients estimated from CFD simulations are highly dependent on the oscillation amplitude, but the results from potential flow theory augmented with Morison-type drag are independent on the oscillation amplitude. Hence, only the CFD results under the oscillation amplitudes which are close to the mean measured amplitudes of motions from experiment of irregular wave are applied for modification. The added mass and damping near the resonance frequencies are replaced with CFD results. For the regions below the resonance frequencies, the gradient remains constant. When the frequency is larger than the resonance frequencies, the gradient varies to ensure a smooth transition from CFD results to WAMIT results. An example is shown in Fig. 3.10. Because the pitch-surge results are equal to the surge-pitch results, only surge, heave, pitch and pitch-surge added mass and damping are modified based on the CFD simulations. The other terms calculated in WAMIT are implemented in the time domain analysis of SIMA.

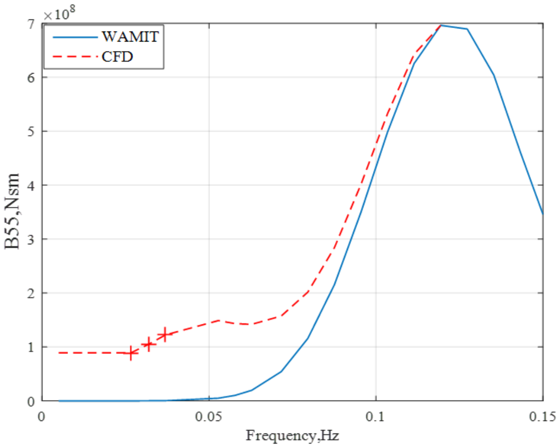

Figure 3.10: Frequency-dependent pitch damping

3.6 Free decay analysis

Free decay tests are used to determine the natural periods and damping of the rigid body motions. In the current research, free decay tests in surge, heave and pitch (Table 2.4) are carried out in the experiments and numerical simulations. Assuming that there is no coupling among motions in different DOFs, a typical decay in still water considering linear stiffness and nonlinear damping follows [143]

$$(m + a)\ddot{X} + B_1\dot{X} + B_2\dot{X}|\dot{X}| + KX = 0, \tag{3.37}$$

where X, $\dot{X}$, $\ddot{X}$ are the motion, velocity and acceleration for the surge, heave or pitch motion. m is the mass or mass moment of inertia in pitch and a is the added mass or mass moment of inertia in pitch. B_1 and B_2 are the linear and quadratic damping coefficients, respectively. K is the linear restoring coefficient.

Natural periods are estimated as the mean duration between two consecutive peaks or troughs. The damping ratio (ξ^*) relative to the critical damping is based on the logarithmic decrement (δ) for each cycle:

$$\delta = \ln \frac{x_n}{x_{n+1}}, \tag{3.38}$$

where x_n and x_{n+1} are two consecutive peaks or troughs. The damping ratio is then calculated as:

$$\xi^* = \frac{1}{\sqrt{1+(\frac{2\pi}{\delta})^2}}. \tag{3.39}$$

In some cases, especially for small motion amplitudes, there are large variations in the damping ratio.

From the method of equivalent linearization, the damping ratio can be expressed as a function of the motion amplitude (X):

$$\xi^* = \frac{B_1 + B_2\frac{8\omega_n}{3\pi}X}{B_{cr}}, \tag{3.40}$$

where ω_n is the oscillation frequency and $B_{cr} = 2\sqrt{((m+a)K)}$ is the critical damping. Based on Eq. 3.39 and Eq. 3.40, the linear and quadratic damping can be obtained from the values of two consecutive peaks or troughs in the decaying motion. If the damping ratio is plotted as function of the motion amplitude (Eq. 3.40), the linear damping is given by the intercept while the quadratic damping is given by the slope. As this estimate is sensitive to the magnitude of the peaks (or troughs), the best signal mean value is subtracted from the original decaying motion by minimizing the linear regression error (sum of squares).

3.7 Response metrics

To assess the accuracy of the modified engineering model in representing physical behavior of the semi-submersible FWT, the numerical results are compared with the experimental measurements under the irregular wave. Some response metrics are identified to represent the important physical quantities of interest. The response metrics are scalar values that can be calculated from the time series of numerical simulations or experiments.

3.7.1 PSD sum

The power-spectral density (PSD) sum (S_{sum}) which was used in the experimental uncertainty analysis for the OC5 DeepCwind semi-submersible [115] is adopted to quantify the dynamic responses both within and outside the wave frequency range and is calculated based on the one-sided, discrete power density functions:

$$S_{sum} = \sum_{i=j}^{k} S_i(f_i)\Delta f, \tag{3.41}$$

where $S_i(f_i)$ represents the discrete PSD of the response at frequency f_i, Δf is the frequency increment, j and k are the indices of the lowest and highest frequency of interest, respectively. The standard deviation is the square root of PSD sum for the signal with zero mean value.

3.7.2 Damage-equivalent loads

Engineering global analysis models can be used to obtain time series of loads in certain FWT components, such as the tower or mooring lines [144, 145]. The total damage (D) for each time series can be determined based on Miner's rule by linearly accumulating the damage from each stress or tension level:

$$D = \sum_i \frac{n_i}{N_i}, \tag{3.42}$$

where n_i is the number of cycles at the ith stress or tension range in the time series and N_i is the number of cycles to failure at the same stress or tension range according to the S-N curve. In the current research, damage-equivalent loads, calculated using a Matlab-based tool (MLife [146]) are used as a metric to quantify the damage. The S-N curve is given as

$$N_i = \left(\frac{\sigma^{ult} - |\sigma^{MF}|}{1/2\sigma_i} \right)^m, \tag{3.43}$$

where σ_i is the ith stress or tension range. σ_{ult} is the ultimate design stress or tension of the material, σ^{MF} is the fixed mean stress or tension value in the time series and m is the Wöhler exponent. The rainflow counting method [147] is applied to count the cycles. The damage-equivalent load σ^E is a constant load amplitude at a fixed frequency that produces equivalent damage by:

$$D = \left(\frac{n}{N} \right)^E, \tag{3.44}$$

$$n^E = f^E T, \tag{3.45}$$

$$N^E = \left(\frac{\sigma^{ult} - |\sigma^E|}{1/2\sigma_i} \right)^m, \tag{3.46}$$

where n^E is the total equivalent damage counts in the time series, f^E is the frequency of the damage equivalent load, T is the duration of the time series (e.g. one hour) and σ^E is found by forcing Eq. 3.44 to be equal to Eq. 3.42.

The damage equivalent load of mooring line is estimated based on the tension and the damage equivalent load at the tower base is calculated based on the axial stress. The frequency f^E is taken as 1 Hz and a Wöhler exponent $m = 3$ is used. The tower base coordinate system is illustrated in Fig. 3.11. Ignoring the cross-section deformation after the loads are exerted, the axial stress is equal to the nominal axial stress:

$$\sigma = \frac{N_z}{A} + \frac{M_y}{I_y} r\cos(\theta) - \frac{M_x}{I_x} r\sin(\theta), \tag{3.47}$$

where N_z is the axial force, A is the nominal cross-sectional area, M_x, M_y are the moments about the local x- and y-axis, respectively. I_x, I_y are the sectional moments of the area with respect to x- and y-axis. r is the cross section radius and θ is the angle from point A to the calculated point in counterclockwise direction. Since the wave propagates along x-axis in the current research, it is sufficient to take the point A ($\theta = 0$) as an example for the damage analysis.

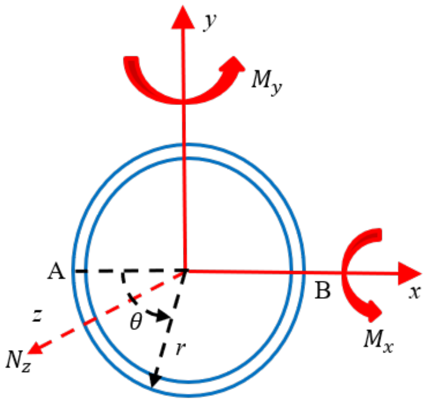

Figure 3.11: Coordinate system of tower base (top view)

3.7.3 Short-term extreme value prediction

The extreme value of a random stochastic process $X(t)$ with zero mean value for a given time duration is defined as the maximum value from a sequence of individual local maxima and minima.

$$X_e = \max\{X_{max1}, X_{max2}, ..., X_{maxn}, |X_{min1}|, |X_{min2}|, ..., , |X_{minn}|\}, \quad (3.48)$$

where X_e represents the extreme value and X_{maxi}, X_{mini} are the individual local maxima and minima, respectively. Based on the assumption that the absolute values of all individual local maxima and minima are independent and identically distributed with a common distribution function $F_X(x)$, the distribution of X_e can be expressed as:

$$F_{X_e} = \text{Prob}\{X_e \leqslant x\} = [F_X(x)]^{2n}. \quad (3.49)$$

When the sample number $2n$ is large enough, the extreme value distribution (Eq. 3.49) will converge towards one of three types of distributions: Gumbel, Fréchet and Weibull distributions. Among them, the Gumbel distribution is the most recommended model for marine structures subjected to wave loads [148] and implemented in the current research. The cumulative distribution probability F_{X_e} can be written as:

$$F_{X_e} = \exp(-\exp(-\alpha(x-\mu))), \quad (3.50)$$

where α is the scale parameter and μ is the location parameter.

In the current research, the extreme value is characterized by the value with an exceedance level of 90% in the three-hours maxima distribution.

Chapter 4

Research Findings

In this chapter, the main research findings about the nonlinear wave loads and resulting global responses of a semi-submersible FWT with heave plates using engineering (SIMA) and high-fidelity numerical (CFD) tools described in Sections 3.1 and 3.2, respectively, are briefly summarized. Available experimental measurements are used to validate the corresponding numerical simulations. The nonlinear wave loads on a constrained floater are regarded as 'wave diffraction loads' and the hydrodynamic loads on a floater in the forced oscillations are considered as 'wave radiation loads', even though superposition isn't strictly valid for nonlinear wave loads.

4.1 Wave diffraction loads

The investigation of nonlinear wave loads on a constrained semi-submersible floater is presented in the following subsections. The studies consider both the upright floater and a trimmed floater, in order to examine the change in nonlinear wave diffraction loads due to the mean pitch angle which occurs during operation of a floating wind turbine. Furthermore, wave diffraction loads on each column are extracted numerically to better understand the effects of the multi-member arrangement.

The engineering tool (SIMA) was used to investigate the contributions from different force components, as summarized in Table 4.1. Furthermore, two different types of wave inputs were applied: for simulations refer to as 'SIMA', the experimentally measured or generated (nonlinear) wave elevation from CFD is used as an input, while simulations indicated as 'Linear' use a fully linear regular wave or take a time series based on the first-order bichromatic theory as input. Unless a fully linear regular wave is used, when a wave signal is input into the SIMA software, it is treated as a superposition of linear regular waves at different frequencies, and all the components are assumed to travel in the positive x-direction (Section 3.1). The comparisons between 'SIMA' and 'Linear' models are used to investigate the effects of the presence of nonlinear wave components on the load predictions from the engineering tool.

Table 4.1: Overview of different settings in SIMA for the investigation of wave diffraction loads (Section 4.1)

Label	Theory
SIMA1/Linear1	Only linear potential flow theory
SIMA2/Linear2	SIMA1/Linear1 with original QTF from WAMIT
SIMA3/Linear3	SIMA2/Linear2 with integration of Morison drag force to mean free surface
SIMA4/Linear4	SIMA2/Linear2 with integration of Morison drag force to the undisturbed linear free surface
SIMA5/Linear5	SIMA4/Linear4 with consideration of axial drag force on the heave plates
SIMA6	SIMA5 with replacement the original QTF from WAMIT with modified QTF from CFD

4.1.1 Higher harmonic wave diffraction loads in regular waves

The higher harmonic wave diffraction loads under the regular wave (Table 2.2) are investigated in this subsection. The amplitude was the average value over the five wave cycles and the phase represented the initial phase of time-series. As mentioned in Section 3.2.2, considering the low KC number of columns, the CFD with the laminar flow model and turbulence model are compared in this part.

The regular wave elevation was firstly examined, as shown in Fig. 4.1. All SIMA simulations and CFD with stream function wave theory can reproduce the experimentally measured regular wave elevation well, except for the fully linear regular wave (Linear). There is no visible numerical dissipation of the wave in the CFD simulation with turbulence model (T.F) by comparing the wave heights for different wave cycles.

Upright condition

The higher harmonic wave diffraction loads on the upright floater are investigated in this part. The second and third harmonic pitch moments are compared in Fig. 4.2. Other results can be found in *Paper 1* in Appendix B.

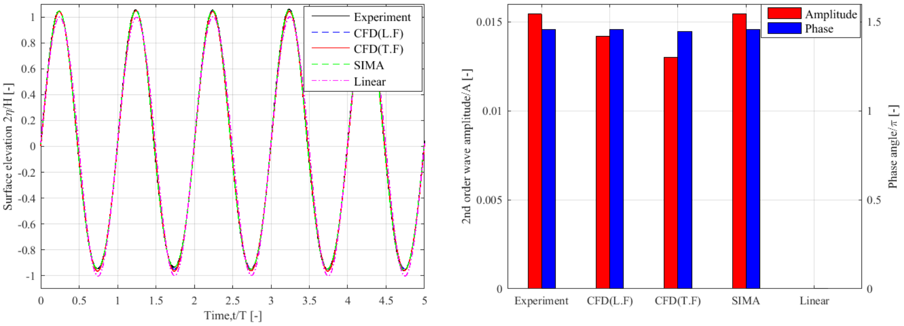

(a) Time series

(b) Amplitude of the second harmonic (at frequency 2ω) of the wave

Figure 4.1: Comparisons of regular wave elevation. H and A are the specified wave height and amplitude, L.F *represents the laminar flow and* T.F *represents the turbulent flow*

For higher harmonic wave diffraction loads, all CFD results show a similar phase as the experiment. Compared to the laminar flow (L.F), the CFD with turbulent flow generally gives the better estimations,considering the fact that the occurrence of weak vortices is not accurately captured by the laminar flow model.

In the potential flow model with Morison-type drag, the nonlinearity in the wave elevation (SIMA1) is the main contribution to the second harmonic wave diffraction loads by combining the linear wave forces transfer functions. The sum-frequency QTF (SIMA2) is the second largest contribution, while the integration of the transverse drag force to the mean (SIMA3 and Linear3) and undisturbed linear free surface (SIMA4 and Linear4) have minor contributions to the second harmonic results. The axial drag force (SIMA5 and Linear5) also has a minor contribution.

The contributions induced by the combination of high-frequency wave components and the sum-frequency QTF (SIMA2) and the nonlinear drag force (SIMA3/5 and Linear3/5) are the only significant contributors to the third harmonic wave diffraction loads.

The estimated higher harmonic wave diffraction loads in all SIMA simulations differ from the experimental results for both amplitude and phase. Tuning the drag coefficient can decrease the amplitude discrepancy in higher harmonic wave diffraction loads, but a phase difference nonetheless exists in the SIMA simulations. This discrepancy demonstrates the limitations of potential flow theory with Morison-type drag for accurately representing the higher harmonic wave diffraction loads on the semi-submersible.

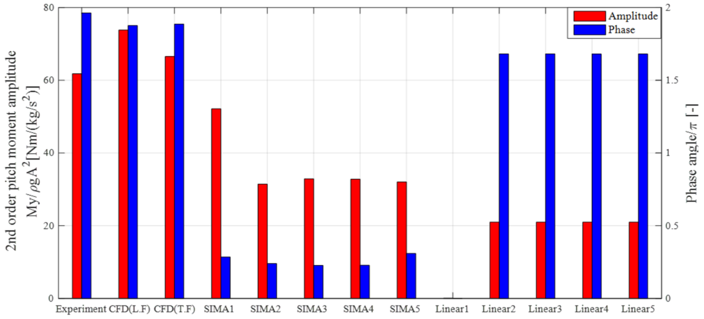

(a) Second harmonic (at frequency 2ω) pitch moment

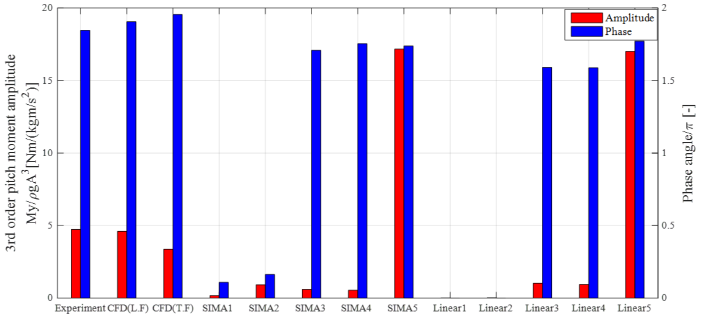

(b) Third harmonic (at frequency 3ω) pitch moment

Figure 4.2: Comparisons of pitch moment under upright condition for the regular wave

Trimmed condition

The effects of 5° mean pitch angle on the higher harmonic wave diffraction loads were also investigated in regular waves, using the same global coordinate system as in the upright condition. For a trimmed floater, the flow separation around the edge of the heave plate is more significant. In engineering tools, this effect is modelled through the Morison drag forces. SIMA4 and SIMA5 contain all the contributions of the Morison drag forces, and are compared with the CFD with turbulent flow in this part. The amplitudes of wave loads divided by the x^{th} $(x = 2, 3)$ power of the displaced submerged volume V $(\times 10^4\ m^3)$ are compared to eliminate the effect of changed submerged volume, which is denoted as '$Amplitude/V^x$' in Fig. 4.3 where the higher harmonic pitch moments are compared. Other results are presented in *Paper 1* in Appendix B.

In the CFD simulations, the higher harmonic wave diffraction loads generally decrease under the trimmed condition, especially when considering the changed volume.

After rotating the floater, the second harmonic surge force and pitch moment increase in SIMA, which is opposite to the CFD results. The reason for the discrepancy is that, in the engineering model, the nonlinear incoming wave components (which were treated as linear wave components) contribute to the second harmonic wave diffraction loads by combining with linear potential flow theory. The wave diffraction loads from linear potential flow theory increase due to trim.

In SIMA, most of the third harmonic wave diffraction loads come from the Morison drag forces. The axial drag forces on the heave plates increase the third harmonic heave force and pitch moment, but decrease the third harmonic surge force, which is due to the phase difference between vertical and horizontal water particle velocity. Normalizing by submerged volume, the third harmonic surge force decreases and there is almost no change in the third harmonic heave force and pitch moment due to trim.

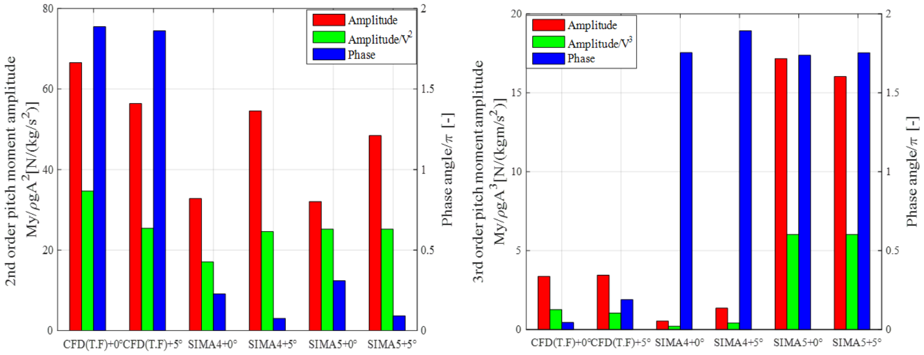

(a) Second harmonic (at frequency 2ω) pitch moment amplitude and phase

(b) Third harmonic (at frequency 3ω) pitch moment amplitude and phase

Figure 4.3: Comparisons of pitch moment under upright and trimmed condition for the regular wave

Surge forces on individual columns

In order to better understand the effects of the multimember arrangement of the semisubmersible, surge forces on each column were extracted, shown in

Fig. 4.4. Here, the sum-frequency QTF is not included in SIMA. Therefore, wave nonlinearity is important for the second harmonic surge forces, while Morison drag forces dominate in the third harmonic surge forces. The large difference in the amplitude of higher harmonic surge forces between SIMA and CFD is due to the constant drag coefficient used in SIMA.

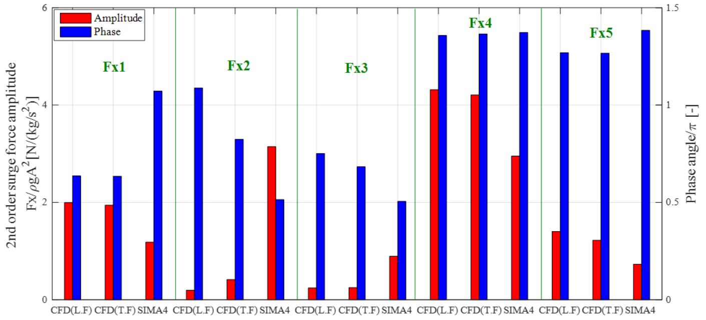

(a) Second harmonic (at frequency 2ω) surge force

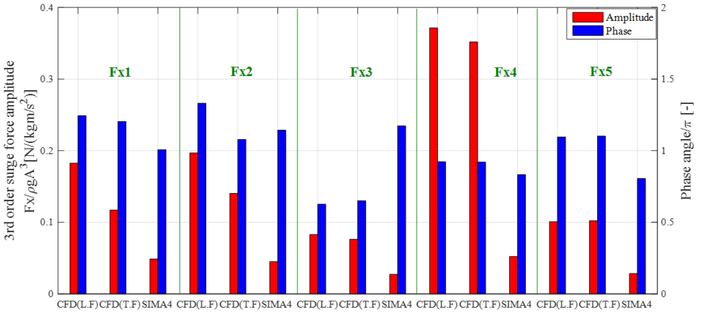

(b) Third harmonic (at frequency 3ω) surge force

Figure 4.4: Comparisons of surge forces on the individual columns of the floater under upright condition for the regular wave. Fx1*: main column,* Fx2*: upper column of upstream column,* Fx3*: heave plate of upstream column,* Fx4*: upper column of starboard column,* Fx5*: heave plate of starboard column. See Fig. 2.3 for the definition of the columns*

For the CFD results, except for the higher harmonic surge force on the upper column of the upstream column (Fx2), the surge forces have similar phase for both laminar and turbulent flow. Additionally, the third harmonic surge forces on the main column (Fx1) and upper column (Fx2 and Fx4) differ between laminar and turbulent flow. Based on the KC number in Table 3.1 and results from other researchers [149], the difference is due to the occurrence of a pair of weak vortices in the wake of main and upper columns which laminar flow model can not accurately simulate.

For both the upstream and starboard column, although the diameter of the heave plate (Fx3 and Fx5) is twice that of the upper column (Fx2 and Fx4), the surge force on the upper column is larger in the SIMA and CFD simulations because the water particle acceleration decreases as one moves downward. This conclusion is frequency-independent.

The higher harmonic surge forces on the starboard column (Fx4 and Fx5) are larger than those on the upstream column (Fx2 and Fx3) under this regular wave (12.1 s), but this conclusion is frequency-dependent (based on potential flow simulations at additional frequencies).

4.1.2 Difference-frequency wave diffraction loads

The difference-frequency wave diffraction loads under bichromatic waves are investigated in this subsection. Considering the better performance of turbulence model in prediction higher harmonic wave diffraction loads in Section 4.1.1, all CFD simulations are carried out with turbulence model in this part. Furthermore, the resulting difference-frequency wave loads are used to modify the QTFs from potential flow solutions. The results are validated by comparing the numerically estimated low-frequency wave loads under the irregular wave against experimental measurements. An example of a bichromatic wave is compared in Fig. 4.5.

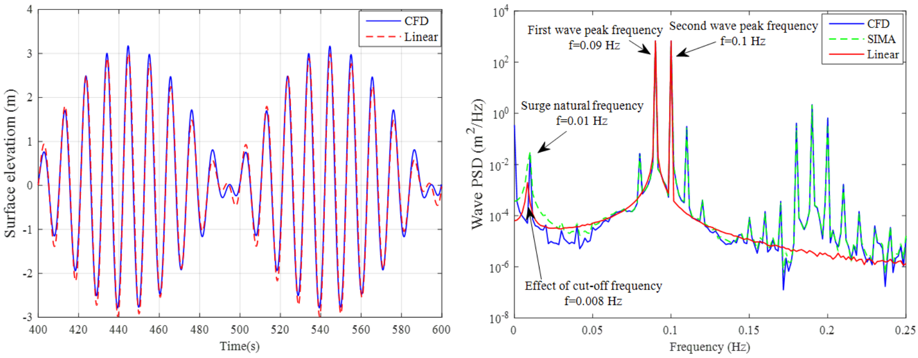

(a) Time series *(b) Wave spectrum*

Figure 4.5: Bichromatic wave simulations

No significant wave damping is observed by comparing the maximum wave elevations at different cycles, which is crucial for accurate estimation of difference-frequency wave diffraction loads. In contrast, the CFD simulations of irregular waves suffered from significant wave damping triggered by an increase in the viscosity around the air-water interface [132]. A comparison of CFD and 'Linear' shows the interaction between two regular waves which leads to the peaks at the difference frequency $f_1 - f_2$ and sum frequencies such as $f_1 + f_2$, or $2f_1$, or $2f_2$ (between 0.15 Hz and 0.25 Hz). As expected, the wave amplitude of the first-order bichromatic wave (Linear) at the difference frequency (surge natural frequency) is negligible. At the difference frequency, the wave amplitude from the CFD model is 9.9% smaller than the second-order analytical solution.

Upright condition

The difference-frequency wave diffraction loads on the upright floater are investigated in this part. The surge forces under the bichromatic waves whose difference coincides with the surge natural frequency of the FWTs are shown in Fig. 4.6 while other results are presented in *Paper 2* in Appendix B.

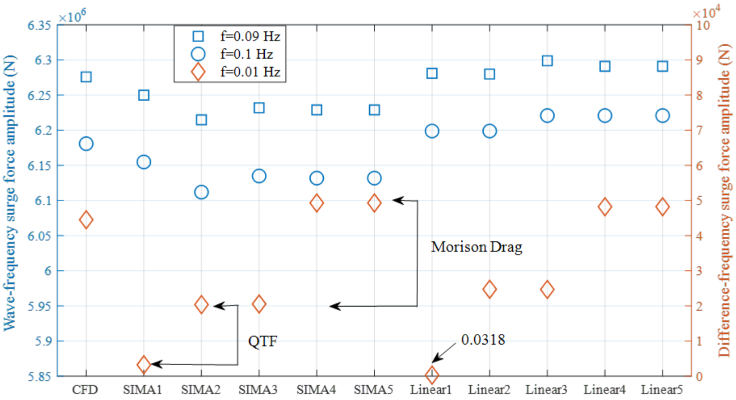

Figure 4.6: Surge force amplitude under upright condition for the bichromatic waves

The difference-frequency surge force at the surge natural frequency is mainly from the integration of Morison drag force to the linear free surface (SIMA4). This contribution decreases with increasing wave frequencies, and the surge force from QTFs becomes dominant (SIMA2), which can be found in Fig. 4.7. At the pitch natural frequency, the pitch moment from QTFs (SIMA2) is dominant, which is valid for all frequencies (Fig. 4.7). In addition, the axial drag forces on the heave plates (SIMA5) have minor contributions to the difference-frequency wave loads. Furthermore, the contribution of difference-frequency wave components via the linear wave force transfer function (SIMA1 vs Linear1) decreases the difference-frequency wave loads

(SIMA2 vs Linear2). From Fig. 4.7, when all force contributions are considered, SIMA (SIMA5) and CFD agree well at the lower wave frequencies, while the CFD predicts larger difference-frequency wave loads at higher wave frequencies.

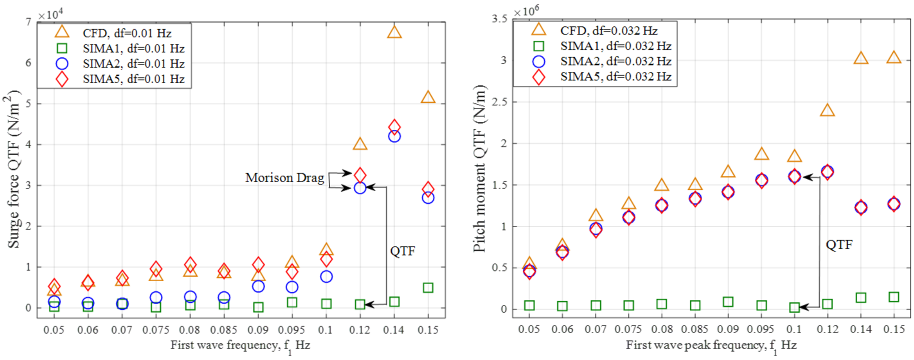

(a) Surge force QTFs *(b) Pitch moment QTFs*

Figure 4.7: The magnitudes of surge force and pitch moment QTFs at different wave frequencies

Trimmed condition

The effects of 5° mean pitch angle during wind turbine operation on the difference-frequency wave diffraction loads are investigated in this part. The surge forces on the trimmed and upright floaters (in the global coordinate system) are compared in Fig. 4.8. To eliminate the effect of changed submerged volume, comparisons between surge force amplitudes normalized by the mean displaced submerged volume V are shown in the right y axis of Fig. 4.8. Other results are compared in *Paper 2* in Appendix B.

At the surge natural frequency, there is an increase in surge force in both CFD and the potential flow model, but the increase in the CFD model is more significant. For a trimmed floater, the flow separation around the edge of heave plate is more significant and the Morison drag forces underestimates this effect. The pitch moments under the trimmed condition are not significantly changed compared to the upright floater (Fig. 10 in *Paper 2* in Appendix B). The axial drag forces on the heave plates (SIMA5) have minor contributions to the difference-frequency wave diffraction loads on the trimmed floater.

The difference-frequency surge forces in the CFD simulations increases more than the change in volume, but this is not the case in the SIMA models and is opposite with the change of the higher harmonic surge force (Section 4.1.1). However, the increase in the pitch moment at the pitch natural frequency is smaller than the increase in the submerged volume (Fig. 10 in *Paper 2* in Appendix B).

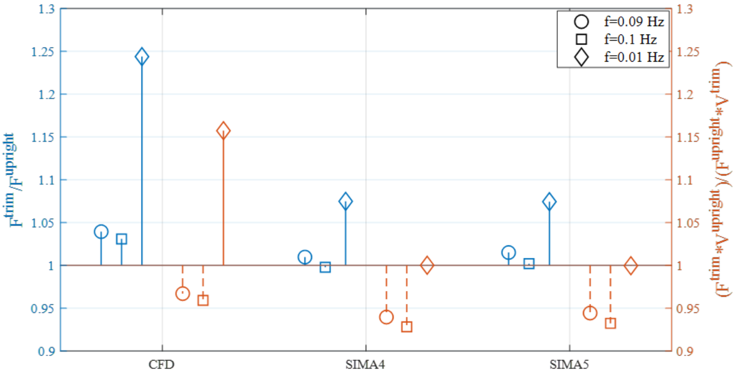

Figure 4.8: Comparisons of wave loads under upright and trimmed condition for the bichromatic waves

Surge forces on individual columns

The wave-frequency and slowly varying surge forces on individual columns of the upright floater are compared to better understand the effects of the multi-member arrangement of the semi-submersible floater, as shown in Fig. 4.9. Due to the lack of the QTF for each column, the surge forces at the difference frequency in the SIMA simulations mainly come from the integration of the Morison drag forces to the linear free surface. Compared to the CFD results, SIMA underpredicts the difference-frequency surge forces on each column and a larger underprediction is seen at the lower part of the columns (Fx3 and Fx5). In addition, in the CFD simulations, the surge forces at the surge natural frequency on the starboard column (Fx4 and Fx5) are smaller than those on the upstream column (Fx2 and Fx3) and a larger reduction is found at the lower part of columns (Fx3 vs Fx5) for the studied bichromatic wave.

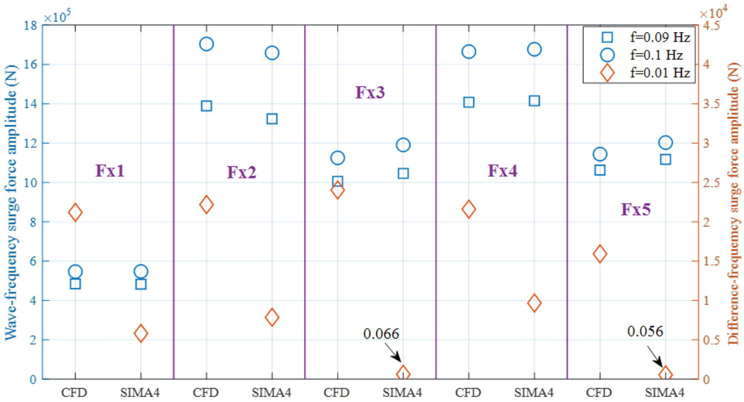

Figure 4.9: Comparisons of surge forces on the individual columns of the floater under upright condition for the bichromatic wave. Fx1*: main column,* Fx2*: upper column of upstream column,* Fx3*: heave plate of upstream column,* Fx4*: upper column of starboard column,* Fx5*: heave plate of starboard column. See Fig. 2.3 for the definition of columns.*

Modification and validation of QTF

All previous comparisons with the SIMA models consider the original QTFs from the second-order potential flow solutions. Here, the modified SIMA model with the estimated QTFs from CFD simulations is considered. The CFD results after subtracting the contributions of Morison-type drag and the difference-frequency wave components through the linear wave force transfer function (Section 3.5.1) are referred to as ‘New QTF’, which are compared with the QTFs estimated in WAMIT (Old QTF) in Fig. 4.10. The magnitude and phase of QTFs were calculated from the difference-frequency surge forces and pitch moments under the bichromatic waves whose difference frequency aligns with either the surge (0.01 Hz) or pitch (0.032 Hz) natural frequency based on Eq. 3.23.

A larger difference is observed at higher wave frequencies (generally $>$ 0.1 Hz) with the CFD model giving larger magnitudes. Interestingly, the CFD model gives approximately the opposite phase compared to the original potential flow results. This large discrepancy can not be captured by tuning the Morison drag term, which simply changes the results 90° out of phase.

The surge force and pitch moment QTFs in the low-frequency range are modified based on the approach described in Section 3.5.1 and compared with those estimated by the potential flow theory in *Paper 2* in Appendix B. In the same paper, the modification of the QTFs was firstly verified by

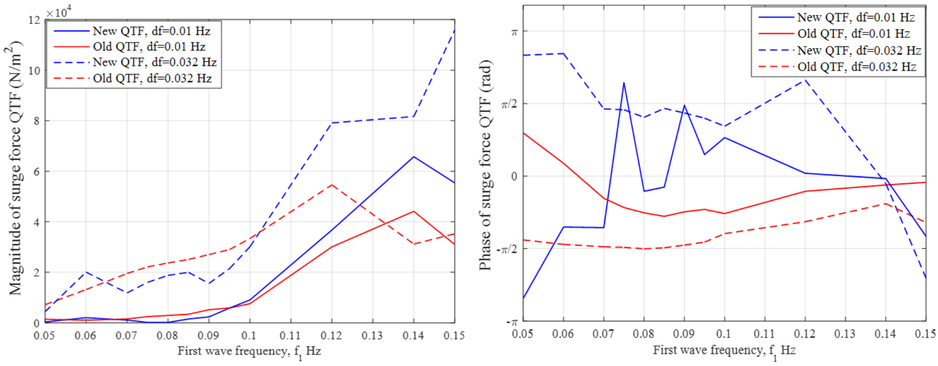

(a) Magnitude of surge force QTF *(b) Phase of surge force QTF*

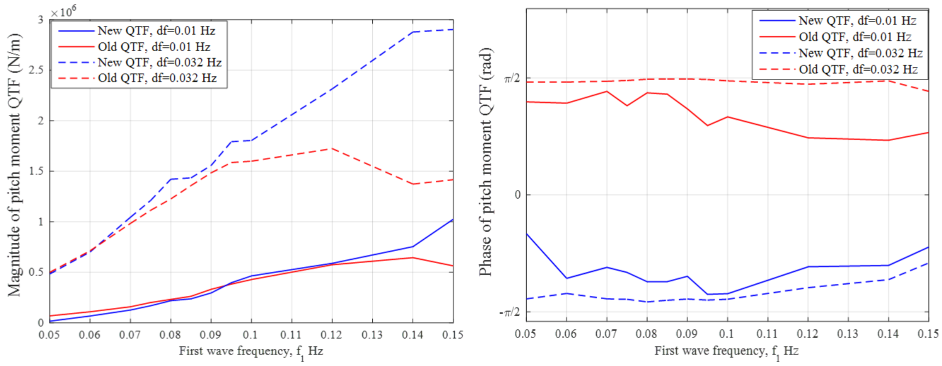

(c) Magnitude of pitch moment QTF *(d) Phase of pitch moment QTF*

Figure 4.10: Comparisons of the QTFs for the fixed condition before and after modification. df represents the difference frequency between two wave components of bichromatic waves

checking that difference-frequency wave loads estimated by the SIMA model with modified QTFs were close to the CFD results in bichromatic waves.

Then these modified QTFs based on the CFD with turbulence model were compared to the experimental measurements of low-frequency wave loads in the irregular wave (Table 2.2). Meanwhile, these low-frequency wave loads were also investigated in the CFD simulations without turbulence model (L.F) by the Navier-Stokes/potential flow solver described in Section 3.2.6 (*Paper 1*).

The low-frequency surge force and pitch moment are compared in Figs. 4.11 and 4.12, respectively. The frequency of PSD sum ranges from 0.005 Hz to 0.05 Hz. The modified QTFs based on the CFD with turbulence model

(SIMA6) significantly reduces the underprediction of difference-frequency wave diffraction loads compared to the QTFs from potential flow theory (SIMA5) and CFD without turbulence model (L.F). These modified QTFs are further used to modify the QTFs for the floating condition in Section 4.3.

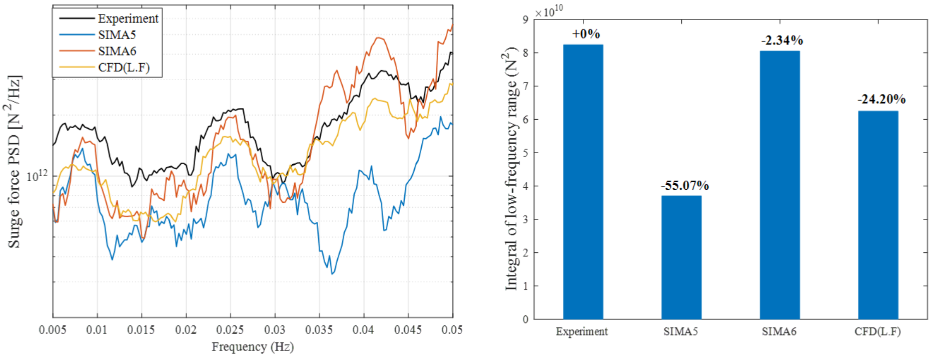

(a) Surge force spectra *(b) Surge force PSD sum*

Figure 4.11: Comparisons of low-frequency surge force in an irregular wave

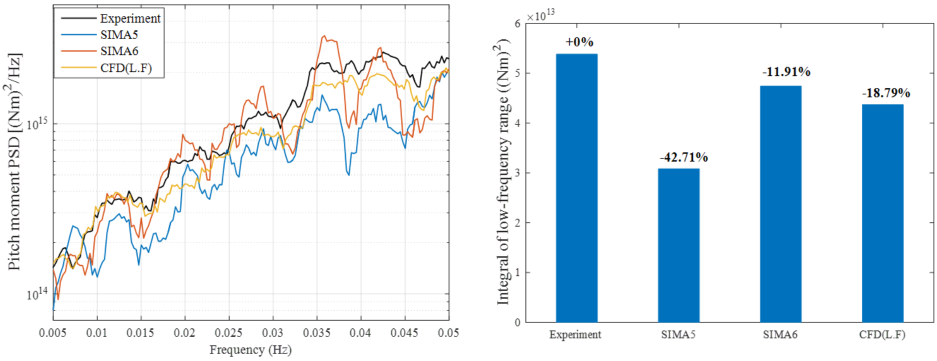

(a) Pitch moment spectra *(b) Pitch moment PSD sum*

Figure 4.12: Comparisons of low-frequency pitch moment in an irregular wave

4.2 Wave radiation loads

The investigation of nonlinear hydrodynamic loads on a semi-submersible floater in the forced oscillations, shown as added mass and linearized damping, are presented in the following subsections. In this part, all CFD simulations are carried out with the turbulence model. The added mass and linearized damping coefficients on the whole floater and each column are investigated. The results are compared with the potential flow solution augmented with Morison-type drag. Different contributions in the potential flow model (WADAM) are investigated, as summarized in Table 4.2.

Table 4.2: Overview of different contributions in WADAM

	Added mass	Damping
WADAM1	Radiation added mass from columns	Radiation damping from columns
WADAM2	WADAM1 with contributions of braces	WADAM1 with contributions of Morison-type drag

Forced oscillations in surge around the natural periods of surge, heave and pitch motion were firstly performed in the CFD model for validation (*Paper 3* in Appendix B). Compared to the experimental results, the maximum difference of 4.6% for the added mass coefficient and 1.9% for the linearized damping coefficient suggests the CFD model can reproduce the correct hydrodynamic characteristics at low oscillation frequency.

In the Sections 4.2.1-4.2.3, all the added mass and linearized damping are non-dimensionalized based on the approaches described in Section 3.4.

4.2.1 Surge added mass and linearized damping

The total surge added mass and linearized damping coefficients are compared in Fig. 4.13. In the CFD simulations, for these long periods, the surge added mass coefficient seems to be independent of the oscillation amplitude for small surge motion (1.91 m and 3.82 m, $KC < 2$) and then decreases with the oscillation amplitude (7.64 m). A slight period dependency can be found in the surge added mass coefficient. Furthermore, the surge linearized damping coefficient increases with longer period and smaller motion amplitude.

The surge added mass and linearized damping coefficients on individual columns (*Paper 3* in Appendix B) are mainly affected by the KC number and follow the relationship of the added mass and damping for a circular cylinder with KC number from Dütsch et al. [150] and Gao et al. [151]. The surge added mass and linearized damping coefficients on the starboard column are slightly larger than on the upstream column in the CFD simulations.

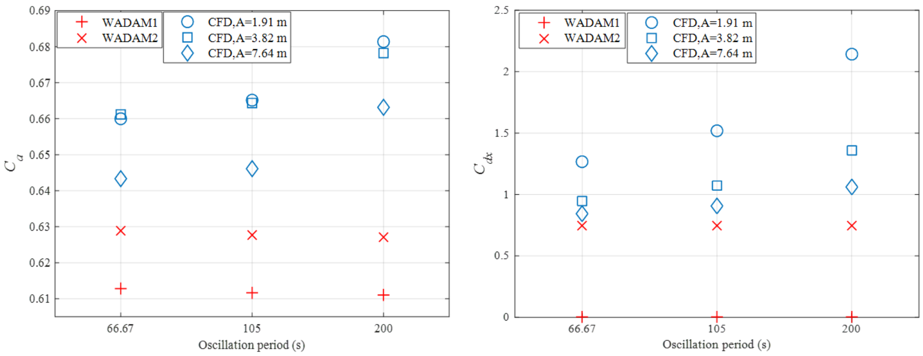

(a) Added mass coefficient *(b) Damping coefficient*

Figure 4.13: Surge added mass and linearized damping coefficients for the whole floater

4.2.2 Heave added mass and linearized damping

The total heave added mass and linearized damping coefficients are compared in Fig. 4.14. The heave added mass and linearized damping coefficients estimated by the CFD model shows, on one hand, a small dependence on the oscillation period and, on the other hand, a larger dependence with the oscillation amplitude.

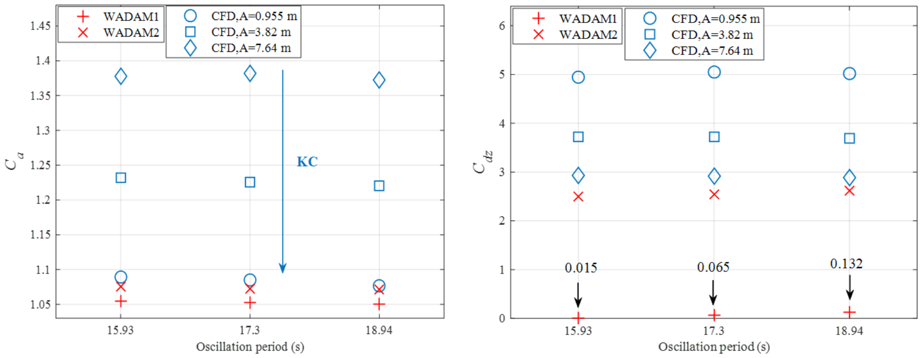

(a) Added mass coefficient *(b) Damping coefficient*

Figure 4.14: Heave added mass and linearized damping coefficients for the whole floater

In the investigation of the heave added mass and linearized damping coefficient of each column (*Paper 3* in Appendix B), when the oscillation amplitude is larger than the distance between the ledge of main column (Fig. 2.3) and still water line (4.25 m), the occurrence of flow separation and eddies at the ledge gives additional added mass in the CFD simulations. The overestimation for the linearized damping coefficient on the main column by Morison-type drag suggests that a smaller axial drag coefficient should be applied for the column without the heave plate. Most of contributions of added mass and linearized damping coefficients come from the heave plates. No difference can be found between the upstream and starboard columns.

4.2.3 Pitch added mass and linearized damping

The total pitch added mass and linearized damping coefficients are compared in Fig. 4.15. In the CFD simulations, a weak dependency of the pitch added mass coefficient on the oscillation amplitude and period is found for small pitch motion. However, the pitch added mass coefficient decreases with oscillation period for large pitch motion. The pitch linearized damping coefficient has similar behavior as the heave linearized damping coefficient.

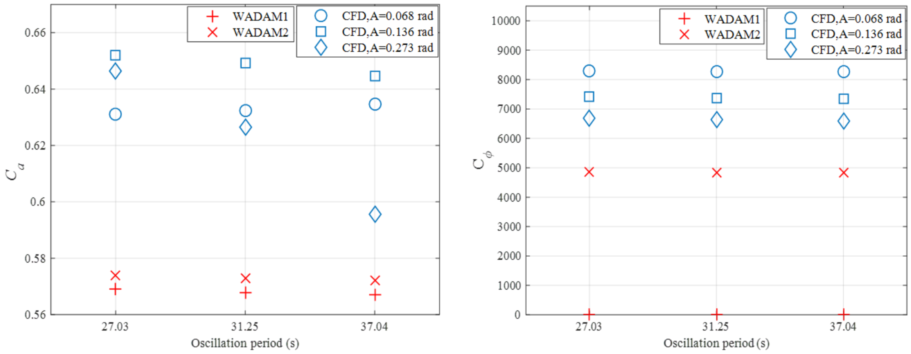

(a) Added mass coefficient *(b) Damping coefficient*

Figure 4.15: Pitch added mass and linearized damping coefficients for the whole floater

The upstream column contributes the most to the added mass and damping when comparing the pitch added mass and linearized damping coefficient of each column (*Paper 3* in Appendix B).

Comparisons between CFD and potential flow solution

The added mass coefficient derived from the CFD simulation is slightly superior to the one estimated by the potential flow theory (WADAM1) in most cases. Viscous effects give an additional added mass. The contribution of braces to the added mass coefficient (WADAM2) is minor for all cases. Regarding the linearized damping, the radiation damping (WADAM1) is completely negligible at these frequencies and the viscous damping from vortex shedding dominates (WADAM2). The accuracy of capturing the vortex shedding using Morison's drag force is sensitive to the drag coefficient.

Comparisons of computational costs in the CFD simulations

For the CFD simulations with long periods, the computational cost becomes the focus and are investigated. The same computational domain with the same number of mesh is applied for all the forced oscillation simulations. The simulation time is five time the oscillation period (model scale) and an adjusted time step with the maximum Courant number of 0.5 is applied. To eliminate the effect of different simulation times, the computational times are divided by the simulation times and compared in Fig. 4.16.

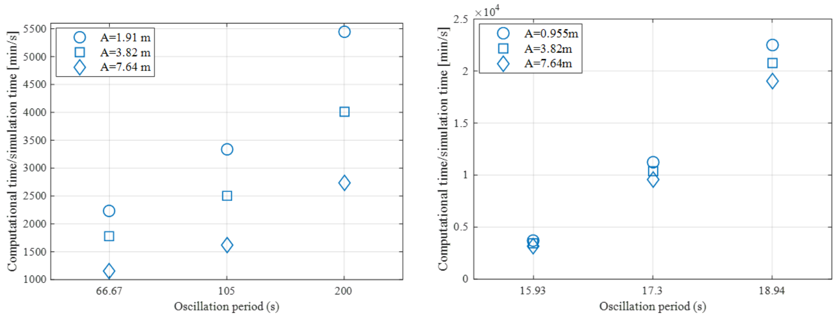

(a) Surge forced oscillation *(b) Heave forced oscillation*

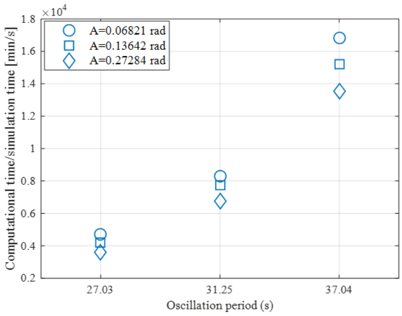

(c) Pitch forced oscillation

Figure 4.16: Computational times in the forced oscillations

4.3 Global responses

The estimated second-order difference-frequency wave loads QTFs in Section 4.1.2 and estimated frequency-dependent added mass and linearized damping in Section 4.2 based on the CFD simulations with turbulence model are used to improve an engineering model (based on potential flow theory with Morison-type drag) in this section. The investigation of the dynamic responses of a semi-submersible FWT based on the modified hydrodynamics are presented in the following subsections.

The surge force and pitch moment QTFs in the low-frequency range for the floating conditions were modified based on the approach described in Section 3.5.1 and compared with those estimated by the potential flow theory in *Paper 4* in Appendix B. The modified QTFs have larger magnitudes, especially at higher wave frequencies. The phases of the modified QTF for the floating condition follow a similar pattern as the potential flow solutions,but differ in value.

The frequency-dependent added mass and damping were modified based on the approaches described in Section 3.5.2 and compared with the potential flow solutions in the *Paper 4* in Appendix B. The potential flow theory underestimates the amplitude of added mass by over 10%. The quadratic damping in Morison drag force also underestimates the nonlinear viscous damping. This depends on the selected drag coefficients.

In SIMA (Eq. 3.1), the retardation function is obtained based on the modified frequency-dependent damping. The resulting retardation functions from WAMIT or from the modified frequency-dependent damping are compared in Fig. 4.17. The infinite-frequency added mass is then modified to give the best match between the added mass calculated from the retardation function and the input (modified) frequency-dependent added mass.

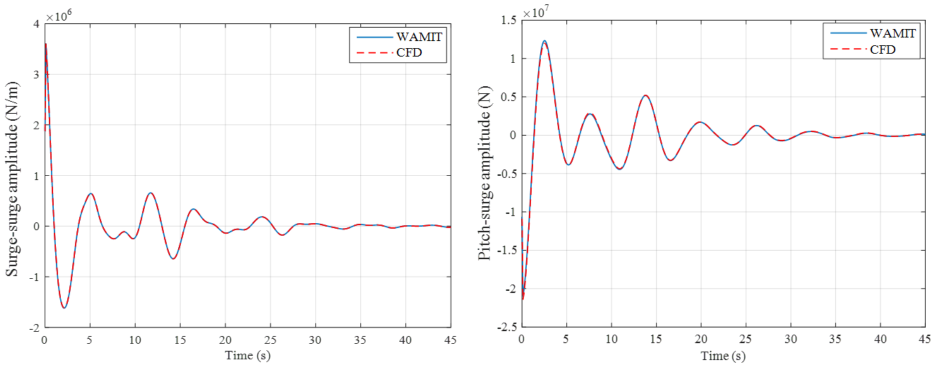

(a) Surge-surge *(b) Pitch-surge*

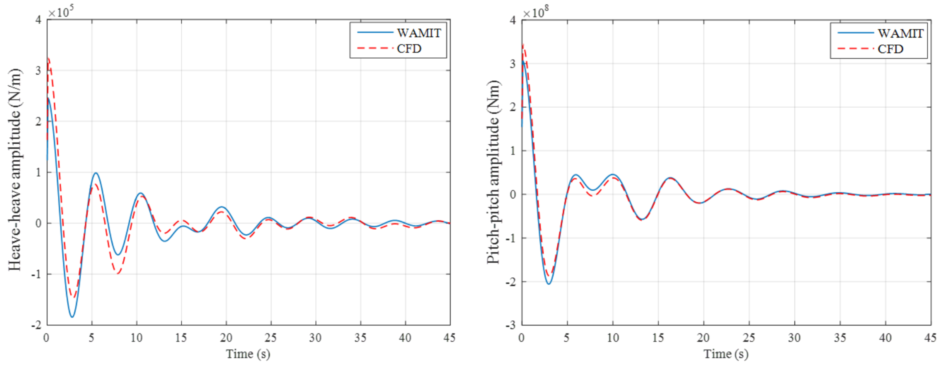

(c) Heave-heave *(d) Pitch-pitch*

Figure 4.17: Comparisons of the retardation function before and after modification

Different combinations of modifications based on CFD are considered in the SIMA simulations, ranging from none (SIMA-W) to all (SIMA-C), as summarized in Table 4.3. All SIMA models include automatically added linear damping to ensure that cutting-off the retardation function does not result in negative damping. In addition, extra linear damping (Table 4.3) which is determined by matching the calculated free decay motions from the CFD simulations is included in SIMA-WL. The variations in the SIMA model are used to separate the effects of the modifications of the difference-frequency QTFs and added mass and damping.

Table 4.3: Overview of different modifications in SIMA for global response calculations

	Difference-frequency QTF	Added mass and damping	Additional linear damping
SIMA-W	Potential flow theory	Potential flow theory	×
SIMA-WL	Potential flow theory	Potential flow theory	√
SIMA-CA	Potential flow theory	CFD(forced oscillations)	×
SIMA-CQ	CFD(bichromatic waves)	Potential flow theory	×
SIMA-C	CFD(bichromatic waves)	CFD(forced oscillations)	×

4.3.1 Floater motions

The free decay motions in still water and freely floating motions under the irregular wave are investigated in this part.

Free decay motions

Free decay tests in surge, heave and pitch (Table 2.4) were carried out experimentally in the OC6 project and using all variations of the engineering model (Table 4.3) as well as CFD with turbulence model. The pitch decay motions are compared in Fig. 4.18 while other decay motions are presented in *Paper 4* in Appendix B.

In the free decay tests, there is no effect of modified difference-frequency QTFs (SIMA-W vs SIMA-CQ). After modifying the frequency-dependent added mass and damping based on the CFD forced oscillation simulations (SIMA-CA and SIMA-C) or adding additional linear damping (SIMA-WL), the underestimation of damping in the potential flow solution reduces and the engineering tool can capture similar damping as the CFD model. Although there are differences in the added mass and damping, the predicted natural periods (*Paper 4* in Appendix B) in all numerical models are close to the experimental results (within 5%).

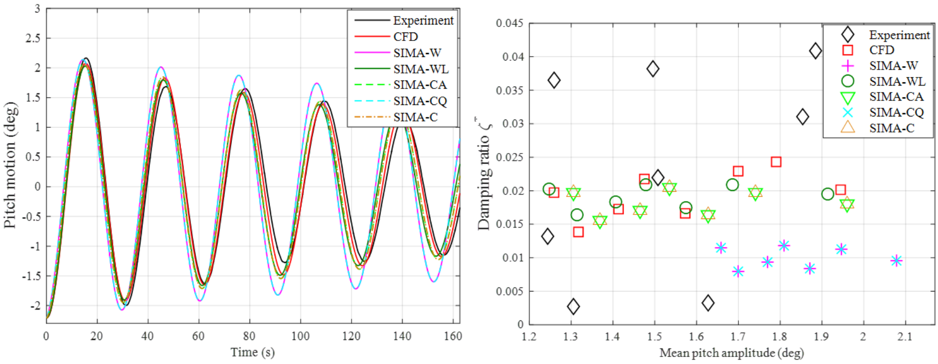

(a) *Decaying pitch motion* (b) *Pitch damping ratio*

Figure 4.18: Pitch decay

Motions under irregular wave

Due to the symmetry of the model, and the fact that the waves travel along an axis of symmetry (Fig. 2.5), surge, heave and pitch motions under the irregular wave (Table 2.2) are investigated in this part. The surge motions are presented in Fig. 4.19 while the comparisons of other motions can be found in *Paper 4* in Appendix B.

The natural frequencies of the floater motions are outside the linear wave-excitation range, and must be excited by some nonlinear forces. The largest contribution to the motions comes from the resonance frequency (shown in the left subplot of Fig. 4.19), except for the heave motion with equal contributions from the resonance and wave frequencies (*Paper 4* in Appendix B). The difference-frequency QTFs from the potential flow theory (SIMA-W) result in underestimation of the responses at resonant frequencies. The additional linear damping for matching calculated free decay motions from the CFD simulations (SIMA-WL) or the modified damping (SIMA-CA) based on the CFD simulations increases this underestimation. However, when the difference-frequency QTFs are modified (SIMA-CQ), the motions are overestimated compared to the experimental data. The overestimation can be reduced by adjusting the frequency-dependent damping at the same time (SIMA-C). The same trend is also valid for the exceedance probability distribution (shown in the right subplot of Fig. 4.19). The effect of modified added mass on the resonant frequency is minor, only making the heave resonant frequency in SIMA-C with larger added mass slightly shift towards the experimental result (*Paper 4* in Appendix B). Furthermore, the low-frequency damping has minor influence on the local maxima.

In conclusion, the best correspondence with the experiment is found in the SIMA-C model with the modified QTFs and added mass and damping from CFD simulations.

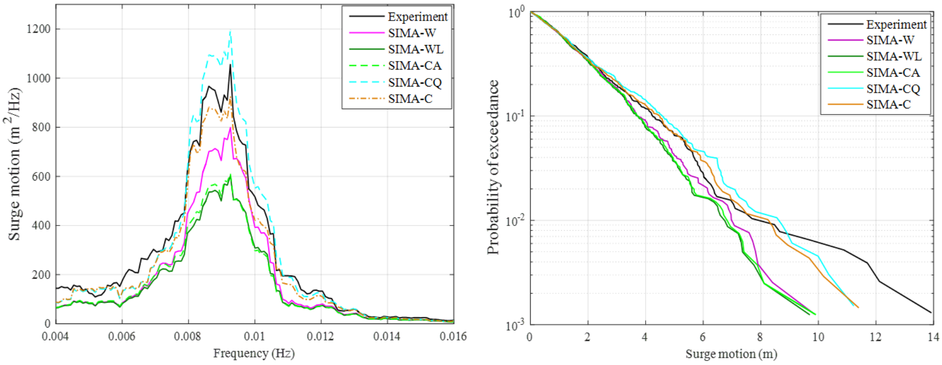

(a) PSD *(b) probability of exceedance*

Figure 4.19: Surge motion under 3-hr irregular wave conditions in the OC6 project

In the experiment, only one realization was generated. For the investigation of short-term extreme value, 20 different random seeds of irregular waves with same sea state were simulated numerically. Applying the modified models with numerically generated realizations results in the distribution of three-hour maxima for the surge motions in Fig. 4.20.

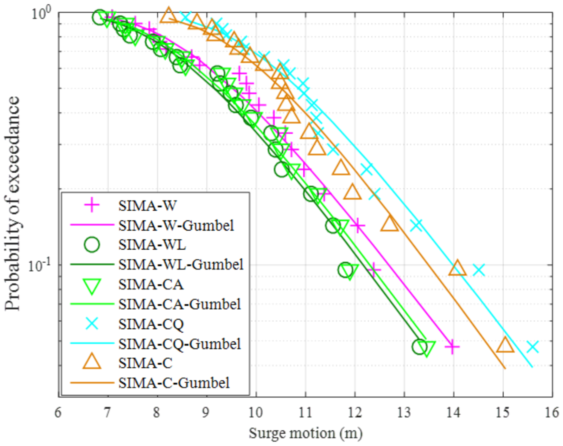

Figure 4.20: Three-hour maximum surge motion in the OC6 project

The solid lines shows a fitted Gumbel distribution while the maxima from each realization are shown as markers. For all SIMA models, the numerical data are well-described by the Gumbel function. It can be noted that the different QTFs and added mass and damping have similar influences on the three-hour maximum surge motion as surge motion under the irregular wave (Fig. 4.19) by comparing the variations among different SIMA models .

4.3.2 Mooring line tension

Considering symmetry, the mooring line tension on the starboard side (mooring line 2 in Fig. 2.5) should be equal to the tension on the port side (mooring line 3 in Fig. 2.5). Therefore, only the tensions of the upwind mooring line (mooring line 1 in Fig. 2.5) and the mooring line on the starboard side are investigated in this part. The tension is mainly driven by the surge response, so the difference-frequency QTFs and added mass and damping influences the tension in the same way as the surge motion.

The damage equivalent tensions for the mooring lines are compared in Fig. 4.21. The percentage on each bar represents the difference compared to the experimental results. The damage-equivalent tension increases when more difference-frequency wave loads are captured and decreases with increasing damping.

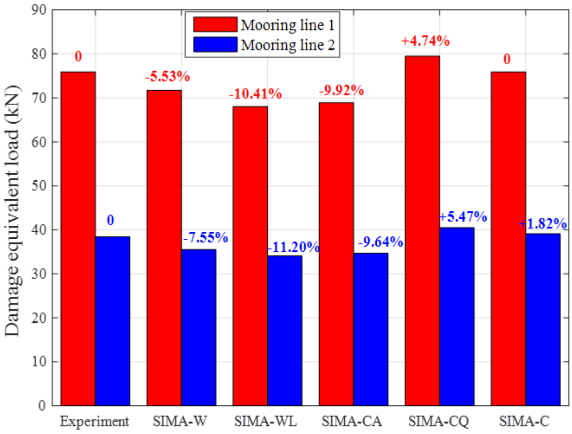

Figure 4.21: Damage equivalent loads for mooring line 1 and 2 in the OC6 project

4.3.3 Tower base load

The tower bending natural frequency is about 0.32 Hz, which is larger than the wave frequency (0.0826 Hz) of the irregular wave and can be excited by the sum-frequency wave loads. Meanwhile, the low-frequency wave loads also contribute to the tower base load for a semi-submersible FWT through inertial and gravitational loads due to low-frequency surge and pitch. An example of tower base fore-aft moment (M_y in Fig. 3.8) is shown in Fig. 4.22. There are three significant contributions: the pitch natural frequency, wave frequency and tower bending natural frequency. SIMA with either sum-frequency ('SF') or difference-frequency ('DF') QTFs underestimates the low-frequency or high-frequency responses, respectively. Therefore, all SIMA models presented in this subsection consider both QTFs, such as SIMA-C, where both low-frequency and high-frequency responses are captured well.

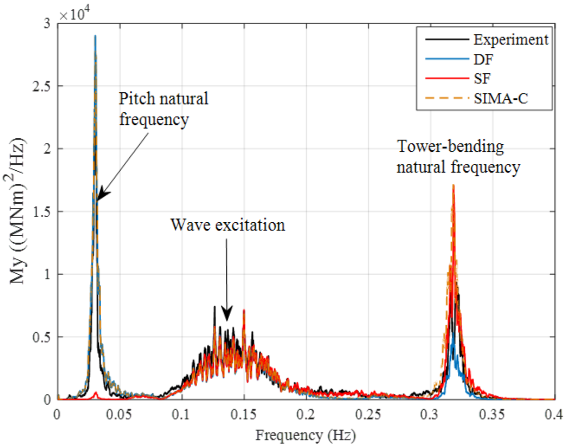

Figure 4.22: PSD of the tower base fore-aft moment in the OC5 project

The modified hydrodynamics from the CFD simulations influences the responses around the pitch natural frequency in the same way as the pitch motion. The same trend is also seen for the exceedance probability distribution and short-term extreme values of moments.

The damage equivalent load of tower base is mainly determined by the high frequency responses, i.e. responses around tower bending natural frequency. The comparisons of the PSD sum of the tower base bending moment (Table 4.4) illustrate that the responses around tower-bending natural frequency are affected by the low-frequency motions. All SIMA models overpredict the responses around the tower-bending natural frequency by over 60%. A larger overprediction up to 101% is seen when the difference-frequency QTF from potential flow solutions (SIMA-W, SIMA-WL, SIMA-CA) is applied.

Table 4.4: Tower bending PSD sum for tower base fore-aft moment in the OC5 project, frequency ranges from 0.31 Hz to 0.33 Hz

	Experiment	SIMA-W	SIMA-WL	SIMA-CA	SIMA-CQ	SIMA-C
PSD sum (mNm^2)	89.04	179.1	170.5	175.8	146.8	145.0

The damage equivalent loads for the tower base are compared in Fig. 4.23. Different SIMA models predict similar wave-frequency responses, but differ in estimating the low- and high-frequency responses. Although the low-frequency moments have a longer period, the more low-frequency responses the model can capture, the more accurate the responses around tower bending natural frequency are, and the better agreement the estimated damage equivalent load is with the experimental data.

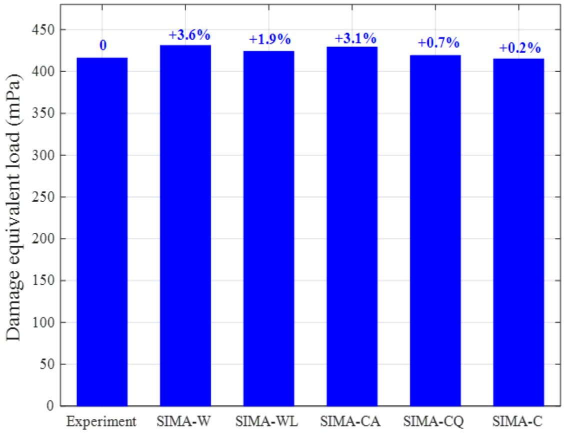

Figure 4.23: Damage equivalent load for the leading edge (Point A in Fig. 3.8) of tower base in the OC5 project

In conclusion, more accurate estimation of nonlinear hydrodynamics on the floater in the CFD simulations reduces the underprediction of the low-frequency dynamic responses of a semi-submersible FWT in the engineering model and shows the best agreement with the experimental measurements.

Chapter 5

Conclusions and Recommendations for Future Work

In this chapter, the main conclusions of this thesis will first be summarized. Based on the limitations identified in the current work, some topics are recommended for future work.

5.1 Conclusions

This thesis investigated nonlinear wave loads on a semi-submersible FWT using a higher-fidelity tool (CFD, OpenFOAM), a simplified engineering tool based on first and second order potential flow theory with Morison-type drag (SIMA), and experiments. The two approaches were first compared with experimental measurements in simplified conditions: such as a constrained structure subjected to regular waves, or imposed harmonic motions in still water. Using these results, a new approach was developed to improve the accuracy of the lower-fidelity engineering tool by using the CFD results to modify the difference-frequency wave load QTFs and frequency-dependent added mass and damping. The coupled model has been validated against the global responses of the FWT from experiments.

First, the CFD model was compared with the engineering model (SIMA) and experiments in predicting the higher harmonic wave diffraction loads on a constrained floater under regular waves. Compared to the experimental measurements, the CFD with turbulence model gave the best estimations.

When the Reynolds number was in 10^4-10^5, the laminar flow in the CFD simulations was not accurate enough, even though when the creation of strong vortices was not expected. The engineering model (SIMA) had large discrepancies in prediction of phase and amplitude. The dominant second harmonic components in SIMA were related to treating a nonlinear wave measurement as a linear input, while the third harmonic components mainly came from the contribution of Morison drag forces. In the trimmed conditions, the higher harmonic wave diffraction loads in the CFD simulations and most of third harmonic components in SIMA generally decreased, while the estimated second harmonic wave diffraction loads in SIMA showed opposite trend. In addition, a larger higher harmonic surge force on the starboard column was found in the CFD simulations.

Compared to the higher harmonic wave loads, the difference-frequency wave loads are even more important for the global responses of a semi-submersible wind turbine. The difference-frequency wave diffraction loads on a constrained floater under the bichromatic waves were investigated numerically. In SIMA, the difference-frequency surge force at the surge natural frequency was mainly from the integration of Morison drag force to the linear free surface. This contribution decreased with increasing wave frequencies, and the surge force from the QTF became dominant. On the other hand, at the pitch natural frequency, the pitch moment from the QTF was dominant. In addition, the axial drag forces on the heave plates had minor contributions to the difference-frequency wave diffraction loads. CFD and SIMA agreed well at the lower wave frequencies, while CFD predicted larger difference-frequency wave diffraction loads at higher wave frequencies. Interestingly, the CFD model gave approximately the opposite phase for the computed QTF compared to the original potential flow results. The trimmed condition, representing the effect of the mean thrust from the wind turbine, increased the difference-frequency surge force, especially in the CFD simulations, but had no significant effect on the difference-frequency pitch moments. A smaller surge forces at the surge natural frequency on the starboard column was found in the CFD simulations.

The investigation of added mass and linearized damping focused on long periods which were close to the natural periods for rigid body FWT motions. A weak dependency of the added mass coefficient on the oscillation period was found except the decreasing pitch added mass coefficient with oscillation period for large pitch motion. For small amplitudes of motions, the surge and pitch added mass coefficients seemed to be independent of the oscillation amplitude while the heave added mass coefficient showed a larger dependence on the oscillation amplitude. The added mass coefficient derived from the CFD simulations was slightly superior to the one estimated by the potential flow theory in most cases, suggesting that viscous effects gave an additional added mass. Regarding the damping, the linearized damping coefficient from the CFD simulations increased towards smaller motion amplitude and showed a small dependence on the oscillation period except the increasing surge linearized damping coefficient towards longer period. The radiation damping from the potential flow solution was completely negligible and viscous effects dominated.

Finally, the engineering model was modified using the CFD results from the constrained structure in bichromatic waves (modified QTFs) and imposed harmonic motions (modified added mass and damping). Experimental results from decay tests in still water and low-frequency wave diffraction loads and dynamic responses under an irregular wave were considered to validate the modified engineering tool. In the decay tests, after modifying the frequency-dependent added mass and damping, the underestimation of damping in the original engineering tool reduced and the modified engineering tool captured similar damping as the CFD model. Although there were differences in the added mass and damping, the predicted natural periods in all numerical models were close to the experimental results.

The modified difference-frequency QTFs for the fixed condition based on the CFD with turbulence model reduce the underprediction of low-frequency wave diffraction loads under an irregular wave compared to those calculated from the potential flow solutions and have a better agreement with experiment measurements than the results directly estimated from the CFD with laminar flow model.

The original difference-frequency QTFs from potential flow theory resulted in underestimation of the low-frequency dynamic responses, such as motions and mooring line tensions. The larger damping in the modified engineering tool increased this underestimation. However, when the more difference-frequency wave diffraction loads were captured, the low-frequency responses were overestimated. The combined modification gave the best agreement of low-frequency responses with the experimental measurements. Although the low-frequency responses had a longer period, the more low-frequency responses the model were captured, the better the agreement in the estimated damage-equivalent load with the experimental data was.

5.2 Recommendations for future work

Based on the work conducted in this thesis, the following topics are recommended for future work:

- *Other types of platform concepts*

  The investigations of nonlinear wave loads and resulting dynamic responses only focus on a particular semi-submersible platform in the current work. Other types of platform concepts should be considered, such as different (i.e. braceless) semi-submersibles, spars, and tension leg platforms, as well as larger FWTs.

- *Approaches to modify the QTFs and added mass and damping*

  The limited CFD simulation data in the current work lead to the implementation of interpolation approaches to modify the QTFs and added mass and damping, which results in additional numerical errors. Large amounts of CFD simulations could be carried out to assess how well the interpolation approach captures the variations, or to avoid the use of interpolation.

- *Analysis of local responses*

  Nonlinear wave loads on each column of the semi-submersible platform are obtained in the present work. The internal loads and local responses of FWTs resulting from these nonlinear wave loads should be investigated by applying these loads in both global and local analysis tools.

- *Freely floating simulations in the CFD model*

  The dynamic responses of FWTs due to nonlinear wave loads are now investigated in the engineering tools with modified hydrodynamics from CFD simulations. Although the computational cost will increase sharply, especially for the irregular wave tests, it is of interest to simulate freely floating FWTs in the CFD model. In order to achieve long simulations, several challenges must be overcome, such as wave damping and computational efficiency.

- *Investigations for the big difference in phases of nonlinear wave diffraction loads*

  The phases of the higher order and difference-frequency wave loads on the constrained floater differ between CFD simulations and potential flow solutions. A simplified model, such as the platform without braces or multiple columns without heave plates, could be established to investigate the flow in the wake of columns to improve the understanding of nonlinear wave loads.

- *Validation under wind-wave conditions*
  The engineering tools with modified hydrodynamics from CFD simulations has been validated against the experimental data under only-wave conditions. It will be interesting to extend the validation by comparing the global responses under combined wind and wave conditions.

- *The selection of drag coefficients*
  A uniform drag coefficient has been applied for the columns and braces in the engineering tools in the current work. However, the drag coefficients depend on the KC and Reynolds numbers. Hence, variable drag coefficients can be used to further improve the engineering tools in the future.

References

[1] Global Wind Energy Council. *Global Wind Report 2019.* 2020. Brussels, Belgium.

[2] Global Wind Energy Council. *Global Offshore Wind Report 2020.* 2020. Brussels, Belgium.

[3] Ramírez, L and Fraile, D and Brindley, G. *Offshore wind in Europe: Key trends and statistics 2019.* 2020.

[4] European Wind Energy Association. *Deep water - The next step for offshore wind energy.* 2013. Brussels, Belgium.

[5] James R, Ros MC. Floating offshore wind: market and technology review. *The Carbon Trust,* 2015; **439**.

[6] Bosch J, Staffell I, Hawkes AD. Global levelised cost of electricity from offshore wind. *Energy,* 2019; **189**:116 357.

[7] WindEurope. *Floating Offshore Wind Energy: A Policy Blueprint for Europe.* 2018.

[8] Li L, Gao Z, Moan T. Joint distribution of environmental condition at five European offshore sites for design of combined wind and wave energy devices. *Journal of Offshore Mechanics and Arctic Engineering,* 2015; **137**(3).

[9] Bak C, Zahle F, Bitsche R, Kim T, Yde A, Henriksen LC, Hansen MH, Blasques JPAA, Gaunaa M, Natarajan A. The DTU 10-MW reference wind turbine. *Danish Wind Power Research 2013*, 2013.

[10] Energy GR. World's most powerful offshore wind platform: Haliade-x. URL `http://www.ge.com/renewableenergy/wind-energy/offshore-wind/haliade-x-offshore-turbine`.

[11] Gaertner E, Rinker J, Sethuraman L, Zahle F, Anderson B, Barter GE, Abbas NJ, Meng F, Bortolotti P, Skrzypinski W, *et al.*. IEA Wind TCP Task 37: Definition of the IEA 15-Megawatt offshore reference wind turbine. *Technical Report*, National Renewable Energy Lab.(NREL), Golden, CO (United States), 2020.

[12] IEA. Offshore Wind Outlook 2019. *Technical Report*, International Energy Agency. 2019.

[13] Jonkman J, Butterfield S, Musial W, Scott G. Definition of a 5-MW reference wind turbine for offshore system Development. *Technical Report*, National Renewable Energy Lab.(NREL), Golden, CO (United States), 2009.

[14] Desmond C, Murphy J, Blonk L, Haans W. Description of an 8 MW reference wind turbine. *Journal of Physics: Conference Series*, vol. 753, IOP Publishing, 2016; 092 013.

[15] Roddier D, Cermelli C, Aubault A, Weinstein A. WindFloat: A floating foundation for offshore wind turbines. *Journal of renewable and sustainable energy,* 2010; **2**(3):033 104.

[16] Wind Europe. *Floating Offshore Wind Vision Statement.* 2017. Brussels, Belgium.

[17] Musial W, Butterfield S, Boone A. Feasibility of floating platform systems for wind turbines. *42nd AIAA aerospace sciences meeting and exhibit*, Reno, Nevada, 2004; 1007.

[18] Huijs F, de Bruijn R, Savenije F. Concept design verification of a semi-submersible floating wind turbine using coupled simulations. *Energy Procedia,* 2014; **53**:2–12.

[19] Fukushima Offshore Wind Consortium. Fukushima Floating Offshore Wind Farm Demonstration Project. 2020.

[20] Lefranc M, Torud A, *et al.*. Three wind turbines on one floating unit, feasibility, design and cost. *Offshore Technology Conference*, 2011.

[21] LIFES50+. *Deliverable D4.2 Public Definition of the Two LIFES50+ 10MW Floater Concepts.* 2018.

[22] Luan C. Design and analysis for a steel braceless semi-submersible hull for supporting a 5-MW horizontal axis wind turbine. PhD Thesis, Norwegian University of Science and Technology, 2018.

[23] Robertson A, Jonkman J, Masciola M, Song H, Goupee A, Coulling A, Luan C. Definition of the semisubmersible floating system for Phase II of OC4. *Technical Report NREL/TP-5000-60601*, National Renewable Energy Lab.(NREL), Golden, CO (United States), 2014.

[24] Robertson A, Jonkman J, Wendt F, Goupee A, Dagher H. Definition of the OC5 DeepCwind semisubmersible floating system. *Technical Report*, National Renewable Energy Lab.(NREL), Golden, CO (United States), 2016.

[25] Robertson AN, Gueydon S, Bachynski E, Wang L, Jonkman J, Alarcón D, Amet E, Beardsell A, Bonnet P, Boudet B, *et al.*. OC6 Phase I: Investigating the underprediction of low-frequency hydrodynamic loads and responses of a floating wind turbine. *Journal of Physics: Conference Series*, vol. 1618, IOP Publishing, 2020; 032 033.

[26] Wei YF, Yang JM, Chen X. A review of the hydrodynamic performance of heave damping plates on spar platform. *China Offshore Platform,* 2010; **25**(6):1–4.

[27] Robertson AN, Wendt F, Jonkman JM, Popko W, Dagher H, Gueydon S, Qvist J, Vittori F, Azcona J, Uzunoglu E, *et al.*. OC5 Project Phase II: Validation of global loads of the DeepCwind floating semisubmersible wind turbine. *Energy Procedia,* 2017; **137**:38–57.

[28] Commission IE. *IEC 61400-3: Wind turbines-Part 3: Design requirements for offshore wind turbines.* 2009. Geneva, Switzerland.

[29] Bulder B, van Hees M, Henderson A, Huijsmans R, Pierik J, Snijders E, Wijnants G, Wolf M. Study to feasibility of and boundary conditions for floating offshore wind turbines. *ECN, MARIN, TNO, TUD, MSC, Lagerway the Windmaster,* 2002; **26**:70–81.

[30] Pinkster JA. Low frequency second order wave exciting forces on floating structures. PhD Thesis, Delft University of Technology, 1980.

[31] Lee KH. Responses of floating wind turbines to wind and wave excitation. PhD Thesis, Massachusetts Institute of Technology, 2005.

[32] Vijayakumar G, Panneer Selvam R. Hydrodynamic analysis of barge floater with moonpool for 5 MW wind turbine using WAMIT. *International Conference on Marine Technology*, Kuala Terengganu, Malaysia, 2012.

[33] Lee CH. *WAMIT theory manual.* Massachusetts Institute of Technology, Department of Ocean Engineering, 1995.

[34] Wayman EN. Coupled dynamics and economic analysis of floating wind turbine systems. PhD Thesis, Massachusetts Institute of Technology, 2006.

[35] Sclavounos P, Tracy C, Lee S. Floating offshore wind turbines: Responses in a seastate Pareto optimal designs and economic assessment. *International Conference on Offshore Mechanics and Arctic Engineering*, vol. 48234, Estoril, Portugal, 2008; 31–41.

[36] Matha D. Model development and loads analysis of an offshore wind turbine on a tension leg platform with a comparison to other floating turbine concepts: April 2009. *Technical Report NREL/SR-500-45891*, National Renewable Energy Lab.(NREL), Golden, CO (United States), 2010.

[37] Jonkman JM. Dynamics modeling and loads analysis of an offshore floating wind turbine. *Technical Report NREL/TP-500-41958*, National Renewable Energy Lab.(NREL), Golden, CO (United States), 2007.

[38] MARINTEK. SIMO—Theory Manual Version 4.0. Marintek Trondheim, Norway, 2012.

[39] Ormberg H, Passano E. RIFLEX Theory Manual. Marintek, Trondheim, 2012.

[40] Larsen TJ, Hansen AM. How 2 HAWC2, the user's manual. *Technical Report*, Wind Energy Division, Technical University of Denmark, 2007.

[41] Withee JE. Fully coupled dynamic analysis of a floating wind turbine system. PhD Thesis, Monterey California. Naval Postgraduate School, 2004.

[42] Bossanyi E. GH bladed theory manual. *GH & Partners Ltd,* 2003; **2**:56–58.

[43] Matha D, Schlipf M, Pereira R, Jonkman J, *et al.*. Challenges in simulation of aerodynamics, hydrodynamics, and mooring-line dynamics of floating offshore wind turbines. *The Twenty-first International Offshore and Polar Engineering Conference*, American Society of Mechanical Engineers: Maui, Hawaii, USA, 2011.

[44] Myhr A, Maus KJ, Nygaard TA, *et al.*. Experimental and computational comparisons of the OC3-Hywind and tension-leg-buoy (TLB) floating wind turbine conceptual designs. *The Twenty-first International Offshore and Polar Engineering Conference*, American Society of Mechanical Engineers: Maui, Hawaii, USA, 2011.

[45] Coulling AJ, Goupee AJ, Robertson AN, Jonkman JM. Importance of second-order difference-frequency wave-diffraction forces in the validation of a FAST semi-submersible floating wind turbine model. *ASME 2013 32nd International Conference on Ocean, Offshore and Arctic Engineering*, American Society of Mechanical Engineers: Nantes, France, 2013.

[46] Bayati I, Jonkman J, Robertson A, Platt A. The effects of second-order hydrodynamics on a semisubmersible floating offshore wind turbine. *Journal of Physics: Conference Series*, vol. 524, IOP Publishing: Copenhagen, Denmark, 2014; 012 094.

[47] Cao Q, Xiao L, Guo X, Liu M. Second-order responses of a conceptual semi-submersible 10 mw wind turbine using full quadratic transfer functions. *Renewable Energy,* 2020; **153**:653–668.

[48] Gueydon S, Duarte T, Jonkman J. Comparison of second-order loads on a semisubmersible floating wind turbine. *International Conference on Offshore Mechanics and Arctic Engineering*, American Society of Mechanical Engineers: San Francisco, California, USA, 2014.

[49] Kvittem MI, Bachynski EE, Moan T. Effects of hydrodynamic modelling in fully coupled simulations of a semi-submersible wind turbine. *Energy Procedia,* 2012; **24**:351–362.

[50] Berthelsen PA, Bachynski EE, Karimirad M, Thys M. Real-time hybrid model tests of a braceless semi-submersible wind turbine: Part III—Calibration of a numerical model. *ASME 2016 35th International Conference on Ocean, Offshore and Arctic Engineering*, American Society of Mechanical Engineers: Busan, South Korea, 2016.

[51] Karimirad M, Bachynski EE, Berthelsen PA, Ormberg H. Comparison of real-time hybrid model testing of a braceless semi-submersible wind turbine and numerical simulations. *ASME 2017 36th International Conference on Ocean, Offshore and Arctic Engineering*, American Society of Mechanical Engineers: Trondheim, Norway, 2017.

[52] Larsen T, Yde A, Verelst D, Pedersen M, Hansen A, Hansen H. Benchmark comparison of load and dynamics of a floating 5MW semisub wind turbine, using three different hydrodynamic approaches. *Technical Report*, DTU Wind Energy, Technical University of Denmark, 2014.

[53] Bingham HB. A hybrid Boussinesq-panel method for predicting the motion of a moored ship. *Coastal Engineering,* 2000; **40**(1):21–38.

[54] Karimirad M, Moan T. Wave-and wind-induced dynamic response of a spar-type offshore wind turbine. *Journal of waterway, port, coastal, and ocean engineering,* 2012; **138**(1):9–20.

[55] Veritas DN. DeepC theory manual. DNV, Oslo, Norway, 2008.

[56] Jonkman J. Definition of the Floating System for Phase IV of OC3. *Technical Report NREL/TP-500-47535*, National Renewable Energy Lab.(NREL), Golden, CO (United States), 2010.

[57] Jonkman J, Musial W. Offshore Code Comparison Collaboration (OC3) for IEA Wind Task 23 offshore wind technology and deployment. *Technical Report NREL/TP-5000-48191*, National Renewable Energy Lab.(NREL), Golden, CO (United States), 2010.

[58] Robertson A, Jonkman J, Vorpahl F, Popko W, Qvist J, Frøyd L, Chen X, Azcona J, Uzunoglu E, Guedes Soares C, *et al.*. Offshore Code Comparison Collaboration Continuation within IEA Wind Task 30: Phase II results regarding a floating semisubmersible wind system. *International Conference on Offshore Mechanics and Arctic Engineering*, American Society of Mechanical Engineers: San Francisco, California, USA, 2014.

[59] Bachynski EE, Moan T. Ringing loads on tension leg platform wind turbines. *Ocean engineering,* 2014; **84**:237–248.

[60] Mercier JA, Leverette SJ, Bliault AL, *et al.*. Evaluation of hutton TLP response to environmental loads. *Offshore technology conference*, Houston, Texas, 1982.

[61] Bachynski EE, Moan T. Hydrodynamic modeling of tension leg platform wind turbines. *International Conference on Offshore Mechanics and Arctic Engineering*, American Society of Mechanical Engineers: Nantes, France, 2013.

[62] Bae Y, Kim M. Turbine-floater-tether coupled dynamic analysis including second-order sum-frequency wave loads for a TLP-type FOWT (Floating Offshore Wind Turbine). *ASME 2013 32nd International Conference on Ocean, Offshore and Arctic Engineering*, American Society of Mechanical Engineers: Nantes, France, 2013.

[63] Benitz MA, Schmidt DP, Lackner MA, Stewart GM, Jonkman J, Robertson A. Validation of hydrodynamic load models using CFD for the OC4-DeepCwind semisubmersible. *International Conference on Offshore Mechanics and Arctic Engineering*, American Society of Mechanical Engineers: St. John's, Newfoundland, Canada, 2015.

[64] Benitz MA, Schmidt DP, Lackner MA, Stewart GM, Jonkman J, Robertson A. Comparison of hydrodynamic load predictions between reduced order engineering models and computational fluid dynamics for the OC4-DeepCwind semi-submersible. *International Conference on Offshore Mechanics and Arctic Engineering*, American Society of Mechanical Engineers: San Francisco, California, USA, 2014.

[65] Wang L, Robertson A, Jonkman J, Yu YH. Uncertainty assessment of CFD investigation of the nonlinear difference-frequency wave loads on a semisubmersible FOWT platform. *Sustainability,* 2021; **13**(1):64.

[66] Siemens P. Simcenter, STAR-CCM+. *Academic Research, Release* 2017; **12**.

[67] ANSYS C. User Manual Release 12.1. ANSYS Inc., 2011.

[68] Weller HG, Tabor G, Jasak H, Fureby C. A tensorial approach to computational continuum mechanics using object-oriented techniques. *Computers in physics,* 1998; **12**(6):620–631.

[69] Lopez-Pavon C, Souto-Iglesias A. Hydrodynamic coefficients and pressure loads on heave plates for semi-submersible floating offshore wind turbines: A comparative analysis using large scale models. *Renewable Energy,* 2015; **81**:864–881.

[70] Bozonnet P, Emery A, *et al.*. CFD simulations for the design of offshore floating wind platforms encompassing heave plates. *The Twenty-fifth International Ocean and Polar Engineering Conference*, International Society of Offshore and Polar Engineers: Kona, Hawaii, USA, 2015.

[71] Zhang S, Ishihara T. Numerical study of hydrodynamic coefficients of multiple heave plates by large eddy simulations with volume of fluid method. *Ocean Engineering,* 2018; **163**:583–598.

[72] Wang B, Xu Z, Li C, Wang D, Ding Q. Hydrodynamic characteristics of forced oscillation of heave plate with fractal characteristics based on floating wind turbine platform. *Ocean Engineering,* 2020; **212**:107 621.

[73] Inc F. Fluent User's Guide, Version 6.1, 2003.

[74] Burmester S, Gueydon S, Vaz G, el Moctar B. Surge decay simulations of a semi-submersible floating offshore wind turbine. *Proceedings of the 20th numerical towing tank symposium*, 2017; 2–3.

[75] Burmester S, Vaz G, Gueydon S, el Moctar O. Investigation of a semi-submersible floating wind turbine in surge decay using CFD. *Ship Technology Research,* 2020; **67**(1):2–14.

[76] Burmester S, Vaz G, el Moctar O. Towards credible CFD simulations for floating offshore wind turbines. *Ocean Engineering,* 2020; **209**:107 237.

[77] Dunbar AJ, Craven BA, Paterson EG. Development and validation of a tightly coupled CFD/6-DOF solver for simulating floating offshore wind turbine platforms. *Ocean Engineering,* 2015; **110**:98–105.

[78] Vaz G, Jaouen F, Hoekstra M. Free-surface viscous flow computations: validation of URANS code FRESCO. *International Conference on Offshore Mechanics and Arctic Engineering*, vol. 43451, 2009; 425–437.

[79] Wang Y, Chen HC, Vaz G, Burmester S. CFD simulation of semi-submersible floating offshore wind turbine under pitch decay motion. *ASME 2019 2nd International Offshore Wind Technical Conference*, American Society of Mechanical Engineers: St. Julian's, Malta, 2019.

[80] Rivera-Arreba I, Bruinsma N, Bachynski EE, Viré A, Paulsen BT, Jacobsen NG. Modeling of a semisubmersible floating offshore wind platform in severe waves. *Journal of offshore mechanics and Arctic engineering,* 2019; **141**(6).

[81] Pinguet R, Kanner S, Benoit M, Molin B. Validation of open-source overset mesh method using free-decay tests of floating offshore wind turbine. *The 30th International Ocean and Polar Engineering Conference*, OnePetro, 2020.

[82] Pinguet R, Kanner S, Benoit M, Molin B. Modeling the dynamics of freely-floating offshore wind turbine subjected to waves with an open-source overset mesh method. *International Conference on Offshore Mechanics and Arctic Engineering*, vol. 84768, American Society of Mechanical Engineers, 2021.

[83] Bruinsma N, Paulsen B, Jacobsen N. Validation and application of a fully nonlinear numerical wave tank for simulating floating offshore wind turbines. *Ocean Engineering,* 2018; **147**:647–658.

[84] Tran TT, Kim DH. The coupled dynamic response computation for a semi-submersible platform of floating offshore wind turbine. *Journal of wind engineering and industrial aerodynamics,* 2015; **147**:104–119.

[85] Ferrandis JdÁ, Bonfiglio L, Rodríguez RZ, Chryssostomidis C, Faltinsen OM, Triantafyllou M. Influence of viscosity and non-linearities in predicting motions of a wind energy offshore platform in regular waves. *Journal of Offshore Mechanics and Arctic Engineering,* 2020; **142**(6).

[86] Wang Y, Chen HC, Vaz G, Burmester S, *et al.*. CFD simulation of semi-submersible floating offshore wind turbine under regular waves. *The 30th International Ocean and Polar Engineering Conference*, International Society of Offshore and Polar Engineers, 2020.

[87] Hu C, Sueyoshi M, Liu C, Liu Y, *et al.*. Hydrodynamic analysis of a semi-submersible type floating wind turbine. *The Eleventh ISOPE Pacific/Asia Offshore Mechanics Symposium*, International Society of Offshore and Polar Engineers: Shanghai, China, 2014.

[88] Liu C, Hu C, *et al.*. CFD simulation of a floating wind turbine platform in rough sea conditions. *The Twenty-fourth International Ocean and Polar Engineering Conference*, International Society of Offshore and Polar Engineers: Busan, Korea, 2014.

[89] Yabe T, Xiao F, Utsumi T. The constrained interpolation profile method for multiphase analysis. *Journal of Computational physics,* 2001; **169**(2):556–593.

[90] Xiao F, Ii S, Chen C. Revisit to the THINC scheme: a simple algebraic VOF algorithm. *Journal of Computational Physics,* 2011; **230**(19):7086–7092.

[91] Beyer F, Arnold M, Cheng PW, *et al.*. Analysis of floating offshore wind turbine hydrodynamics using coupled CFD and multibody methods. *The twenty-third international offshore and polar engineering conference*, International Society of Offshore and Polar Engineers: Anchorage, Alaska, 2013.

[92] Nematbakhsh A, Olinger D, Tryggvason G. Development and validation of a computational model for floating wind turbine platforms. *50th AIAA Aerospace Sciences Meeting including the New Horizons Forum and Aerospace Exposition*, Nashville, Tennessee, 2012; 373.

[93] Nematbakhsh A, Olinger DJ, Tryggvason G. A nonlinear computational model of floating wind turbines. *Journal of fluids Engineering,* 2013; **135**(12).

[94] Nematbakhsh A, Bachynski EE, Gao Z, Moan T. Comparison of wave load effects on a TLP wind turbine by using computational fluid dynamics and potential flow theory approaches. *Applied Ocean Research,* 2015; **53**:142–154.

[95] Zhang Y, Kim B. A fully coupled computational fluid dynamics method for analysis of semi-submersible floating offshore wind turbines under wind-wave excitation conditions based on OC5 data. *Applied Sciences,* 2018; **8**(11):2314.

[96] Zhao W, Wan D. Numerical study of interactions between Phase II of OC4 wind turbine and its semi-submersible floating support system. *J. Ocean Wind Energy,* 2015; **2**(1):45–53.

[97] Tran TT, Kim DH. Fully coupled aero-hydrodynamic analysis of a semi-submersible FOWT using a dynamic fluid body interaction approach. *Renewable energy,* 2016; **92**:244–261.

[98] Liu Y, Xiao Q, Incecik A, Peyrard C, Wan D. Establishing a fully coupled CFD analysis tool for floating offshore wind turbines. *Renewable Energy,* 2017; **112**:280–301.

[99] Tran TT, Kim DH. A CFD study of coupled aerodynamic-hydrodynamic loads on a semisubmersible floating offshore wind turbine. *Wind Energy,* 2018; **21**(1):70–85.

[100] Neville A. Hywind floating wind turbine, North Sea, Norway. *Power,* 2009; **153**(12):40–40.

[101] Bossler A. *Floating offshore wind foundations: industry consortia and projects in the United States, Europe and Japan.* Maine International Consulting, LLC, 2013.

[102] Skaare B, Hanson TD, Nielsen FG, Yttervik R, Hansen AM, Thomsen K, Larsen TJ. Integrated dynamic analysis of floating offshore wind turbines. *European wind energy conference and exhibition*, vol. 3, Citeseer, 2007; 1929–1939.

[103] Tomasicchio GR, D'Alessandro F, Avossa AM, Riefolo L, Musci E, Ricciardelli F, Vicinanza D. Experimental modelling of the dynamic behaviour of a spar buoy wind turbine. *Renewable Energy,* 2018; **127**:412–432.

[104] Cermelli C, Roddier D, Aubault A. WindFloat: A floating foundation for offshore wind turbines—Part II: hydrodynamics analysis. *International Conference on Offshore Mechanics and Arctic Engineering*, American Society of Mechanical Engineers: Honolulu, Hawaii, USA, 2009.

[105] Bachynski EE, Thys M, Sauder T, Chabaud V, Sæther LO. Real-time hybrid model testing of a braceless semi-submersible wind turbine: Part II—Experimental results. *ASME 2016 35th International Conference on Ocean, Offshore and Arctic Engineering*, American Society of Mechanical Engineers: Busan, South Korea, 2016.

[106] Lopez-Pavon C, Watai RA, Ruggeri F, Simos AN, Souto-Iglesias A. Influence of wave induced second-order forces in semisubmersible FOWT mooring design. *Journal of Offshore Mechanics and Arctic Engineering,* 2015; **137**(3).

[107] Simos AN, Ruggeri F, Watai RA, Souto-Iglesias A, Lopez-Pavon C. Slow-drift of a floating wind turbine: An assessment of frequency-domain methods based on model tests. *Renewable energy,* 2018; **116**:133–154.

[108] Goupee AJ, Koo B, Lambrakos K, Kimball R, *et al.*. Model tests for three floating wind turbine concepts. *Offshore technology conference*, Houston, Texas, USA, 2012.

[109] Cozijn H, Uittenbogaard R, Brake Et, *et al.*. Heave, roll and pitch damping of a deepwater CALM buoy with a skirt. *The Fifteenth International Offshore and Polar Engineering Conference*, International Society of Offshore and Polar Engineers: Seoul, Korea, 2005.

[110] Moreno J, Cameron M, Thiagarajan KP, Mendoza CAG, *et al.*. Hydrodynamic performance of heave plates on floating offshore wind turbine platforms. *The Twenty-fifth International Ocean and Polar Engineering Conference*, International Society of Offshore and Polar Engineers: Kona, Hawaii, USA, 2015.

[111] Philip NT, Nallayarasu S, Bhattacharyya S. Experimental investigation and CFD simulation of heave damping effects due to circular plates attached to spar hull. *Ships and Offshore Structures,* 2019; **14**(4):396–411.

[112] Nallayarasu S, Bairathi K. Hydrodynamic response of spar hulls with heave damping plate using simplified approach. *Ships and Offshore Structures,* 2014; **9**(4):418–432.

[113] Chua KH, Clelland D, Huang S, Sworn A. Model experiments of hydrodynamic forces on heave plates. *International Conference on Offshore Mechanics and Arctic Engineering*, American Society of Mechanical Engineers: Halkidiki, Greece, 2005.

[114] Tao L, Dray D. Hydrodynamic performance of solid and porous heave plates. *Ocean engineering,* 2008; **35**(10):1006–1014.

[115] Robertson A, Bachynski EE, Gueydon S, Wendt F, Schünemann P. Total experimental uncertainty in hydrodynamic testing of a semisubmersible wind turbine, considering numerical propagation of systematic uncertainty. *Ocean Engineering,* 2020; **195**:106 605.

[116] Goupee AJ, Fowler MJ, Kimball RW, Helder J, de Ridder EJ. Additional wind/wave basin testing of the DeepCwind semi-submersible with a performance-matched wind turbine. *International Conference on Offshore Mechanics and Arctic Engineering*, American Society of Mechanical Engineers: San Francisco, California, USA, 2014.

[117] Wendt FF, Robertson AN, Jonkman JM. FAST model calibration and validation of the OC5-DeepCwind floating offshore wind system against wave tank test data. *International Journal of Offshore and Polar Engineering,* 2019; **29**(01):15–23.

[118] Robertson AN, *et al.*. Uncertainty analysis of OC5-DeepCwind floating semisubmersible offshore wind test campaign. *The 27th International Ocean and Polar Engineering Conference*, International Society of Offshore and Polar Engineers: San Francisco, California, USA, 2017.

[119] Veritas DN. SESAM User Manual. WADAM: Wave Analysis by Diffraction and Morison Theory. Høvik, Norway 2013.

[120] Faltinsen O. *Sea loads on ships and offshore structures.* Cambridge university press, 1993.

[121] Jacobsen NG, Fuhrman DR, Fredsøe J. A wave generation toolbox for the open-source CFD library: OpenFoam®. *International Journal for numerical methods in fluids,* 2012; **70**(9):1073–1088.

[122] Hirt CW, Nichols BD. Volume of fluid (VOF) method for the dynamics of free boundaries. *Journal of computational physics,* 1981; **39**(1):201–225.

[123] Engsig-Karup AP, Bingham HB, Lindberg O. An efficient flexible-order model for 3D nonlinear water waves. *Journal of computational physics,* 2009; **228**(6):2100–2118.

[124] Paulsen BT, Bredmose H, Bingham HB. An efficient domain decomposition strategy for wave loads on surface piercing circular cylinders. *Coastal Engineering,* 2014; **86**:57–76.

[125] Berberović E, van Hinsberg NP, Jakirlić S, Roisman IV, Tropea C. Drop impact onto a liquid layer of finite thickness: Dynamics of the cavity evolution. *Physical Review E,* 2009; **79**(3):036 306.

[126] Menter F, Ferreira JC, Esch T, Konno B, Germany A. The SST turbulence model with improved wall treatment for heat transfer predictions in gas turbines. *Proceedings of the international gas turbine congress*, vol. 1, 2003; 2–7.

[127] Wilcox DC, *et al.*. *Turbulence modeling for CFD.* DCW industries La Canada, CA, 1998.

[128] Launder BE, Spalding DB. The numerical computation of turbulent flows. *Numerical prediction of flow, heat transfer, turbulence and combustion.* Elsevier, 1983; 96–116.

[129] Rahman MM, Karim MM, Alim MA. Numerical investigation of unsteady flow past a circular cylinder using 2-D finite volume method. *Journal of Naval Architecture and Marine Engineering,* 2007; **4**(1):27–42.

[130] Brown SA, Magar V, Greaves DM, Conley DC. An evaluation of RANS turbulence closure models for spilling breakers. *Coastal Engineering Proceedings,* 2014; (34):5–5.

[131] Menter FR, Kuntz M, Langtry R. Ten years of industrial experience with the SST turbulence model. *Turbulence, heat and mass transfer,* 2003; **4**(1):625–632.

[132] Devolder B, Rauwoens P, Troch P. Application of a buoyancy-modified $k-\omega$ SST turbulence model to simulate wave run-up around a monopile subjected to regular waves using OpenFOAM®. *Coastal Engineering,* 2017; **125**:81–94.

[133] Fan W, Anglart H. varRhoTurbVOF: A new set of volume of fluid solvers for turbulent isothermal multiphase flows in OpenFOAM. *Computer Physics Communications,* 2020; **247**:106 876.

[134] Li H, Bachynski EE. Experimental and numerical investigation of nonlinear diffraction wave loads on a semi-submersible wind turbine. *Renewable Energy,* 2021; **171**:709–727.

[135] Madsen PA, Fuhrman DR. Third-order theory for bichromatic bidirectional water waves. *Journal of Fluid Mechanics,* 2006; **557**:369.

[136] Spalding D. A single formula for the "law of the wall". *ASME,* 1961; :455–458.

[137] Causin P, Gerbeau JF, Nobile F. Added-mass effect in the design of partitioned algorithms for fluid–structure problems. *Computer methods in applied mechanics and engineering,* 2005; **194**(42-44):4506–4527.

[138] Ferziger JH, Perić M, Street RL. *Computational methods for fluid dynamics*, vol. 3. Springer, 2002.

[139] Bachynski EE, Pákozdi C, Östman A, Stansberg CT. Computational fluid dynamics reproduction of nonlinear loads on a vertical column during extreme irregular wave events. *Journal of Offshore Mechanics and Arctic Engineering,* 2018; **140**(6).

[140] Pessoa Jo, Fonseca N, Guedes Soares C. Experimental and numerical study of the depth effect on the first order and slowly varying motions of a floating body in bichromatic waves. *International Conference on Offshore Mechanics and Arctic Engineering*, American Society of Mechanical Engineers: Shanghai, China, 2010.

[141] Fonseca N, Pessoa J, Mavrakos S, Le Boulluec M. Experimental and numerical investigation of the slowly varying wave exciting drift forces on a restrained body in bi-chromatic waves. *Ocean engineering,* 2011; **38**(17-18):2000–2014.

[142] Tom N, Robertson A, Jonkman J, Wendt F, Böhm M. Bichromatic wave selection for validation of the difference-frequency transfer function for the OC6 validation campaign. *ASME 2019 2nd International Offshore Wind Technical Conference*, American Society of Mechanical Engineers: St. Julian's, Malta, 2019.

[143] Chakrabarti SK. *Advanced Series on Ocean Engineering, Volume 9: Offshore Structure modeling.* World Scientific, 1994.

[144] Li H, Hu Z, Wang J, Meng X. Short-term fatigue analysis for tower base of a spar-type wind turbine under stochastic wind-wave loads. *International Journal of Naval Architecture and Ocean Engineering,* 2018; **10**(1):9–20.

[145] Kvittem MI, Moan T. Time domain analysis procedures for fatigue assessment of a semi-submersible wind turbine. *Marine Structures,* 2015; **40**:38–59.

[146] Hayman G. MLife theory manual for version 1.00. National Renewable Energy Laboratory (NREL), 2012.

[147] Matsuishi M, Endo T. Fatigue of metals subjected to varying stress. *Japan Society of Mechanical Engineers, Fukuoka, Japan,* 1968; **68**(2):37–40.

[148] Naess A, Moan T. *Stochastic dynamics of marine structures.* Cambridge University Press, 2013.

[149] Halse KH. On vortex shedding and prediction of vortex-induced vibrations of circular cylinders. PhD Thesis, Norwegian University of Science and Technology, 1997.

[150] Dütsch H, Durst F, Becker S, Lienhart H. Low-Reynolds-number flow around an oscillating circular cylinder at low Keulegan–Carpenter numbers. *Journal of Fluid Mechanics,* 1998; **360**:249–271.

[151] Gao Z, Efthymiou M, Cheng L, Zhou T, Minguez M, Zhao W. Hydrodynamic damping of a circular cylinder at low KC: Experiments and an associated model. *Marine Structures,* 2020; **72**:102 777.

Appendix A

Approaches to modify the QTF matrix

To address the problem of using a small number of CFD simulation results to modify the whole QTF matrix, three different interpolation approaches have been proposed.

Approach 1:

In the first approach, the magnitudes and phases of QTF values from CFD simulations and potential flow theory (WAMIT) are separately interpolated to obtain values at denser sets of frequencies (using an interval of 0.001 Hz). Then, the interpolated results from WAMIT along the surge and pitch natural frequencies are replaced with the interpolated results from CFD simulations. The magnitudes or phases with the same f_2 (Fig. 3.7 in Section 3.5.1) are extracted and a smoothing spline is used to fit all the data with the modified QTF values from CFD simulations. An example is shown in the left subplot of Fig. A.1. Finally, this modified QTF matrix is downsampled to an interval of 0.05 Hz and implemented in the SIMA model. As shown in Fig. A.1, this approach changes the local values close to the QTF values from CFD, but has no effect on the values far away from the frequencies at which CFD simulations are available.

Approach 2:

The second approach is the one presented in Section 3.5.1. This approach assumes that the QTF value varies with frequency in the same way before and after the modification. For the region with two values from the CFD model, given that the variations of these two values may not be identical, the gradient is assumed to vary linearly to make sure the modified QTF values along the surge and pitch natural frequencies are equal to the estimated values from CFD simulations while keeping the trends of QTF values as a function of frequency the same before and after the modification.An example is shown in the left subplot of Fig. A.1.

Approach 3:

In the third approach, the QTF values (magnitude A_i^o and phase angle θ_i^o) estimated based on potential flow (WAMIT) are computed at the frequency pairs where the CFD simulations are carried out. By building contour matrices for these QTF values from WAMIT, all sets of frequencies which have the same QTF value are identified. An example is shown in the right subplot of Fig. A.1. Assuming the magnitudes and phase angles of QTF values have same shape before and after the modification, the original magnitudes and phase angles (A_i^o, θ_i^o) from WAMIT at all the sets of frequencies are replaced with the new ones (A_i^n, θ_i^n) from CFD simulations to build new contour matrices. The new contour matrices are interpolated using cubic interpolation based on triangulation to compute the modified QTF values at any sets of frequencies. The procedure is summarized in Fig. A.2. This approach uses the contour matrix to keep the shape of QTF the same before and after the modification.

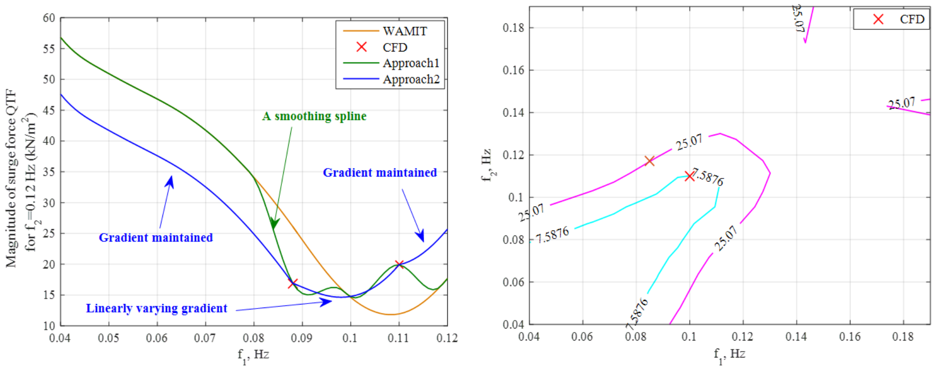

(a) Approach 1 and 2 (Surge force QTF with same f_2 but different f_1)

(b) Approach 3(Number represents the magnitude of surge force QTF)

Figure A.1: Explanations for different approaches

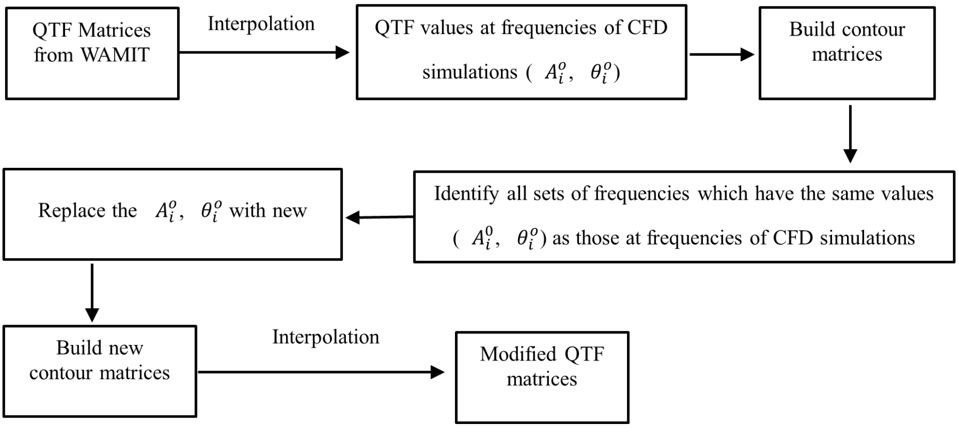

Figure A.2: Approach 3 to modify the QTFs

Comparisons :

The magnitudes of surge force QTFs for f_2=0.12 Hz among different approaches are compared in Fig. A.3. Approach 3 overpredicts the magnitude at lower frequencies. From the right subplot of Fig. A.1, the lower frequencies have the same QTF magnitudes as those at higher frequencies because they are located on the same contour.

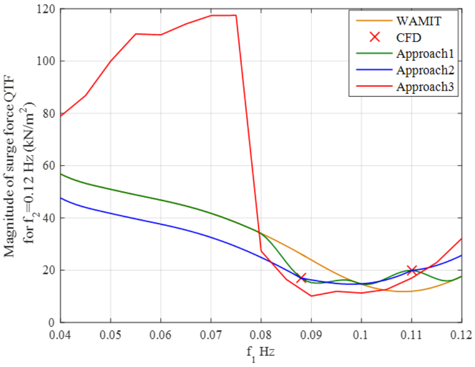

Figure A.3: Comparisons of magnitude of surge force QTF for f_2 = 0.12 Hz among different methods

The comparisons of modified surge force and pitch moment QTFs in the low-frequency range among different approaches are compared in Figs. A.4-A.6.

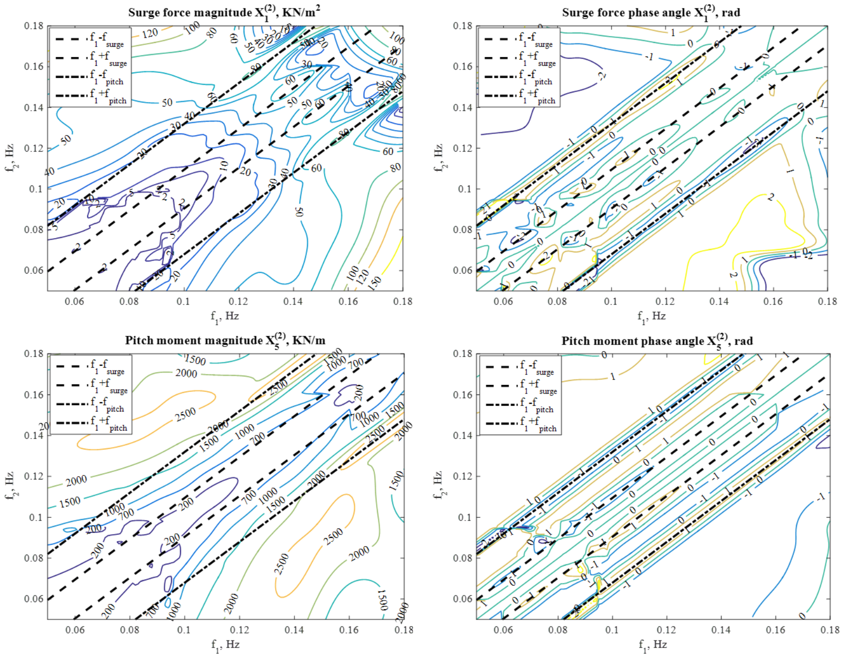

Figure A.4: Modified QTFs using Approach 1

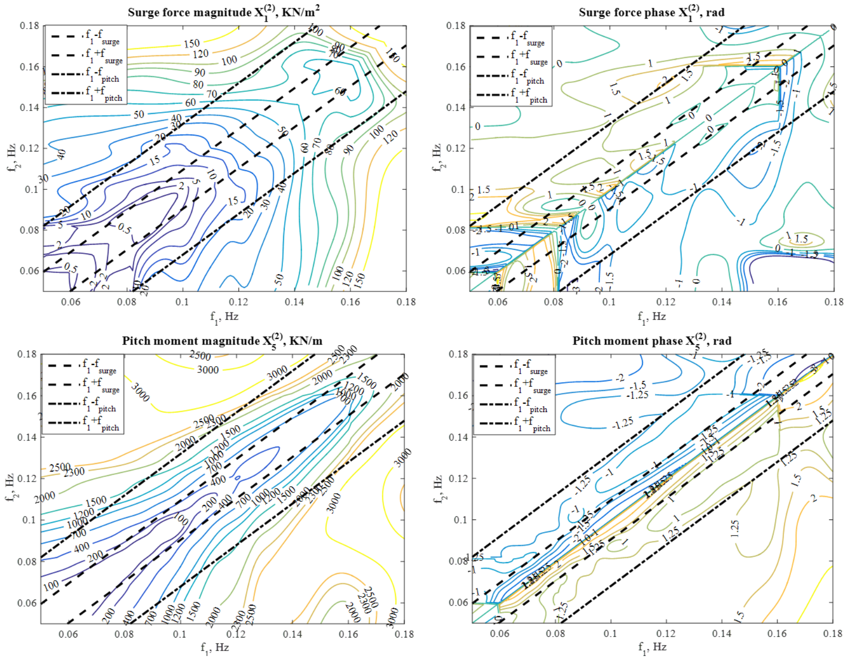

Figure A.5: Modified QTFs using Approach 2

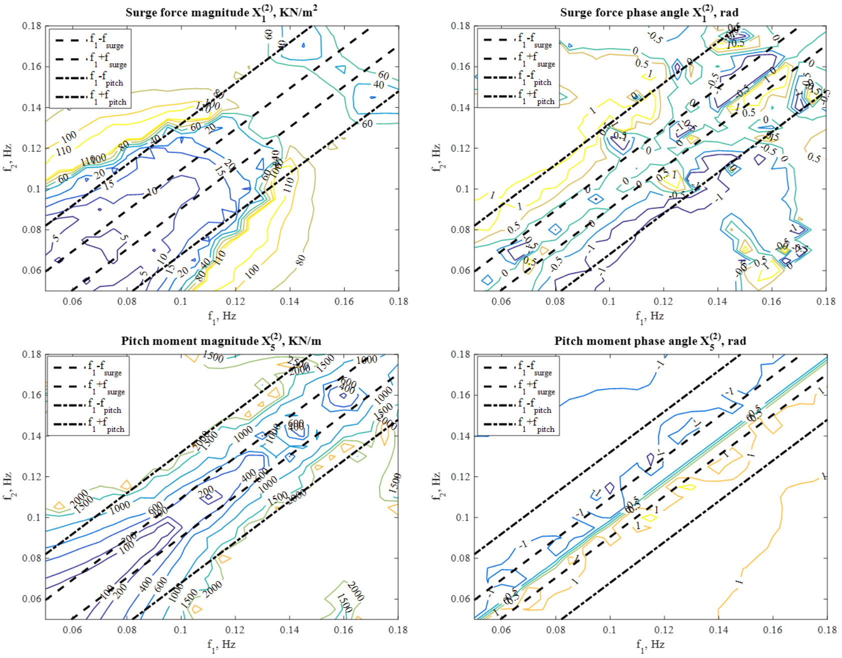

Figure A.6: Modified QTFs using Approach 3

The estimated low-frequency wave loads on the constrained floater by these three different approaches are compared in Fig. A.7 and Table A.1. Approach 1 significantly underpredicts the difference-frequency wave loads, because only the local values near the modified QTF values from CFD simulations are modified. Approach 3 overpredicts the responses, especially for surge force at the high frequencies.That is because there are some peak QTF values at these frequencies (Fig. A.6). The Approach 2 has the best agreement with the experimental data and is presented in the Section 3.5.1.

Table A.1: Comparisons of difference-frequency PSD sum metric for different approaches, frequency ranges from 0.005 Hz to 0.05 Hz

	Surge PSD sum (N^2)	Pitch PSD sum($(Nm)^2$)
Experiment	8.242E+10	5.382E+13
SIMA5	3.703E+10	3.084E+13
SIMA6 with Approach 1	4.581E+10	3.565E+13
SIMA6 with Approach 2	8.049E+10	4.741E+13
SIMA6 with Approach 3	1.079E+11	6.207E+13

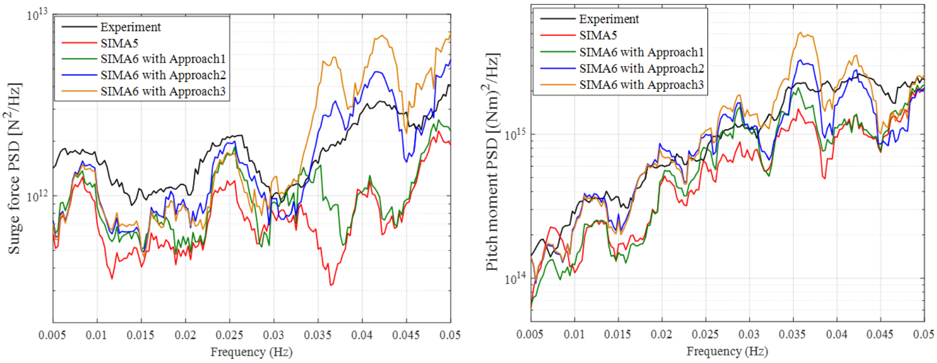

(a) Surge force *(b) Pitch moment*

Figure A.7: Comparisons of spectra in low-frequency range for different approaches

These interpolation approaches are used for the limited CFD simulation data. When large amounts of CFD simulation data are obtained, there is no need for interpolation. However, the computational cost in the CFD simulations will increase sharply.

Appendix B

Appended Papers

B.1 Paper 1

Paper 1:
Haoran Li and Erin E. Bachynski. Experimental and numerical investigation of nonlinear diffraction wave loads on a semi-submersible wind turbine. *Renewable Energy* 2021; **171**:709-721. `https://doi.org/10.1016/j.renene.2021.02.152`

Renewable Energy 171 (2021) 709–727

Contents lists available at ScienceDirect

Renewable Energy

journal homepage: www.elsevier.com/locate/renene

Experimental and numerical investigation of nonlinear diffraction wave loads on a semi-submersible wind turbine

Haoran Li [a], [*], Erin E. Bachynski [a], [b]

[a] Department of Marine Technology, Norwegian University of Science and Technology (NTNU) Trondheim, Norway
[b] Centre for Autonomous Marine Operations and Systems (AMOS), NTNU, Trondheim, Norway

A R T I C L E I N F O

Article history:
Received 5 April 2020
Received in revised form
9 February 2021
Accepted 25 February 2021
Available online 1 March 2021

Keywords:
Floating wind turbine
Semi-submersible
CFD
Potential flow theory
Nonlinear wave diffraction loads

A B S T R A C T

In a severe sea state, nonlinear wave loads can excite resonant responses of floating wind turbines either at high (structural) or low (rigid body motions) natural frequencies. In the present work, a computational fluid dynamics (CFD) model and an engineering model based on potential-flow theory with Morison-type drag are developed to investigate nonlinear wave loads on a stationary, rigid semi-submersible wind turbine under regular and irregular waves. The numerical results are validated against experimental measurements. A trimmed floater is modelled to examine the change in nonlinear wave loads due to the mean pitch angle which occurs during operation of a floating wind turbine. Furthermore, wave loads on each column are investigated numerically. Compared to the experimental measurements, the CFD model gives better estimations than the engineering model for the first, second and third order wave diffraction loads. The engineering model based on the first- and second-order potential-flow theory has large discrepancies in the phase of high order wave diffraction loads and underpredicts the amplitude of low-frequency wave loads. In the CFD simulations for the studied wave period (12.1 s), the second and third harmonic surge forces on the starboard columns are significantly larger than those on the upstream column, while first harmonic results are consistent with potential flow. The trim angle (5°) results in an increasing surge force and pitch moment but a decreasing heave force.

1. Introduction

Recently, there has been a huge increase in the use of wind turbines for generating electricity. To access a larger wind resource and reduce visual and acoustic pollution, a growing number of offshore wind turbines (OWTs) has been installed in recent years. In shallow and intermediate water depths, bottom-fixed OWTs are employed. However, in deep water, the costs of bottom-fixed foundations rise sharply, so a wide variety of floating wind turbine (FWT) concepts have been proposed, such as spar, semi-submersible and tension leg platforms (TLP). With increasing water depth, FWTs may be exposed to harsh environments and steep waves which induce highly nonlinear wave loads on the floater of FWTs. The high-frequency loads can cause springing and ringing, while the low-frequency loads can lead to the resonance in surge, sway and yaw of a moored platform. Mercier et al. [1] showed the importance of high order wave loads on TLPs through experiments. Coulling et al. [2] also used experiments and numerical tools to stress the importance of second-order difference-frequency wave forces in capturing the global response of a semi-submersible FWT. As the responses of FWTs are largely affected by nonlinear wave loads, validated modelling tools should be developed to predict these loads more accurately while keeping the computational efficiency at a reasonable level.

Most of the investigations of nonlinear hydrodynamic loads on different types of wind turbines are based on low order potential flow models [3–7]. This limits hydrodynamic modeling to linear or weakly nonlinear models and may be less reliable for analysis of FWTs in extreme condition. Some studies use high order commercial or in-house CFD codes to investigate wave loads and motion responses on various types of FWTs, as summarized in Table 1.

Although the offshore oil and gas industry has demonstrated the long-term survivability of semi-submersible platforms and can provide some guidelines for design, significant differences exist. With a smaller payload and no permanent residences for personnel, FWTs are significantly smaller than oil and gas platforms

---

[*] Corresponding author. Otto Nielsens veg 10, Marine Technology Centre, 2nd floor, Trondheim, 7491, Norway.
E-mail address: haoran.li@ntnu.no (H. Li).

https://doi.org/10.1016/j.renene.2021.02.152

Table 1
Overview of investigations of FWTs using CFD.

Reference	Methods	Conditions	Main conclusions
Beyer et al. [8]	1. RANS equation 2. VOF for free surface 3.SST turbulence model 4. Multi-body system for calculating motion	Surge free decay test of OC3 spar-buoy wind turbine in still water	Pitch motion was excited due to vortex-induced forces on the platform
Benitz et al. [9,10]	1. RANS equation 2. VOF for free surface 3. Spalart-Allmaras turbulence model 4. Wave2Foam for wave	Hydrodynamic loads on OC4 semi-submersible platform under current-only and wave-only conditions	Shadowing effects and transverse forces from vortex shedding can be captured.
Rivera-Arreba et al. [11]	1. NS equation 2. VOF for free surface 3. Laminar flow 4. Wave2Foam for wave	Heave and pitch free decay and responses of OC5 semi-submersible platform under heave resonance and large steepness wave conditions	For free decay cases, the heave response of the potential-flow model showed an amplitude 40% lower than CFD model. However, the heave responses under different regular waves were slightly lower in CFD model.
Nematbakhsh et al. [12–14]	1. One-fluid NS equation. 2. Level set method for free surface 3. Laminar flow 4. The loads from structural model are included in NS equation.	Surge and heave free decay tests and responses of TLP wind turbine under regular wave condition	The chance of strong vortex shedding behind the TLP is small due to the large diameter of the TLP tank and the small Keulegan–Carpenter (KC) number. A higher mean surge motion is noticed due to better representation of nonlinear effects.
Hu and Liu et al. [15,16]	1. CIP method [17] 2. THINC [18]for free surface 3. ImmersedBoundary Method for fluid-structure interaction	Surge, heave and pitch RAO of two types of semi-submersible wind turbines	CFD simulations can study the nonlinear phenomena in large amplitude wave conditions.

[19]. Semi-submersible FWTs are usually made of three or four vertical columns connected by cross braces which affect the flow regimes around columns. In addition, heave plates are often attached to the bottom of the columns to increase the added mass and damping. An additional lift force on heave plates due to vortex shedding may also appear [10]. Another difference between FWTs and oil and gas platforms is a mean pitch angle for the wind platform during operation due to the aerodynamic thrust force.

To better understand the nonlinear diffraction wave loads on a semi-submersible FWT, a CFD model and a potential flow theory model are used to simulate the interaction of a semi-submersible FWT with regular and irregular waves. The numerical results are compared with experimental data. Higher order sum-frequency wave loads are examined for a regular wave condition; an irregular wave state is chosen to investigate the wave loads around natural periods of rigid body motions. Because a fixed platform is considered here, we cannot directly compare responses around low frequencies. However, some qualitative conclusions are also drawn from the results.

A trimmed condition under regular wave is also modelled to examine the change of nonlinear wave loads due to the trim induced by the mean aerodynamic thrust force. In addition, wave loads on each column are extracted to better understand the effects of the multimember arrangement of the semisubmersible.

Section 2 briefly describes the experiment for comparison, while Section 3 describes the CFD and potential flow theory models. In Section 4, the wave loads on the upright and trimmed floater under regular wave condition are analyzed. Then, the wave loads due to irregular waves are examined. Finally, conclusions are presented in Section 5.

2. Review of experiment

In the present work, experimental results for the wave loads on the floater are from Phase I of the Offshore Code Comparison Collaboration, Continued, with Correlation, and unCertainty (OC6) project [20]. The model test was performed in the concept basin of the Maritime Research Institute Netherland (MARIN). The geometry of the floater corresponds to the DeepCwind semi-submersible floater [21] at 1:50 scale. The right-handed coordinate system used in this research originates at the center of the main column at the still water line, with positive x being in the direction of propagating waves, and z being up. The tower of the wind turbine was removed and the floater was attached to the carriage through a frame, as shown in Fig. 1. Wave loads on the stationary model were measured using a six-component gauge connecting the floater and the frame. The results presented in this paper are calculated based on the shown coordinate system. All data and results are given at full scale, except when explicitly mentioned. The uncertainty in the experiment is about 2% for the measured force and 5% for the measured moments [20].

One regular wave with height $H = 7.1$ m and period $T = 12.1$ s, and an irregular wave with significant wave height $H_s = 7.1$ m and peak period $T_p = 12.1$ s were selected for this research. The irregular wave was generated based on the JONSWAP spectrum with the peak enhancement factor equal to 3.3.

3. Computational model

The same global coordinate system as in the experiment (Fig. 1) is implemented in the computational model.

3.1. CFD model

The multiphase interFoam solver of OpenFOAM [22] is a fully nonlinear Navier-Stokes/VOF solver. Extending the interFoam solver with the wave generation and absorption toolbox, waves2Foam, developed by Jacobsen et al. [23], generates the waveFoam solver. Furthermore, a fully nonlinear potential flow solver, Oceanwave3D [24], is coupled with the waveFoam solver to minimize numerical diffusion and reduce the computational time for the irregular wave case [25].

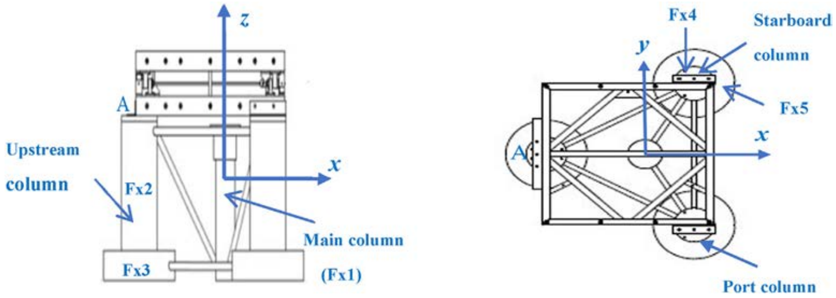

Fig. 1. Side (left) and top (right) view of the constrained model [20].

3.1.1. Governing equations

The waveFoam solver utilizes the two-phase incompressible Navier-Stokes equations to compute the fluid flow around the stationary semi-submersible. The governing equations consist of mass conservation and momentum conservation:

$$\frac{\partial u_i}{\partial x_i} = 0 \tag{1}$$

$$\frac{\partial \rho u_i}{\partial t} + \frac{\partial \rho u_j u_i}{\partial x_j} = -\frac{\partial p^*}{\partial x_i} + F_{b,i} + \frac{\partial}{\partial x_j}\left[\mu_{eff}\frac{\partial u_i}{\partial x_j}\right] \tag{2}$$

where u_i $(i = x, y, z)$ are the fluid velocity in Cartesian coordinates, ρ is the fluid density, p^* is pressure in excess of the hydrostatic pressure, $F_b$is an external body force including gravity and μ_{eff} is the effective dynamic viscosity. For laminar flow, μ_{eff} is equal to the laminar dynamic viscosity. For turbulent flow, it should include turbulent dynamic viscosity $\rho\nu_t$.

The local density ρ and the effective dynamic viscosity μ_{eff} are defined by the volume fraction α which is bounded between 0 (air) and 1 (water). The turbulent dynamic viscosity $\rho\nu_t$ is neglected in laminar flow model.

$$\rho = \alpha\rho_{water} + (1-\alpha)\rho_{air} \tag{3}$$

$$\mu_{eff} = \alpha\mu_{water} + (1-\alpha)\mu_{air} + \rho\nu_t \tag{4}$$

The air-water interface is tracked by the volume of fluid VOF method [26] in OpenFoam. The volume fraction is advanced in time once the velocity is known, following scalar advection equation:

$$\frac{\partial \alpha}{\partial t} + \frac{\partial u_i \alpha}{\partial x_i} + \frac{\partial u_{r,i}\alpha(1-\alpha)}{\partial x_i} = 0 \tag{5}$$

The smearing of the interface is vastly reduced by the introduction of the artificial velocity u_r. It is only active in the vicinity of the interface where $0 < \alpha < 1$, see Berberovic et al. [27] for details. To ensure the boundedness of solution, a multi-dimensional flux limited scheme (MULES) is applied. To identify the free surface elevation, the volume fraction$\alpha$is integrated along a vertical line around the air-water interface.

3.1.2. Turbulence modelling

The effects of turbulence are incorporated in the governing equations by using different transport equations to calculate the turbulent kinematic viscosity ν_t. The $k-\omega$ SST turbulence model has shown good results for simulating two-phase flow and predicting wave elevation [28,29] and is applied in this paper. The incompressible $k-\omega$ SST model for a single fluid is a two-equation model and is given in OpenFoam as:

$$\frac{\partial k}{\partial t} + \frac{\partial u_j k}{\partial x_j} - \frac{\partial}{\partial x_j}\left[(\nu + \sigma_k \nu_t)\frac{\partial k}{\partial x_j}\right] = P_k - \beta^* \omega k \tag{7}$$

$$\frac{\partial \omega}{\partial k} + \frac{\partial u_j \omega}{\partial x_j} - \frac{\partial}{\partial x_j}\left[(\nu + \sigma_\omega \nu_t)\frac{\partial \omega}{\partial x_j}\right] = \frac{\gamma}{\nu_t}G - \beta\omega^2 + 2(1-F_1)\frac{\sigma_{\omega 2}}{\omega}\frac{\partial k}{\partial x_j}\frac{\partial \omega}{\partial x_j} \tag{8}$$

where k is the turbulent kinetic energy, P_k is the production term of k, ν is kinematic viscosity, ν_t is the turbulent kinematic viscosity, ω is the specific dissipation rate, as described in detail by Menter et al. [30]. In the present work, to avoid significant wave damping induced by increasing turbulent viscosity [31,32], a modified waveFoam solver is built to explicitly consider the variable density in the $k-\omega$ SST model [32].

Table 2 shows the Keulegan-Carpenter (KC) and Reynolds numbers at model scale, assuming the wave is fully linear. The inflow velocity is the maximum horizontal water particle velocity. The KC number is around 1 for most of components. Hence, weak vortices are expected in the experiment and CFD simulations. Although the Reynolds numbers are on the order of 10^4-10^5, previous studies considering the same geometry suggest that the turbulence model is not essential for the CFD simulations due to the low KC number of upper column and heave plate [33]. For regular wave cases, simulations using both laminar (L.F) and turbulent (T.F) flow are carried out for comparison.

3.1.3. Numerical domain

To reduce the computational time, CFD simulations with a stationary semi-submersible floater were carried out at model scale (1:50). In this section, all data are given at model scale.

The width (3.72 m) and water depth (3.6 m) of the experimental wave flume are modelled. The numerical wave tank (36 m) is shorter than the experimental wave flume, but long enough to dissipate the reflected waves. Fig. 2 shows good agreement in the overlayed wave elevation at the center of floater for three cycles separated in time: before reflections can reach the center of the floater, after reflections from the outlet are expected, and after reflections from both inlet and outlet are expected. The height of

Table 2
KC and Reynolds numbers for different parts of floater for regular wave realization (model scale).

	Main column	Upper column	Heave plate	Cross brace
KC (−)	2.89–3.43	1.86	0.93	13.94
Re (× 10^5)	0.33–0.40	0.62	1.23	0.08

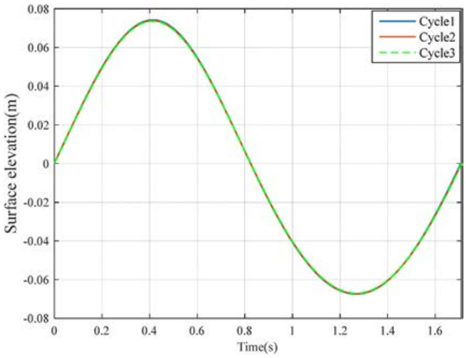

Fig. 2. Surface elevation at the center of floater at different times, no semi-submersible present (Cycle1: only incident wave. Cycle2: incident wave with reflected wave from outlet boundary. Cycle3: incident wave with reflected wave from inlet and outlet boundaries).

the air regime is set to 1 m. Fig. 3 shows a plan view of the numerical wave tank with floater.

After spatial discretization, the size of a cell in all directions is 0.12 m. Thereafter, for the air-water interface, the mesh was refined. A mesh convergence study for free surface elevation and calculated wave loads was carried out. In Table 3, the wave height at origin (center of floater) is compared to the specified wave height at inlet (H = 0.142 m) and the wave loads are compared to those with the finest mesh size (Level 4) for three different spatial discretizations. The 3-3 level of refinement, resulting in a mesh size of 0.015 m ($\approx$H/10), is applied for the air-water interface and surface of columns. Around the cross braces, which have a smaller diameter, the 4-4 level is applied, leading to cross brace mesh size 0.0075 m ($\approx$H/20). This local refinement allows for a high-resolution interface while keeping the total number of computational cells relatively low. For the turbulent flow model, 25 cell layers adjacent to the floater surface are generated. The thickness of the first layer is 2.0 μm and its expansion ratio is 1.2.

3.1.4. Boundary conditions

In the Navier-Stokes/VOF solver, boundary conditions are imposed on all surfaces in the numerical domain. The general denomination of boundary surfaces is given in Fig. 4.

The velocity and the volume fraction boundary conditions are given by stream function wave theory at the inlet and a constant current with zero velocity at the outlet. The floater surfaces and tank bottom are modelled as fixed walls. For the laminar flow model, a slip condition is applied, which means the effect of viscosity and turbulence generation are neglected. For the turbulent flow model, wall functions are applied for k (1e-5 m^2/s^2) and ω (1.0 1/s). A continuous wall function based on Spadling's law [34] is implemented for the turbulent viscosity. Furthermore, a Dirichlet boundary condition is set for the velocity while a Neumann condition is used for pressure and volume fraction on the fixed walls. A slip condition is applied to the front and back walls. At the atmosphere boundary, the total pressure is set to zero and an atmospheric boundary condition is applied for the velocity and volume fraction. This means that air and water are allowed to leave the numerical domain, while only air is allowed to flow back in.

The Waves2Foam toolbox [23] implements relaxation zones (blue part in Fig. 4) to avoid wave reflection from the outlet boundary (II) and to prevent internally reflected waves (I). Rectangular relaxation zones are defined in this work, as in Bruinsma's work [35].

3.1.5. Temporal discretization

To ensure numerical stability, the temporal discretization is determined based on the Courant-Friedrichs-Lewy condition. Different fixed time steps were chosen to carry out a time step convergence study. In Table 4, the errors are relative to the specified wave height at inlet (0.142 m, model scale) or the numerical results with the smallest time step. To limit computational effort while obtaining sufficient accuracy, a fixed time step (0.001414 s, model scale) is used in the rest of this work.

The Richardson extrapolation with the standard power-law error estimator [36] is used to obtain the wave loads at the limit of infinite temporal and spatial resolution. The resulting apparent order of convergence is 2. The discretization uncertainty is defined as the estimated discretization error multiplied to a suitable safety factor (1.25 following the recommendation from Eça and Hoekstra [37]). The total uncertainty is given by combining the temporal and spatial discretization uncertainties in the root-sum-of-squares fashion, shown in the last column of Table 6.

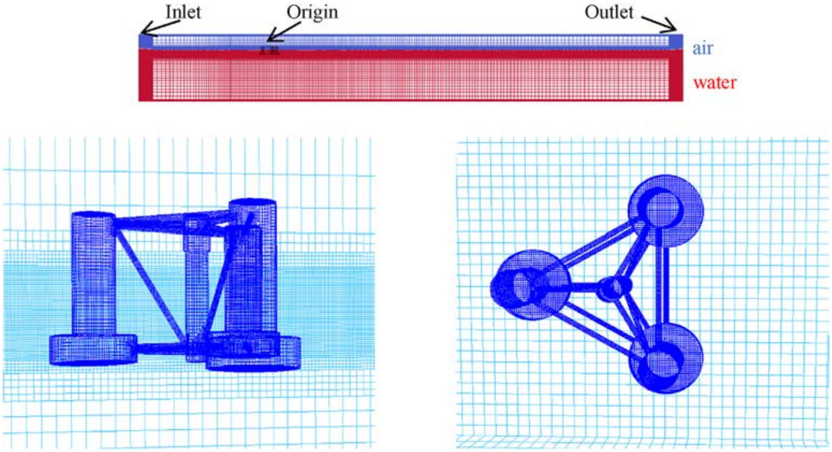

Fig. 3. The computational domain (top) and mesh around the floater (bottom) in CFD simulations.

Table 3

Mesh convergence study (model scale, same time step). Errors in the forces/moments are computed with reference to the Level 4 results.

Spatial discretization	Calculated wave height at origin (m)	Error	Calculated surge force (N)	Error	Calculated heave force (N)	Error	Calculated pitch moment (Nm)	Error
Level 2 (≈H/5)	0.1413	0.493%	223.08	0.52%	61.40	9.44%	68.11	3.41%
Level 3 (≈H/10)	0.1416	0.282%	224.20	0.13%	64.07	5.50%	68.41	2.97%
Level 4 (≈H/20)	0.1417	0.211%	224.25	–	67.80	–	70.52	–

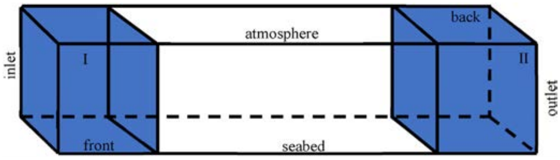

Fig. 4. Schematic representation of computational domain.

3.1.6. Coupling of Navier-Stokes and potential flow solver

For the irregular wave case, an efficient domain decomposition strategy is implemented. As illustrated in Fig. 5, the smaller CFD domain Γ where the Navier-Stokes/VOF equations are solved is coupled with a larger potential flow domain Ω, where a larger mesh size can be applied. The coupling zones are the relaxation zones in the waves2Foam toolbox. The coupling strategy is based on one-way coupling, where the information only propagates from outer domain to inner domain. No target solution for the air velocity is provided in the potential flow solver, and zero air velocity is strongly imposed on the coupling domain boundaries. Domain A and B are the relaxation zones in the potential flow solver. More details regarding the coupling method can be found in the work of Paulsen et al. [25].

3.2. Potential flow theory model

In addition to the CFD model, a numerical model based on potential flow theory has been built using the software SIMA (SIMO-RIFLEX) [38,39], developed by SINTEF Ocean and widely used in the analyses of numerous types of offshore platforms and wind turbines.

In present simulations, only the stationary semi-submersible floater is modelled. First order potential flow forces, such as the wave excitation force, and second-order sum-frequency and difference-frequency wave force transfer functions (QTFs) are estimated based on a potential flow solution (WAMIT [40]) and subsequently input to SIMA. In addition, viscous effects are considered by applying drag forces from Morison's equation to the columns and cross braces. A constant drag coefficient in the normal direction (0.774, based on towing tests [20]) is applied for each part of the floater. The axial drag force on the heave plate is calculated based on Equation (9). D is the diameter of the heave plate. U is the water particle velocity along the axial direction. Here, we use $C_{da} = 2.48$ based on previous comparisons of a similar engineering tool with experimental data from the DeepCwind test campaign [41].

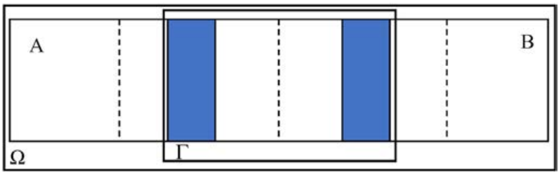

Fig. 5. Schematic representation of the potential solver domain Ω, and waveFoam solver domain. Γ

$$F_{DA} = \frac{1}{2}\rho C_{da}\frac{\pi D^2}{4}U|U| \tag{9}$$

In the SIMA simulations, different force contributions are investigated, as summarized in Table 5. For simulations labelled 'SIMA', the experimentally measured wave elevation is used as input, while simulations indicated as 'Linear' use a fully linear regular wave (same period and height as experimental wave). When the experimentally measured wave elevation is used as input, all components are treated as linear, and all components are assumed to travel in the positive x-direction.

4. Results

In this section, nonlinear wave diffraction loads on a semi-submersible FWT are studied in detail, and all the results are shown at full scale. Considering symmetry, nonlinear wave loads on the starboard column are presented for only one of the trailing columns (starboard, see Fig. 1).

4.1. Regular wave

In the examination of regular wave results, wave amplitudes and loads are extracted from five out of 20 steady-state wave cycles. First, second and third harmonic components are obtained by filtering the signals to keep components around 1ω, 2ω and 3ω, where ω is the wave frequency. The amplitude is the average value over the five wave cycles and the phase represents the initial phase. The uncertainty in the measured wave elevation is estimated as 0.03 m full scale [42].

Numerically calculated waves at the center of floater are compared against the experimental results in Fig. 6, which shows a good agreement except for a fully linear regular wave (SIMA + Linear). The small difference between SIMA and

Table 4

Time step convergence study (model scale, Level 3 spatial discretization). Errors in forces/moments are computed with reference to the result for the smallest time step.

Temporal discretization (s)	Calculated wave height at origin (m)	Error	Calculated surge force (N)	Error	Calculated heave force (N)	Error	Calculated pitch moment (Nm)	Error
0.00707	0.1390	2.11%	219.45	2.43%	61.17	9.54%	64.40	7.80%
0.002828	0.1410	0.70%	223.05	0.83%	63.23	6.49%	67.64	3.16%
0.001414	0.1416	0.28%	224.20	0.32%	64.07	5.25%	68.41	2.06%
0.000707	0.1418	0.14%	224.92	–	67.62	–	69.85	–

Table 5
Overview of different settings in SIMA.

Label	Theory
SIMA1/Linear1	Only linear potential flow theory
SIMA2/Linear2	SIMA1/Linear1 with sum-frequency (for regular wave case)/difference frequency (for irregular wave case) wave force transfer function (QTF)
SIMA3/Linear3	SIMA2/Linear2 with integration of Morison drag force to mean free surface
SIMA4/Linear4	SIMA2/Linear2 with integration of Morison drag force to the undisturbed linear free surface
SIMA5/Linear5	SIMA4/Linear4 with consideration of axial drag force on the heave plates

experiment is caused by a low-pass filter used in SIMA. This filtering also results in the non-dimensional wave amplitude of the fully linear regular wave deviating slightly from unity. Additionally, the numerical damping is negligible in the CFD simulations. Moreover, the numerical wave with laminar flow (L.F) has a smaller variation in the wave height over different cycles, with a standard deviation of 0.0018 m, compared to 0.0047 m for the turbulent flow (T.F) model and 0.0067 m for the experiment. Compared to the experimental results, the CFD-generated waves can capture the first harmonic wave elevation but have less wave energy at twice the wave frequency. The reduction in second harmonic wave elevation with turbulent flow is due to viscous damping.

4.1.1. Upright condition

The surge forces on the upright floater are presented in Fig. 7. SIMA5 is not shown because the axial drag force on the heave plate (z direction) does not contribute to the surge force (x direction) on the upright floater. The amplitude and phase for the total and first harmonic surge force are predicted very well (within 2.5%) by all numerical simulations. For higher order surge forces, CFD results show a similar phase as the experiment. The simulations with laminar flow overpredict the second harmonic surge force and underpredict the third harmonic, while CFD results with turbulent flow are closer to the experimental measurements. Compared to the laminar flow, the turbulent flow has a lower pressure drag contribution and a higher friction drag contribution. In SIMA, the viscous effects are considered through the water particle velocity. Because the mass loads, proportional to water particle acceleration, dominate for the considered structure and wave, the phase difference between water particle acceleration and velocity leads to a phase-lead in the SIMA 4 surge force compared to the experiment. Furthermore, SIMA 4 underpredicts the third harmonic surge force,

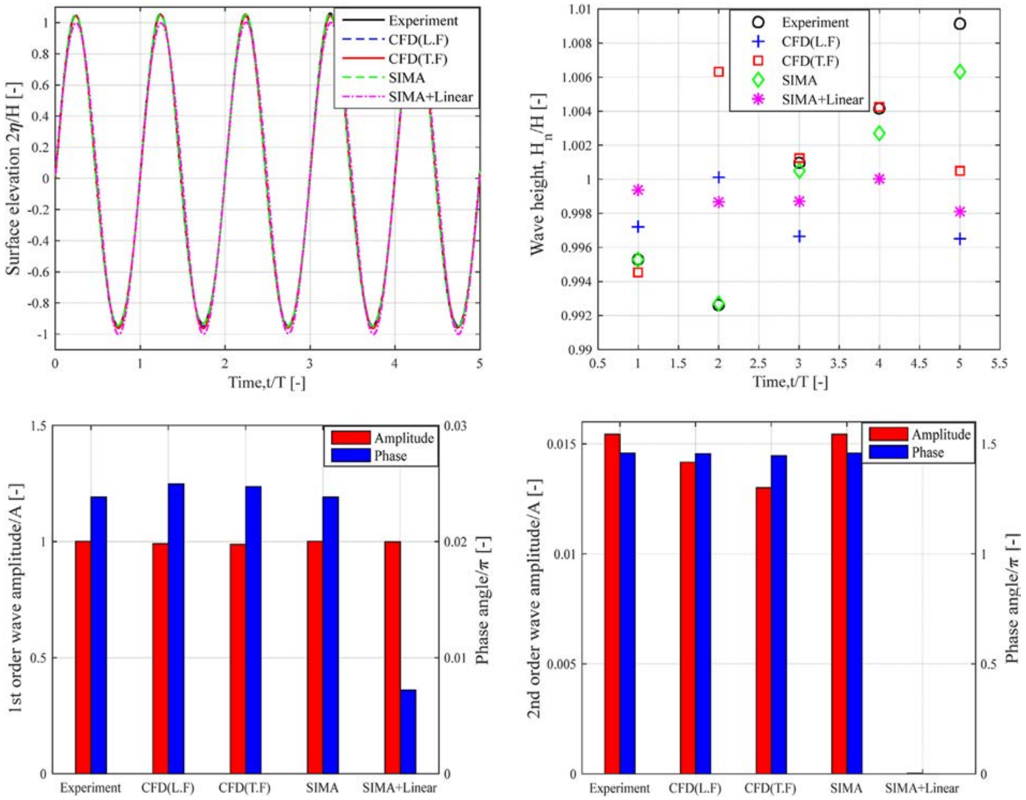

Fig. 6. Comparisons of the free surface elevation for the regular wave. H and A are the specified wave height and wave amplitude while H_n is the measured or simulated wave height. Top left: time series of total surface elevation, top right: total wave height over time, bottom left: average first harmonic wave amplitude, bottom right: average second harmonic wave amplitude.

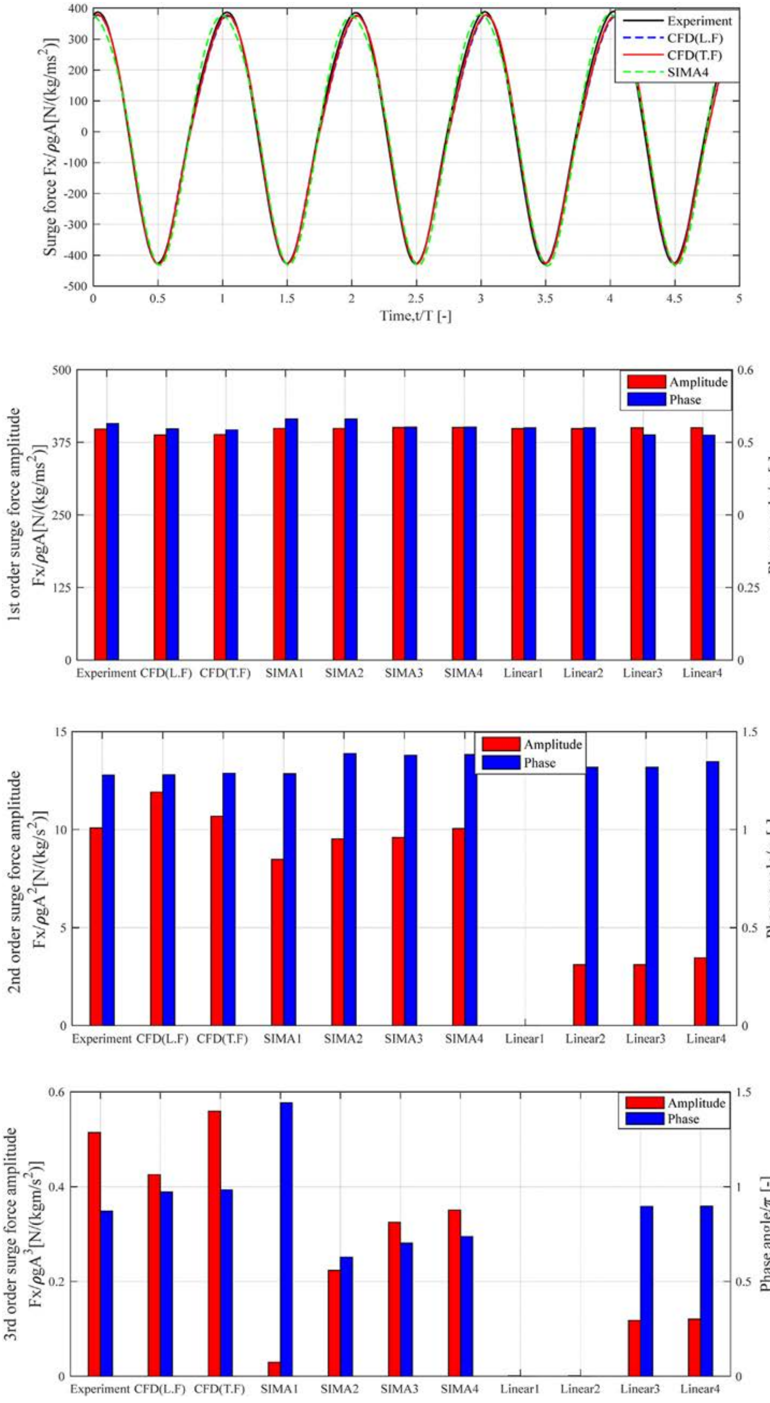

Fig. 7. Comparisons of surge force (CFD, SIMA and experiment) under upright condition for the regular wave (from top to bottom: time series of total surge force, amplitude and phase of first harmonic, second harmonic and third harmonic surge force).

and there is a phase difference between SIMA and experiment for higher order results, which can be explained by decomposing the higher order surge forces.

Even though the experimental wave is treated as a linear wave in SIMA, the measurements contain higher order components compared to the fully linear regular wave. A comparison of SIMA 1–4 and the 'Linear' results shows that the nonlinearity in the wave elevation dominates the higher order surge forces. Additionally, the sum-frequency QTF and integration of the drag force to the undisturbed linear free surface contribute to the second harmonic surge force. In the SIMA 2–4 models, the combination of high-frequency wave components and the sum-frequency QTF lead to a third harmonic surge force. The nonlinear drag force also contributes to the third harmonic surge force. The 'Linear' results show good phase agreement compared to the experiment. For the SIMA 1–4 results, the treatment of nonlinear components of the incoming wave leads to phase discrepancy. The applied constant normal drag coefficient in SIMA may also contribute to amplitude differences in the higher order surge forces.

The heave forces on the upright floater are compared in Fig. 8. SIMA 1–4 and CFD with laminar flow underestimate the amplitude by 15%, while CFD with turbulent flow agrees well with the experiment (within 5.8%). Turbulent flow increases the first and third harmonic heave force but reduces the second harmonic. Flow separation around the edge occurs due to the geometric singularity and leads to a larger vertical drag force. However, the RANS model used in this paper may not simulate this effect correctly, and overpredicts the third harmonic heave force by over 50%. Like the surge force, the CFD model has a similar phase as the experiments, while SIMA 1–4 deviates for all harmonics.

When axial drag forces on the heave plates are not included (SIMA 1–4), most of the heave excitation comes from potential flow theory, and the first and third harmonic heave forces are underpredicted, while the second harmonic is overpredicted. Additionally, the normal drag force on the cross braces slightly increases the third harmonic heave force (SIMA 2 vs SIMA 3). From the comparisons between SIMA 1–4 and the 'Linear' results, nonlinear incoming wave also contributes to the higher order heave forces. Furthermore, the phase of the higher order heave force also deviates from the experiments in the 'Linear' results.

The axial drag force (SIMA 5 and Linear 5) increases the first and third harmonic heave force, while the integration of the drag force to the linear free surface also increases the second harmonic. SIMA 5 predicts the phase better than SIMA 1–4, but still differs from the experimental results in the higher order results. This suggests that potential flow theory and Morison-type drag with a tuned axial drag coefficient can predict the amplitude of the heave force very well, without really capturing the physics, as evidenced by the difference in the phase.

Fig. 9 compares the numerically estimated pitch moment against the measured result. All numerical models underpredict the first harmonic amplitudes (from 1.6% for SIMA 5–7.8% for CFD with turbulent flow) but have similar phase as the experimental data. The discrepancy in amplitude may be caused by the underprediction of the heave forces. In the CFD simulation, the second harmonic pitch moment performs similarly as the surge and heave forces, but for the third harmonic, the model with turbulent flow underestimates the amplitude by 28%. The SIMA 1–4 simulations underpredict higher order amplitudes and differ in phase from the experimental results. The phase difference also exists when the axial drag force on the heave plate is included (SIMA 5).

For the second harmonic pitch moment, a comparison of the SIMA and Linear 1–4 models shows that nonlinearity in the incoming wave is important (linear potential flow theory dominates). Furthermore, the sum-frequency QTF reduces the amplitude (SIMA 2 vs. SIMA 1). The normal drag force has no obvious effect on the second harmonic pitch moment.

For the third harmonic, the moment induced by the sum-frequency QTF is more important than other contributions for SIMA 1–4. Meanwhile, by comparing SIMA 3–4 and 'Linear' results, the third order contributions from normal drag forces due to high-frequency wave components reduce the amplitude. The axial drag force (SIMA 5 and Linear 5) mainly contributes to the third harmonic pitch moment and has no significant effect on the first or second harmonic. In conclusion, the first and second harmonic pitch moments in SIMA are mainly from potential flow theory and only the axial drag forces on the heave plates have a significant effect on the third harmonic.

The differences between measured wave loads in the experiment and calculated wave loads in the CFD with turbulence model are compared with the estimated uncertainty in Table 6. As shown, the differences for the total wave loads are within the range of sum of uncertainties in experiment and numerical results. Both the differences and uncertainties in higher order components may be larger, however.

The experiments do not measure surge forces on individual columns, but this comparison can be carried out numerically, shown in Fig. 10 and Fig. 11. Here, the sum-frequency QTF is not included in SIMA. Therefore, wave nonlinearity is important for the first and second harmonic surge forces, while the drag force is dominant in third harmonic in these results.

For the first harmonic surge force, SIMA and CFD are in better agreement for the upper column (within 2.4%) than for the heave plate (within 10.2%). In the CFD model, the intersections between heave plates and cross braces are modelled, which reduces the heave plate flank area where the pressures are integrated by 1.33%. The SIMA model considers the heave plates as closed cylinders. As with the total force, due to the constant drag coefficient in SIMA, there is a large difference in the amplitude and phase of higher harmonic surge forces between SIMA and CFD.

For the CFD results, except for the higher order surge force on the upper column of the upstream column (Fx2), the surge forces have similar phase for both laminar and turbulent flow in each harmonic. According to the KC number in Table 2 and results from other researchers [43], a pair of weak vortices is formed in the wake of upper column of upstream column which laminar flow model cannot simulate. In Fig. 10, the flattened peak value of the surge force on the main column (Fx1) is due to the geometry: the top of main column has larger diameter which leads to a ledge (see left part of Fig. 1). This ledge leads to the large difference in the third harmonic surge force of main column between laminar and turbulent flow model. This phenomenon is not modelled in SIMA.

For both the upstream and starboard column, although the diameter of the heave plate is twice that of the upper column, the surge force on the upper column is larger because the water particle acceleration decreases as one moves downward. To better understand these results, the surge forces on each column under fully linear regular waves with different wave periods and the same wave steepness were estimated using the SIMA 4 model, shown in Fig. 12. Based on the previous analysis (Fig. 7), the main difference between the total and first order amplitude (right part of Fig. 12) is due to the third harmonic drag force. The total surge forces on the upper column (Fx2 and Fx4) are also larger than the forces on the heave plate (Fx3 and Fx5), and the discrepancy increases for shorter waves. Comparisons among the higher order surge forces lead to the same conclusions, but the discrepancy depends on frequency.

Comparing the forces on components of the upstream column and starboard column in the CFD simulations (Fig. 11), the amplitude of higher order surge forces on the starboard column is larger than those on the upstream column. The same can be observed in

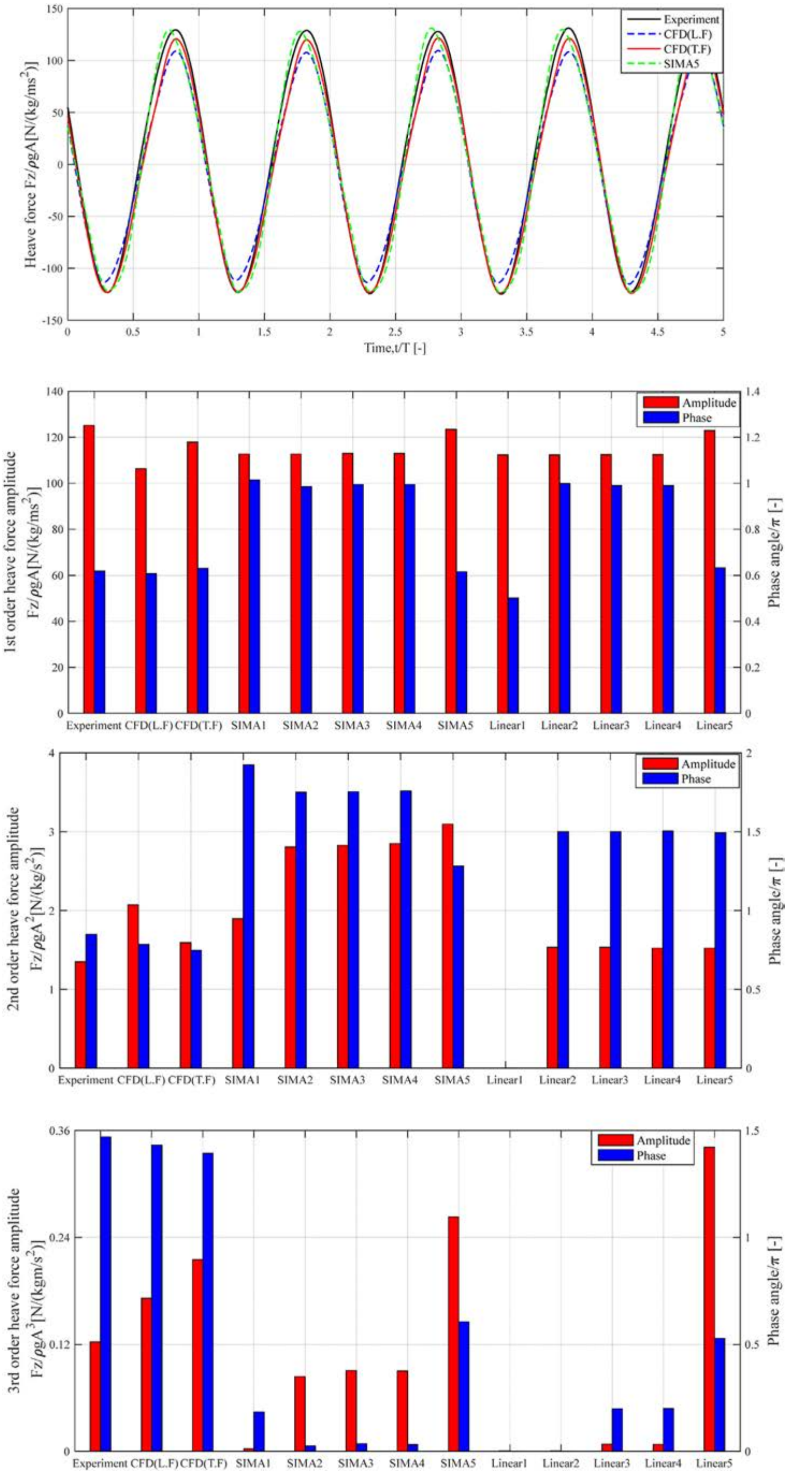

Fig. 8. Comparisons of heave force (CFD, SIMA and experiment) under upright condition for the regular wave (from top to bottom: time series of total heave force, amplitude and phase of first harmonic, second harmonic and third harmonic heave force).

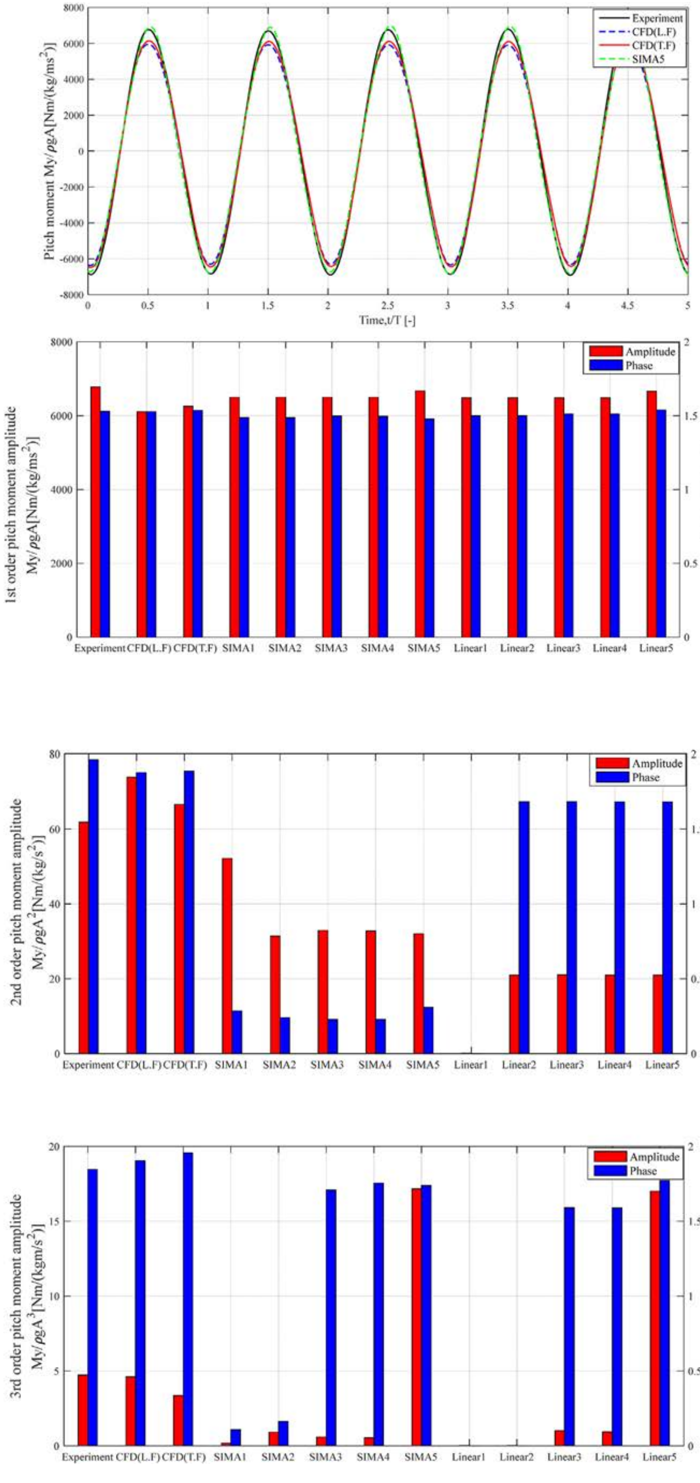

Fig. 9. Comparisons of pitch moment (CFD, SIMA and experiment) under upright condition for the regular wave (from top to bottom: time series of total pitch moment, amplitude and phase of first harmonic, second harmonic and third harmonic pitch moment).

Table 6
Comparisons of differences between experiments and CFD simulations and uncertainties for the total wave loads under upright condition.

	Difference between experiment and CFD with turbulence model	Uncertainty in experiment	Uncertainty in numerical results
Surge force	2.5%	2%	0.60%
Heave force	5.8%	2%	14.28%
Pitch moment	7.8%	5%	5.71%

the first and third order surge forces in SIMA simulations (Fig. 11) while the opposite is seen in the second order surge force. The results under different wave periods (Fig. 12) show that the surge force comparison between the starboard and upstream column depends on frequency.

4.1.2. Trimmed condition

Considering the existence of a mean pitch angle for the wind turbine during operation, nonlinear wave diffraction loads on a 5° trimmed floater are studied in this section. The floater is rotated 5° clockwise around Point A shown in Fig. 1. No corresponding experimental data are available. Only results from CFD with turbulent flow and the SIMA model are shown in this section. Furthermore, we focus on the integrated wave loads on the complete floater. Surge force (along x axis), heave force (along z axis) and pitch moment (around y axis) are calculated in the same global coordinate system as the upright condition which is shown in Fig. 1. The amplitudes of load responses divided by the xth (x = 1,2,3) power of the displaced submerged volume V (x10^4 m^3) are also compared to eliminate the effect of changed submerged volume, which is denoted as 'Amplitude/V^x' in Figs. 13–15.

The surge forces under upright and trimmed conditions are presented in Fig. 13. The first harmonic surge force under trimmed condition increases (4.8% for CFD and 2.4% for SIMA) compared to the upright condition. After rotating the floater, a larger portion of the columns are submerged, but the water particle acceleration at the same position of columns decreases. Hence, considering the changed volume, the first harmonic surge force under trimmed condition decreases (5.2% for CFD and 4.7% for SIMA). The higher order results generally decrease, especially when considering the changed volume.

As shown by 'SIMA5+5°' in Fig. 13, the axial drag force increases the first harmonic surge force by 3.2% and decreases the third harmonic by 4.2% (SIMA5 has the same value as SIMA4 under upright condition). For the trimmed floater, the axial drag forces on the heave plates have a component along x direction. The water particle velocity along the column axis is the resultant velocity of the vertical and horizontal water particle velocity, which have a phase difference. Hence, the contribution of this additional drag force depends on the phase.

The heave forces under upright and trimmed position are compared in Fig. 14. All harmonics of the heave force decrease after rotating the floater except for a slightly increased second harmonic CFD result. Considering the changed volume, all harmonics decrease. The increased heave force on the upper column cannot compensate for the loss of heave force on the heave plate. In the SIMA 4 model without axial drag force, this decreasing heave force relates to the change of immersed geometry. By comparing 'SIMA4+5°' and 'SIMA5+5°', the axial drag force increases the heave force in each harmonic, especially at the third harmonic (around 200%). Furthermore, the axial drag force (SIMA5+5°) is mainly calculated based on the vertical water particle velocity, which leads to a phase shift for each harmonic heave force compared to the 'SIMA4+5°'. Normalizing by submerged volume, there is almost no change in the SIMA5 results due to trim.

The comparisons of numerically estimated pitch moment are shown in Fig. 15. For the CFD simulations, except for the deceasing second harmonic results (15.3%), there is an increasing pitch moment (within 9.3%) on the trimmed floater. All harmonic pitch moments in SIMA 4 model increase (around 7% for the first harmonic, 60% for the second harmonic, 100% for the third harmonic) in the trimmed condition due to the changed results from linear potential flow theory. The axial drag force increases the third harmonic pitch moment (14 times larger) and decreases second harmonic pitch moment (11.2%) by comparing 'SIMA4+5°' and 'SIMA5+5°'. However, the total pitch moment increases by 1%. Similar to the heave force, when dividing by submerged volume, there is almost no change in the SIMA5 results due to trim.

4.2. Irregular wave

An irregular wave state ($H_s = 7.1$ m and $T_p = 12.1$ s) is considered to investigate the wave loads near natural periods of rigid body motion. In the CFD model, as the wave maker motion in the experiment is not available, the measured irregular wave at the center of body is used to generate a time series of wave elevation at the wave maker as an input signal at the inlet of potential flow domain, following the procedure shown by Bachynski et al. [44]. The outlet boundary of the potential flow domain is defined by setting a constant current with zero velocity. The spatial discretization in the CFD domain is the same as in the regular wave case. The cell size in the potential flow domain is 10 times larger. The center of the two computational domains is co-located with the center of the floater. Due to excessive numerical damping for wave generation with a turbulence model, the CFD laminar flow model is used. The wave in SIMA is obtained by filtering the measured wave elevation at the origin with a 0.025 Hz cut-off frequency. For the SIMA 2 model, the sum-frequency QTF is replaced with the difference-frequency QTF. In this section, the power spectral density (PSD) of responses is calculated based on the time series from 1200s to 4800s and we only focus on low frequencies. In the wave-frequency region, the agreement is very good among all results, and is not shown.

Experimental and numerical time series of 20 wave cycles extracted from 1-h simulations and the wave power spectra (in log scale) for the full hour are compared in Fig. 16. Although there is a difference in the low-frequency domain, the values are quite small compared to the ones in the wave-frequency domain where good agreement occurs and have no significant effect on the obtained wave energy. Hence, to be fair, CFD can reproduce the wave elevation very well. Based on the difference between wave power spectrum at inlet and center of CFD domain, most of numerical damping in the CFD domain occurs in the low-frequency domain. The effect of the cut-off frequency (0.025 Hz) is visible in the SIMA simulations.

The numerically estimated low-frequency surge force power spectra are compared against experimental results in Fig. 17 (left). SIMA underestimates the low-frequency surge forces, and by 26.6% at surge natural frequency. CFD also underpredicts the surge forces by 16.2% at the surge natural frequency. On the other hand, CFD results have more significant wave energy (within 20%) at low frequencies.

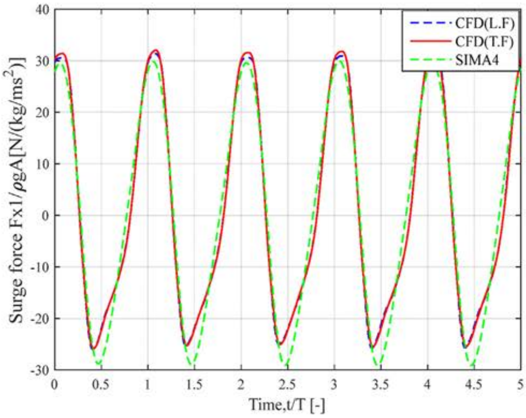

a) main column (Fx1)

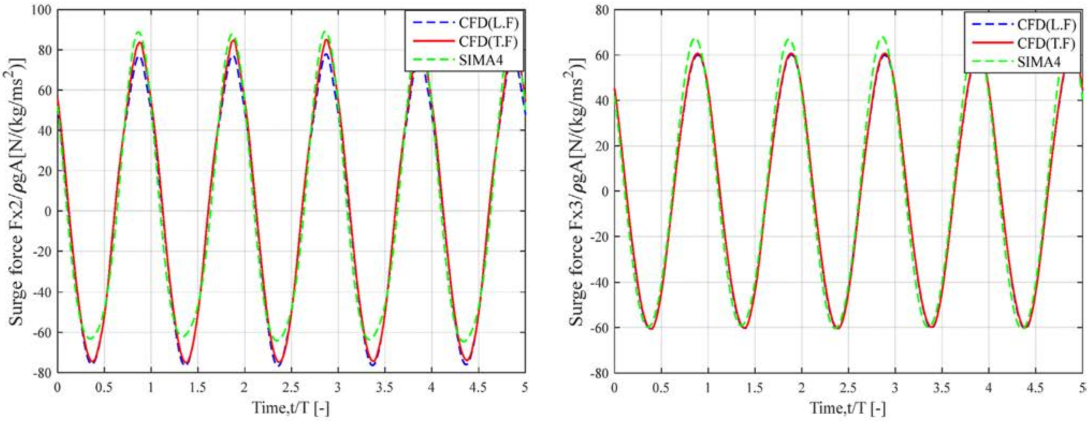

b) upper column of upstream column (Fx2)

c) heave plate of upstream column (Fx3)

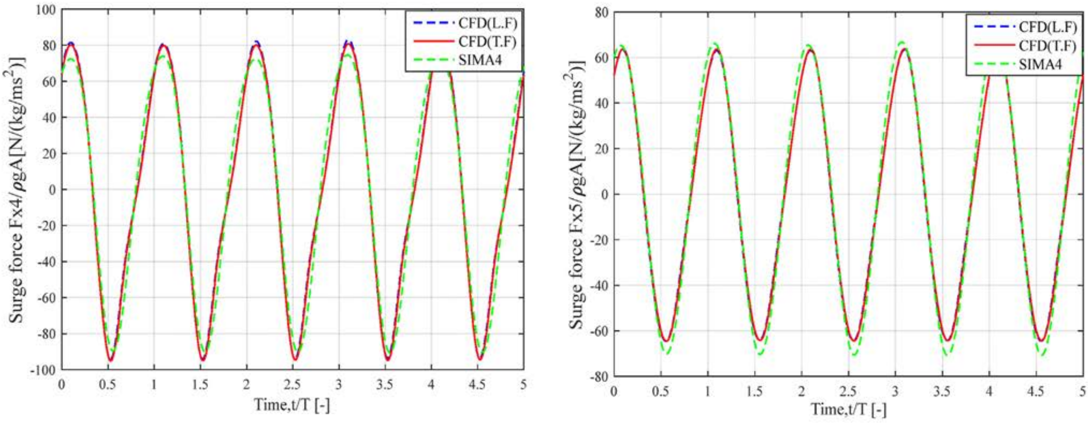

d) upper column of starboard column (Fx4)

e) heave plate of starboard column (Fx5)

Fig. 10. Comparisons of time series of total surge forces on the individual columns of the floater (CFD and SIMA) under upright condition for regular wave.

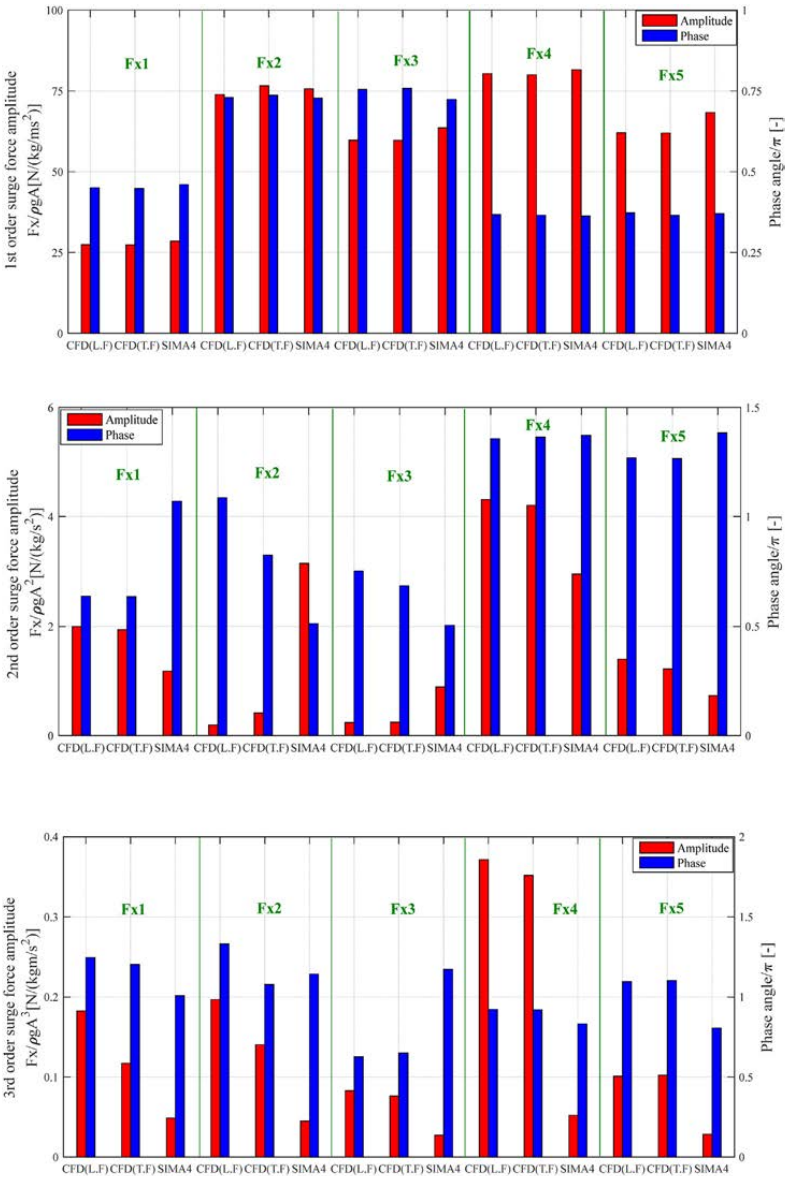

Fig. 11. Comparisons of first, second and third harmonic surge forces on the individual columns of the floater (CFD and SIMA) under upright condition for the regular wave (from top to bottom: amplitude and phase of first, second and third harmonic surge force on different columns, Fx1: main column, Fx2: upper column of upstream column, Fx3: heave plate of upstream column, Fx4: upper column of starboard column, Fx5: heave plate of starboard column. See Fig. 1 for the definitions of columns).

Fig. 17 (right) presents the low-frequency surge force spectra considering different force contributions in SIMA. All of the components of the measured irregular wave are treated linearly in SIMA. The surge natural frequency is below the cut-off frequency, so there is no significant linear wave excitation (SIMA 1) at surge natural frequency. The difference-frequency QTF (SIMA 2) has a slight influence on the low-frequency surge force. The surge force at surge natural frequency is mainly from integration of the Morison drag force to the linear free surface (SIMA 4). The axial drag forces on the heave plates have no effect on the low-frequency surge force (SIMA 5 vs SIMA 4).

The heave force spectra are compared in Fig. 18 (left). SIMA underestimates the low-frequency heave forces, and by 20.5% at the heave natural frequency. The CFD model shows better predictions of heave forces, however, there is also significantly less wave energy (18%) at the heave natural frequency in the CFD model. It is important to note that the laminar flow model used in CFD simulation cannot correctly capture the flow around the heave plate. A

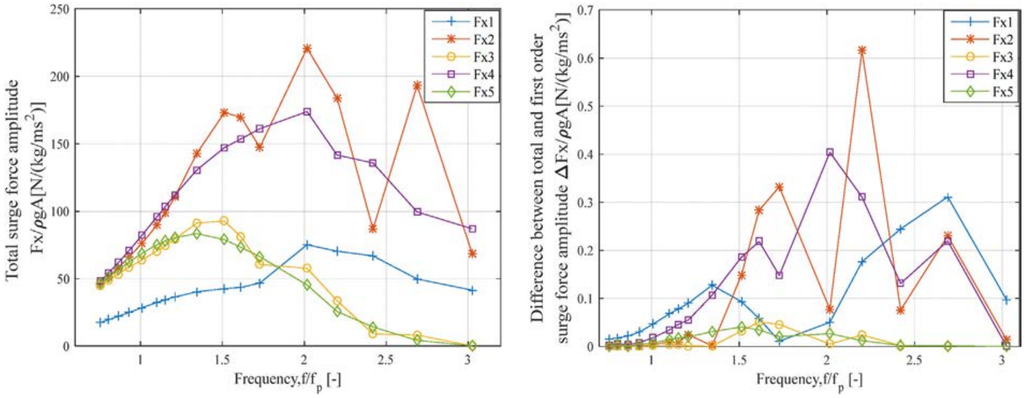

Fig. 12. Comparisons of total (left) and difference between total and first order (right) surge forces on the individual columns of the floater (SIMA 4) under upright condition for a series of fully linear regular waves with different wave periods and the same wave steepness with one used in this paper. (f_p is wave frequency used in Fig. 11). Fx1: main column, Fx2: upper column of upstream column, Fx3: heave plate of upstream column, Fx4: upper column of starboard column, Fx5: heave plate of starboard column. See Fig. 1 for the definitions of columns).

large part of the heave force comes from linear potential flow theory (SIMA 1), see right part of Fig. 18. The difference-frequency QTF (SIMA 2) and the normal drag forces (SIMA 3 and 4) have minor effects on the heave force. The axial drag forces on the heave plates (SIMA 5) increase the heave force by 89.5% at the heave natural frequency.

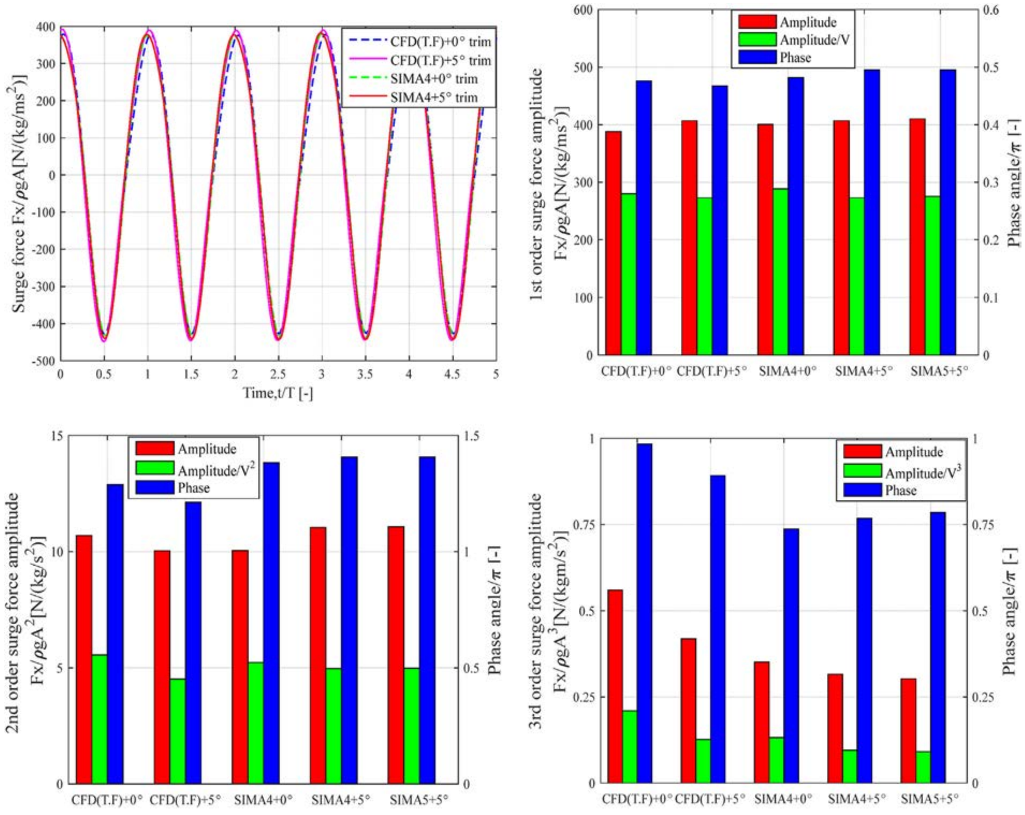

Fig. 13. Comparisons of surge forces (CFD and SIMA) under upright and trimmed condition for the regular wave (Top left: time series of total surge force, top right: amplitude and phase of first harmonic surge force, bottom left: amplitude and phase of second harmonic surge force, bottom right: amplitude and phase of third harmonic surge force).

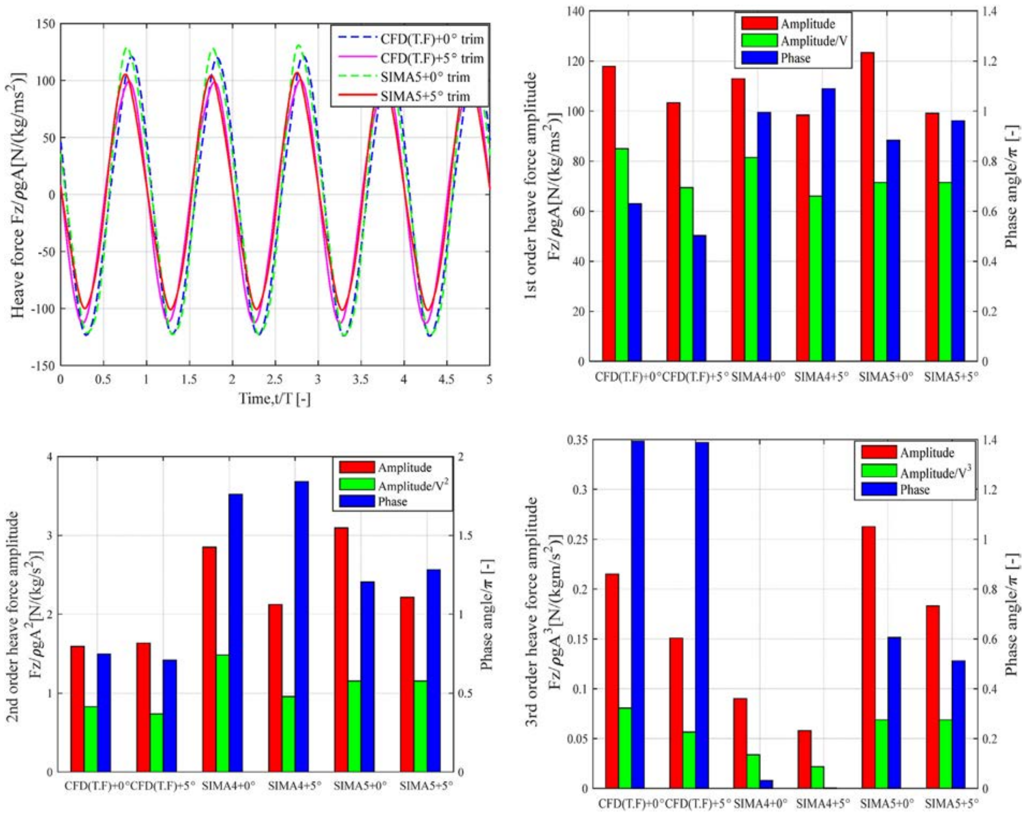

Fig. 14. Comparisons of heave forces (CFD and SIMA) under upright and trimmed condition for the regular wave (Top left: time series of total heave force, top right: amplitude and phase of first harmonic heave force, bottom left: amplitude and phase of second harmonic heave force, bottom right: amplitude and phase of third harmonic heave force).

Fig. 19 (left) compares the low-frequency pitch moment spectra. Similar to the surge and heave forces, SIMA underpredicts the pitch moment. This is consistent with previous results showing five times smaller load responses at the pitch natural frequency of a mooring FWT seen in simulations using the engineering tools compared to the experimental measurements [5]. The CFD model underpredicts the low-frequency pitch moment by about 10%. Again, this underprediction may in fact be more severe than it seems, as the CFD model includes more wave energy at low frequencies.

The comparisons of low-frequency pitch moment spectra with different force contributions in SIMA are shown in Fig. 19 (right). The pitch moment from the difference-frequency QTF (SIMA 2) is significant. In addition, the normal drag forces (SIMA 3) and integrations to the linear free surface (SIMA 4) have little effect on the pitch moment at low frequencies. The axial drag forces on the heave plates (SIMA 5) increase the moment at very low frequencies, but the results remain lower than experimental measurements.

5. Conclusions

Nonlinear wave loads are important for designing the floater and mooring system for FWTs. In this paper, nonlinear diffraction wave loads on a semi-submersible FWT are studied using two numerical approaches based on CFD and potential flow theory as well as experimental measurements.

Based on the comparisons under a regular wave, good agreement (within 10%) between numerical models and experiment is achieved for wave-frequency loads. For higher order wave loads, CFD correctly estimates the phase, and CFD with the turbulence model generally give the best results. The lower heave force and pitch moment in the laminar flow may be due to the lack of simulation for weak flow separation occurring around heave plate. SIMA (potential flow with Morison drag) has large discrepancies in prediction of phase and amplitude of higher order wave loads. The dominant higher order components in SIMA are related to treating a nonlinear wave measurement as a linear input, which leads to phase discrepancy against CFD and experimental measurements. The normal drag force of columns and cross braces in SIMA model has significant contributions to the surge force while the axial drag forces on the heave plates increase the heave force and the pitch moment. The proper drag coefficient can decrease the amplitude discrepancy in higher order loads, but a phase difference nonetheless exists in the SIMA results. This discrepancy demonstrates the limitation of potential flow theory with Morison-type drag for estimating high order diffraction wave loads.

Regarding the low-frequency wave loads on the fixed structure under an irregular wave, both CFD and SIMA underpredict the loads, but the discrepancy for CFD results is smaller. In SIMA, all of the components of the measured irregular wave are treated linearly. The difference-frequency QTF has significant contributions to the pitch moment. Normal drag forces on the columns and cross

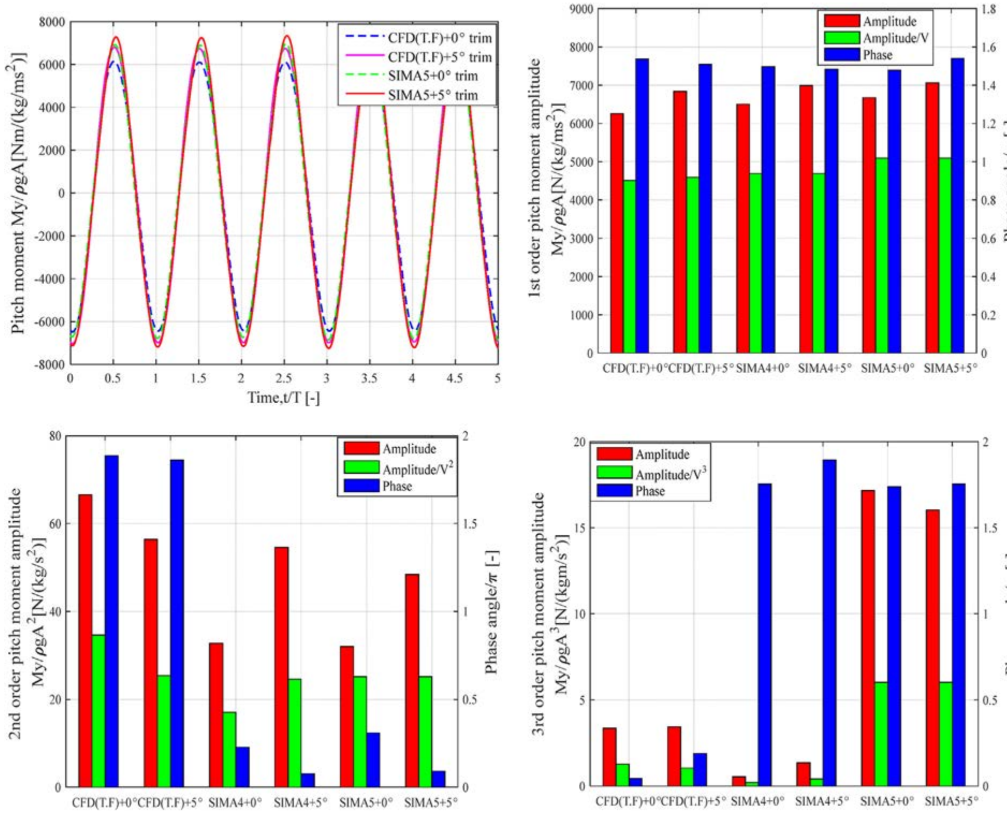

Fig. 15. Comparisons of pitch moments (CFD and SIMA) under upright and trimmed condition for the regular wave (Top left: time series of total pitch moment, top right: amplitude and phase of first harmonic pitch moment, bottom left: amplitude and phase of second harmonic pitch moment, bottom right: amplitude and phase of third harmonic pitch moment).

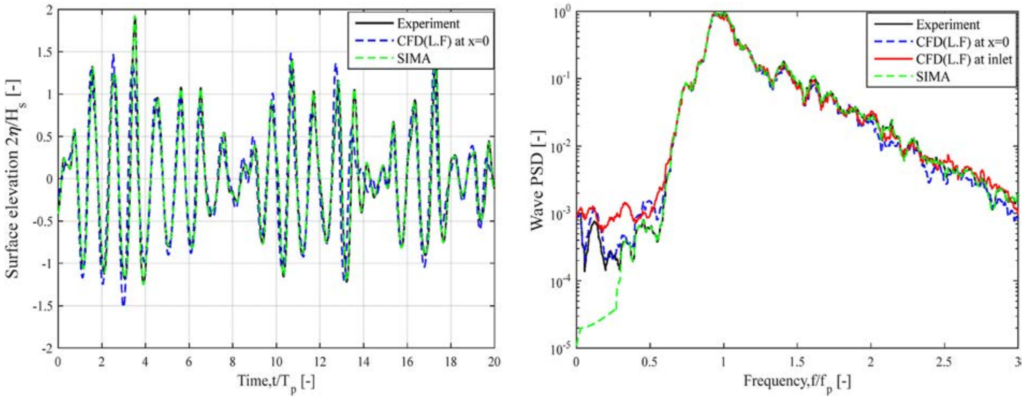

Fig. 16. Comparisons of the free surface elevation for the irregular wave (left: time series, right: wave spectra).

braces lead to an increased surge force at surge natural frequency. In addition, the axial drag forces on the heave plates largely increase the heave force at heave and pitch natural frequencies, but only contribute to the pitch moment at very low frequencies. Due to excessive numerical damping of the wave using a turbulence model in CFD, only laminar flow was considered in the irregular waves. Further developments of hybrid methods with CFD with a turbulence model and potential flow theory models are needed.

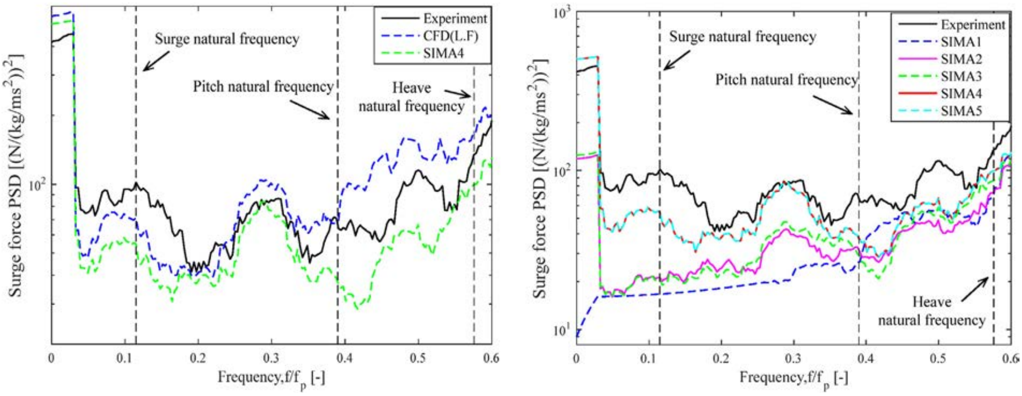

Fig. 17. Comparisons of low-frequency surge force spectra under upright position for the irregular wave (left: comparison among CFD, SIMA and experiment, right: different force contributions in SIMA).

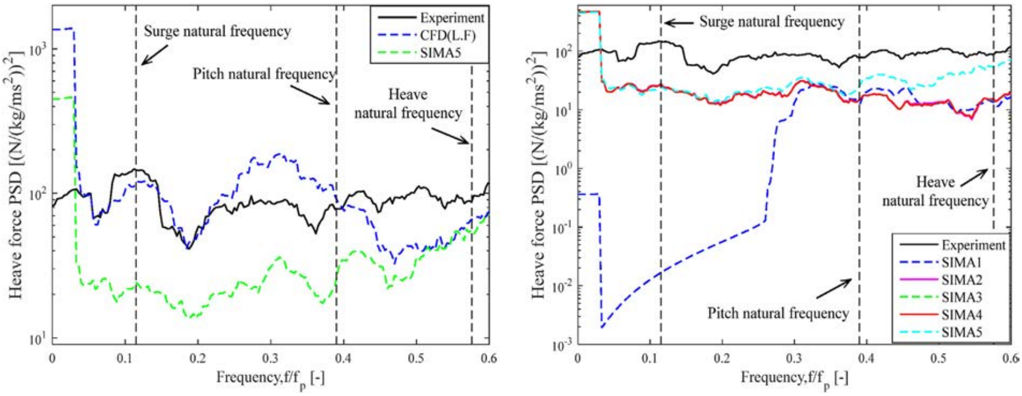

Fig. 18. Comparisons of low-frequency heave force spectra under upright position for the irregular wave (left: comparison among CFD, SIMA and experiment, right: different force contributions in SIMA).

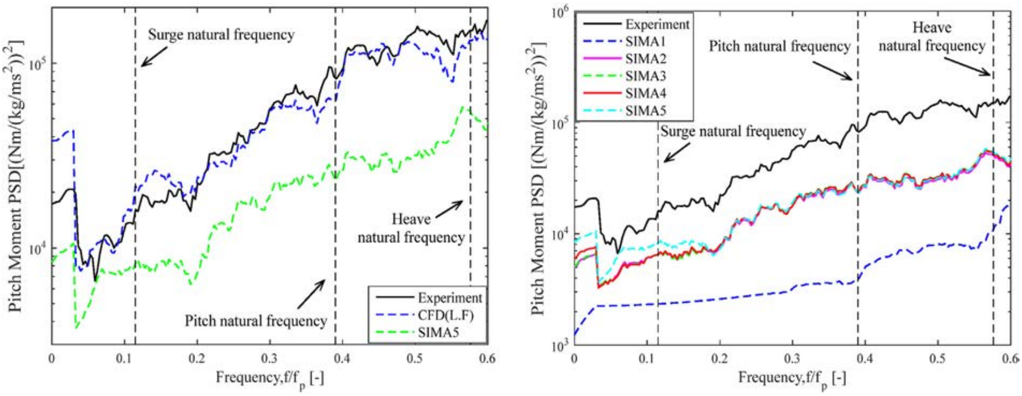

Fig. 19. Comparisons of low-frequency pitch moment spectra under upright position for the irregular wave (left: comparison among CFD, SIMA and experiment, right: different force contributions in SIMA).

In order to better understand the effects of the multimember arrangement of the semisubmersible, surge forces on each column are extracted. Higher order surge forces on the starboard column are larger than those on the upstream column in the CFD simulations under this regular wave (12.1 s), but this conclusion is frequency-dependent (based on potential flow simulations at additional frequencies). Furthermore, the total surge force on the upper column is larger than the force on the heave plate, and this discrepancy increases for shorter waves.

The effects of 5° mean pitch angle on the nonlinear wave loads are also investigated in regular waves, using the same global coordinate system as in the upright condition. In the trimmed condition, the surge force and pitch moment increase while the heave force decreases. Furthermore, this 5° mean pitch angle reduces the higher order surge and heave forces while increasing the higher order pitch moment. In SIMA, the axial drag forces on the heave plates increase the third harmonic heave force and pitch moment, but decrease the third harmonic surge force, which is due to the phase difference between vertical and horizontal water particle velocity. Considering the effect of changed volume, the surge and heave forces decrease, and the pitch moment slightly increases under trimmed position.

CRediT authorship contribution statement

Haoran Li: Conceptualization, Methodology, Software, Validation, Investigation, Formal analysis, Data curation, Writing – original draft. **Erin E. Bachynski:** Conceptualization, Methodology, Resources, Writing – review & editing, Supervision.

Declaration of competing interest

The authors declare that they have no known competing financial interests or personal relationships that could have appeared to influence the work reported in this paper.

Acknowledgements

The authors are grateful for the experimental data from the MARINET2 (European Union's Horizon 2020 grant agreement 731084), and OC6 Projects. Computing time on Vilje is granted by the Norwegian Research Council (Program for Supercomputing, under project nn9676k). The author Haoran Li gratefully acknowledges the financial support from China Scholarship Council (CSC). The discussions with Irene Rivera-Arreba are greatly appreciated.

References

[1] J.A. Mercier, S.J. Leverette, A.L. Bliault, Evaluation of Hutton TLP response to environmental loads, in: Offshore Technology Conference, 1982. Offshore Technology Conference.

[2] A.J. Coulling, et al., Importance of Second-Order Difference-Frequency Wave-Diffraction Forces in the Validation of a FAST Semi-submersible Floating Wind Turbine Model. No. NREL/CP-5000-57697, in: ASME 2013 32nd International Conference on Ocean, Offshore and Arctic Engineering, American Society of Mechanical Engineers Digital Collection, 2013.

[3] A. Robertson, et al., Offshore Code Comparison Collaboration Continuation within IEA Wind Task 30: Phase II Results Regarding a Floating Semi-submersible Wind System. No. NREL/CP-5000-61154, in: ASME 2014 33rd International Conference on Ocean, Offshore and Arctic Engineering, American Society of Mechanical Engineers Digital Collection, 2014.

[4] A.N. Robertson, et al., OC5 Project Phase I: Validation of Hydrodynamic Loading on a Fixed Cylinder, National Renewable Energy Lab.(NREL), Golden, CO (United States), 2015. No. NREL/CP-5000-63567.

[5] A.N. Robertson, et al., OC5 project phase II: validation of global loads of the DeepCwind floating semisubmersible wind turbine, Energy Procedia 137 (2017) 38–57.

[6] E.E. Bachynski, T. Moan, Ringing loads on tension leg platform wind turbines, Ocean Eng. 84 (2014) 237–248.

[7] M. Karimirad, T. Moan, Wave-and wind-induced dynamic response of a spar-type offshore wind turbine, J. Waterw. Port, Coast. Ocean Eng. 138 (1) (2012) 9–20.

[8] F. Beyer, M. Arnold, P.W. Cheng, Analysis of Floating Offshore Wind Turbine Hydrodynamics Using Coupled CFD and Multibody Methods, 2013.

[9] M.A. Benitz, et al., Validation of Hydrodynamic Load Models Using CFD for the OC4-DeepCwind Semisubmersible. No. NREL/CP-5000-63751, in: ASME 2015 34th International Conference on Ocean, Offshore and Arctic Engineering, American Society of Mechanical Engineers Digital Collection, 2015.

[10] M.A. Benitz, et al., Comparison of Hydrodynamic Load Predictions between Reduced Order Engineering Models and Computational Fluid Dynamics for the Oc4-Deepcwind Semi-submersible. No. NREL/CP-5000-61157, in: ASME 2014 33rd International Conference on Ocean, Offshore and Arctic Engineering, American Society of Mechanical Engineers Digital Collection, 2014.

[11] I. Rivera-Arreba, et al., Modeling of a semisubmersible floating offshore wind platform in severe waves, J. Offshore Mech. Arctic Eng. 141 (6) (2019).

[12] A. Nematbakhsh, D.J. Olinger, G. Tryggvason, A nonlinear computational model of floating wind turbines, J. Fluid Eng. 135 (12) (2013).

[13] A. Nematbakhsh, et al., Comparison of wave load effects on a TLP wind turbine by using computational fluid dynamics and potential flow theory approaches, Appl. Ocean Res. 53 (2015) 142–154.

[14] A. Nematbakhsh, D. Olinger, G. Tryggvason, Development and Validation of a Computational Model for Floating Wind Turbine Platforms. In *50th* AIAA Aerospace Sciences Meeting Including the New Horizons Forum and Aerospace Exposition, 2012.

[15] C. Hu, et al., Hydrodynamic analysis of a semi-submersible type floating wind turbine, in: The Eleventh ISOPE Pacific/Asia Offshore Mechanics Symposium., International Society of Offshore and Polar Engineers, 2014.

[16] C. Liu, C. Hu, CFD simulation of a floating wind turbine platform in rough sea conditions, in: The Twenty-Fourth International Ocean and Polar Engineering Conference, International Society of Offshore and Polar Engineers, 2014.

[17] T. Yabe, F. Xiao, T. Utsumi, The constrained interpolation profile method for multiphase analysis, J. Comput. Phys. 169 (2) (2001) 556–593.

[18] F. Xiao, S. Ii, C. Chen, Revisit to the THINC scheme: a simple algebraic VOF algorithm, J. Comput. Phys. 230 (19) (2011) 7086–7092.

[19] W. Musial, S. Butterfield, A. Boone, Feasibility of floating platform systems for wind turbines, in: t*42nd* AIAA Aerospace Sciences Meeting and Exhibi, 2004.

[20] A. Robertson, et al., OC6 Phase I: investigating the underprediction of low-frequency hydrodynamic loads and responses of a floating wind turbine, in: TORQUE, 2020.

[21] A.J. Goupee, et al., Model tests for three floating wind turbine concepts, in: Offshore Technology Conference, 2012. Offshore Technology Conference.

[22] H.G. Weller, et al., A tensorial approach to computational continuum mechanics using object-oriented techniques, Comput. Phys. 12 (6) (1998) 620–631.

[23] N.G. Jacobsen, D.R. Fuhrman, J. Fredsøe, A wave generation toolbox for the open-source CFD library: OpenFoam®, Int. J. Numer. Methods Fluid. 70 (9) (2012) 1073–1088.

[24] A.P. Engsig-Karup, H.B. Bingham, O. Lindberg, An efficient flexible-order model for 3D nonlinear water waves, J. Comput. Phys. 228 (6) (2009) 2100–2118.

[25] B.T. Paulsen, H. Bredmose, H.B. Bingham, An efficient domain decomposition strategy for wave loads on surface piercing circular cylinders, Coast Eng. 86 (2014) 57–76.

[26] C.W. Hirt, B.D. Nichols, Volume of fluid (VOF) method for the dynamics of free boundaries, J. Comput. Phys. 39 (1) (1981) 201–225.

[27] E. Berberović, et al., Drop impact onto a liquid layer of finite thickness: dynamics of the cavity evolution, Phys. Rev. 79 (3) (2009), 036306.

[28] M.M. Rahman, M.M. Karim, M.A. Alim, Numerical investigation of unsteady flow past a circular cylinder using 2-D finite volume method, J. Nav. Architect. Mar. Eng. 4 (1) (2007) 27–42.

[29] S.A. Brown, et al., An evaluation of rans turbulence closure models for spilling breakers, Coast. Eng. Proc. (34) (2014), 5-5.

[30] F. Menter, et al., The SST turbulence model with improved wall treatment for heat transfer predictions in gas turbines, in: Proceedings of the International Gas Turbine Congress, 2003.

[31] B. Devolder, P. Rauwoens, P. Troch, Application of a buoyancy-modified k-ω SST turbulence model to simulate wave run-up around a monopile subjected to regular waves using OpenFOAM®, Coast Eng. 125 (2017) 81–94.

[32] W. Fan, H. Anglart, varRhoTurbVOF, A new set of volume of fluid solvers for turbulent isothermal multiphase flows in OpenFOAM, Comput. Phys. Commun. 247 (2020) 106876.

[33] T.T. Tran, D.-H. Kim, The coupled dynamic response computation for a semi-submersible platform of floating offshore wind turbine, J. Wind Eng. Ind. Aerod. 147 (2015) 104–119.

[34] S. Dudley Brian, A single formula for the "law of the wall, J. Appl. Mech. 28 (3) (1961) 455–458.

[35] N. Bruinsma, B. Paulsen, N. Jacobsen, Validation and application of a fully nonlinear numerical wave tank for simulating floating offshore wind turbines, Ocean Eng. 147 (2018) 647–658.

[36] L. Eça, M. Hoekstra, A procedure for the estimation of the numerical uncertainty of CFD calculations based on grid refinement studies, J. Comput. Phys. 262 (2014) 104–130.

[37] L. Eça, M. Hoekstra, On the influence of the iterative error in the numerical uncertainty of ship viscous flow calculations, in: 26th Symposium on Naval Hydrodynamics, Italy, Rome, 2006.

[38] Marintek, SIMO—Theory Manual Version 4.0, Marintek Trondheim, Norway, 2012.

[39] H. Ormberg, E. Passano, RIFLEX Theory Manual, Marintek, Trondheim, 2012.

[40] C.-H. Lee, WAMIT Theory Manual, Massachusetts Institute of Technology, Department of Ocean Engineering, 1995.

[41] A. Robertson, et al., Definition of the Semisubmersible Floating System for Phase II of OC4. No. NREL/TP-5000-60601, National Renewable Energy Lab.(NREL), Golden, CO (United States), 2014.

[42] A. Robertson, et al., Total experimental uncertainty in hydrodynamic testing of a semisubmersible wind turbine, considering numerical propagation of systematic uncertainty, Ocean Eng. 195 (2020) 106605.

[43] K.H. Halse, On Vortex Shedding and Prediction of Vortex-Induced Vibrations of Circular Cylinders, Norwegian University of Science and Technology, 1997.

[44] E.E. Bachynski, et al., Computational fluid dynamics reproduction of nonlinear loads on a vertical column during extreme irregular wave events, J. Offshore Mech. Arctic Eng. 140 (6) (2018).

B.2 Paper 2

Paper 2:

Haoran Li and Erin E. Bachynski-Polić. Analysis of difference-frequency wave loads and quadratic transfer functions on a restrained semi-submersible floating wind turbine. *Ocean Engineering* 2021; **232**:109165. `https://doi.org/10.1016/j.oceaneng.2021.109165`

Ocean Engineering 232 (2021) 109165

Contents lists available at ScienceDirect

Ocean Engineering

journal homepage: www.elsevier.com/locate/oceaneng

Analysis of difference-frequency wave loads and quadratic transfer functions on a restrained semi-submersible floating wind turbine

Haoran Li [a,*], Erin E. Bachynski-Polić [a,b]

[a] Department of Marine Technology, Norwegian University of Science and Technology (NTNU), Trondheim, Norway
[b] Centre for Autonomous Marine Operations and Systems (AMOS), NTNU, Trondheim, Norway

ARTICLE INFO

Keywords:
Semi-submersible floating wind turbine
CFD
Potential flow theory
Difference-frequency loads
Quadratic transfer functions

ABSTRACT

One of the concerns regarding numerical simulation of floating wind turbines (FWTs) in waves is underprediction of resonant responses in the low-frequency range. In the present work, the difference-frequency wave loads on a restrained semi-submersible FWT subject to bichromatic waves are investigated by higher-fidelity tools (Computational Fluid Dynamics, CFD) and simplified engineering tools based on potential flow theory with Morison type drag. The effects of mean pitch angle (trim) and the wave force distribution on the multimember semisubmersible are assessed. Compared to the CFD results, wave loads estimated by engineering models are in good agreement at the wave frequencies, while slightly larger differences occur at the surge and pitch natural frequencies. The most significant underprediction of the surge force at the surge natural frequency occurs in the heave plate of the floater. Compared to the upright floater, the increased wave loads on the trimmed floater at the surge natural frequency are more significant than those at the pitch natural frequency. Furthermore, quadratic transfer functions (QTFs) are estimated based on the CFD model with a set of bichromatic wave cases. A new approach is found to use the CFD results to modify the QTFs in lower-fidelity engineering tools. This approach is validated against experimental measurements in irregular waves. Good agreement is achieved between measured and numerically estimated difference-frequency wave loads by engineering tools with modified QTFs.

1. Introduction

Floating wind turbines (FWTs) can harness the energy from winds over deep water and farther offshore. However, this technology is still at an early stage of development. Well-validated modelling tools are needed to capture highly nonlinear wave loads on the floater induced by the harsh environments and steep waves. In this paper, the focus is on a semi-submersible FWT.

The international collaboration projects known as OC4 (Phase II) and OC5 (Phase II) verified and validated semi-submersible FWT modelling tools through code-to-code and code-to-data comparisons. Larger differences between simulated loads/motions and measurements were seen in the low-frequency domain (Robertson et al. 2014, 2017). Although the low-frequency wave exciting loads are small, these loads can result in large motions due to resonant responses in surge and pitch. Accurate estimation of difference-frequency wave loads is therefore important for capturing global responses (Coulling et al., 2013). Other investigations (Bachynski et al., 2016; Berthelsen et al., 2016; Luan et al., 2016) have similar findings as the OC4 projects: the predictions of low-frequency motions were very sensitive to the viscous drag coefficients on the columns and pontoons.

Given that engineering tools based on first- and second- order potential flow theory with or without Morison-type drag limit hydrodynamic modelling to linear or weakly nonlinear models and generally underpredict the highly nonlinear difference-frequency wave loads, it is reasonable to consider higher-fidelity modelling tools that account for the fully nonlinear terms of the Navier-stokes equations, such as computational fluid dynamics (CFD). CFD has been shown to improve predictions of nonlinear wave loads and motions of semi-submersible FWTs, such as capturing shadowing effects and transverse forces from vortex shedding and nonlinear phenomena in steep wave conditions (Benitz et al. 2014, 2015; Hu et al., 2014; Liu and Hu, 2014; Rivera-Arreba et al., 2019). Ideally, one would like to carry out irregular wave simulations to study the difference-frequency loads. However, the substantial computational time of CFD tools makes it difficult to carry out long simulations of irregular waves, and CFD simulations of irregular

---

[*] Corresponding author.
E-mail address: haoran.li@ntnu.no (H. Li).

https://doi.org/10.1016/j.oceaneng.2021.109165
Received 27 September 2020; Received in revised form 13 April 2021; Accepted 10 May 2021

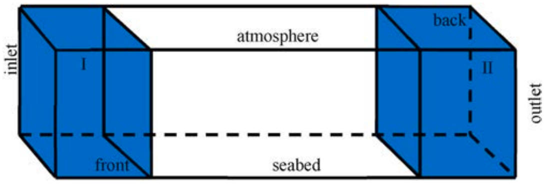

Fig. 1. Schematic representation of computational domain.

waves may suffer from significant wave damping triggered by an increase in the viscosity around the air-water interface (Devolder et al., 2017). Therefore, bichromatic waves are applied to study the difference-frequency wave loads and quadratic transfer functions (QTFs) in this paper. Modified QTFs based on the CFD results are validated against experimental results in irregular waves.

Bichromatic waves have also been used to examine the difference-frequency wave loads and motions of floating systems by other researchers. Pessoa and Fonseca (Pessoa et al., 2010; Fonseca et al., 2011; Pessoa and Fonseca, 2015) investigated the slowly-varying wave exciting forces and motions of a body with a simple geometry in bichromatic waves experimentally and numerically. The numerical models were able to qualitatively represent the measured slowly-varying forces, namely the order of magnitude of the forces, the tendencies along the mean wave period range and the increase with the decreasing water depth. Ohyama and Hsu (1995) examined the slow sway motion of a rectangular body in response to bichromatic waves and found the second-order approximation was applicable in a small-amplitude range. Lopez-Pavon et al. (2015) measured second-order loads on a semi-submersible FWT directly in biochromatic waves and found full QTFs instead of Newman's approximation should be implemented for accurate estimation of difference-frequency wave loads. Simos et al. (2018) investigated the second-order hydrodynamics of a semisubmersible FWT in bichromatic waves, and the measured results matched well with the numerical estimations by QTFs.

The focus of present study, which is inspired by the ongoing Offshore Code Comparison Collaboration, Continued, with Correlation, and unCertainty (OC6) project (Wang et al., 2021), is on the investigation of nonlinear difference-frequency wave loads on a restrained semi-submersible FWT subjected to bichromatic waves by CFD and engineering tools. The bichromatic waves are generated by adding together two regular waves at different frequencies whose difference coincides with either the surge or pitch natural frequency of the FWT. A trimmed floater is additionally modelled to examine the change of wave loads due to trim induced by the mean aerodynamic thrust force. Meanwhile, wave loads on individual columns are extracted to better understand how the nonlinear wave loads change among the different components of semi-submersible FWTs.

In order to be able to use the CFD results in practical simulations, the difference-frequency wave loads from the bichromatic waves are used to modify the QTFs calculated using potential flow theory. Finally, the modified QTFs in the engineering tools are validated by comparing the numerically estimated difference-frequency wave loads in irregular waves against experimental measurements. The experimental measurements of wave loads on the restrained semi-submersible FWT are from Phase I of the OC6 project (Robertson et al., 2020). An irregular wave with significant wave height $H_s = 7.1$ m and peak period $T_p = 12.1$ s, following the JONSWAP wave spectrum with peak enhancement factor equal to 3.3, is considered. All data and results are given at full scale.

Sections 2 and 3 describe the CFD and potential flow theory models, respectively. The approaches for estimating and modifying the QTFs are described in Section. 4. In Section 5, comparisons of wave exciting loads on the upright and trimmed semi-submersible FWT by CFD and engineering tools are shown first, followed by the estimations and modifications of QTFs in bichromatic waves and the validations in irregular waves. The conclusions are presented in Sec. 6.

2. Computational fluid dynamics (CFD) model

The multiphase interFoam solver in OpenFOAM (Weller et al., 1998) is a fully nonlinear Navier-Stokes/Volume-Of-Fluid (VOF) solver which can accurately simulate complex free surface flows and fluid-structure interaction. Extending the interFoam solver with the implementation of the wave generation and absorption toolbox, waves2Foam, developed by Jacobsen et al. (2012), generates the waveFoam solver used

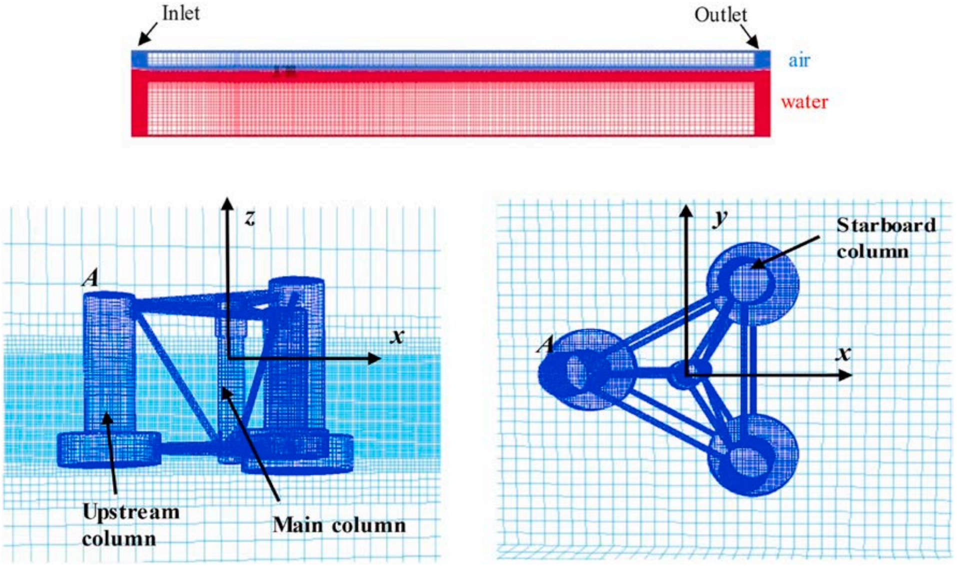

Fig. 2. The computational domain (top) and mesh around floater of wind turbine (bottom) in the CFD simulations.

Table 1
Bichromatic wave parameters (full scale).

$df = 0.01$ Hz (Surge natural frequency)

Wave index	T1 (s)	T2 (s)	A1 (m)	A2 (m)
S1	20	16.81	1.67	1.79
S2	16.67	14.39	1.79	1.74
S3	14.29	12.58	1.74	1.74
S4	13.33	11.83	1.74	1.73
S5	12.50	11.17	1.73	1.71
S6	11.87	10.58	1.57	1.26
S7	11.11	10.05	1.50	1.50
S8	10.53	9.57	0.94	0.64
S9	10.00	9.13	0.84	0.54
S10	8.33	7.72	0.31	0.21
S11	7.14	6.69	0.22	0.16
S12	6.67	6.27	0.17	0.12

$df = 0.032$ Hz (Pitch natural frequency)

Wave index	T1 (s)	T2 (s)	A1 (m)	A2 (m)
P1	20	12.20	1.67	1.74
P2	16.67	10.87	1.79	1.73
P3	14.29	9.80	1.74	1.70
P4	13.33	9.35	1.74	1.66
P5	12.50	8.93	1.50	1.50
P6	11.87	8.55	1.59	0.86
P7	11.11	8.20	1.44	0.76
P8	10.53	7.87	1.28	0.70
P9	10.00	7.58	1.13	0.64
P10	8.33	6.58	0.41	0.19
P11	7.14	5.81	0.22	0.12
P12	6.67	5.50	0.18	0.10

throughout the current work.

2.1. Governing equations

The governing equations are the two-phase incompressible RANS equations, consisting of a mass conservation and a momentum conservation equation for an incompressible flow of air and water, expressed as:

$$\frac{\partial u_i}{\partial x_i} = 0 \tag{1}$$

$$\frac{\partial \rho u_i}{\partial t} + \frac{\partial \rho u_j u_i}{\partial x_j} = -\frac{\partial p^*}{\partial x_i} + F_{b,i} + \frac{\partial}{\partial x_j}\left[\mu_{eff}\frac{\partial u_i}{\partial x_j}\right] \tag{2}$$

where u_i $(i = x, y, z)$ are the fluid velocity in Cartesian coordinates, ρ is the fluid density, p^* is pressure in excess of the hydrostatic pressure, F_b is an external body force including gravity and μ_{eff} is the effective dynamic viscosity.

Furthermore, in the VOF method, the local density ρ within a computational cell is given by water volume fraction α. The effective dynamic viscosity μ_{eff} is calculated by combining a weighted value based on the volume fraction α with the additional turbulent dynamic viscosity $\rho\nu_t$.

$$\rho = \alpha\rho_{water} + (1-\alpha)\rho_{air} \tag{3}$$

$$\mu_{eff} = \alpha\mu_{water} + (1-\alpha)\mu_{air} + \rho\nu_t \tag{4}$$

where α is one for water, zero for air, and in between zero and one for all intermediate values.

The VOF method (Hirt and Nichols, 1981) is used to track the air-water interface. The volume fraction α is advanced in time once the velocity is found by Eqs. (1) and (2), following an advection equation (Eq. (5)).

$$\frac{\partial \alpha}{\partial t} + \frac{\partial u_i \alpha}{\partial x_i} + \frac{\partial u_{r,i}\alpha(1-\alpha)}{\partial x_i} = 0 \tag{5}$$

Using a standard finite-volume approximation for solving Eq. (5) will lead to significant smearing of the interface. The last term on the left-hand side of Eq. (5) is introduced as an interface compression term (Berberović et al., 2009). It is only active in the vicinity of the interface, $0 < \alpha < 1$. To ensure the stability of the solution, a multi-dimensional flux limited scheme (MULES) is applied.

To identify the free surface elevation, the volume fraction$\alpha$is integrated over a vertical line around the air-water interface in the waves2Foam package.

2.2. Turbulence model

Turbulent effects are incorporated in the governing equations by using different transport equations to calculate the turbulent kinematic viscosity. The $k-\omega$ SST turbulence model (Menter et al., 2003), a blending of the $k-\omega$ (Wilcox, 1998) and the $k-\varepsilon$ (Launder and Spalding, 1983) models, has shown good results for simulating two-phase flow and predicting wave elevation (Rahman et al., 2007, Brown et al., 2014) and is applied in this paper. The equations for the incompressible $k-\omega$ SST turbulence model for a single fluid in OpenFoam are given as:

$$\frac{\partial k}{\partial t} + \frac{\partial u_j k}{\partial x_j} - \frac{\partial}{\partial x_j}\left[(\nu + \sigma_k\nu_t)\frac{\partial k}{\partial x_j}\right] = P_k - \beta^*\omega k \tag{6}$$

$$\frac{\partial \omega}{\partial k} + \frac{\partial u_j \omega}{\partial x_j} - \frac{\partial}{\partial x_j}\left[(\nu + \sigma_\omega\nu_t)\frac{\partial \omega}{\partial x_j}\right] = \frac{\gamma}{\nu_t}G - \beta\omega^2 + 2(1-F_1)\frac{\sigma_{\omega 2}}{\omega}\frac{\partial k}{\partial x_j}\frac{\partial \omega}{\partial x_j} \tag{7}$$

where k is the turbulent kinetic energy, and P_k is the production term of k. ν is the kinematic viscosity, ν_t is the turbulent kinematic viscosity, and ω is the specific dissipation rate. See Menter et al. (2003) for details. In the present work, in order to avoid excessive wave damping due to the increased viscosity around the air-water interface (Devolder et al., 2017; Fan and Anglart, 2020), a modified waveFoam solver is built to explicitly consider the density in the incompressible $k-\omega$ SST model (Fan and Anglart, 2020).

2.3. Boundary conditions

To solve the governing equations of the Navier-Stokes/VOF solver, boundary conditions are imposed to all the surfaces in the numerical domain. The general denomination of boundary surfaces is given in Fig. 1.

- The velocity and the α field at the inlet are given by the applied wave theory. Here, second order bichromatic wave theory (Madsen and Fuhrman, 2006) is used. The parameters of bichromatic waves are described in Table 1. The pressure is specified as zero normal gradient at the inlet boundary. k is fixed at zero and ω is set as 0.001 1/s.
- At the outlet, all the boundaries are specified as zero normal gradient.
- On the floater surface, a no-slip boundary condition (zero velocity) is specified, and the pressure is set as zero normal gradient. k is fixed at 1e-5 m^2/s^2 and ω is set as 1.0 1/s.
- For the atmosphere, the total pressure is set as zero and an atmospheric boundary condition is set for the velocity and the α field. This means that air and water are allowed to leave the numerical domain, while only air is allowed to flow back in. k is fixed at zero and ω is specified as zero normal gradient.
- At the front, back and bottom, all the conditions are set as zero normal condition.
- A continuous wall function based on Spadling's law (Dudley Brian, 1961) switching between low and high Reynolds numbers is implemented for the turbulent viscosity. Hence, it requires that the non-dimensional wall distance y^+ should be between 10 and 300.

Table 2
Mesh convergence studies, P5 (Time step = 0.001414 s).

Cell size	Frequency (Hz)	Analytical solution	Level 2	Error (%)	Level 3	Error (%)	Level 4	Error (%)
			0.03 m		0.015 m		0.0075 m	
Wave (m)	0.08	1.501	1.488	0.87	1.495	0.40	1.497	0.27
	0.112	1.498	1.442	3.74	1.475	1.54	1.489	0.60
	0.032	0.0257	0.0310	20.74	0.0268	4.20	0.0261	1.39
Surge force (KN)	0.08	–	6691	3.54	6804	1.92	6937	–
	0.112	–	5749	3.33	5903	0.74	5947	–
	0.032	–	56.46	9.79	59.95	4.22	62.59	–
Pitch moment (MNm)	0.08	–	89.35	1.54	90.37	0.42	90.75	–
	0.112	–	112.2	3.11	114.4	1.21	115.8	–
	0.032	–	5.921	8.38	5.648	3.39	5.463	–

For the modified waveFoam solver, the bichromatic wave elevation will decrease at the end of simulation if a uniform turbulent viscosity is implemented. Different values of the turbulent kinetic energy (k) and specific dissipation rate (ω) at the inlet and floater surface are applied to accurately simulate the flow around the floater while reducing the wave damping.

The bichromatic waves considered here are chosen such that the first order components are around the peak periods (12.1 s) of the irregular wave event, and the difference frequency aligns with either the surge (S) or pitch (P) natural frequency where the largest wave-induced responses can be excited in irregular waves. The desired wave amplitude (approximately 1.75 m) was selected such that the calculated maximum wave height when two waves are added linearly is close to the significant wave height of the irregular-wave spectrum (7.1 m) (Tom et al., 2019). However, for shorter wave periods, the same wave amplitude results in steeper waves and increased viscosity around the air-water interface. As a result, the generated wave elevation in the CFD simulation attenuates over the time. To avoid excessive attenuation, smaller wave heights are applied for the shorter wave periods.

2.4. Relaxation zones

The relaxation zones (blue part in Fig. 1) in the waves2Foam toolbox (Jacobsen et al., 2012) are implemented to avoid wave reflection from outlet boundary (II) and also to prevent internally reflected waves (I). Rectangular relaxation zones are defined in this work. See Bruinsma's work (2018) for details.

2.5. Computational domain

The floater at scale 1:50 was built in the CFD simulations based on the OC5-DeepCwind floating wind system (Robertson et al., 2016). The right-handed coordinate system originates at the center of the main column at the still water line, with positive x being in the direction of propagating waves, and z being up, as shown in Fig. 2. The width (3.72 m) and water depth (3.6 m) of the numerical wave tank are equal to those of the experimental facility. The same length (36 m) as one in the previous study (Li and Bachynski, 2021) is implemented to ensure the reflected waves are dissipated thoroughly. In addition, the height of the air regime is set to 1 m. Fig. 2 shows the numerical wave tank and floater.

2.6. Spatial and temporal discretization

OpenFOAM is based on finite volume discretization. The computational domain is discretized into finite regions in space known as cells. The size of a cell in all the directions is 0.12 m after discretization. Thereafter, for the wave generating regime and the floater surface, the mesh is refined. Mesh convergence studies for different mesh levels with 0.001414 s time step (Table 2) were carried out by comparing the wave elevations and calculated wave loads at wave- and difference-frequencies for wave P5. The analytical solutions of wave are calculated from second-order bichromatic wave theory (Marthinsen and Winterstein, 1992). The errors in wave elevations are shown relative to the analytical solutions while the wave loads are compared to those with the finest mesh size (Level 4).

Globally, the 3-3 level of refinement with 4-4 refinement locally around the cross braces is applied in subsequent simulations. In addition, 25 cell layers adjacent to the floater surface are generated for the turbulence modelling. The thickness of the first layer is 2.0 μm and its expansion ratio is 1.2. The local refinement allows for a high-resolution interface while keeping the total number of computational cells (around 17 million) relatively low.

In order to ensure numerical stability, the Courant-Friedrichs-Lewy (CFL) condition is implemented to determine the time step. Different fixed time steps with the 3-3 level of mesh refinement are chosen to carry out the time step convergence study of the wave elevations and calculated wave loads for wave P5 and shown in Table 3. All the results are obtained through the same method as the mesh convergence studies. Considering the computational time, 'time step 3' is used in this work.

The wave loads at the limit of infinite temporal and spatial resolution are calculated based on the Richardson extrapolation with the standard power-law error estimator (Eça and Hoekstra, 2014). The resulting apparent order of convergence if found to be 2. The discretization

Table 3
Time step convergence study, P5 (same spatial discretization, Level 3).

	Frequency (Hz)	Analytical solution (m)	Time step 1 (m)	Error (%)	Time step 2 (m)	Error (%)	Time step 3 (m)	Error (%)	Time step 4 (m)	Error (%)
Time step (s)			7.07E-3		2.828E-3		1.414E-3		7.07E-4	
Wave (m)	0.08	1.501	1.463	2.53	1.49	0.73	1.495	0.40	1.496	0.33
	0.112	1.498	1.385	7.54	1.453	3.00	1.475	1.54	1.491	0.47
	0.032	0.0257	0.0327	27.2	0.0298	16.1	0.0268	4.20	0.0261	1.56
Surge force (KN)	0.08	–	6703	3.57	6783	2.08	6804	1.78	6927	–
	0.112	–	5797	2.67	5866	1.51	5903	0.89	5956	–
	0.032	–	55.36	9.11	58.49	3.97	59.95	1.58	60.91	–
Pitch moment (MNm)	0.08	–	89.50	1.15	90.17	0.41	90.37	0.19	90.54	–
	0.112	–	112.1	3.03	113.4	1.90	114.4	1.04	115.6	–
	0.032	–	6.074	8.81	5.761	3.21	5.648	1.18	5.582	–

Table 4
Estimated uncertainties in the CFD simulations.

	Difference frequency 0.032 Hz	First wave frequency 0.08 Hz	Second wave frequency 0.112 Hz
Wave elevation	4.2%	0.40%	1.54%
Surge force	8.11%	3.99%	2.14%
Pitch moment	6.69%	0.78%	2.99%

Table 5
Overview of different settings in SIMA.

Label	Load model
SIMA1/ Linear1	Only linear potential flow theory
SIMA2/ Linear2	SIMA1/Linear1 with original quadratic transfer function (QTF) from WAMIT
SIMA3/ Linear3	SIMA 2/Linear2 with integration of Morison drag force to mean free surface
SIMA4/ Linear4	SIMA 2/Linear2 with integration of Morison drag force to the undisturbed linear free surface
SIMA5/ Linear5	SIMA 4/Linear4 with consideration of axial drag force on the heave plates
SIMA6	SIMA5 with replacement of the original QTF from WAMIT with modified QTF from CFD

uncertainty of wave loads is identified as the estimated discretization error multiplied by a suitable safety factor of 1.25 (Eça and Hoekstra, 2006). The total uncertainty of wave loads is calculated by combining the temporal and spatial discretization uncertainties in the root-sum-of-squares fashion. The uncertainty in the incident wave amplitude is defined as the discretization error of the selected mesh size and time step relative to the analytical solution. The results are shown in Table 4. The uncertainties in the difference-frequency components tend to be much larger than those at the wave frequencies, especially for the wave elevation.

3. Potential flow theory model

A numerical model based on potential flow theory is built in SIMA (SIMO-RIFLEX), developed by SINTEF Ocean. SIMA is a state-of-the-art time-domain code that can address both the hydrodynamic loads (SIMO (MARINTEK, 2012)) and the structural dynamic problem (RIFLEX (Ormberg and Passano, 2012)) in a fully coupled way and has been used to study numerous types of floating wind turbines.

In present simulations, only the floater of the wind turbine is modelled. The frequency-dependent hydrodynamic properties, such as first-order potential flow forces and QTFs, are estimated based on potential flow theory (WAMIT (Lee, 1995)) or modified based on the CFD simulations and subsequently input to SIMA. The viscous forces on the columns and cross braces of the floater are considered by including the drag forces from Morison's equation. A constant transverse drag coefficient (0.744 based on towing tests (Robertson et al., 2020)) is applied for each component of the floater. Additionally, the axial drag force for the heave plate is calculated based on Eq. (8), where D is the diameter of the heave plate and U is the axial wave velocity. Here, the axial drag coefficient $C_{da} = 2.48$ based on previous comparisons of a similar engineering tool with experimental data from the DeepCwind test campaign (Robertson et al., 2014).

$$F_{DA} = \frac{1}{2}\rho C_{da}\frac{\pi D^2}{4}U|U| \tag{8}$$

In the potential flow theory model, different force contributions are investigated, as summarized in Table 5. For simulations referred to as 'SIMA', the generated (nonlinear) wave elevation from CFD is used as an input, while simulations indicated as 'Linear' take a time series based on the first-order bichromatic theory (a simple linear super-position of sine signals) as input. All simulations are carried out in the SIMA software. In both cases, when a wave signal is input into the SIMA software, it is treated as a superposition of linear regular waves at different frequencies, and all the components are assumed to travel in the positive x-direction. Additionally, the time series of bichromatic waves are input into SIMA software by a high-pass filter with a 0.008 Hz cut-off frequency for all simulations in the current work. The difference between 'SIMA' and 'Linear' can be seen in the bottom subplot of Fig. 4. The comparisons of 'SIMA' and 'Linear' models are used to investigate the effects of nonlinear wave component on the wave- and difference-frequency wave loads.

4. QTF estimation and modification

4.1. Analysis of the numerical data

The harmonic components (mean values and all first- and second-order harmonics) of wave elevation and wave loads are identified by fitting a second order expansion model to the steady-state part of the numerical time signal with a least squares procedure. In bichromatic waves, the wave elevations and wave loads are approximated by Eq. (9). Components above the 2nd order are found to be negligible.

$$\begin{aligned} I(t) = \overline{I} &+ I_1^{c(1)}\cos(\omega_1 t) + I_1^{s(1)}\sin(\omega_1 t) + I_2^{c(1)}\cos(\omega_2 t) + I_2^{s(1)}\sin(\omega_2 t) \\ &+ I_1^{c(2)}\cos(2\omega_1 t) + I_1^{s(2)}\sin(2\omega_1 t) + I_2^{c(2)}\cos(2\omega_2 t) + I_2^{s(2)}\sin(2\omega_2 t) \\ &+ I^{c(+)}\cos\{(\omega_1+\omega_2)t\} + I^{s(+)}\sin\{(\omega_1+\omega_2)t\} \\ &+ I^{c(-)}\cos\{(\omega_1-\omega_2)t\} + I^{s(-)}\sin\{(\omega_1-\omega_2)t\} \end{aligned} \tag{9}$$

In Eq. (9), I is the quantity of interest (the wave elevation η or wave loads F), and ω_1, ω_2 are the two incident wave frequencies. Each harmonic component is represented by a sum of cosine and sine parts, thus allowing the identification of the phase. The first-order harmonics at the incident wave frequencies I_1, I_2 and the second-order difference-frequency component $I^{(-)}$ are all computed in this way.

Considering the computational time of CFD simulations, the estimation of harmonic components of wave elevation and wave loads from Eq. (9) are calculated based on 10-min steady-state simulations. The estimated pitch moments in P5 from the CFD simulations at different time durations are compared in Table 6. As shown, the difference-frequency wave loads based on 300 s are within 7% of the results after 600 s.

4.2. Estimation of the QTF

The QTF values can be represented by a series of complex numbers ($a + bi$ for $\omega_1 \geq \omega_2$ and $a - bi$ for $\omega_1 \leq \omega_2$). Hence, the difference-frequency wave loads in bichromatic waves are approximated by

$$\begin{aligned} F_d(t) = F_{12}(t) + F_{21}(t) &= \mathrm{Re}\big[A_1A_2\big\{(a+bi)e^{-i((\omega_1 t-\xi_1)-(\omega_2 t-\xi_2))} \\ &\quad + (a-bi)e^{-i((\omega_2 t-\xi_2)-(\omega_1 t-\xi_1))}\big\}\big] \\ &= 2A_1A_2\{[a\cos(\xi_1-\xi_2)+b\sin(\xi_1-\xi_2)]\cos(\omega_1 t-\omega_2 t) \\ &\quad + [-a\sin(\xi_1-\xi_2)+b\cos(\xi_1-\xi_2)]\sin(\omega_1 t-\omega_2 t)\} \end{aligned} \tag{10}$$

where $A_1, A_2, \omega_1, \omega_2, \xi_1, \xi_2$ are the two incident wave amplitudes, frequencies and phases which can be calculated by Eq. (9). Given the cosine (F_d^c) and sine (F_d^s) parts of second-order difference-frequency wave loads from Eq. (9), the real (a) and imaginary (b) parts of the QTF can be found by solving Eq. (11).

$$\begin{cases} 2A_1A_2[a\cos(\xi_1-\xi_2)+b\sin(\xi_1-\xi_2)] = F_d^c \\ 2A_1A_2[-a\sin(\xi_1-\xi_2)+b\cos(\xi_1-\xi_2)] = F_d^s \end{cases} \tag{11}$$

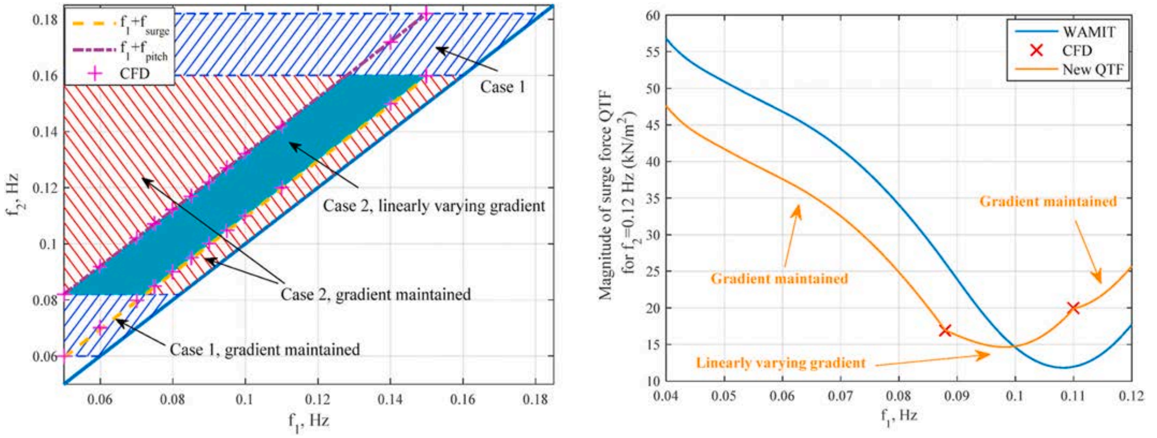

Fig. 3. Different regions of QTF for modification.

4.3. *Modifying the QTFs in the SIMA models based on the CFD results*

Using symmetry relations, only the upper-left-half ($f_2 \geq f_1$ in the left subplot of Fig. 3) is considered when modifying the potential flow QTFs. First, based on the CFD simulations, the surge force QTF and pitch moment QTF along the surge and pitch natural frequencies (dashed line and dashed-dotted line in the left subplot of Fig. 3) are obtained through the method presented in Sec. 4.2. Next, the magnitudes and phases of these QTFs and the QTFs estimated by potential flow theory (WAMIT) are separately interpolated to obtain values at denser sets of frequencies (using an interval of 0.001 Hz).

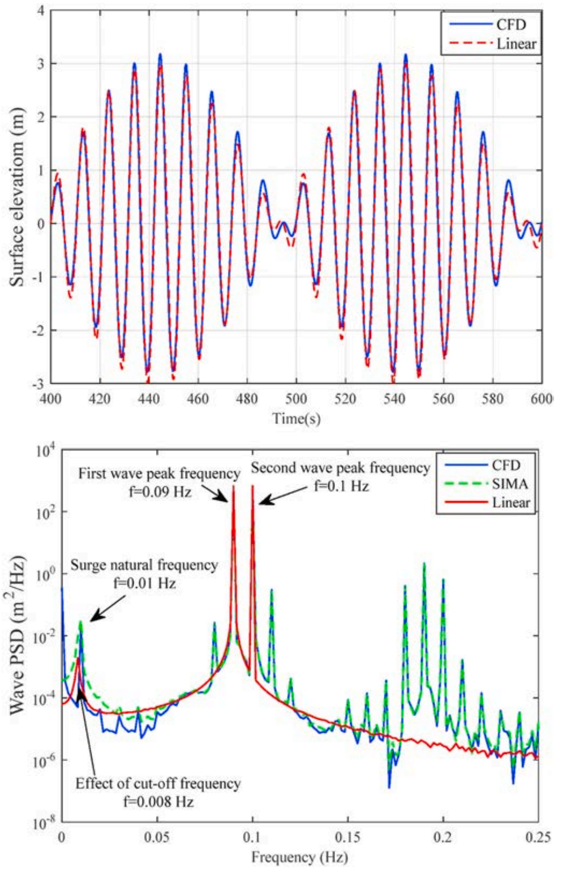

Fig. 4. Wave simulations, Wave S7 (Top: Time series of wave elevation in the CFD and Linear model, Bottom: Wave spectra).

Table 6
Comparisons of the estimated pitch moment at different time durations in the CFD simulations of P5.

Time (s)	1–100	1–200	1–300	1–400	1–500	1–600
0.08 Hz (MNm)	91.49	91.25	91.26	91.07	90.81	90.37
0.112 Hz (MNm)	110.7	112.5	113.4	114.1	114.5	114.4
0.032 Hz (MNm)	6.158	6.058	5.999	5.841	5.713	5.648

Then, the interpolated results from WAMIT along the surge and pitch natural frequencies are replaced with the interpolated results from CFD simulations. To propagate the correction to other parts of the QTF, the WAMIT magnitudes or phases with the same f_2 are extracted and corrected based on the results from CFD model. There are two diff erent cases: (1) regions with only one value from CFD model ($f_2 < 0.082$ Hz or $f_2 > 0.16$ Hz), (2) regions with two values from CFD model (0.082 Hz $\leq f_2 \leq 0.16$ Hz). In case (1), the gradient is maintained to be the same before and after modification. In case (2), the gradient is maintained outside of the surge and pitch natural frequencies ($f_1 < f_2 - 0.032$ Hz or $f_1 > f_2 - 0.01$ Hz) while the gradient varies linearly between surge and pitch natural frequencies ($f_2 - 0.032$ Hz $\leq f_1 - 0.01$ Hz). An example is shown in the right subplot of Fig. 3. Finally, this modified QTF matrix is downsampled to an interval of 0.05 Hz and implemented in the SIMA model.

5. Results

5.1. *Wave loads on the upright and trimmed semi-submersible FWT in bichromatic waves*

First, we examine the details of difference-frequency wave loads on a restrained semi-submersible FWT in two bichromatic waves (wave index: S7, P5). The surge forces at the wave and surge natural frequencies in wave S7 are presented in Sec. 5.1.1 and the pitch moments at the wave and pitch natural frequencies in wave P5 are shown in Sec. 5.1.2. Considering the existence of mean pitch angle for wind turbine during operation, wave loads on a 5° trimmed floater are also included. The floater is rotated 5° clockwise around Point A shown in Fig. 2. The surge force (along x axis) and pitch moment (around y axis) are

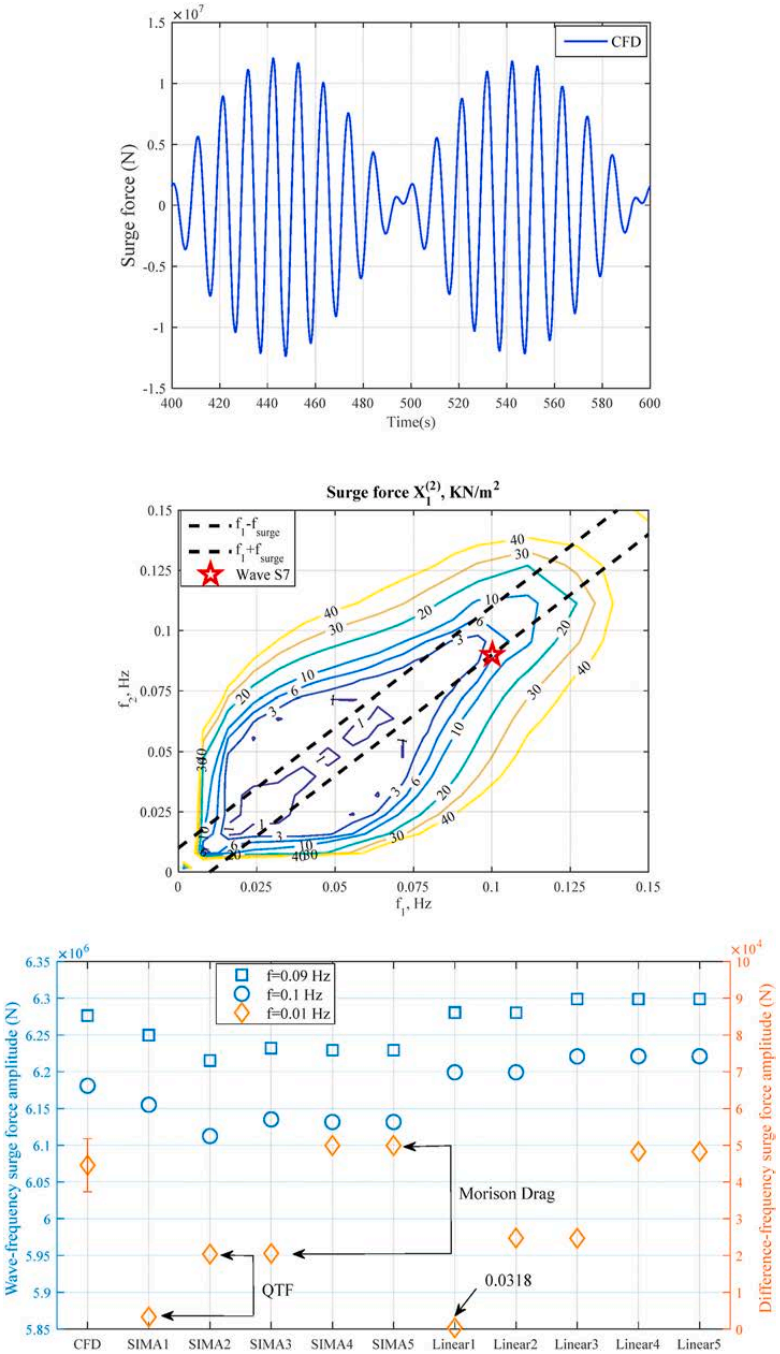

Fig. 5. Surge forces on the upright floater, Wave S7 (Top: time series of total surge forces in CFD simulations, Middle: QTF used in SIMA simulations, Bottom: Surge forces at the wave frequencies and surge natural frequency. The uncertainty bar represents the numerical uncertainty of difference-frequency surge force, the uncertainty in the wave-frequency surge force from CFD is given in Table 4).

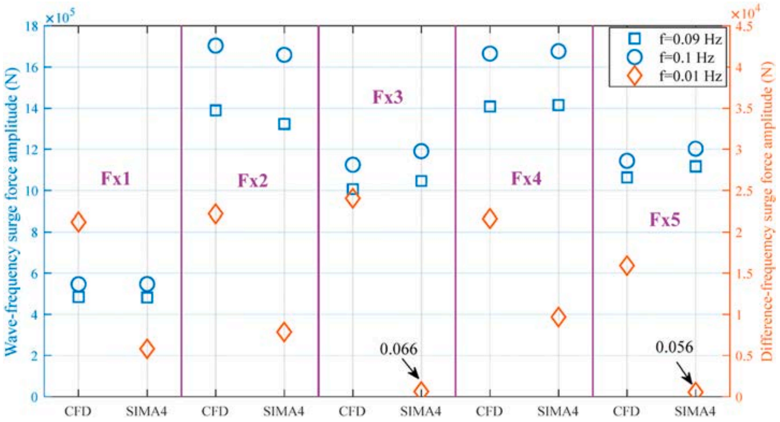

Fig. 6. Surge forces on the separated columns of upright floater, Wave S7 (Fx1: main column, Fx2: upper part of upstream column, Fx3: lower part of upstream column, Fx4: upper part of starboard column, Fx5: lower part of starboard column. See Fig. 2 for the definitions of columns).

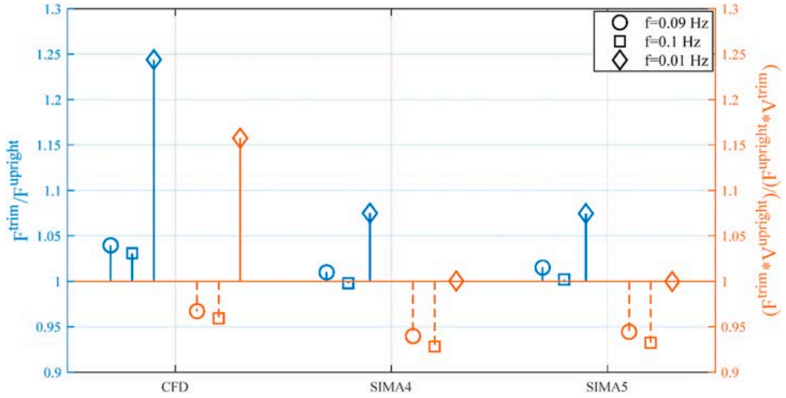

Fig. 7. Comparisons of surge forces on the upright and trimmed floaters, Wave S7.

calculated in the same global coordinate system as the upright condition (Fig. 2).

5.1.1. *Bichromatic wave S7*

The wave elevation for wave S7 in the CFD and SIMA models is shown in Fig. 4. No significant wave damping can be observed at the end of the CFD simulations. A comparison of CFD and 'Linear' shows the interaction between two regular waves which leads to the peaks between 0.15 Hz and 0.25 Hz, at frequencies such as $f_1 + f_2$, or $2f_1$, or $2f_2$. The wave amplitudes at these sum frequencies are much smaller than the wave-frequency amplitudes (note the log scale in the PSD). The wave amplitudes at the wave frequencies agree with the analytical solution (1.5 m) within 1%. At the difference frequency (the surge natural frequency), the wave amplitude from the CFD model is 9.9% smaller than the second order analytical solution (0.0101 m). As expected, the wave amplitude of the first-order bichromatic wave (Linear) at the surge natural frequency is negligible (0.001 m). The effect of the cut-off frequency (0.008 Hz) is, however, visible in the PSD of the 'Linear' wave elevation.

The total surge force on the upright floater from the CFD simulation is presented together with SIMA simulations in Fig. 5. There is a small numerical damping of the surge force caused by the large turbulent viscosity at the floater boundaries in the CFD simulation.

Compared to the CFD simulations, SIMA slightly underpredicts the surge forces at the wave frequencies (within 1.2%, smaller than the uncertainty of CFD results). In the SIMA models, the linear wave force transfer function dominates at the wave frequencies. The surge forces at the surge natural frequency are mainly from the QTF (SIMA2) and the integration of the Morison drag forces to the linear free surface (SIMA4). SIMA4 overpredicts the surge force at the surge natural frequency by 11% compared to the CFD estimations. The axial drag forces on the heave plates have no effect on the surge forces (SIMA4 vs SIMA5). The surge forces using the first-order bichromatic wave (Linear) are also shown in Fig. 5. A comparison of 'SIMA1' vs 'SIMA2' and 'Linear1' vs 'Linear2', shows that the force contributions from the QTF reduce the surge forces at the wave frequencies if the difference frequency between wave components at other frequencies (Fig. 4) coincides with wave frequencies. Furthermore, the contribution of difference-frequency wave components via the linear wave force transfer function (SIMA1 vs Linear1) decreases the difference-frequency surge force (SIMA2 vs Linear2). In addition, 'Linear' models give the same conclusions as 'SIMA' models.

Fig. 6 compares the surge forces on individual columns of the upright floater between SIMA and CFD simulations. In these cases, the QTF for each column is not included in SIMA results. For each column, the surge forces at the second wave frequency (0.1 Hz) are larger than the forces at

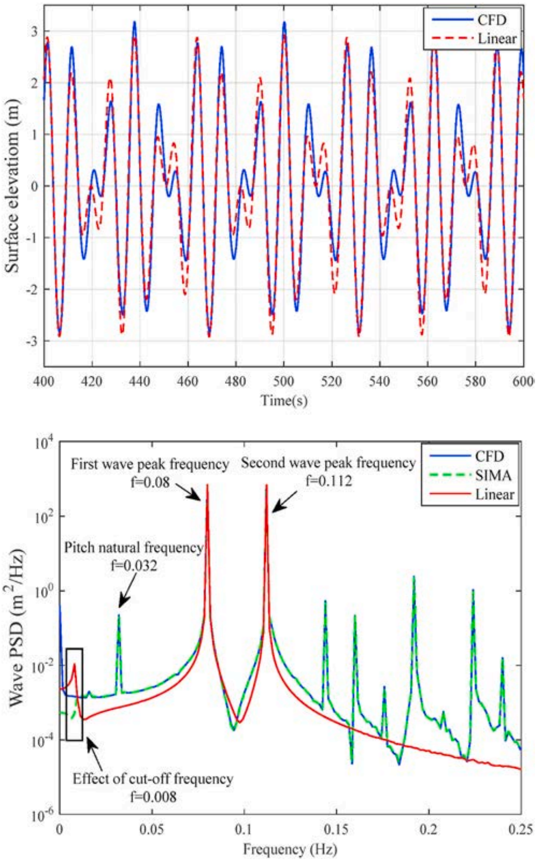

Fig. 8. Wave simulations, Wave P5 (Top: Time series of wave elevation in the CFD model, Bottom: Wave spectra).

the first wave frequency (0.09 Hz), which is opposite the results for total surge forces (Fig. 5). This is due to the frequency-dependent phase differences of surge forces on each column. In addition, all the numerical models predict similar results for the surge forces at the wave frequencies. No matter for the upstream column or the starboard column, although the diameter of lower part is twice than that of upper part, the surge force on the upper part (Fx2 and Fx4) is larger compared to the force on the lower part (Fx3 and Fx5) at the wave frequencies. That is because the wave acceleration decreases as one moves further downward. The surge forces at the wave frequencies on the starboard column (Fx4 and Fx5) are not significantly different from those on the upstream column (Fx2 and Fx3).

Due to the lack of the QTF for each column, the surge forces at the difference frequency in the SIMA simulations mainly come from the integration the Morison drag force to the linear free surface. Compared to the CFD results, one can observe that SIMA underpredicts the surge forces on each column at the surge natural frequency and larger underprediction occurs at the lower part of columns (Fx3 and Fx5). In addition, in the CFD simulations, the surge forces at the surge natural frequency on the starboard column (Fx4 and Fx5) are smaller than those on the upstream column (Fx2 and Fx3) and a larger reduction (33%) is found at the lower part of columns (Fx3 vs Fx5).

The surge forces on the trimmed and upright floaters are compared in Fig. 7. For the CFD simulations, the surge forces on the trimmed floater at the wave frequencies increase by 4% compared to the upright condition. In the SIMA4 model, the linear wave force transfer function is dominant at the wave frequencies. Hence, for the trimmed floater, the increasing or decreasing surge forces at the wave peak frequencies mainly depend on the effect of the changed immersed geometry of the floater on the first-order hydrodynamic properties. The effect of axial drag forces is shown in ‘SIMA5’ of Fig. 7. As expected, for the trimmed floater, the axial drag forces on the heave plates have a component along the x axis which slightly increases the surge force. To eliminate the effect of changed submerged volume, comparisons between surge force amplitudes normalized by the mean displaced submerged volume V are shown in the right y axis of Fig. 7. A larger portion of the columns is under water after rotating the floater. Meanwhile, the water particle acceleration at the same position on the columns decreases for the trimmed floater. Considering the changed volume, the surge forces at the wave frequencies under trimmed condition decrease in all the numerical simulations.

An increased surge force at the surge natural frequency is seen for the trimmed condition. Compared to the CFD simulations, the increases in the SIMA models are small. In the SIMA simulations, the axial drag forces on the heave plates have minor contributions to the surge force on the trimmed floater at the surge natural frequency (SIMA4 vs SIMA5), considering small trimmed angle. The difference-frequency force in CFD increases more than the change in volume, but this is not the case in the SIMA models. For a trimmed floater, the flow separation around the edge of heave plate is more significant and the Morison drag force underestimates this effect. This big difference also highlights that the accuracy of estimated difference-frequency wave loads in the engineering tools is sensitive to the drag coefficients. Even a small change can result in a large variation for the drag coefficients.

5.1.2. *Bichromatic wave P5*

The wave simulations of Wave P5 are compared in Fig. 8. Like Wave S7, no significant wave damping can be seen at the end of the CFD simulations and interaction between two regular waves is also observed (CFD vs Linear). There is good agreement (within 1.67%) between the analytical solution and different numerical models at the wave frequencies. The wave amplitude at the pitch natural frequency in the CFD model is 4.2% larger than the analytical solution of 0.0257 m.

The pitch moments on the upright floater estimated by the CFD model are compared with SIMA models in Fig. 9. Like the surge force, at the end of the CFD simulations, the pitch moment slightly attenuates with time due to the increased turbulent viscosity at the boundaries of the floater.

Compared to the CFD simulations, all the SIMA models predict similar pitch moments at the wave frequencies (within 2.6%, smaller than the uncertainty of CFD results) and pitch natural frequency (within 3.6%) except for a large underprediction of pitch moment at the pitch natural frequency using SIMA1 model. Both in the ‘SIMA’ and ‘Linear’ models, the linear wave force transfer function is dominant at the wave frequencies. Meanwhile, the axial drag forces on the heave plates (SIMA5 and Linear5) increase the pitch moments at the wave frequencies. The pitch moment from the QTF (SIMA2 and Linear2) dominates at the pitch natural frequency. The effect of difference-frequency wave components on the difference-frequency pitch moment is minor (SIMA2 vs Linear2). Other force contributions have minor influence at the pitch natural frequency.

The numerically estimated pitch moments on the upright and trimmed floater are compared in Fig. 10. For the CFD simulations, the pitch moment on the trimmed floater increases by about 11% at the first wave frequency (0.08 Hz), but decreases slightly (0.15%) at the second wave frequency (0.112 Hz) compared to the moments on the upright floater. In the SIMA4 simulations, for the trimmed floater, an increasing moment (8.8%) occurs at the first wave frequency and a reduction of moment (4.5%) appears at the second wave frequency. All the variations at the wave frequencies are due to the changed frequency-dependent hydrodynamic properties of the floater. Combining the exact values in Fig. 9

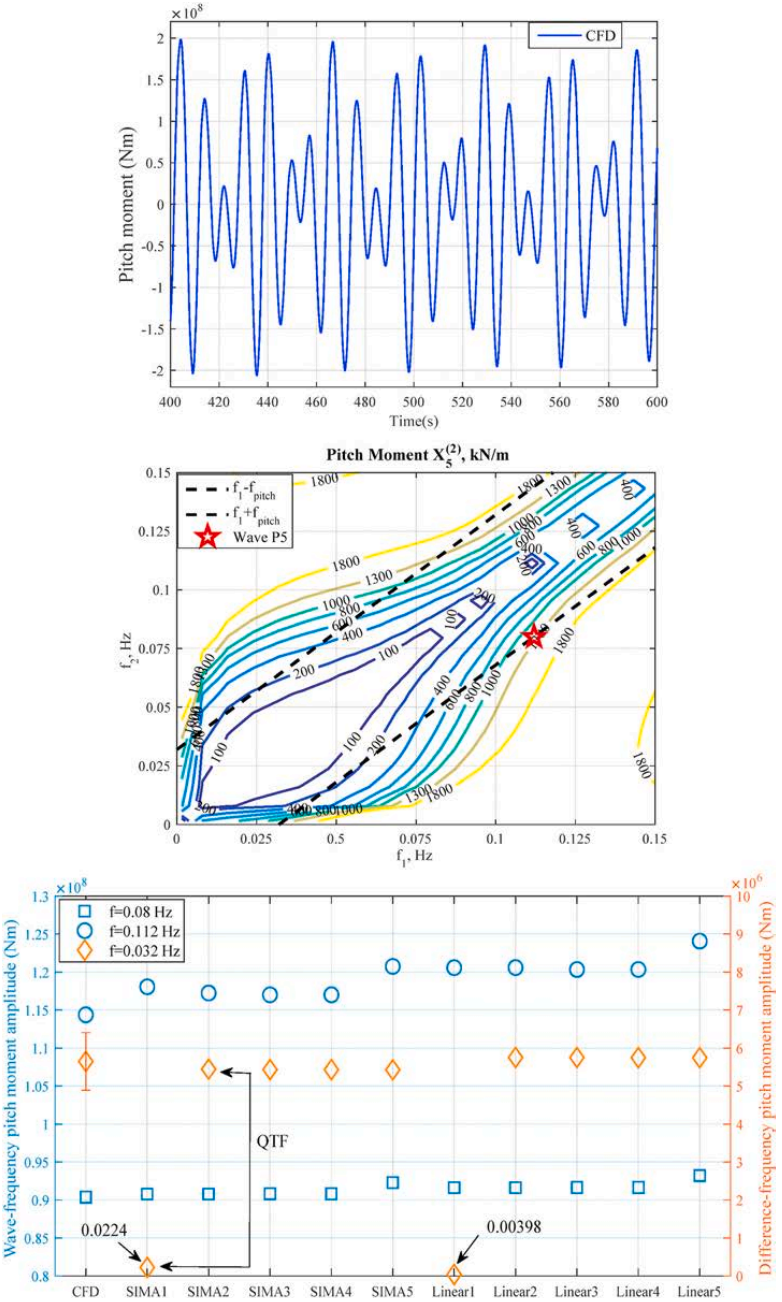

Fig. 9. Pitch moments on the upright floater, Wave P5 (Top: Time series of total pitch moments in CFD simulations, Middle: QTF used in SIMA simulations, Bottom: Pitch moments at the wave frequencies and pitch natural frequency. The uncertainty bar represents the numerical uncertainty of difference-frequency pitch moment, the uncertainty for the wave-frequency pitch moment from CFD can be found in Table 4.).

and ratios in Fig. 10, pitch moments on the trimmed floaters slightly increase both at the first and second wave frequency compared to the upright floater when considering the axial drag forces on the heave plate (SIMA5). Like the surge forces, the effect of changed volume is removed in the comparison of pitch moments shown in the right *y* axis of Fig. 10. Consideration of changed volume leads to a decreasing pitch moment at the second wave frequency under trimmed condition and has minor influence at the first wave frequency in all the numerical simulations.

The pitch moment on the trimmed floater at the pitch natural frequency increases by 1.7% for the CFD model compared to the one under

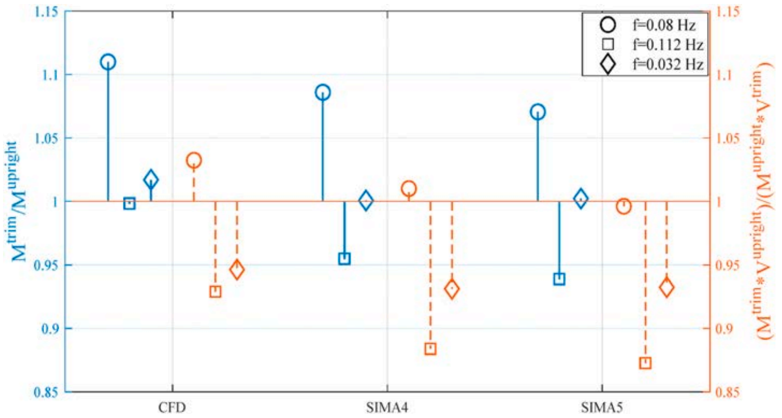

Fig. 10. Comparisons of the pitch moment on the upright and trimmed floaters, Wave P5.

Table 7
Pitch moment amplitudes at the pitch natural frequency, SIMA 2, Wave P5.

	Pitch Moment amplitude (Nm)
Upright position	5.4433E6
Trimmed position	5.4183E6

upright condition. In SIMA models, the effect of 5° mean pitch angle on the pitch moment at the pitch natural frequency is not significant. This is mainly caused by the small change in the contribution from the QTF, which is shown in Table 7. Like the upright condition, the axial drag forces on the heave plates (SIMA5) have minor contributions at the pitch natural frequency. Furthermore, the increase in the pitch moment at the pitch natural frequency is smaller than the increase in the submerged volume.

5.2. *Comparisons and modifications of QTFs in bichromatic waves*

As shown in Table 1, 24 sets of bichromatic waves were selected to calculate the QTFs of a restrained upright semi-submersible FWT and modify the QTFs from potential flow theory. The QTFs before modification are presented in Sec. 5.2.1, while modifications are presented in Sec. 5.2.2, and the validations in an irregular wave are shown in Sec. 5.3.

5.2.1. *Initial QTF comparisons*

Using the approach from Sec. 4.2, the magnitudes of surge force and pitch moment QTFs are calculated based on different numerical models and presented in Fig. 11. CFD and SIMA5 model agree well at the lower wave frequencies, while the CFD model predicts larger difference-frequency wave loads at higher wave frequencies. The contributions of the difference-frequency wave by linear wave force transfer function (SIMA1) are negligible in the low-frequency range except for the surge forces at the pitch natural frequency. For the surge forces at the surge natural frequency, the contributions of Morison drag forces (differences between SIMA2 and SIMA5) decrease with increasing wave frequencies, while the influences of Morison drag forces on the surge forces at the pitch natural frequency are not significant. In addition, the pitch moments from the QTFs (SIMA2 vs SIMA5) dominate in the low-frequency range in the SIMA model.

5.2.2. *QTF modification*

Prior to following the modification procedure from Sec. 4.3, several effects must be treated specially. In the SIMA model, viscous effects are considered by a Morison-type load model. Furthermore, the difference-frequency wave components (from treating the CFD-generated wave elevation as linear) also contribute to the difference-frequency wave loads through the linear wave force transfer function. Hence, these two effects are removed from the QTFs estimated from CFD simulations. The CFD results after subtracting these effects are referred to as 'New QTF'. 'Old QTF' is the QTFs estimated in WAMIT. Assuming that the Morison model captures the viscous effects up to third order and that even higher order effects are small, the 'New QTFs' are directly applied in the validation against the irregular wave (Section 5.3) even though the wave height in the bichromatic wave conditions (Table 1) differs from the wave height in the irregular-wave spectrum (7.1 m).

The magnitudes and phases of surge force and pitch moment QTFs estimated based on the CFD results are compared with the potential flow theory calculations in Fig. 12. At the lower wave frequencies (generally <0.1 Hz), there is little discrepancy between CFD and potential flow theory in predicting the magnitudes of surge force and pitch moment QTFs. However, a larger difference is observed at higher wave frequencies (generally >0.1 Hz) with the CFD model giving larger magnitudes. For the phase of surge force and pitch moment QTFs, the CFD model gives approximately the opposite phase compared to the potential flow theory, which illustrates the limitation of the engineering tools in accurately estimating the phase of difference-frequency wave loads. This large discrepancy cannot be captured by tuning the Morison drag term, which simply changes the results 90° out of phase.

The magnitudes and phases of modified surge force QTFs in the low-frequency range are presented together with the QTFs from potential flow theory in Fig. 13. Close to the surge natural frequency, the new QTFs have smaller magnitudes for lower incident wave frequencies (0.05–0.09 Hz). For higher incident wave frequencies, the new QTFs have higher magnitudes. Furthermore, for low incident wave frequencies, the phase is approximately opposite compared to the phase of QTFs from potential flow theory.

The comparisons of pitch moment QTFs in the low-frequency range are presented in Fig. 14. Compared to the QTFs from potential flow theory, the modified QTFs have similar shape and magnitude except for the larger values at the higher wave frequencies. Like the surge force QTFs, the modified pitch moment QTFs have almost opposite phases compared to the QTFs from potential flow theory. Furthermore, the modified QTFs have a bigger gradient in the phase around the mean drift moment diagonal. The phase of QTFs from potential flow theory has a local peak/trough around the pitch natural frequency. However, this local peak/trough is transferred to the regions between surge and pitch natural frequencies in the modified QTFs due to the approach applied in the QTF modification.

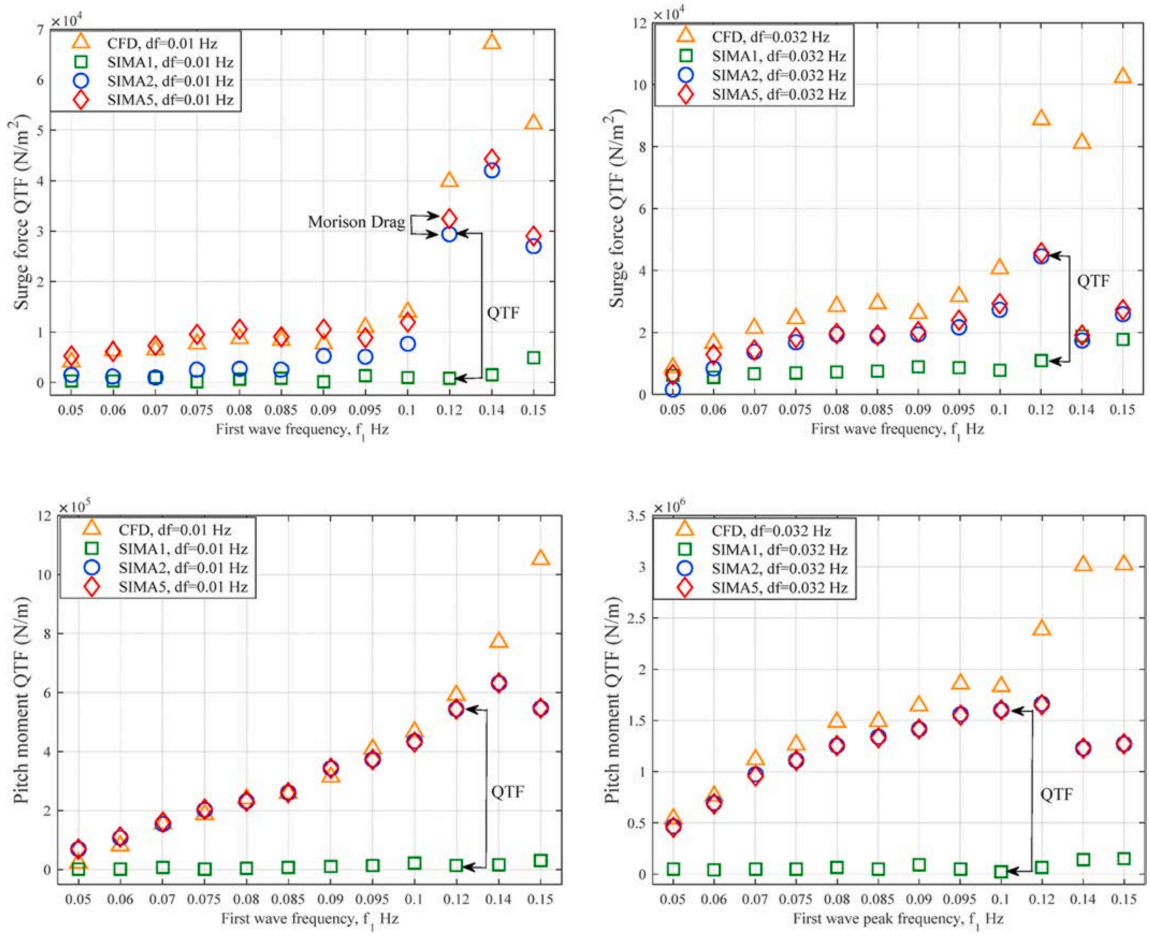

Fig. 11. The magnitudes of surge force and pitch moment QTFs at different wave frequencies (Top: Surge force QTF at the surge (left) or pitch (right) natural frequency, Bottom: Pitch moment QTF at the surge (left) or pitch (right) natural frequency).

To check the implementation of the QTF modification, the difference-frequency wave loads predicted by the SIMA model with modified QTFs (SIMA6) in bichromatic waves are compared against the CFD results in Fig. 15. The difference-frequency wave loads estimated by the SIMA model with modified QTFs (SIMA6) are, as expected, close to the CFD results. There is a better agreement among different numerical models at the surge natural frequency compared to the results at the pitch natural frequency. In the current study, the bichromatic waves are chosen such that the difference corresponds to the surge or pitch natural frequency. Hence, there is a lack of CFD results in the upper-left and lower-right corners of QTF matrix (Fig. 3), which leads to a slightly larger difference at the pitch natural frequency. The largest difference occurs when estimating the wave loads at the pitch natural frequency with the maximum first wave frequency (0.15 Hz). Here, the second wave frequency is 0.182 Hz, close to the maximum frequency (0.185 Hz) in the QTFs from WAMIT. The uncorrected data between 0.182 Hz and 0.185 Hz can explain the difference. Overall, around the peak frequencies of the irregular wave in Sec. 5.3 (0.083 Hz), the numerically estimated difference-frequency wave loads by SIMA model with modified QTFs agree well with CFD results.

5.3. *Validation of modified QTFs against experimental data*

In this part, the experimentally measured wave elevation at the origin is input into SIMA software by a high-pass filter with a 0.008 Hz cut-off frequency. In order to assess the capability of modified QTFs in estimating the difference-frequency wave loads, a response metric (referred to ‘PSD sum’) is adopted in the current study based on work from Robertson et al., (2020). The ‘PSD sum’ is an integration of the force or moment spectrum in the low-frequency range. The frequency limits for the integration are 0.005–0.05 Hz.

The numerically estimated difference-frequency surge forces in SIMA model with modified QTFs (SIMA6) and QTFs from WAMIT (SIMA5) are compared against experimental measurements in Fig. 16. Compared to the results with QTFs from WAMIT, the difference-frequency surge force estimated by the modified QTFs agrees better with the experiment data. However, around the surge natural frequency, the modified QTFs still underpredict the wave loads. As shown in the right subplot of Fig. 16, the difference-frequency surge force PSD sums are calculated for both experimental and numerical results. The improvement using the modified QTFs is significant. The underestimation of the PSD sum is reduced to 2.34% for modified QTFs from 55.07% for the QTFs from WAMIT. This validation also indicates that the CFD model can give better

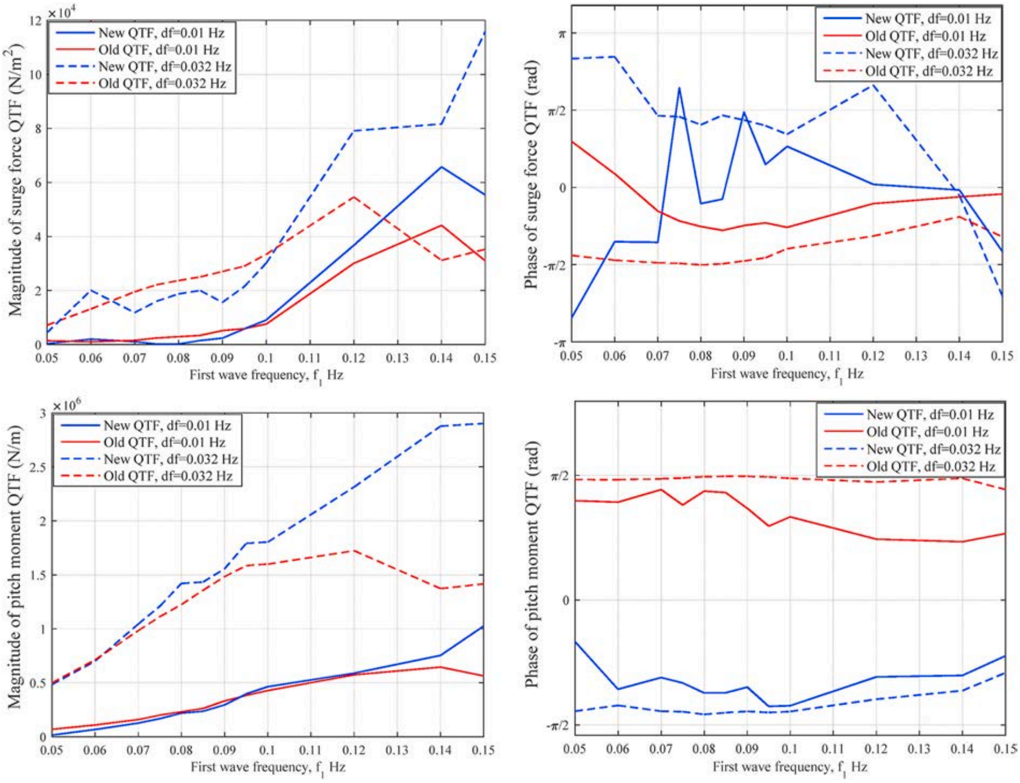

Fig. 12. The magnitudes and phases of the calculated QTFs at the surge and pitch natural frequency based on CFD simulations and potential flow theory.

estimation of difference-frequency surge forces, but has limitations in capturing the surge forces at even lower frequencies.

The numerically estimated difference-frequency pitch moments are compared against experimental measurements in Fig. 17. Like the modified surge force QTFs, there is a better agreement of difference-frequency pitch moment between experiment and SIMA model with the modified QTFs (SIMA6). Compared to the experimental results, the difference-frequency pitch moment PSD sum with modified QTFs is 11.91% smaller while the result with the QTFs from WAMIT is 42.71% smaller.

Overall, one can conclude that the SIMA with modified QTFs (SIMA6) can better capture difference-frequency wave loads than the QTFs from potential flow theory. This also demonstrates the advantages of the CFD model in capturing the nonlinear difference-frequency wave loads. The more CFD simulations at different sets of frequencies are carried out, the more accurate the modified QTFs are, and the better the difference-frequency wave loads are captured by SIMA models with modified QTFs.

5. Conclusions

In the current work, two numerical models are used to study the nonlinear difference-frequency wave loads on a restrained semi-submersible FWT in bichromatic waves: a CFD model and a potential flow theory model with Morison-type drag (SIMA). Furthermore, the results from CFD model are used to modify the QTFs from potential flow theory, and the resulting model is validated against experimental data in an irregular wave.

The wave loads from CFD and the potential flow model are in good agreement at the wave frequencies. In the SIMA model, the difference-frequency surge force at the surge natural frequency is mainly from the integration of Morison drag force to the linear free surface. This contribution decreases with increasing wave frequencies, and the surge force from QTFs becomes dominant. At the pitch natural frequency, the pitch moment from QTFs is dominant. In addition, the axial drag forces on the heave plates only increase the pitch moment at the wave frequencies and have minor contributions to the difference-frequency wave loads.

In order to better understand the effects of the multimember arrangement of the semi-submersible floater, surge forces on each column are extracted. Compared to the CFD results, SIMA underpredicts the difference-frequency surge forces on each column and a larger underprediction is seen at the lower part of the columns. In addition, in the CFD simulations, the surge forces at the surge natural frequency on the starboard column are smaller than those on the upstream column and a larger reduction is found at the lower part of columns.

The effects of 5° mean pitch angle during wind turbine operation on the difference-frequency wave loads are also investigated. The wave loads are calculated based on the global coordinate system used in upright condition. The variations at the wave frequencies are mostly due to the changed immersed geometry and correspondingly changed first-order hydrodynamic properties of the floater. At the surge natural frequency, there is an increase in surge force in both CFD and the potential flow model, but the increase in the CFD model is more significant. The pitch moments under the trimmed condition are not significantly changed compared to the upright floater. However, the effects of trim on the motions and loads in the mooring system of FWTs are of still interest in the future research.

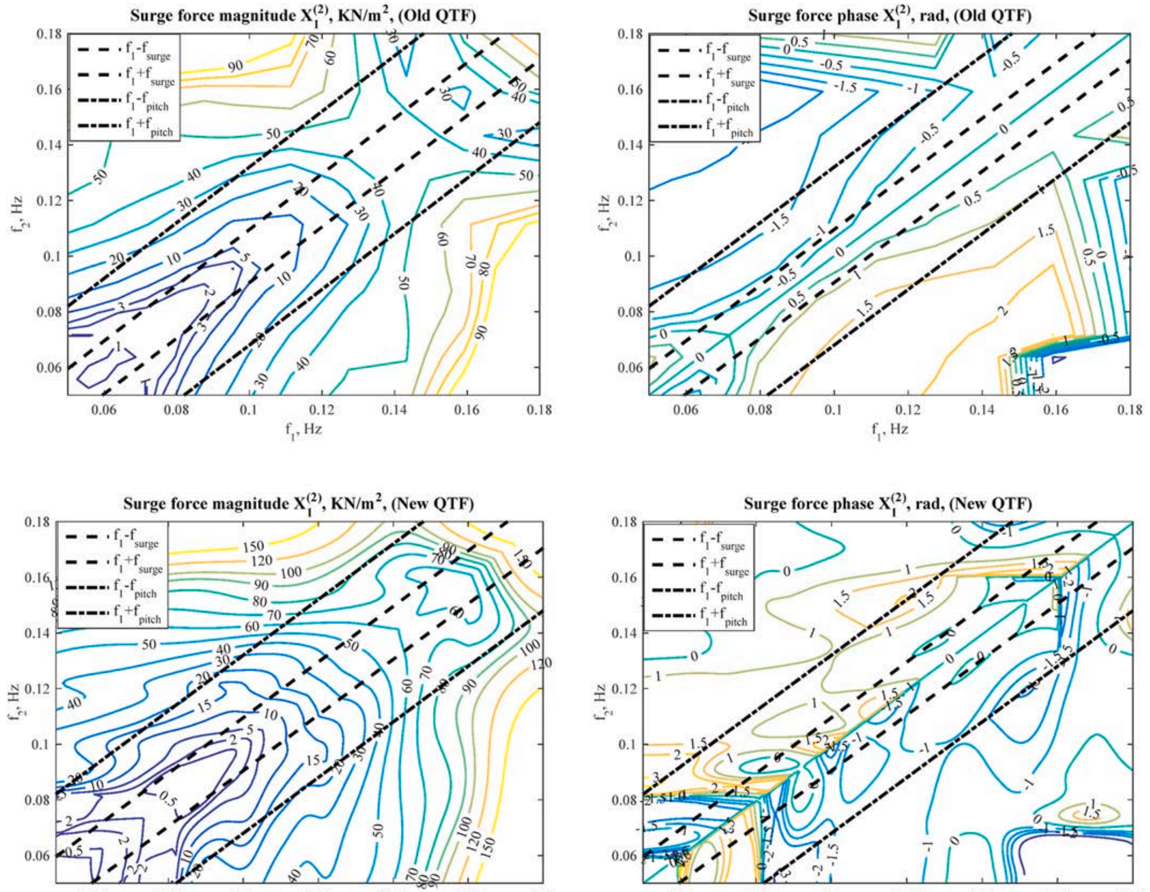
Surge force magnitude $X_1^{(2)}$, KN/m^2, (Old QTF)

Surge force phase $X_1^{(2)}$, rad, (Old QTF)

Surge force magnitude $X_1^{(2)}$, KN/m^2, (New QTF)

Surge force phase $X_1^{(2)}$, rad, (New QTF)

Fig. 13. Magnitudes and phases of surge force QTFs in the low-frequency range.

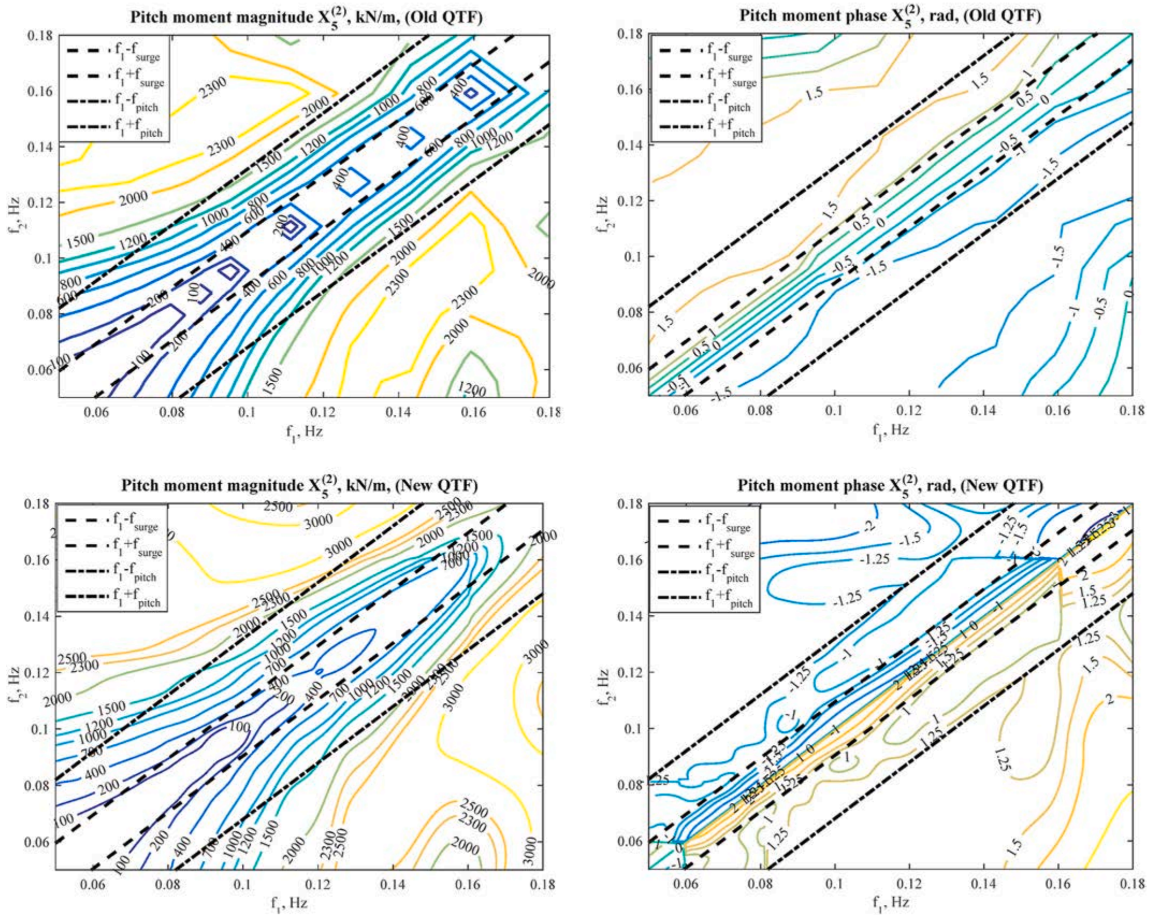

Fig. 14. Magnitudes and phases of pitch moment QTFs in the low-frequency range.

When modifying the QTFs based on CFD simulations, larger modifications in the magnitude are seen to be required at higher wave frequencies. Interestingly, the CFD model gives approximately the opposite phase compared to the original potential flow results. The modification of the QTFs is verified by checking that difference-frequency wave loads estimated by the SIMA model with modified QTFs are close to the CFD

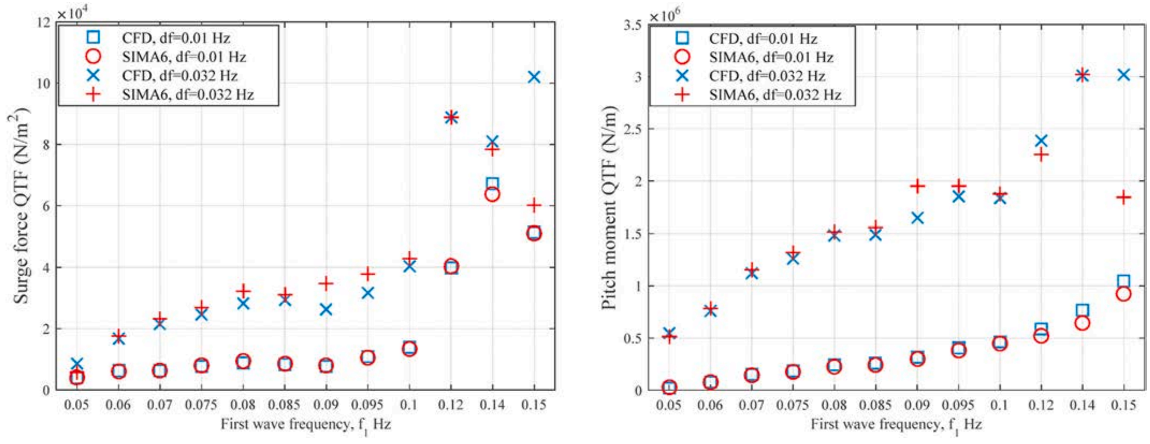

Fig. 15. Difference-frequency wave loads estimated in CFD model and SIMA model with modified QTFs.

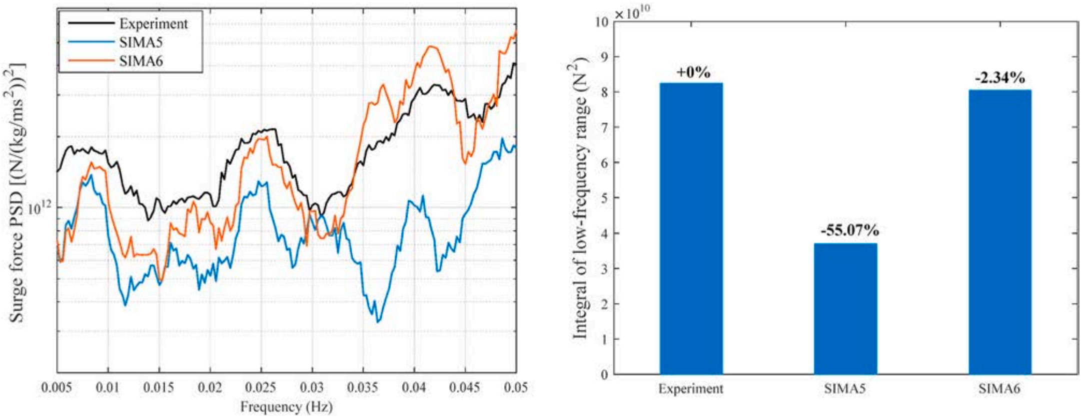

Fig. 16. Difference-frequency surge force in an irregular wave (left: surge force spectra in low-frequency range, right: difference-frequency surge force PSD sum metric).

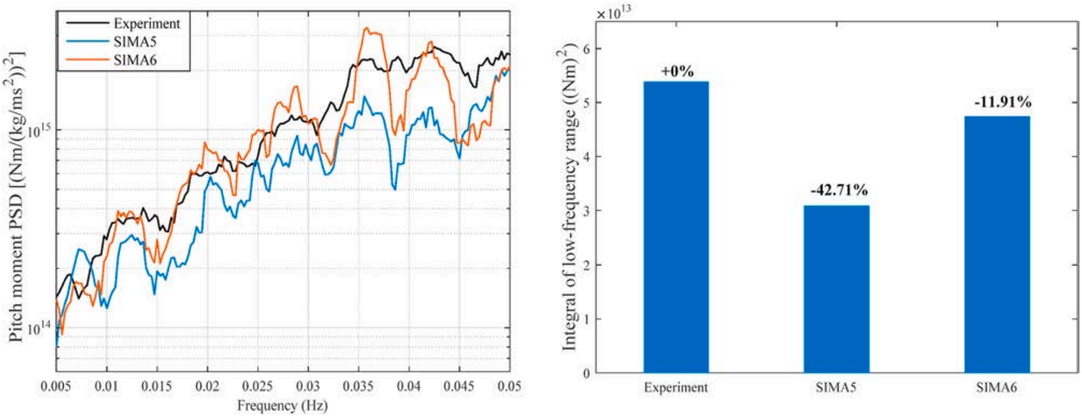

Fig. 17. Difference-frequency pitch moment in an irregular wave (left: pitch moment spectra in low-frequency range, right: difference-frequency pitch moment PSD sum metric).

results in bichromatic waves. The approach is then compared to experimental measurements of difference-frequency wave loads in an irregular wave. The modified QTFs significantly reduce underprediction of difference-frequency wave loads compared to the QTFs from potential flow theory.

CRediT authorship contribution statement

Haoran Li: Conceptualization, Methodology, Software, Validation, Investigation, Formal analysis, Data curation, Writing – original draft. **Erin E. Bachynski-Polić:** Conceptualization, Methodology, Resources, Writing – review & editing, Supervision.

Declaration of competing interest

The authors declare that they have no known competing financial interests or personal relationships that could have appeared to influence the work reported in this paper.

Acknowledgements

The author Haoran Li gratefully acknowledges the financial support from China Scholarship Council (CSC). Computing time on Vilje is granted by the Norwegian Research Council (Program for Supercomputing, under project nn9676k). The discussions with Prof. Trygve Kristiansen are greatly appreciated.

References

Bachynski, E.E., Thys, M., et al., 2016. Real-time Hybrid Model Testing of a Braceless Semi-submersible Wind Turbine: Part II—Experimental Results. ASME 2016 35th International Conference on Ocean, Offshore and Arctic Engineering. American Society of Mechanical Engineers Digital Collection.

Benitz, M.A., Schmidt, D.P., et al., 2014. Comparison of Hydrodynamic Load Predictions between Reduced Order Engineering Models and Computational Fluid Dynamics for the OC4-DeepCwind Semi-submersible. No. NREL/CP-5000-61157. ASME 2014 33rd International Conference on Ocean, Offshore and Arctic Engineering. American Society of Mechanical Engineers Digital Collection.

Benitz, M.A., Schmidt, D.P., et al., 2015. Validation of Hydrodynamic Load Models Using CFD for the OC4-DeepCwind Semisubmersible. No. NREL/CP-5000-63751. ASME 2015 34th International Conference on Ocean, Offshore and Arctic Engineering. American Society of Mechanical Engineers Digital Collection.

Berberović, E., van Hinsberg, N.P., et al., 2009. Drop impact onto a liquid layer of finite thickness: dynamics of the cavity evolution. Phys. Rev. 79 (3), 036306.

Berthelsen, P.A., Bachynski, E.E., et al., 2016. Real-time Hybrid Model Tests of a Braceless Semi-submersible Wind Turbine: Part III—Calibration of a Numerical Model. ASME 2016 35th International Conference on Ocean, Offshore and Arctic Engineering. American Society of Mechanical Engineers Digital Collection.

Brown, S.A., Magar, V., et al., 2014. An evaluation of RANS turbulence closure models for spilling breakers. Coastal Engineering Proceedings (34), 5-5.

Bruinsma, N., Paulsen, B., et al., 2018. Validation and application of a fully nonlinear numerical wave tank for simulating floating offshore wind turbines. Ocean. Eng. 147, 647–658.

Coulling, A.J., Goupee, A.J., et al., 2013. Importance of Second-Order Difference-Frequency Wave-Diffraction Forces in the Validation of a FAST Semi-submersible Floating Wind Turbine Model. No. NREL/CP-5000-57697. ASME 2013 32nd International Conference on Ocean, Offshore and Arctic Engineering. American Society of Mechanical Engineers Digital Collection.

Devolder, B., Rauwoens, P., et al., 2017. Application of a buoyancy-modified k-ω SST turbulence model to simulate wave run-up around a monopile subjected to regular waves using OpenFOAM®. Coast Eng. 125, 81–94.

Dudley Brian, S., 1961. A single formula for the "law of the wall. J. Appl. Mech. 28 (3), 455–458.

Eça, L., Hoekstra, M., 2006. On the Influence of the Iterative Error in the Numerical Uncertainty of Ship Viscous Flow Calculations. 26th Symposium on Naval Hydrodynamics, Rome, Italy.

Eça, L., Hoekstra, M., 2014. A procedure for the estimation of the numerical uncertainty of CFD calculations based on grid refinement studies. J. Comput. Phys. 262, 104–130.

Fan, W., Anglart, H., 2020. varRhoTurbVOF: a new set of volume of fluid solvers for turbulent isothermal multiphase flows in OpenFOAM. Comput. Phys. Commun. 247, 106876.

Fonseca, N., Pessoa, J., et al., 2011. Experimental and numerical investigation of the slowly varying wave exciting drift forces on a restrained body in bi-chromatic waves. Ocean Eng. 38 (17–18), 2000–2014.

Hirt, C.W., Nichols, B.D., 1981. Volume of fluid (VOF) method for the dynamics of free boundaries. J. Comput. Phys. 39 (1), 201–225.

Hu, C., Sueyoshi, M., et al., 2014. Hydrodynamic Analysis of a Semi-submersible Type Floating Wind Turbine. The Eleventh ISOPE Pacific/Asia Offshore Mechanics Symposium. International Society of Offshore and Polar Engineers.

Jacobsen, N.G., Fuhrman, D.R., et al., 2012. A wave generation toolbox for the open-source CFD library: OpenFoam®. Int. J. Numer. Methods Fluid. 70 (9), 1073–1088.

Launder, B.E., Spalding, D.B., 1983. The Numerical Computation of Turbulent Flows. Numerical Prediction of Flow, Heat Transfer, Turbulence and Combustion. Elsevier, pp. 96–116.

Lee, C.-H., 1995. WAMIT Theory Manual. Massachusetts Institute of Technology, Department of Ocean Engineering.

Li, H., Bachynski, E.E., 2021. Experimental and numerical investigation of nonlinear diffraction wave loads on a semi-submersible wind turbine. Renew. Energy: Accepted for publication 171, 709–727.

Liu, C., Hu, C., 2014. CFD simulation of a floating wind turbine platform in rough sea conditions. In: The Twenty-Fourth International Ocean and Polar Engineering Conference. International Society of Offshore and Polar Engineers.

Lopez-Pavon, C., Watai, R.A., et al., 2015. Influence of wave induced second-order forces in semisubmersible fowt mooring design. J. Offshore Mech. Arctic Eng. 137 (3).

Luan, C., Gao, Z., et al., 2016. Design and Analysis of a Braceless Steel 5-MW Semi-submersible Wind Turbine. ASME 2016 35th International Conference on Ocean, Offshore and Arctic Engineering. American Society of Mechanical Engineers Digital Collection.

Madsen, P.A., Fuhrman, D.R., 2006. Third-order theory for bichromatic bi-directional water waves. J. Fluid Mech. 557, 369–397.

Marintek, 2012. SIMO—Theory Manual Version 4.0. Marintek Trondheim, Norway.

Marthinsen, T., Winterstein, S.R., 1992. On the skewness of random surface waves. In: The Second International Offshore and Polar Engineering Conference. International Society of Offshore and Polar Engineers.

Menter, F., Ferreira, J.C., et al., 2003. The SST turbulence model with improved wall treatment for heat transfer predictions in gas turbines. Proceedings of the international gas turbine congress 1, 2–7.

Menter, F.R., Kuntz, M., et al., 2003. Ten years of industrial experience with the SST turbulence model. Turbulence, heat and mass transfer 4 (1), 625–632.

Ohyama, T., Hsu, J.R., 1995. Nonlinear wave effect on the slow drift motion of a floating body. Appl. Ocean Res. 17 (6), 349–362.

Ormberg, H., Passano, E., 2012. RIFLEX Theory Manual. Marintek, Trondheim.

Pessoa, J., Fonseca, N., 2015. Second-order low-frequency drift motions of a floating body calculated by different approximation methods. J. Mar. Sci. Technol. 20 (2), 357–372.

Pessoa, J.o., Fonseca, N., et al., 2010. Experimental and Numerical Study of the Depth Effect on the First Order and Slowly Varying Motions of a Floating Body in Bichromatic Waves. International Conference on Offshore Mechanics and Arctic Engineering.

Rahman, M.M., Karim, M.M., et al., 2007. Numerical investigation of unsteady flow past a circular cylinder using 2-D finite volume method. J. Nav. Architect. Mar. Eng. 4 (1), 27–42.

Rivera-Arreba, I., Bruinsma, N., et al., 2019. Modeling of a semisubmersible floating offshore wind platform in severe waves. J. Offshore Mech. Arctic Eng. 141 (6).

Robertson, A., Bachynski, E.E., et al., 2020. Total experimental uncertainty in hydrodynamic testing of a semisubmersible wind turbine, considering numerical propagation of systematic uncertainty. Ocean. Eng. 195, 106605.

Robertson, A., Jonkman, J., et al., 2014a. Definition of the Semisubmersible Floating System for Phase II of OC4. No. NREL/TP-5000-60601. National Renewable Energy Lab.(NREL), Golden, CO (United States).

Robertson, A., Jonkman, J., et al., 2014b. Offshore Code Comparison Collaboration Continuation within IEA Wind Task 30: Phase II Results Regarding a Floating Semisubmersible Wind System. No. NREL/CP-5000-61154. ASME 2014 33rd International Conference on Ocean, Offshore and Arctic Engineering. American Society of Mechanical Engineers Digital Collection.

Robertson, A., Jonkman, J., et al., 2016. Definition of the OC5 DeepCwind Semisubmersible Floating System. Technical report NREL.

Robertson, A.N., Gueydon, S., et al., 2020. OC6 Phase I: Investigating the Under-prediction of Floating Wind Turbine Loads at Their Natural Frequencies. The Science of Making Torque from Wind (TORQUE 2020). National Renewable Energy Lab. (NREL), Golden, CO (United States).

Robertson, A.N., Wendt, F., et al., 2017. OC5 project phase II: validation of global loads of the DeepCwind floating semisubmersible wind turbine. Energy Procedia 137, 38–57.

Simos, A.N., Ruggeri, F., et al., 2018. Slow-drift of a floating wind turbine: an assessment of frequency-domain methods based on model tests. Renew. Energy 116, 133–154.

Tom, N., Robertson, A., et al., 2019. Bichromatic wave selection for validation of the difference-frequency transfer function for the OC6 validation campaign. In: International Conference on Offshore Mechanics and Arctic Engineering. American Society of Mechanical Engineers.

Wang, L., Robertson, A., et al., 2021. Investigation of nonlinear difference-frequency wave excitation on a semisubmersible offshore-wind platform with bichromatic-wave CFD simulations. In: Proceedings of the ASME 2020 3rd International Offshore Wind Techanical Conference. Boston, MA, USA.

Weller, H.G., Tabor, G., et al., 1998. A tensorial approach to computational continuum mechanics using object-oriented techniques. Comput. Phys. 12 (6), 620–631.

Wilcox, D.C., 1998. Turbulence Modeling for CFD. DCW industries La Canada, CA.

B.3 Paper 3

Paper 3:

Haoran Li and Erin E. Bachynski-Polić. Experimental and numerically obtained low-frequency radiation characteristics of the OC5-DeepCwind semisubmersible. *Ocean Engineering* 2021; **232**:109130. `https://doi.org/10.1016/j.oceaneng.2021.109130`

Ocean Engineering 232 (2021) 109130

Contents lists available at ScienceDirect

Ocean Engineering

journal homepage: www.elsevier.com/locate/oceaneng

Experimental and numerically obtained low-frequency radiation characteristics of the OC5-DeepCwind semisubmersible

Haoran Li [a,*], Erin E. Bachynski-Polić [a,b]

[a] Department of Marine Technology, Norwegian University of Science and Technology (NTNU), Trondheim, Norway
[b] Centre for Autonomous Marine Operations and Systems (AMOS), NTNU, Trondheim, Norway

ARTICLE INFO

Keywords:
Semi-submersible floating wind turbine
CFD
OpenFOAM
Potential flow theory
Added mass
Hydrodynamic damping

ABSTRACT

Added mass and damping play a significant role in accurate prediction of floating wind turbine (FWT) motions, especially near the resonance frequencies. This paper investigates the still-water hydrodynamic characteristics of a semi-submersible FWT around the natural periods of surge, heave and pitch motion. A higher-fidelity tool (Computational Fluid Dynamics, CFD) based on OpenFOAM is employed in the numerical computations. The tool is validated against experimental measurements (decay tests and forced surge motions) and then applied to investigate the hydrodynamic characteristics of the whole floater and each column at different amplitudes of forced motions. The heave and pitch decay match well with the experimental measurements, whereas the CFD simulations underestimate the damping in the surge decay. However, better agreement is obtained between measured and numerically estimated surge force in the forced oscillations in surge. Furthermore, the added mass derived from the CFD simulation is around 12% larger than that estimated by the potential flow theory, except the estimated heave added mass under the largest heave motion (up to 35% larger). This additional added mass in the CFD simulations is due to the viscous effects. The damping shows a small dependence on the oscillation period and a larger dependence on the oscillation amplitude within the tested period range. At these frequencies, radiation damping is completely negligible compared to the viscous damping due to vortex shedding, and the accuracy of Morison's drag forces in capturing the viscous damping is sensitive to the drag coefficient.

1. Introduction

As a promising way of harnessing the energy from winds over deep water and farther offshore, floating wind turbines (FWTs) have gained more and more attentions in recent years, especially semi-submersible FWTs (Peiffer et al., 2011). One type of semi-submersible FWTs consists of four cylindrical columns linked with a set of braces (Robertson et al., 2014, 2016). In order to reduce the amplitude of the heave resonance and move the heave resonance periods outside the wave frequency range, heave plates are attached to the base of some columns. These plates provide additional added mass and enhance the flow separation and vortex shedding processes that provide viscous damping (WEI et al., 2010). All these factors reduce the floater motions, but also generate more stringent requirements for the fidelity of simulation tools. Most approaches use potential flow theory and Morison's equation to evaluate the hydrodynamic forces on the floater (Cordle and Jonkman, 2011). However, in Phase II of the OC5 Project (Robertson et al., 2017), these approaches significantly underestimated the wave-induced floater motions at the natural frequencies outside the linear wave-excitation region. These results suggest that better models are needed for the hydrodynamic coefficients for nonlinear wave excitation. In the present work, the focus is on the added mass or damping coefficient for different motion amplitudes and periods.

The hydrodynamic coefficients in still water are characterized by two parameters: the motion amplitude and period. The nondimensional parameters are then the Keulegan-Carpenter (KC) number and the Stokes number β. Alternatively, one of the control parameters can be replaced by the Reynolds number ($Re = KC \cdot \beta$).

Cozijn et al. (2005) performed experiments with a buoy with a skirt to investigate the heave, roll and pitch damping and found that the heave and pitch damping contain linear and quadratic components, where KC is in the range of 2–5 and β is from 76,923 to 200,000. Moreno et al. (2015), Philip et al. (2019) and Nallayarasu et al. (2014) experimentally investigated the hydrodynamic coefficients of heave plates on a spar platform at small KC (0.2–1) and high β (up to 31,250) values. The added mass and damping increased with KC number, independent of

---

* Corresponding author.
E-mail address: haoran.li@ntnu.no (H. Li).

https://doi.org/10.1016/j.oceaneng.2021.109130
Received 8 December 2020; Received in revised form 24 March 2021; Accepted 5 May 2021

frequency except for the increasing damping coefficients towards larger frequency at higher frequencies. For the hydrodynamic coefficients of heave plates of a semi-submersible FWT, Lopez-Pavon et al. (2015) also confirmed there is a relatively weak dependence on oscillation frequencies, and a large dependence on KC number, considering KC from 0.3 to 0.86 and Re from 79,695 to 446,294.

Model tests are the main means to study the hydrodynamic characteristics of FWTs, but due to limitations of the test conditions and accuracy of the test equipment, the conclusions of Chua et al. (2005) are not completely consistent with the results of Tao and Dray (2008) when investigating the effect of oscillation frequency on the damping of heave plate under similar KC (0.2–1.2) and β (16,000-160,000) values. Therefore, a series of numerical studies of hydrodynamic coefficients of FWT have been conducted.

Based on offshore oil and gas industry experience, Borg et al. (2013) and Lefebvre et al. (2012) suggested that the additional damping ratio generated by the vortex shedding is from 10% to 15%. Lopez-Pavon et al. (2015) computed, with a CFD commercial code (ANSYS CFX) and frequency domain panel method (WADAM), the hydrodynamic characteristics on heave plates of a semi-submersible FWT, and found added mass and damping were largely dependent on the motion amplitude. Furthermore, WADAM did not predict the increased added mass due to the edge of heave plates, especially for larger KC values. Bozonnet et al. (2015) used CFD tool OpenFOAM to calibrate and validate added mass and drag coefficients for a platform encompassing heave plates, where KC is in the range of 0.36–1.07 and β is from 8.80E+07 to 2.77E+08. The added mass was found to be slightly larger than the one predicted by potential flow theory and viscous effects were predominant in the damping term. The influence of different shapes of heave plates on hydrodynamic coefficients at small KC value (0.06–0.25) with β = 1.1E+08 were investigated by Wang et al. (2020). The results showed the added mass coefficient increases with KC number whereas the damping coefficient decreases with KC number for all types of heave plates. Zhang et al. (2018) examined the hydrodynamic coefficients of multiple heave plates by large eddy simulations with volume of fluid method and found that an accurate simulation of the unsteady flow separation around the sharp edges of the heave plates was essential for accurately predicting the drag coefficient.

The above numerical simulations studied the hydrodynamic coefficients using forced oscillation tests; free decay is another approach to estimate the hydrodynamic damping around the natural periods. Burmester et al. (2017, 2020b) investigated the surge decay of a moored semi-submersible FWT using CFD methods. The results showed the linear damping was largely influenced by the free surface and coupled motions increased the linear and quadratic damping slightly. Dunbar et al. (2015) compared the discrepancy of heave and pitch decay of a semi-submersible FWT between CFD methods and engineering tools and found the discrepancy is associated with Reynolds-number-dependent viscous effects.

Most existing studies focus on the hydrodynamic characteristics associated with one cylindrical column attached with a very thin heave plate. That is not completely consistent with the configuration of a semi-submersible FWT whose heave plate has a certain thickness (Robertson et al., 2016). The possible mutual effects of different columns have not been considered in the studies of one cylindrical column. In addition, little attention has been paid to the hydrodynamic characteristics at large KC value and longer period, such as natural periods of rigid-body motions of FWTs. Therefore, it is interesting to examine the hydrodynamic characteristics of a semi-submersible FWT at different KC numbers around the natural periods of rigid-body motions and to understand the variations of hydrodynamic characteristics among different columns.

In this study, a CFD model of a semi-submersible FWT is validated against experimental measurements including free decay and forced oscillation in surge. Then, several forced oscillations with different motion amplitudes around the surge, heave and pitch natural periods are performed using the validated numerical model to identify the added mass and damping coefficients on the whole floater. In addition, hydrodynamic characteristics on each column are extracted to better understand the effects of the multimember arrangement of the semisubmersible. Meanwhile, a potential flow model is used to estimate the added mass and damping coefficients and compare with the CFD model. The objective of this paper is to provide improved knowledge about the hydrodynamic characteristics of a semi-submersible FWT that can be potentially applied in engineering tools.

The organization of this paper is as follows. Section 2 describes the experimental setup. The CFD tool is described in Sec. 3 together with an introduction of the frequency domain panel method in WADAM based on potential flow theory. Numerical results of surge, heave and pitch decay are compared to the experimental data in Sec. 4, while the added mass and damping estimated by the forced oscillations are analyzed in Sec. 5. Conclusions are drawn in Sec. 6.

2. Experiment set up

In the present work, experimental data are from Phase I of the Offshore Code Comparison Collaboration, Continued, with Correlation, and unCertainty (OC6) project (Robertson et al., 2020b). The experiments were conducted in the concept basin of the Maritime Research Institute Netherland (MARIN) for the OC5-DeepCwind semi-submersible floater (Robertson et al., 2016) at 1:50 scale. The right-handed coordinate system used here originates at the center of the floater at the still water line, with positive y towards the starboard column, and z upward. All data and results are given at full scale in this paper, except when explicitly mentioned.

For the configuration of free decay shown in Fig. 1, the wind turbine was removed, but the inertial properties of the floater with tower correspond to the total inertial properties of OC5 system. The mooring system was replaced with 3 taut-spring-lines to reproduce the equivalent linear response behavior of the original catenary system. Robertson et al. (2020a, 2020b) provide the dimensions and structural properties of the platform and the configuration of the mooring lines. The global motions, including surge (x-displacement), heave (z-displacement) and pitch (y-rotation), were measured. The initial offsets for the surge, heave and pitch decay are given in Table 1.

For forced oscillation, the wind turbine and tower were removed, and the floater was attached to the carriage through a frame (Fig. 2). The floater was forced to oscillate in the surge (x-direction). Total forces on the floater were measured using a six-component gauge installed between the frame and floater. The details of the forced oscillation tests are provided in Table 2. Assuming the frequency of the radiated wave is the oscillation frequency, the length of the radiated wave can be obtained by the dispersion relation. The ratios between oscillation amplitudes (A) and radiated wave lengths (L) are given in Table 2.

3. Numerical model

3.1. CFD model

High-fidelity numerical simulations are performed with the open-source CFD toolbox OpenFOAM (Weller et al., 1998). The multiphase interDyMFoam solver is a fluid-structure interaction solver, where the Navier-Stokes and 6-degree of freedom (DOF) equations are solved in a coupled manner. The standard interDyMFoam with wave absorption toolbox waves2Foam (Jacobsen et al., 2012) is referred to as the waveDyMFoam solver, which is applied in the current research.

3.1.1. Governing equations

The waveDyMFoam solver utilizes the two-phase incompressible Reynolds-averaged Navier–Stokes equations (RANS) to compute the fluid-structure interaction. The governing equations consist of a mass and a momentum conservation equation, expressed as:

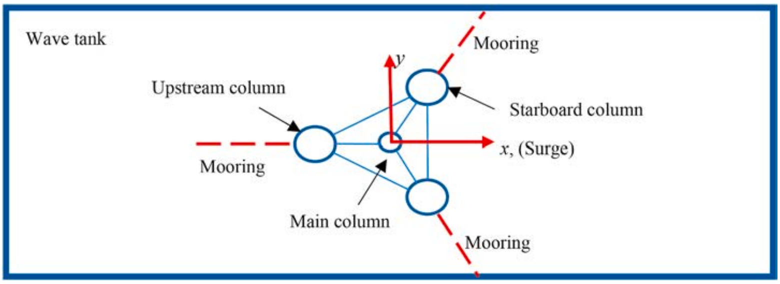

Fig. 1. The free decay configuration.

Table 1
Specifications for free decay tests in the experiments.

Load case	Mode	Initial offset
LC1.1	Surge	−1.86 m
LC1.2	Heave	−1.06 m
LC1.3	Pitch	−2.21°

$$\frac{\partial u_i}{\partial x_i} = 0 \tag{1}$$

$$\frac{\partial \rho u_i}{\partial t} + \frac{\partial \rho u_j u_i}{\partial x_j} = -\frac{\partial p^*}{\partial x_i} + F_{b,i} + \frac{\partial}{\partial x_j}\left[\mu_{eff}\frac{\partial u_i}{\partial x_j}\right] \tag{2}$$

where u_i $(i = x, y, z)$ are the fluid velocity in Cartesian coordinates, ρ is the fluid density, p^* is the pressure in excess of the hydrostatic pressure, $F_b$is the external body force including the gravity and mooring forces, and μ_{eff} is the effective dynamic viscosity.

The interface between air and water is tracked by the volume of fluid (VOF) method (Hirt and Nichols, 1981). The local fluid density ρ within a computational cell is calculated by the volume fraction α: for water $\alpha = 1$, for air $\alpha = 0$, and $0 < \alpha < 1$for all the intermediate values. The effective dynamic viscosity μ_{eff} is obtained by the sum of a calculated value based on the volume fraction and an additional turbulent dynamic viscosity $\rho\nu_t$:

$$\rho = \alpha\rho_{water} + (1-\alpha)\rho_{air} \tag{3}$$

Table 2
Specifications for surge forced oscillation in the experiment. L represents the wavelength of a linear wave at the oscillation period.

Load case	Amplitude, A(m)	Period (s)	A/L
LC2.1	30.07	104.5	1.75E-3
LC2.2	9.54	31.2	6.21E-3
LC2.3	3.37	21.0	4.93E-3

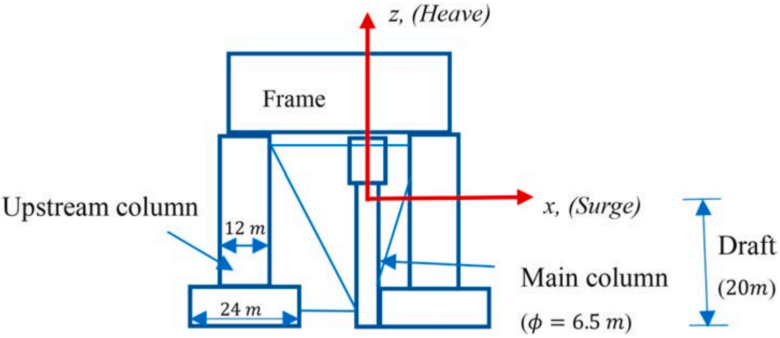

Fig. 2. The experimental configuration for forced oscillation.

Table 3
Specifications for forced oscillations in the CFD model.

Surge forced oscillation			Heave forced oscillation			Pitch forced oscillation		
T	A	A/L	T	A	A/L	T	A	A/L
(s)	(m)	(-)	(s)	(m)	(-)	(s)	(rad)	(rad/m)
200	1.91	3.06E-5	18.94	0.955	1.70E-3	37.04	0.068	3.17E-5
	3.82	6.12E-5		3.82	6.82E-3		0.136	6.35E-5
	7.64	1.22E-4		7.64	1.36E-2		0.273	1.27E-4
105	1.91	1.11E-4	17.30	0.955	2.04E-3	31.25	0.068	4.46E-5
	3.82	2.22E-4		3.82	8.17E-3		0.136	8.92E-5
	7.64	4.44E-4		7.64	1.63E-2		0.273	1.79E-4
66.67	1.91	2.75E-4	15.93	0.955	2.41E-3	27.03	0.068	5.96E-5
	3.82	5.50E-4		3.82	9.64E-3		0.136	1.19E-4
	7.64	1.10E-3		7.64	1.93E-2		0.273	2.39E-4

$$\mu_{eff} = \alpha\mu_{water} + (1-\alpha)\mu_{air} + \rho\nu_t \tag{4}$$

After the velocity field is known, the volume fraction is advanced in time by an advection equation:

$$\frac{\partial\alpha}{\partial t} + \frac{\partial u_i\alpha}{\partial x_i} + \frac{\partial u_{r,i}\alpha(1-\alpha)}{\partial x_i} = 0 \tag{5}$$

The last term on the left-hand side of Eq. (5), u_r, is introduced as an artificial compression term to decrease the smearing of the interface. It is only active in the vicinity of the interface, $0 < \alpha < 1$ (see Berberović et al. (2009) for details). A multi-dimensional flux limited scheme is applied to ensure stability.

The $k-\omega$ SST turbulence model (Menter et al., 2003b) is applied, consisting of a blending of the $k-\omega$ (Wilcox, 1998) and the $k-\ \varepsilon$ (Launder and Spalding, 1983) models. This model has shown good performance in simulating two-phase flow and wave elevation (Brown et al., 2014; Rahman et al., 2007), as discussed by Menter et al. (2003a). For the two-phase fluid in OpenFOAM, there is significant wave damping in the interface between air and water induced by increasing turbulent viscosity (Devolder et al., 2017; Fan and Anglart, 2020) when using this turbulence model. Hence, a modified waveDyMFoam solver is built to explicitly consider the variable density in the $k-\ \omega$ SST model (Fan and Anglart, 2020).

3.1.2. Boundary conditions

To solve the governing equations, boundary conditions are imposed on all the surfaces in the numerical domain. The general denomination of boundary surfaces is given in Fig. 3.

- At the inlet and outlet, the velocity, α field and the pressure are specified as zero normal gradient. The turbulent kinetic energy k and the specific dissipation rate ω are set as zero normal gradient.
- On the floater surface, a no-slip boundary condition (zero velocity) is specified, and the pressure is set as zero normal gradient. k is fixed at 1e-5 m^2/s^2 and ω is set as 1.0 1/s.
- For the atmosphere, the total pressure is set as zero and an atmospheric boundary condition is set for the velocity and α field. This means that air and water are allowed to leave the numerical domain, while only air is allowed to flow back in. k is fixed at zero and ω is specified as zero normal gradient.
- At the front, back and bottom of the domain, all the conditions are set as zero normal condition. Different k and ω values at floater and other boundaries are applied to accurately simulate the flow around the floater and reduce the influences of increasing turbulence viscosity around air-water interface.
- For the free decay, the displacement of the floater is calculated based on the total forces, while a prescribed sinusoidal displacement is applied for the forced oscillation. In addition to the forced surge oscillations in the experiment (Table 2), forced oscillations with different motion amplitudes (A) and periods (T) are carried out in the CFD model following Table 3. The displacements of other boundaries are set to zero.
- A continuous wall function based on Spadling's law (Dudley Brian, 1961) switching between low and high Reynolds numbers is implemented for the turbulent viscosity.

As in Table 2, the ratios between oscillation amplitudes (A) and radiated wave lengths (L) are also given in Table 3.

3.1.3. Relaxation zones

The Waves2Foam toolbox provides the relaxation zones (Region I and II in Fig. 3) to minimize the reflected wave from the inlet and outlet boundaries. Rectangular relaxation zones are defined in this work. See Bruinsma's work (Bruinsma et al., 2018) for details.

3.1.4. Coupling of Navier-Stokes/6-DOF solver

A partitioned fluid-structure model is applied to simulate the flow-dependent motion of a floating structure in OpenFOAM. Total forces on the body are calculated by solving the RANS equations for fluid and 6-DOF motion equations are used to obtain the rigid body motion. The stability of solutions can be ensured with a tighter coupling between fluid and motion solver. OpenFOAM provides two different methods: an under-relaxation and a predictor-corrector method (Ferziger et al., 2002). Based on Bruinsma's work (Bruinsma et al., 2018), the predictor-corrector method is more effective at eliminating the oscillations in the force profile. In order to reduce the computational time, the fixed number of subiteration loops to correct pressure in the predictor-corrector method is replaced with a quite small tolerance (10^{-8} Pa) when solving the pressure in this paper. No significant oscillation is seen in the resulting forces (shown in later sections of the paper, i.e. Fig. 11 in Section 5.1.1).

A deforming mesh technique is employed to conform to the moving boundary of the floater. For the free decay, the solver allows for specification of an innerDistance and an outerDistance. The mesh nodes within innerDistance move with the floater, while the mesh nodes between innerDistance and outerDistance morph. No morphing occurs for the mesh nodes outside the outerDistance. The solver of the forced oscillation uses a diffusivity function to control how the mesh morphing is distributed: farther away from the floater, there is less mesh morphing. The diffusivity function is the square of the inverse distance between the floater and mesh position.

The restraints for the floater are implemented by a linear spring without considering interaction with the fluid. The spring is given a simple constant stiffness and a rest length without any damping. The force in the spring follows Hooke's law. When the length of spring is equal to the rest length, the force in the spring is zero.

3.1.5. Computational domain

The floater at scale 1:50 was built in the numerical wave tank, mimicking the experimental set-up. The same coordinate system is also used in the CFD model, as shown in Fig. 4. The width (3.72 m, model scale) and water depth (3.6 m, model scale) of the numerical wave flume are equal to those of the experimental facility. The length of numerical wave tank should be long enough to dissipate the reflected waves from the boundaries. For the heave and pitch decays, the length is 4 m (model

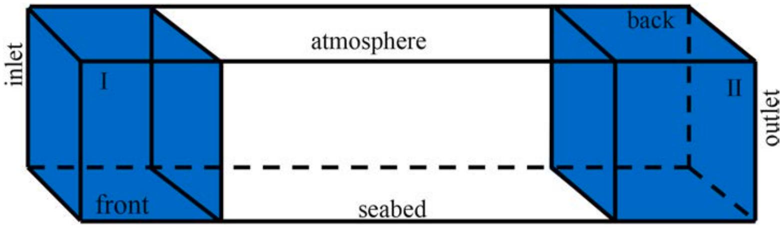

Fig. 3. Schematic representation of computational domain.

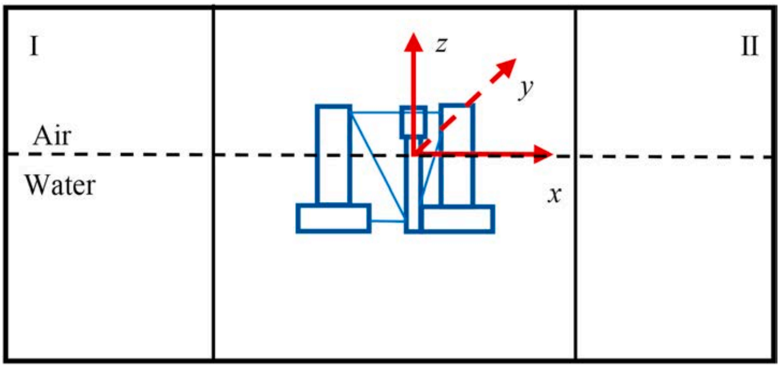

Fig. 4. Overview of the numerical wave tank with a semi-submersible FWT.

scale). Considering the longer period of surge decay and relatively larger amplitudes of the forced oscillations in surge, the length increases to 8 m (model scale). Half of the computational domain consists of the relaxation zones. In addition, the height of the air regime is set to 1 m (model scale). Fig. 4 shows a plan view of the numerical wave tank with floater which is placed at the origin of the numerical domain.

3.1.6. Temporal and spatial discretization

The Courant-Friedrichs-Lewy condition is implemented for the temporal discretization. A maximum Courant number of 0.3 is set to determine each time step.

Based on the finite volume method, the computational domain is discretized into finite regions in space known as cells where the conservation principles are applied. The size of a background cell in all the directions is 0.1 m (model scale) after discretization. Thereafter, the mesh needs to be refined towards the floater and free surfaces. 10 viscous layer cells adjacent to the floater surface are generated. An example of the mesh topology is shown in Fig. 5. Three different meshes used for the mesh convergence studies in the heave decay (LC1.2) are summarized in Table 4.

The time series of heave motions with different mesh sizes are compared in Fig. 6. A small difference is noticeable. Table 5 compares the reduction in the amplitude ("amplitude drop") and the duration of the first cycle. The numerical solution is converging with decreasing mesh size. The medium mesh (M2) is selected for the following simulations based on the small difference in results compared to the finest mesh, and the computational demands.

Table 4
Mesh size for mesh convergence study (model scale).

Mesh	Towards free surface	Towards floater
M1	2-2 level (0.025 m)	4-4 level (0.00625 m)
M2	3-3 level (0.0125 m)	4-4 level (0.00625 m)
M3	3-3 level (0.0125 m)	5-5 level (0.003125 m)

3.2. WADAM model

The frequency domain analysis for the hydrodynamic characteristics is conducted with WADAM (Veritas, 2010). A panel model (potential flow) is used for the columns and a Morison model is implemented for the braces. The radiation calculation results include the frequency-dependent linear added mass and damping coefficients. The braces contribute to the added mass through the inertial term of Morison's equation (added mass coefficient is 1.0), which is frequency-independent. The viscous contributions of the columns and braces to the damping are taken into account by including the drag term from Morison's equation.

Based on Morison's equation, the total viscous surge, heave force $F_{x,z-visc}(t)$ and pitch moment $M_{y-visc}(t)$ on the floater are evaluated by adding the viscous contributions of each column and brace.

$$F_{x,z-visc}(t) = \sum_i \frac{1}{2} \cdot \rho \cdot C_d \cdot A_{s,i} \cdot v_i(t) \cdot |v_i(t)| \tag{6}$$

$$M_{y-visc}(t) = \sum_i \frac{1}{2} \cdot \rho \cdot C_d \cdot A_{s,i} \cdot (R_i \cdot \theta_i(t)) \cdot |R_i \cdot \theta_i(t)| \cdot R_i \tag{7}$$

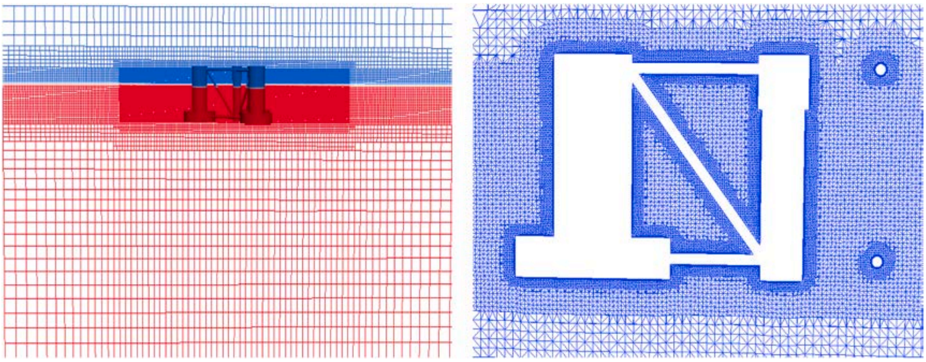

Fig. 5. Refined mesh towards the floater and the free surface.

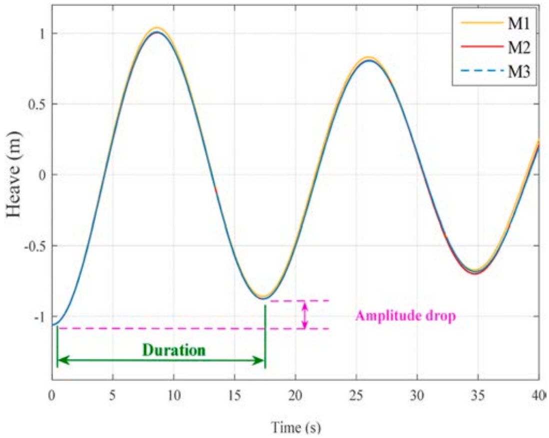

Fig. 6. Time series of heave motion with different mesh sizes in heave decay.

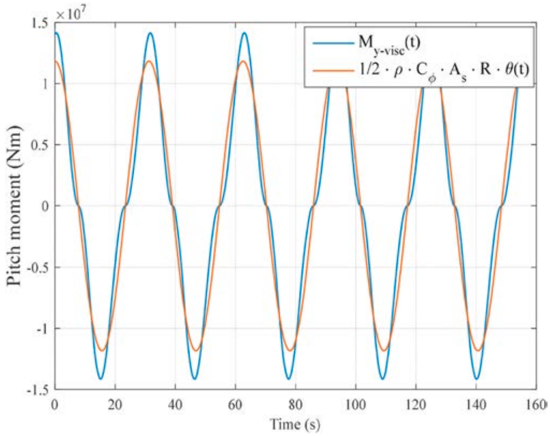

Fig. 7. Linearized total pitch moment, $T = 31.25$ s, $A = 0.136$ rad.

Table 5
Mesh for mesh convergence study.

Mesh	Amplitude drop (m)	Difference (%)	Duration (s)	Difference (%)
M1	0.2010	9.54	17.345	0.15
M2	0.1856	1.14	17.329	0.058
M3	0.1835	0	17.319	0

where ρ is water density, C_d is the quadratic drag coefficient in Morison's equation (0.744 in transverse direction from towing tests (Robertson et al., 2020b) and 2.48 in axial direction by matching experimental data in heave direction (Robertson et al., 2014)), $A_{s,i}$ is the projected area of each column or brace along x or z direction, $v_i(t)$ is the horizontal (surge force) or vertical (heave force) velocity and $\theta_i(t)$ is the angular (pitch moment) velocity at the center of wetted part of each column or brace and R_i is the distance between the center of the wetted part of column or brace and the origin of coordinate system.

Frequency-dependent linearized equivalent damping coefficients are then obtained for surge (C_{dx}), heave (C_{dz}) and pitch (C_φ) damping coefficients by fitting the time series of total viscous surge, heave force and pitch moment, minimizing the error, i.e. $\left|F_{x,z-visc}(t) - \frac{1}{2}\cdot\rho\cdot C_{dx,dz}\cdot A_s\cdot v(t)\right|$ and $\left|M_{y-visc}(t) - \frac{1}{2}\cdot\rho\cdot C_\varphi\cdot A_s\cdot R\cdot\theta(t)\right|$ with A_s being the project area of the whole floater along x or z direction, $v(t)$ being the horizontal or vertical velocity and $\theta(t)$ being the angular velocity at the center of wetted part of the whole floater and R being the distance between the center of wetted part of the whole floater and the origin of coordinate system. An example is shown in Fig. 7. These coefficients depend on two fundamental non-dimensional parameters (KC number and the Stokes number β) that are defined as

$$KC = \frac{2\pi A}{D} \tag{8}$$

$$\beta = \frac{D^2}{\nu T} \tag{9}$$

where D is the diameter of each column and ν is the kinematic viscosity of water.

In the present work, only the diagonal terms in the damping matrix are investigated, i.e. the total viscous surge forces are estimated due to surge motions but not the coupling between surge and pitch motions. Furthermore, different contributions in the WADAM model are investigated, as summarized in Table 6.

4. Free decay tests

Free decay tests are used to determine the natural periods and damping of the rigid body motions. In the current work, free decay tests in surge, heave and pitch (Table 1) were carried out in the experiments and numerical simulations. Assuming that there is no coupling among motions in different DOFs, a typical motion equation of a free decay test in calm water considering linear stiffness and nonlinear damping can be written as follows (Chakrabarti, 1994):

$$(m+a)\ddot{X} + B_1\dot{X} + B_2\dot{X}\left|\dot{X}\right| + KX = 0 \tag{10}$$

where X, $\dot{X}$ and $\ddot{X}$ are the motion, velocity and acceleration for the surge, heave or pitch motion. m is the mass or mass moment of inertia in pitch of rigid body and a is the added mass or mass moment of inertia in pitch. B_1 and B_2 are the linear and quadratic damping coefficients, respectively. K is the restoring coefficient.

Natural periods are estimated as the mean duration between two consecutive peaks or troughs. The damping ratio (ξ^*) relative to the critical damping is based on the logarithmic decrement (δ) for each cycle:

$$\delta = \ln\frac{x_n}{x_{n+1}} \tag{11}$$

where x_n and x_{n+1} are two consecutive peaks or troughs. The damping ratio is then calculated as:

$$\xi^* = \frac{1}{\sqrt{1+\left(\frac{2\pi}{\delta}\right)^2}} \tag{12}$$

In some cases, especially for small motion amplitudes, there are large variations in the damping ratio.

From the method of equivalent linearization, the damping ratio can

Table 6
Overview of different contributions in WADAM.

	Added mass coefficient	Damping coefficient
WADAM1	Radiation added mass from panel model	Radiation damping from panel model
WADAM2	WADAM1 with contributions of braces	WADAM1 with contributions of Morison-type drag

be expressed as a function of the decay motion amplitude (X):

$$\xi^* = \frac{B_1 + B_2 \frac{8\omega_n}{3\pi} X}{B_{cr}} \tag{13}$$

where ω_n is the oscillation frequency, $B_{cr} = 2\cdot\sqrt{(m+a)\cdot K}$ is the critical damping. Based on Eq. (12) and Eq. (13), the linear and quadratic damping in the decaying motion can be obtained by the values of two consecutive peaks or troughs. As this estimate is sensitive to the magnitude of the peaks (or troughs), the best signal mean value is subtracted from the original decaying motion by minimizing the linear regression error (sum of squares).

4.1. Surge decay test

The surge decay results are presented in Fig. 8. The difference of motion amplitude between CFD simulation and experimental data is small at the beginning of the simulation, but increases with time. The comparison of damping ratio shows the surge decay is less damped in the CFD model. Furthermore, for large surge amplitude (>0.6 m), the linear component (given by the intercept) dominates. The linear damping estimated by the CFD model is approximately 30% smaller than the one predicted in the experiment. This large difference might be caused by the following reasons.

In the experiment, taut-spring-lines are connected with the floater by the pulleys (Robertson et al., 2020b). Some sources of mechanical friction, such as the damping between spring lines and pulley, are not quantified and are not considered in the CFD model. This mechanical friction may be the reason for the upturning tail in the damping ratio at small surge amplitudes (<0.6 m) in the experiment. There are also uncertainties related to performing a single experimental test. Furthermore, the post-processing method is important: the difference might be up to 10% when comparing the damping estimated by a least-squares approach and the classical peak-to-peak analysis (Burmester et al., 2020b).

The surge natural periods are compared in Table 7. Compared to the large difference of the linear damping, the difference in the natural periods is small. There is significant uncertainty in the mooring line axial stiffness (Robertson et al., 2020a): considering the upper limit of the mooring system stiffness would result in a surge natural period of 105.14 s in the CFD simulations. The uncertainty in measured motion is estimated as 5 mm full scale in the experiments; additional uncertainties exist in the mass and geometry of the model (Robertson, 2017).

4.2. Heave decay test

The comparisons of heave decay are presented in Fig. 9. The motion amplitudes between experiment and CFD model are in close proximity of each other. The comparison of damping ratio confirms that the heave damping at the small heave amplitude (<0.5 m) shows more linear behavior, while the damping becomes nonlinear as the heave amplitude increases. Compared to the experiment, the CFD model captures more linear damping (given by the intercept) and less quadratic damping (given by the slope). Despite the small difference in damping, the CFD model shows good correspondence with the experiment in predicting the heave natural period (within 0.4%) as presented in Table 7.

Table 7
Natural periods obtained from experiments and CFD simulations.

Mode of Motion	Experiment (s)	CFD (s)	Difference (%)
Surge	104.1	108.4	4.13
Heave	17.32	17.39	0.40
Pitch	31.29	31.07	0.70

4.3. Pitch decay test

For the pitch decay, interaction between pitch and surge motions was observed in the experimental results whereas no such interaction was found in the CFD simulation. Hence, motions at the surge natural frequency are removed from the experimental signal by a high-pass filter with a 0.015 Hz cut-off frequency. The filtered experimental pitch motion is presented in Fig. 10 together with the original CFD results. The CFD simulation captures both the period and damping well. Linear damping dominates the pitch damping, although the overall damping level shows large variations.

In conclusion, the CFD model is generally able to reproduce the natural periods and damping levels of the semi-submersible FWT floater. Better correspondence is observed in the heave and pitch decay tests with shorter natural periods. For the surge decay with longer period, there are some differences between CFD simulations and experimental measurements. Similar differences are also found in other work (Burmester et al., 2020a, 2020b, 2020b). Nevertheless, these differences are considered acceptable, given the differences between the experimental and numerical models and the uncertainties.

5. Forced oscillation tests

In the forced oscillations, harmonic motion is imposed on the floater. The position of the floater is:

$$X(t) = A\,\sin(\omega t) \tag{14}$$

where $X(t)$ represents surge motion along the x axis, $x(t)$, heave motion along the z axis, $z(t)$, or pitch motion around y axis, $\theta(t)$. For pitch, the center of rotation is located at the origin of the coordinate system. A is

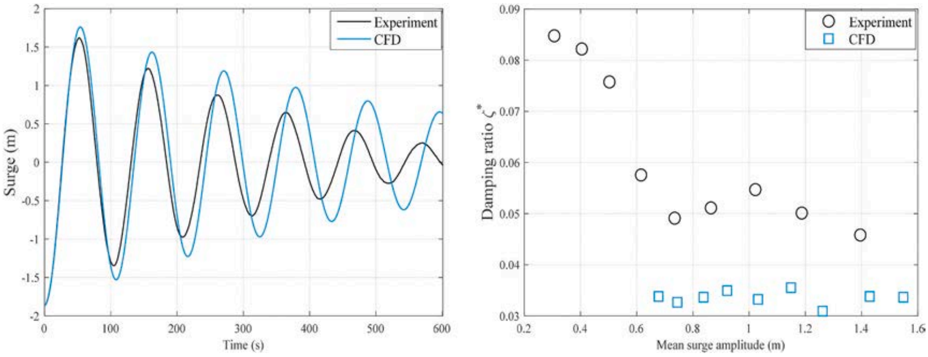

Fig. 8. Surge decay (left: original decaying surge motion, right: surge damping ratio).

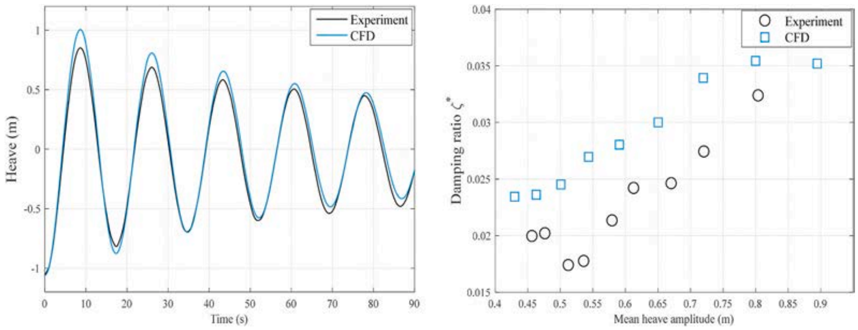

Fig. 9. Heave decay (left: original decaying heave motion, right: heave damping ratio).

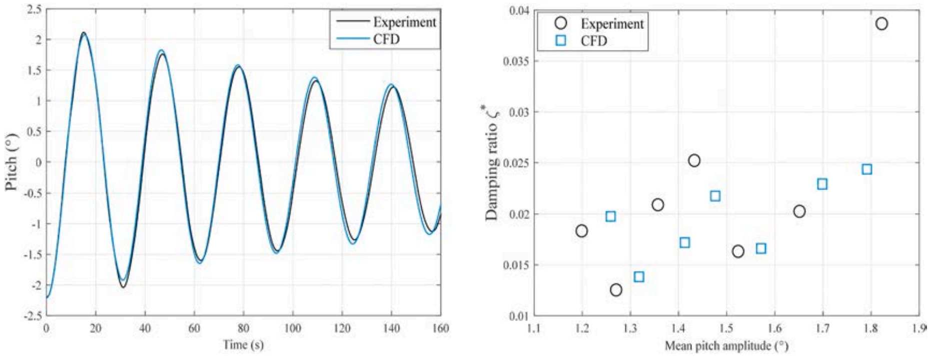

Fig. 10. Pitch decay (left: decaying pitch motion, Experiment: high-pass filtered results, right: pitch damping ratio).

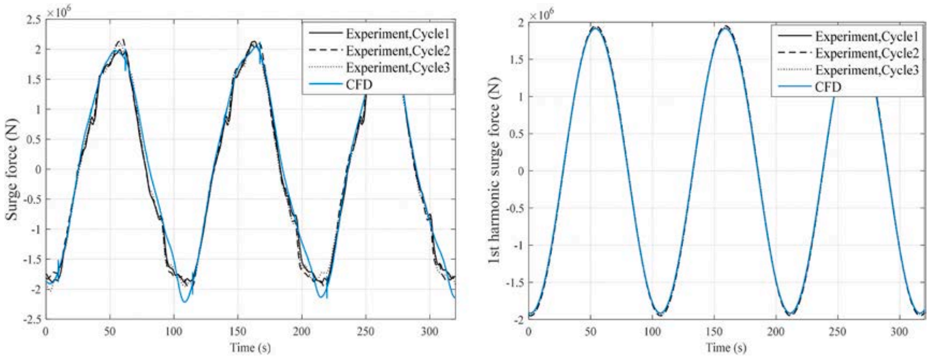

Fig. 11. Time series of surge force, LC2.1 (left: total hydrodynamic force, right: 1st harmonic hydrodynamic force).

the oscillation amplitude and ω is the oscillation frequency.

The hydrodynamic force on the floater, $F_H(t)$, is obtained by subtracting the inertial force, $F_I(t)$, and the linear hydrostatic restoring force, $F_K(t)$, from the measured or simulated total force, $F_T(t)$. That is:

$$F_H(t) = F_T(t) - F_I(t) - F_K(t) \tag{15}$$

The detailed expressions of inertial force and linear hydrostatic restoring force in the experimental and numerical results are given in Table 8. In the CFD simulation, the estimated total force is the integral of the hydrodynamic pressure along the surface of the floater, which does not include inertial forces. The linear hydrostatic restoring coefficient

Table 8
Motion, inertial force and linear restoring force in the experimental and numerical results. In the experiments, forced oscillations were only carried out in surge.

	$X(t)$		$F_I(t)$		$F_K(t)$	
Motion	Experiment	CFD	Experiment	CFD	Experiment	CFD
Surge	$x(t)$	$x(t)$	$-m\cdot\ddot{x}(t)$	0	0	0
Heave	N/A	$z(t)$	N/A	0	N/A	$K_{33}\cdot z(t)$
Pitch	N/A	$\theta(t)$	N/A	0	N/A	$K_{55}\cdot\theta(t)$

can be obtained from the variation of buoyancy loads due to small displacements in still water. Hence, the linear restoring coefficient in surge is zero and the linear restoring coefficient in heave, K_{33}, and in pitch, K_{55}, can be written as:

$$K_{33} = \rho g A_{wp} \tag{16}$$

$$K_{55} = \rho g V Z_B + \rho g \int_{A_{wp}} x^2 ds \tag{17}$$

where ρ is water density, g is the acceleration due to gravity, A_{wp} is the waterplane area, V is the volume of the floater, Z_B is the vertical coordinate of the center of buoyancy and the integral of Eq. (17) represents the waterplane area moment of inertia about y axis. In Eq. (17), the effect of weight is not included, because the estimated total force in the CFD simulation does not include the weight. For the main column, there is a ledge due to the large diameter for the upper part (see Fig. 2). When the heave oscillation amplitude exceeds the distance between the ledge and the still water line, varying waterplane area is used in the K_{33}.

The first harmonic component of hydrodynamic force, $F_H^{(1)}(t)$, or moment $M_H^{(1)}(t)$,with the same frequency as the motion, ω, is extracted and decomposed into in-phase and out-of-phase components:

$$F_H^{(1)}(t) = F_{H,\cos}^{(1)} \cdot \cos(\omega t) + F_{H,\sin}^{(1)} \cdot \sin(\omega t) \tag{18}$$

$$M_H^{(1)}(t) = M_{H,\cos}^{(1)} \cdot \cos(\omega t) + M_{H,\sin}^{(1)} \cdot \sin(\omega t) \tag{19}$$

The first-order hydrodynamic force or moment on the floater can be expressed based on the added mass and linearized damping coefficients as

$$F_H^{(1)}(t) = -\rho \cdot C_a \cdot V \cdot \ddot{X}(t) - \frac{1}{2} \rho \cdot C_{dx,dz} \cdot A_s \cdot \frac{8}{3\pi} \cdot \omega \cdot A \cdot \dot{X}(t) \tag{20}$$

$$M_H^{(1)}(t) = -C_a \cdot I \cdot \ddot{X}(t) - \frac{1}{2} \cdot \rho \cdot C_\varphi \cdot A_s \cdot R \cdot \frac{8}{3\pi} \cdot \omega \cdot A \cdot \dot{X}(t) \tag{21}$$

where I is the mass of moment inertia about the y axis.

Then, the added mass and linearized damping coefficients are found:

$$C_a = \frac{F_{H,\sin}^{(1)}}{\rho \cdot V \cdot \omega^2 \cdot A} \quad or \quad C_a = \frac{M_{H,\sin}^{(1)}}{I \cdot \omega^2 \cdot A} \tag{22}$$

$$C_{dx,dz} = -\frac{F_{H,\cos}^{(1)}}{4/3\pi \cdot \rho \cdot A_s \cdot \omega^2 \cdot A^2} \quad or \quad C_\varphi = -\frac{M_{H,\cos}^{(1)}}{4/3\pi \cdot \rho \cdot A_s \cdot R \cdot \omega^2 \cdot A^2} \tag{23}$$

where A is equal to 1 for the linear radiation damping considering the columns (WADAM1). The projected area for the pitch damping coefficient is the same as the surge damping coefficient. The estimated linearized damping coefficient from the CFD simulations includes both radiation damping and viscous damping.

5.1. Forced oscillations in surge

5.1.1. Validations against the experimental measurements

The numerical estimated total and first harmonic hydrodynamic forces under the forced oscillations in surge are compared against the experimental measurements in Fig. 11. The numerical solution remains stable and has a small oscillation at the larger surge force amplitude. Meanwhile, the total surge force reveals weak cycle-to-cycle variations. These fluctuations are also found in the experiments, considering the differences of total surge forces at the start (Cycle1), middle (Cycle2) and end (Cycle3) of the steady-state experimental data. Some possible reasons for these variations are the mechanical vibrations of the measuring equipment (for the experiment) and the nonlinear characteristics of hydrodynamic force and interaction between body motion with the radiated wave, which was produced by the previous motion. Furthermore, the numerically estimated first harmonic surge force is in good agreement with the experimental measurements (within 0.2%).

Fig. 12 compares the surge added mass and damping coefficients of the whole floater obtained from experiments and CFD simulations. The difference in the estimated added mass coefficient varies from 1.1% (T = 105 s) to 4.6% (T = 31.2 s). However, the estimated damping coefficient shows better agreement, and the largest difference occurs at T = 21 s (1.9%). Considering the ratios of oscillation amplitudes over radiated wave lengths (Table 2), the smaller the ratio is, the lower the radiated wave steepness is, the more dominant the linear effects are, and the better the estimated added mass and damping coefficients from CFD simulation approximate those from experiments.

In the experiments, the motion and forces were measured by different measurement devices. Whether the force and motion signals are measured synchronously or not is crucial for the estimations of added mass and damping coefficients. There is no accurate evaluation of time-lag between different signals in the experiments, so time lags of either 0.01 s (sampling interval in the experiments) and 0.02 s are used to investigate this effect. This estimated time lag is similar to the time lag observed in hybrid testing of a floating wind turbine (Sauder et al., 2016). The added mass and damping coefficients under motion-lead or force-lead are estimated and shown in the uncertainty bars of Fig. 12. The time-lag between motion and force has minor influence on the calculated added mass coefficients, but its impact on the calculated damping coefficients is more significant for shorter oscillation periods. The same trend is observed for the different time-lags.

Generally, good agreement is obtained between measured and numerically estimated hydrodynamic surge force and added mass and damping coefficients, which suggests that it is possible to reproduce the correct hydrodynamic characteristics at low oscillation frequency in the CFD model.

5.1.2. Forced oscillation in surge in the CFD model

Based on Eq. (8), the KC numbers of each column of floater under forced oscillations in surge in the CFD model are presented in Fig. 13. The KC numbers vary from 0.5 to 7.4 and β is from 2.11E+05 to 8.64E+06.

Fig. 14 compares the total surge added mass and linearized damping coefficients calculated from the CFD simulations and the values due to linear radiation considering the columns (WADAM1) and the contributions of Morison's added mass and drag terms on the braces (WADAM2). The CFD simulations lead to similar added mass coefficients for smaller amplitudes (1.91 m and 3.82 m). However, for the largest amplitude (7.64 m), the added mass coefficient is 2.7% smaller. This decrease is closely related with the variation of KC numbers on each column. More details can be found in the discussions about the added mass coefficients for different columns. Compared to the CFD model, potential flow theory (WADAM1) underestimates the added mass (up to 10%). Furthermore, the contribution of braces only accounts for 2.5 percent in the potential flow added mass (WADAM1 vs WADAM2). In addition, the results also highlight the weak dependency of added mass on oscillation period.

In the CFD simulations, the linearized damping coefficient decreases with oscillation amplitude and increases with oscillation period. Considering the definition of linearized damping coefficient in Eq. (23), the damping has opposite trend with the linearized damping coefficient. That means the faster the surge motion is, the larger the damping is. In the potential flow results, the radiation damping (WADAM1) is completely negligible with respect to the viscous damping (WADAM2). The linearized damping coefficient in the WADAM2 model is close to the quadratic damping coefficient (0.744) in Morison's equation. Compared to the CFD results, Morison-type drag coefficient based on the towing tests in WADAM2 underestimates the viscous damping.

The obtained surge added mass and linearized damping coefficients on individual columns are compared numerically in Fig. 15. Based on other research (Dütsch et al., 1998; Gao et al., 2020), the added mass

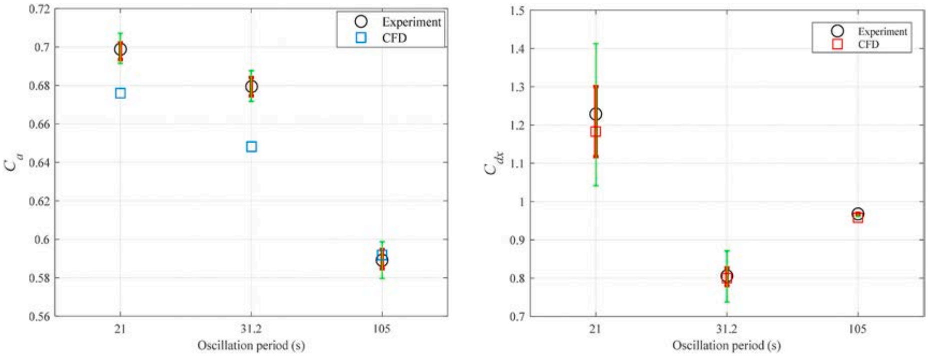

Fig. 12. Surge added mass and damping coefficients, LC2.1-LC2.3. Red and green uncertainty bars represent the influences of 0.01 s and 0.02 s (model scale) time-lags between different signals in the experiments, respectively. (For interpretation of the references to colour in this figure legend, the reader is referred to the Web version of this article.)

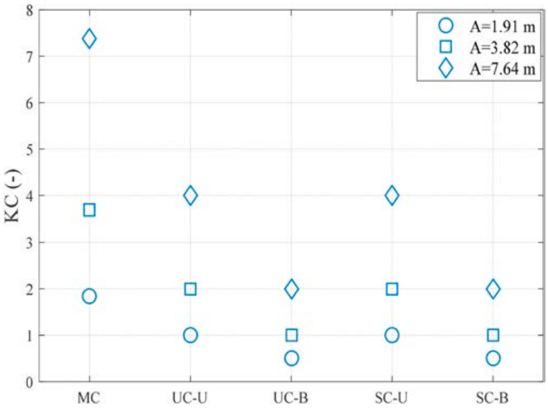

Fig. 13. KC numbers of each column under forced oscillations in surge (MC: main column, UC-U: upper part of upstream column, UC-B: heave plate of upstream column, SC-U: upper part of starboard column, SC-B: heave plate of starboard column. See Figs. 1 and 2 for the definitions of columns).

coefficient of a circular cylinder is weakly dependent on the KC number when KC < 3. For larger KC number, the added mass coefficient decreases as KC increases and achieves the minimum value around KC = 15. Then the added mass coefficient increases with KC. Hence, for the main column (KC > 2), the added mass coefficient decreases with increasing oscillation amplitude. For the upper part of column, the added mass coefficient has similar results (within 1%) under two smaller oscillation amplitudes (KC < 2), and significantly reduces for the largest amplitude (KC = 4). For the heave plates (KC < 2), the weak dependency of added mass coefficient on oscillation amplitudes seems to be valid for longer oscillation period (slow surge motion), but the added mass coefficient increases with KC for shorter oscillation period. All the changes are due to the variations of vortex pattern around the floater.

The computed hydrodynamic pressures on the aft (Point B) and starboard sides (Point A) of upper part of starboard column are shown in Fig. 16. The double frequency and negative mean value of hydrodynamic pressures on the starboard side show the occurrence of vortex shedding in the CFD simulations. Compared to the CFD results, potential flow predicts smaller added mass coefficient with a maximum difference of 15.6% (200 s, SC-B) except a larger added mass coefficient under largest oscillation amplitude for the upper part of columns (UC-U,SC-U). Additionally, the added mass coefficient on the starboard column is larger than the one on the upstream column, and this increase is more significant in the CFD simulations.

Dütsch et al. (1998) show that the drag coefficient decreases with increasing KC numbers for KC < 3. When 3<KC < 15, the drag coefficient is weakly dependent on the KC number. The same trends can be seen in the CFD simulations (Fig. 15). The linearized damping coefficient decreases as KC increases. However, for larger KC values, such as larger amplitude for the main column (MC) and upper part of upstream and starboard column (UC-U, SC-U), the variations of linearized damping coefficients over oscillation amplitude are quite small.

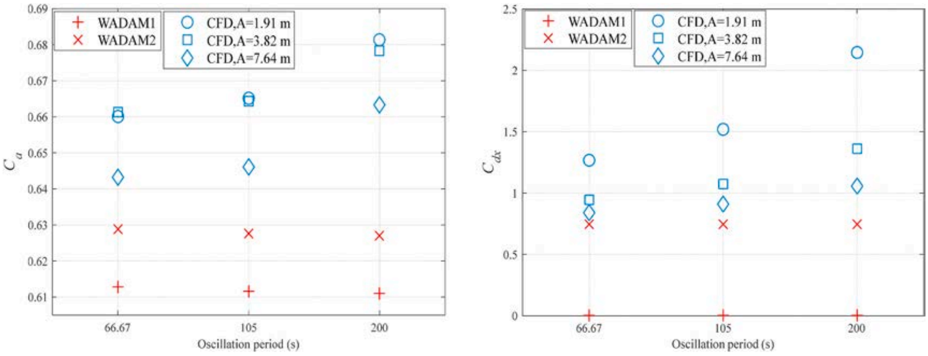

Fig. 14. Surge added mass and linearized damping coefficients for the whole floater.

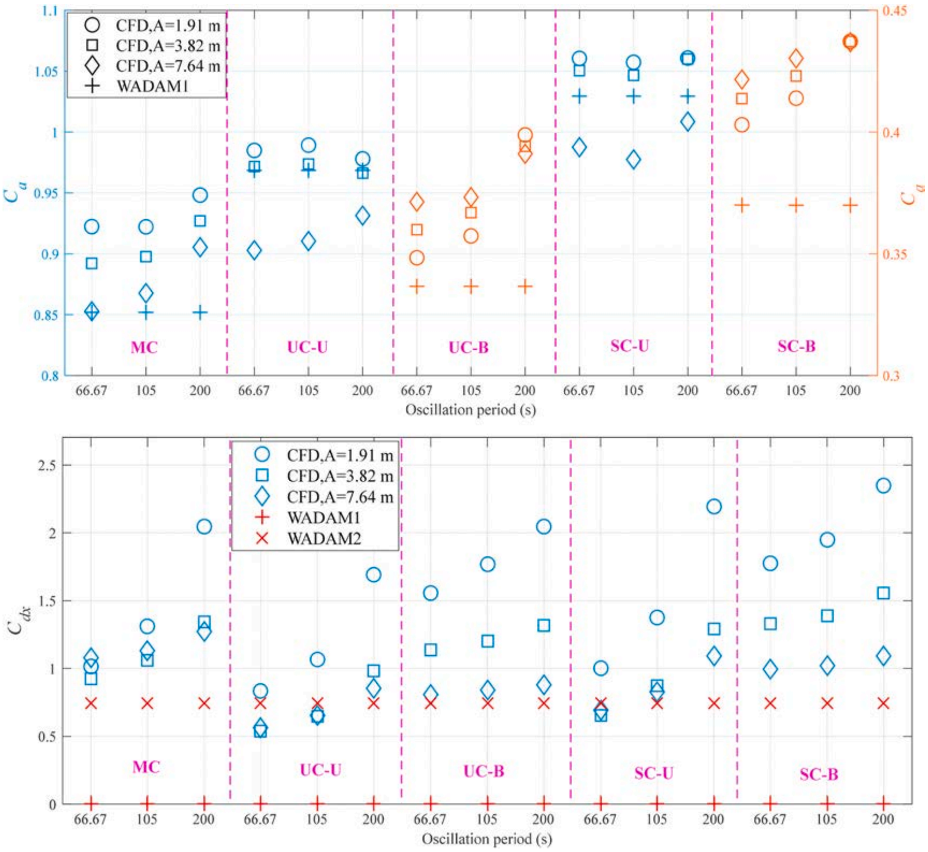

Fig. 15. Surge added mass and linearized damping coefficients for each column of the floater (MC: main column, UC-U: upper part of upstream column, UC-B: heave plate of upstream column, SC-U: upper part of starboard column, SC-B: heave plate of starboard column. See Figs. 1 and 2 for the definitions of columns. Top: The added mass coefficient of MC,UC-U and SC-U corresponds to the left *y* axis while the added mass coefficient of UC-B and SC-B corresponds to the right *y* axis. Bottom: The linearized damping coefficient of each column uses the left *y* axis.).

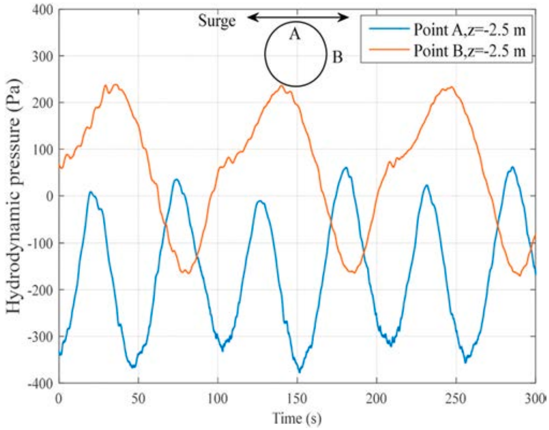

Fig. 16. Hydrodynamic pressures around upper part of starboard column, T = 105 s, A = 7.64 m.

Furthermore, the linearized damping coefficient of each column increases with oscillation period. The damping coefficient for each column in WADAM model has similar results as the total damping coefficient. However, the underestimation of viscous damping by Morison-type drag (WADAM2) does not seems to be valid for all comparisons. This also highlights the different drag coefficients instead of a uniform one should be applied in accurate estimations of viscous damping for each column. Furthermore, in the CFD simulations, the starboard column has a slightly larger damping compared to the upstream column. The shorter distance from the main column along the *x* direction and the effect of the portside column can explain this additional damping.

In order to validate whether there are consistent conclusions between free decay and forced oscillation or not, the durations of different cycles in the surge free decay are given in Table 9. The small variations in durations suggest that the motion amplitude has minor effect on the added mass, considering the maximum KC number is 1.8. Furthermore, from Fig. 8, the damping is also weakly dependent on the KC in the free decay, which is not consistent with conclusions in the forced oscillation.

Table 9
Durations of different cycles under the surge free decay in the CFD model.

	Cycle1	Cycle2	Cycle3	Cycle4	Cycle5
Duration (s)	108.6	108.1	108.2	108.3	108.6

The possible reason is that linear damping dominates for very small motion. However, when the mean motion amplitude in the free decay is close to the motion amplitude in the forced oscillation, the estimated added mass and damping are in good agreement, as shown in Table 10.

5.2. Forced oscillations in heave

For the forced oscillations in heave, the KC number is defined based on the heave plate diameter for the upstream and starboard columns. The corresponding KC numbers are presented in Fig. 17, ranging from 0.25 to 7.4. The β varies from 2.23E+06 to 3.62E+07.

The total heave added mass and linearized damping coefficients are presented in Fig. 18. The added mass coefficient increases with oscillation amplitude. For all cases, the calculated added mass coefficient from the CFD simulations is higher than the one derived from the potential flow theory (WADAM1), with a maximum increase of 32% (7.64 m). Similar results can be found in previously published research (Cozijn et al., 2005; Lopez-Pavon and Souto-Iglesias, 2015). A possible explanation for this increase is that the flow separation and the formation of eddies at the edge of heave plates for the large motion change the phase difference between the pressure and the motion of floater. The braces give minor contributions to the total added mass coefficient (within 2%). Finally, the added mass coefficient is independent of the oscillation period.

The linearized damping coefficient is independent of the oscillation period and decreases as the oscillation amplitude increases in the CFD simulations. By comparing WADAM1 and WADAM2, viscous damping dominates and the radiation damping is completely negligible. The difference of the computed linearized damping coefficient between WADAM1 and WADAM2 is close to the quadratic drag coefficient (2.48 by matching the experimental data) in Morison's equation, which underestimates the viscous damping.

The heave added mass and linearized damping coefficients among different columns are compared in Fig. 19. The added mass and linearized damping coefficients of the main column are much smaller than the upstream and starboard columns, even when dividing by the small diameter, which is related to the lack of a heave plate. For smaller oscillation amplitudes (0.955 m and 3.82 m), CFD and potential flow theory predict similar added mass coefficients for the main column, which seems to be independent of the oscillation period and amplitude. However, for the largest oscillation amplitude (7.64 m), the added mass increases sharply and shows significant dependency on the oscillation period. This is because the oscillation amplitude is larger than the distance between the ledge (see Fig. 2) and still water line (4.25 m) and the occurrence of flow separation and eddies at the ledge gives additional added mass. The overestimation for the linearized damping coefficient on the main column by Morison-type drag suggests that a smaller axial drag coefficient should be applied for the column without the heave plate.

The contribution of the heave plate is dominant for the heave forces, and the added mass and linearized damping coefficients for the upstream and starboard columns show similar trends as the total added mass and linearized damping coefficients. Furthermore, there are no significant differences between the upstream and starboard columns.

The consistency of conclusions based on free decay and forced oscillation in heave is also investigated. From Fig. 18, the radiation added mass gives a good estimate of the added mass with small heave motion. The heave free decay considers motion amplitudes which are smaller than the forced oscillations, and there is no significant change in the duration of different cycles during the decay (Table 11). From Fig. 9, the linear damping increases with the motion amplitude. Considering the definition of linearized damping coefficient in Eq. (23), the linearized damping coefficient decreases as the motion amplitude increases, which is the same conclusion as the free decay tests. Table 12 compares the estimated heave added mass and damping with similar motion amplitude in free decay and forced oscillation. The added mass agrees well, whereas the damping is quite sensitive to the motion amplitude.

Table 10
Comparisons of surge added mass and damping between free decay and forced oscillation in the CFD model.

	Free decay	Forced oscillation
Amplitude (m)	1.584	1.91
Added mass (kg)	8.98E6	9.23E6
Damping (Ns/m)	8.97E4	9.70E4

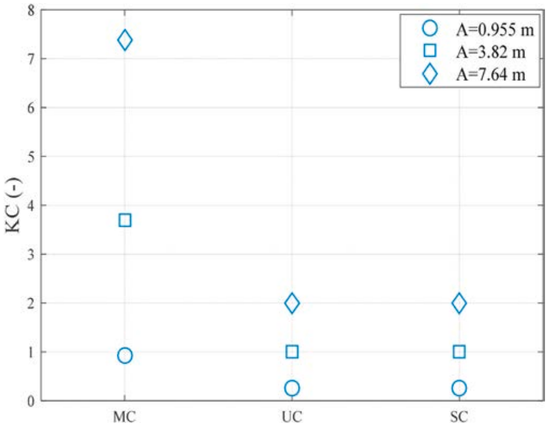

Fig. 17. KC numbers of each column under different heave forced oscillations (MC: main column, UC: upstream column, SC: starboard column. See Figs. 1 and 2 for the definitions of columns).

5.3. Forced oscillations in pitch

The total pitch added mass and linearized damping coefficients are compared in Fig. 20. For small pitch motion, the total added mass coefficient is independent of the oscillation period and increases slightly with oscillation amplitude. However, the total added mass coefficient decreases with oscillation period for the largest pitch motion (0.273 rad). A possible explanation is that complex vortex-vortex and vortex-column interaction can change the vortex pattern around the column for large pitch motions. There is a significant underestimation of the pitch added mass coefficient using potential flow theory. The contribution of braces to the total pitch added mass coefficient is less than 1%.

The pitch linearized damping coefficient decreases with the oscillation amplitude and shows a weaker dependency on the oscillation period. Furthermore, the viscous damping dominates and the radiation damping can be neglected (WADAM1 vs WADAM2). The applied Morison's drag coefficients by matching experimental data underpredict the viscous damping.

Since the mass distributions of each column are unknown, the mass of moment inertia about y axis (Eq. (22)) is calculated assuming the mass is uniformly distributed. The pitch added mass and linearized damping coefficients among different columns can be seen in Fig. 21. In the CFD model, the main column has some "openings" at the intersection with the braces where no pressure results are obtained. The loss of pressure at these openings leads to the negative added mass coefficient of the main column in the CFD simulations. In the potential flow calculation, the main column is considered as a closed cylinder. This effect on the added mass and linearized damping coefficients is shown in Table 13 with a difference in percentage from the results with braces. When the main column is built as a closed cylinder (without brace) in the CFD simulation, the added mass coefficient changes to positive (Table 13), but is also smaller than the potential flow solution presented in Fig. 21.

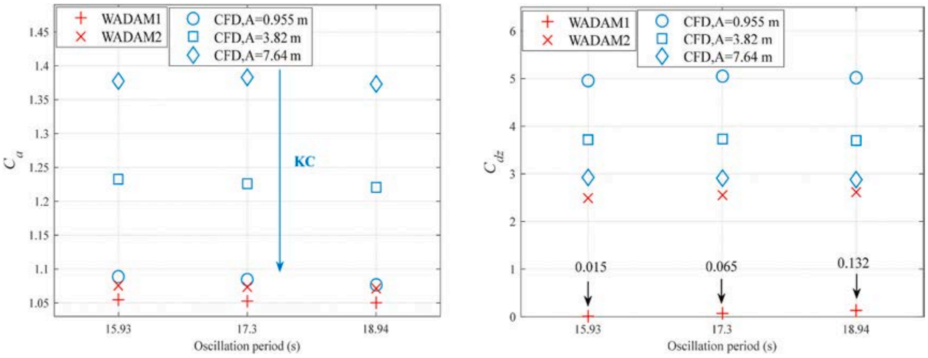

Fig. 18. Heave added mass and linearized damping coefficients for the whole floater.

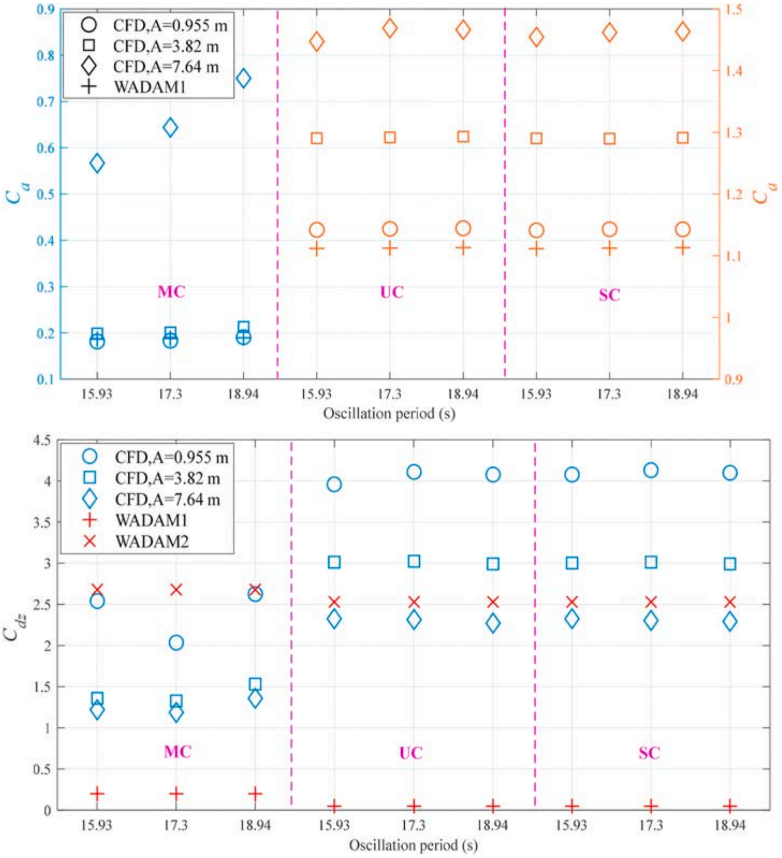

Fig. 19. Heave added mass and linearized damping coefficients for each column of the floater (MC: main column, UC: upstream column, SC: starboard column. See Figs. 1 and 2 for the definitions of columns. Top: The added mass coefficient of MC corresponds to the left y axis while the added mass coefficient of UC and SC corresponds to the right y axis. Bottom: The linearized damping coefficient of each column uses the left y axis.).

Table 11
Durations of different cycles under the heave free decay in the CFD model.

	Cycle1	Cycle2	Cycle3	Cycle4	Cycle5
Duration (s)	17.3	17.4	17.4	17.4	17.4

Furthermore, the added mass coefficient of the main column seems to be independent of the oscillation amplitude, but its magnitude increases with the oscillation period. The negative added mass coefficient of main column is useful to consider for further modification of potential flow results in order to better simulate local responses on the semi-submersible FWT. The interaction between heave plate and braces has

Table 12
Comparisons of heave added mass and damping between free decay and forced oscillation in the CFD model.

	Free decay	Forced oscillation
Amplitude (m)	0.894	0.955
Added mass (kg)	1.504E7	1.507E7
Damping (Ns/m)	7.439E5	9.046E5

minor influence on the added mass coefficient for the upstream and starboard columns (Table 13). The added mass coefficient of the upstream column has similar behavior as the total added mass coefficient because most of total pitch moment arises from the contribution of the upstream column. The added mass coefficient of the starboard column also shows similar trends as the total added mass coefficient except a slight decrease with the oscillation period for the smaller oscillation amplitude. Linear potential flow theory underestimates the added mass coefficient of upstream column, but overestimates the results for the main and starboard columns.

The pitch linearized damping coefficients of different columns (Fig. 21) appear to weakly depend on the oscillation period and decrease with the oscillation amplitude. Given both the magnitude of the linearized damping coefficient and the projected area (Eq. (23)), the upstream column contributes the most to the damping. The Morison-type drag coefficients by matching experimental data underestimate the viscous pitch damping. The interaction between columns and braces reduces the damping on each column (Table 13), with a minimum decrease of 0.59% for the upstream column and a maximum decrease of 31.44% for the main column.

Similar conclusions can be found between free decay and forced oscillations in pitch. The small variations of duration for different cycles (Table 14) in the pitch free decay are consistent with the constant added mass for small pitch motion in the forced oscillations in pitch. Furthermore, from Fig. 10, the linear damping increases with the motion amplitude. Considering the definition of linearized damping coefficient (Eq. (23)), the linearized damping coefficient decreases as the motion amplitude increases, which is the same conclusion as the forced oscillations. Table 15 compares the added mass and damping coefficient for the maximum mean pitch motion in the free decay and the minimum pitch motion in the forced oscillation. The estimated added mass is in good agreement whereas the calculated damping has a linear relationship with the amplitude.

6. Conclusions

In order to investigate the still-water hydrodynamic characteristics of the floater for a semi-submersible FWT, a series of free decay and forced oscillation tests have been conducted in experiments and in a CFD model. The focus is on long periods which are close to the natural periods for rigid body FWT motions. In the current work, the KC number varies from 0.25 to 7.4 and β is in the range of 2.11E+05 to 3.62E+07.

For the free decay, better correspondence can be found in the heave and pitch decay with shorter natural periods. However, for the surge decay with longer period, CFD underestimates the damping by 30% compared to the experiment. It is hypothesized that the additional damping between spring lines and pulleys, as well as coupling of rigid body motions increases the damping in the experiment. The uncertainty of experimental data and post-processing also contributes to this difference. Furthermore, the linear damping dominates the surge and pitch damping while quadratic damping is found in the heave damping due to the vortex shedding around the edge of heave plates. The estimated natural periods of the floater motion are in good agreement with ones calculated from the experiments (within 4.5%).

Forced oscillations in surge around the natural periods of surge, heave and pitch motion are firstly performed in the CFD model for validation. Compared to the experimental results, the maximum difference of 4.6% for the added mass coefficient and 1.9% for the damping coefficient suggest the CFD model can reproduce the correct hydrodynamic characteristics at low oscillation frequency. Next, the hydrodynamic characteristics of the whole floater and each column are analyzed using the CFD model. The results are compared with the results from the potential flow theory with Morison-type drag. The drag coefficients are determined by matching the experimental data.

For these long periods, the surge added mass coefficient seems to be independent of the oscillation amplitude for small surge motion (KC < 2) and then decreases with the oscillation amplitude. A slight period dependency can be found in the surge added mass coefficient. Furthermore, the surge linearized damping coefficient increases towards longer period and smaller motion amplitude. The surge added mass and linearized damping coefficients on the starboard column are slightly larger than on the upstream column.

The heave added mass and linearized damping coefficients show, on one hand, a small dependence on the oscillation period and, on the other hand, a larger dependence with the oscillation amplitude. Most of contributions of added mass and linearized damping coefficients come from the heave plates. No difference can be found between the upstream and starboard columns.

A weak dependency of the pitch added mass coefficient on the oscillation amplitude and period is found for small pitch motion. However, the pitch added mass coefficient decreases with oscillation period for large pitch motion. The pitch linearized damping coefficient has similar behavior as the heave linearized damping coefficient.

The added mass coefficient derived from the CFD simulation is slightly superior to the one estimated by the potential flow theory in most cases. Viscous effects give an additional added mass. Regarding the

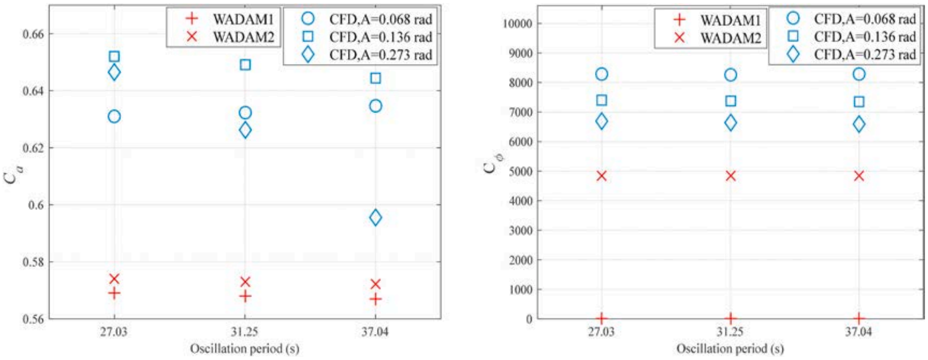

Fig. 20. Pitch added mass and linearized damping coefficient for the whole floater.

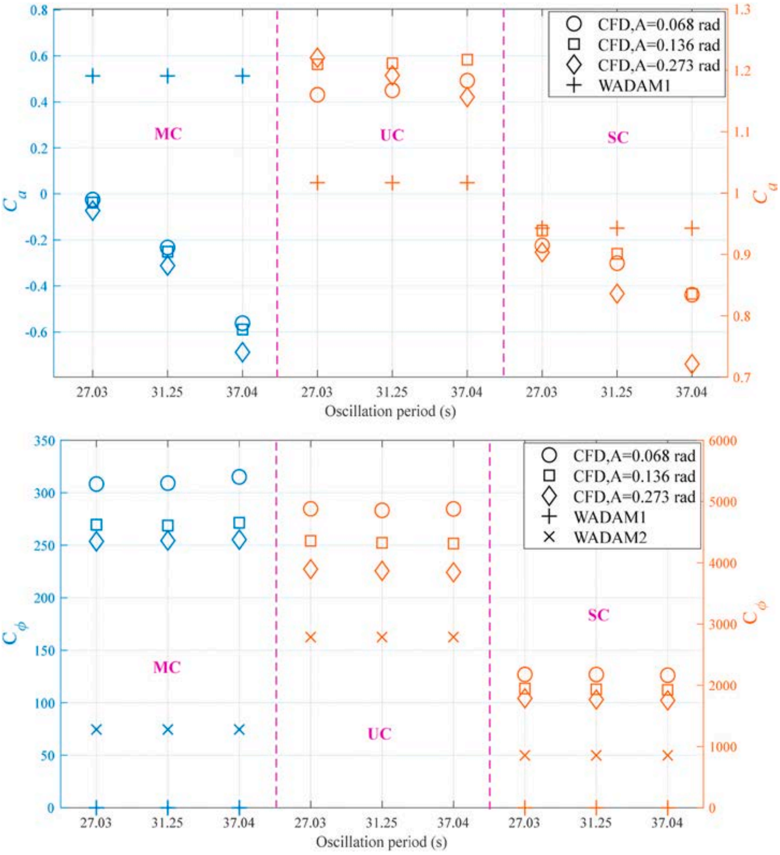

Fig. 21. Pitch added mass and linearized damping coefficients for each column of the floater (MC: main column, UC: upstream column, SC: starboard column. See Figs. 1 and 2 for the definitions of columns. The added mass and linearized damping coefficients of MC correspond to the left y axis while the added mass and linearized damping coefficients of UC and SC correspond to the right y axis).

Table 13
The effects of brace on the pitch added mass and damping coefficient on each column in the CFD simulations, T = 31.25 s, A = 0.136 rad.

		with brace	without brace	Difference (%)
Added mass coefficient	MC	−0.251	0.268	206.8
	UC	1.211	1.125	7.43
	SC	0.901	0.860	4.55
Linearized damping coefficient	MC	268.72	184.34	31.44
	UC	4326.5	4280.0	1.07
	SC	1934.0	1922.5	0.59

Table 14
Durations of different cycles under the pitch free decay in the CFD model.

	Cycle1	Cycle2	Cycle3	Cycle4	Cycle5
Duration (s)	31.1	31.1	31.1	31.0	31.1

damping, the radiation damping is completely negligible and the viscous damping from vortex shedding dominates. The accuracy of capturing the vortex shedding using Morison's drag force is sensitive to the drag coefficient.

Finally, free decay and forced oscillation tests give consistent conclusions about the trend of added mass and damping coefficients over the amplitude.

Table 15
Comparisons of pitch added mass and damping between free decay and forced oscillation in the CFD model.

	Free decay	Forced oscillation
Amplitude (rad)	0.031	0.068
Added mass (kgm^2)	8.817E9	8.533E9
Damping (Nm)	2.227E8	4.593E8

CRediT authorship contribution statement

Haoran Li: Conceptualization, Methodology, Software, Validation, Investigation, Formal analysis, Data curation, Writing – original draft. **Erin E. Bachynski-Polić:** Conceptualization, Methodology, Resources, Writing – review & editing, Supervision.

Declaration of competing interest

The authors declare that they have no known competing financial interests or personal relationships that could have appeared to influence the work reported in this paper.

Acknowledgements

The author Haoran Li gratefully acknowledges the financial support from China Scholarship Council (CSC). Computing time on Vilje is granted by the Norwegian Research Council (Program for Supercomputing, under project nn9676k).

Appendix A. Supplementary data

Supplementary data to this article can be found online at https://doi.org/10.1016/j.oceaneng.2021.109130.

References

Berberović, E., van Hinsberg, N.P., Jakirlić, S., Roisman, I.V., Tropea, C., 2009. Drop impact onto a liquid layer of finite thickness: dynamics of the cavity evolution. Phys. Rev. 79 (3), 036306.

Borg, M., Utrera Ortigado, E., Collu, M., Brennan, F.P., 2013. Passive Damping Systems for Floating Vertical axis Wind Turbines Analysis. European wind energy Conference, pp. 3–7.

Bozonnet, P., Emery, A., 2015. CFD simulations for the design of offshore floating wind platforms encompassing heave plates. In: The Twenty-Fifth International Ocean and Polar Engineering Conference. International Society of Offshore and Polar Engineers.

Brown, S.A., Magar, V., Greaves, D.M., Conley, D.C., 2014. An evaluation of RANS turbulence closure models for spilling breakers. Coast. Eng. Proc. (34) 5-5.

Bruinsma, N., Paulsen, B., Jacobsen, N., 2018. Validation and application of a fully nonlinear numerical wave tank for simulating floating offshore wind turbines. Ocean Eng. 147, 647–658.

Burmester, S., Gueydon, S., Vaz, G., el Moctar, B., 2017. Surge decay simulations of a semi-submersible floating offshore wind turbine. In: Proceedings of the 20th Numerical Towing Tank Symposium, pp. 2–3.

Burmester, S., Vaz, G., el Moctar, O., 2020a. Towards credible CFD simulations for floating offshore wind turbines. Ocean Eng. 209, 107237.

Burmester, S., Vaz, G., Gueydon, S., el Moctar, O., 2020b. Investigation of a semi-submersible floating wind turbine in surge decay using CFD. Ship Technol. Res. 67 (1), 2–14.

Chakrabarti, S.K., 1994. Advanced series on ocean engineering. In: Offshore Structure Modeling, vol. 9. World scientific.

Chua, K.H., Clelland, D., Huang, S., Sworn, A., 2005. Model experiments of hydrodynamic forces on heave plates. Int. Conf. Offshore Mech. Arctic Eng. 943–948.

Cordle, A., Jonkman, J., 2011. State of the Art in Floating Wind Turbine Design Tools. National Renewable Energy Lab.(NREL), Golden, CO (United States).

Cozijn, H., Uittenbogaard, R., Brake, E.t., 2005. Heave, roll and pitch damping of a deepwater CALM buoy with a skirt. In: The Fifteenth International Offshore and Polar Engineering Conference. International Society of Offshore and Polar Engineers.

Devolder, B., Rauwoens, P., Troch, P., 2017. Application of a buoyancy-modified k-ω SST turbulence model to simulate wave run-up around a monopile subjected to regular waves using OpenFOAM®. Coast. Eng. 125, 81–94.

Dudley Brian, S., 1961. A single formula for the "law of the wall. J. Appl. Mech. 28 (3), 455–458.

Dunbar, A.J., Craven, B.A., Paterson, E.G., 2015. Development and validation of a tightly coupled CFD/6-DOF solver for simulating floating offshore wind turbine platforms. Ocean Eng. 110, 98–105.

Dütsch, H., Durst, F., Becker, S., Lienhart, H., 1998. Low-Reynolds-number flow around an oscillating circular cylinder at low Keulegan–Carpenter numbers. J. Fluid Mech. 360, 249–271.

Fan, W., Anglart, H., 2020. varRhoTurbVOF: a new set of volume of fluid solvers for turbulent isothermal multiphase flows in OpenFOAM. Comput. Phys. Commun. 247, 106876.

Ferziger, J.H., Perić, M., Street, R.L., 2002. Computational Methods for Fluid Dynamics. Springer.

Gao, Z., Efthymiou, M., Cheng, L., Zhou, T., Minguez, M., Zhao, W., 2020. Hydrodynamic damping of a circular cylinder at low KC: experiments and an associated model. Mar. Struct. 72, 102777.

Hirt, C.W., Nichols, B.D., 1981. Volume of fluid (VOF) method for the dynamics of free boundaries. J. Comput. Phys. 39 (1), 201–225.

Jacobsen, N.G., Fuhrman, D.R., Fredsøe, J., 2012. A wave generation toolbox for the open-source CFD library: OpenFOAM®. Int. J. Numer. Methods Fluid. 70 (9), 1073–1088.

Launder, B.E., Spalding, D.B., 1983. The Numerical Computation of Turbulent Flows, Numerical Prediction of Flow, Heat Transfer, Turbulence and Combustion. Elsevier, pp. 96–116.

Lefebvre, S., Collu, M., 2012. Preliminary design of a floating support structure for a 5 MW offshore wind turbine. Ocean Eng. 40, 15–26.

Lopez-Pavon, C., Souto-Iglesias, A., 2015. Hydrodynamic coefficients and pressure loads on heave plates for semi-submersible floating offshore wind turbines: a comparative analysis using large scale models. Renew. Energy 81, 864–881.

Menter, F., Ferreira, J.C., Esch, T., Konno, B., Germany, A., 2003a. The SST turbulence model with improved wall treatment for heat transfer predictions in gas turbines. Proc. Int. Gas Turbine Congr. 2–7.

Menter, F.R., Kuntz, M., Langtry, R., 2003b. Ten years of industrial experience with the SST turbulence model. Turbulence, Heat Mmass Transfer 4 (1), 625–632.

Moreno, J., Cameron, M., Thiagarajan, K.P., Mendoza, C.A.G., 2015. Hydrodynamic performance of heave plates on floating offshore wind turbine platforms. In: The Twenty-Fifth International Ocean and Polar Engineering Conference. International Society of Offshore and Polar Engineers.

Nallayarasu, S., Bairathi, K., 2014. Hydrodynamic response of spar hulls with heave damping plate using simplified approach. Ships Offshore Struct. 9 (4), 418–432.

Peiffer, A., Roddier, D., Aubault, A., 2011. Design of a point absorber inside the WindFloat structure. Int. Conf. Offshore Mech. Arctic Eng. 247–255.

Philip, N.T., Nallayarasu, S., Bhattacharyya, S., 2019. Experimental investigation and CFD simulation of heave damping effects due to circular plates attached to spar hull. Ships Offshore Struct. 14 (4), 396–411.

Rahman, M.M., Karim, M.M., Alim, M.A., 2007. Numerical investigation of unsteady flow past a circular cylinder using 2-D finite volume method. J. Nav. Architect. Mar. Eng. 4 (1), 27–42.

Robertson, A., Bachynski, E.E., Gueydon, S., Wendt, F., Schünemann, P., 2020a. Total experimental uncertainty in hydrodynamic testing of a semisubmersible wind turbine, considering numerical propagation of systematic uncertainty. Ocean Eng. 195, 106605.

Robertson, A., Gueydon, S., Bachynski, E., Wang, L., Jonkman, J., Alarcón, D., Amet, E., Beardsell, A., Bonnet, P., Boudet, B., 2020b. OC6 Phase I: Investigating the Underprediction of Low-Frequency Hydrodynamic Loads and Responses of a Floating Wind Turbine. TORQUE.

Robertson, A., Jonkman, J., Masciola, M., Song, H., Goupee, A., Coulling, A., Luan, C., 2014. Definition of the Semisubmersible Floating System for Phase II of OC4. No. NREL/TP-5000-60601. National Renewable Energy Lab.(NREL), Golden, CO (United States).

Robertson, A., Jonkman, J., Wendt, F., Goupee, A., Dagher, H., 2016. Definition of the OC5 DeepCwind Semisubmersible Floating System. Technical report NREL.

Robertson, A.N., 2017. Uncertainty Analysis of OC5-DeepCwind Floating Semisubmersible Offshore Wind Test Campaign. NREL/CP-5000-68035. National Renewable Energy Lab.(NREL), Golden, CO (United States).

Robertson, A.N., Wendt, F., Jonkman, J.M., Popko, W., Dagher, H., Gueydon, S., Qvist, J., Vittori, F., Azcona, J., Uzunoglu, E., 2017. OC5 project phase II: validation of global loads of the DeepCwind floating semisubmersible wind turbine. Energy Procedia 137, 38–57.

Sauder, T., Chabaud, V., Thys, M., Bachynski, E.E., Sæther, L.O., 2016. Real-time hybrid model testing of a braceless semi-submersible wind turbine: Part I—the hybrid approach. In: ASME 2016 35th International Conference on Ocean, Offshore and Arctic Engineering. American Society of Mechanical Engineers Digital Collection.

Tao, L., Dray, D., 2008. Hydrodynamic performance of solid and porous heave plates. Ocean Eng. 35 (10), 1006–1014.

Veritas, D.N., 2010. WADAM User Manual. Høvik, Norway.

Wang, B., Xu, Z., Li, C., Wang, D., Ding, Q., 2020. Hydrodynamic characteristics of forced oscillation of heave plate with fractal characteristics based on floating wind turbine platform. Ocean Eng. 212, 107621.

Wei, Y.-f., Yang, J.-m., Chen, X., 2010. A Review of the Hydrodynamic Performance of Heave Damping Plates on Spar Platform [J]. China Offshore Platform 6.

Weller, H.G., Tabor, G., Jasak, H., Fureby, C., 1998. A tensorial approach to computational continuum mechanics using object-oriented techniques. Comput. Phys. 12 (6), 620–631.

Wilcox, D.C., 1998. Turbulence Modeling for CFD. DCW industries La Canada, CA.

Zhang, S., Ishihara, T., 2018. Numerical study of hydrodynamic coefficients of multiple heave plates by large eddy simulations with volume of fluid method. Ocean Eng. 163, 583–598.

B.4 Paper 4

Paper 4:

Haoran Li and Erin E. Bachynski-Polić. Validation and application of nonlinear hydrodynamics from CFD in an engineering model of a semi-submersible floating wind turbine. *Marine Structures* 2021. **79**:103054. `https://doi.org/10.1016/j.marstruc.2021.103054`

Marine Structures 79 (2021) 103054

Contents lists available at ScienceDirect

Marine Structures

journal homepage: www.elsevier.com/locate/marstruc

Validation and application of nonlinear hydrodynamics from CFD in an engineering model of a semi-submersible floating wind turbine

Haoran Li [a,*], Erin E. Bachynski-Polić [a,b]

[a] *Department of Marine Technology, Norwegian University of Science and Technology (NTNU), Trondheim, Norway*
[b] *Centre for Autonomous Marine Operations and Systems (AMOS), NTNU, Trondheim, Norway*

ARTICLE INFO

Keywords:
Semi-submersible floating wind turbine
QTF
Added mass
Damping
Dynamic responses
Damage equivalent load

ABSTRACT

Nonlinear hydrodynamics play a significant role in accurate prediction of the dynamic responses of floating wind turbines (FWTs), especially near the resonance frequencies. This study investigates the use of computational fluid dynamics (CFD) simulations to improve an engineering model (based on potential flow theory with Morison-type drag) by modifying the second-order difference-frequency quadratic transfer functions (QTFs) and frequency-dependent added mass and damping for a semi-submersible FWT. The results from the original and modified engineering models are compared to experimental data from decay tests and irregular wave tests. In general, the CFD results based on forced oscillation tests suggest increasing the frequency-depending added mass and damping at low frequencies compared to first order potential flow theory. The modified engineering model predicts natural periods close to the experimental results in decay tests (within 5%), and the underprediction of the damping is reduced compared to the original engineering model. The motions, mooring line tensions and tower-base loads in the low-frequency response to an irregular wave are underestimated using the original engineering model. The additional linear damping increases this underestimation, while the modified QTFs based on CFD simulations of a fixed floater in bichromatic waves result in larger difference-frequency wave loads. The combined modifications give improved agreement with experimental data in terms of damage equivalent loads for the mooring lines and tower base.

1. Introduction

One of the challenges facing the development of floating wind turbines (FWTs) is to accurately predict the global responses due to nonlinear hydrodynamic loads on the floater [1–5]. In the present work, the focus is on a semi-submersible FWT, known as "DeepCWind", which consists of four cylindrical columns linked with a set of braces, defined by Robertson et al. [6,7].

Numerous investigations [8–12] have used potential flow theory, typically combined with a Morison-type viscous drag model, to predict the hydrodynamic loads on various semi-submersible FWTs. The second-order sum- and difference-frequency wave-excitation loads have been shown to excite eigenfrequencies of semi-submersible floating systems, leading to larger low-frequency motions that strain the mooring system [9] or to structural vibrations [12]. The use of the full QTF instead of Newman's approximation is known to

---

[*] Corresponding author.
E-mail address: haoran.li@ntnu.no (H. Li).

https://doi.org/10.1016/j.marstruc.2021.103054
Received 24 March 2021; Received in revised form 28 April 2021; Accepted 2 June 2021

better simulate the dynamic responses of semi-submersible FWTs [12]. Gueydon et al. [10] concluded that the second-order difference-frequency loads have significant effects on the dynamic responses of semi-submersible FWTs, while sum-frequency loads have negligible contributions to the motions. Additionally, Xu et al. [13] found the effect of difference-frequency wave loads on the responses of FWTs was more significant as the water depth decreased. Furthermore, Luan et al. [14] illustrated the importance of the viscous drag force from Morison's equation, especially related to the excitation and damping of resonant motions. Correctly choosing the drag coefficient often requires model tests or higher fidelity numerical models.

In the present work, an approach with first and second order potential flow theory combined with Morison-type drag will be referred to as an "engineering model". In the international collaboration project known as OC5 (Phase II) [4], Robertson et al. found that engineering models severely underpredicted the low-frequency nonlinear wave loads and dynamic responses of a semi-submersible FWT because these models limit hydrodynamic modeling to linear or weakly nonlinear models. In the OC5 project [4], all of the participants who used a combination of potential flow and Morison-type drag underestimated both the extreme tower base loads and damage equivalent loads in a wave-only condition by 10–40% compared to the experimental results. The main underprediction was attributed to the responses at the pitch natural frequency. On the other hand, Wang et al. [15] and Benitz et al. [16,17] demonstrated that computational fluid dynamics (CFD) methods have the potential ability to more precisely predict nonlinear difference-frequency wave loads and capture shadowing effects and transverse forces from vortex shedding, but at a significantly higher computational cost.

In addition to the nonlinear wave loads, hydrodynamic coefficients, such as added mass or damping coefficients, also significantly affect the dynamic responses of a semi-submersible FWT when using engineering models. For example, Wei et al. [5] found the heave plates of a semi-submersible FWT provide additional added mass and enhance the flow separation and vortex shedding processes. The existence of heave plates (see the left subplot of Fig. 1) together with the interactions between columns and braces generate more stringent requirements for the fidelity of simulation tools. Compared to CFD methods, Lopez-Pavon et al. [18] and Bozonnet et al. [19] found potential flow theory did not predict the increased added mass due to the edge of heave plates and underestimated the added mass for a platform with heave plates. In addition, CFD methods found the added mass and damping were largely dependent on the motion amplitude and viscous effects were predominant in the damping term, both of which are incompatible with the assumptions of linear potential flow theory. Some studies [19–21] extracted the damping coefficients from CFD simulations of free decay motions of a semi-submersible FWT and demonstrated that CFD methods can better quantify the viscous damping characteristics.

Dynamic responses of FWTs to regular waves have been simulated and compared by the engineering models and CFD methods [22–25]. When nonlinear phenomenon were not dominant, the results obtained by the engineering models and CFD methods showed reasonable agreement, while larger discrepancies occurred for highly nonlinear regular waves.

In the current study, the difference-frequency surge force and pitch moment QTFs from second-order potential flow theory are modified based on the estimated difference-frequency wave loads on a restrained floater subjected to bichromatic waves in the CFD simulations. The frequency-dependent added mass and damping coefficients from the first-order potential flow theory are modified based on the calculated linearized added mass and damping coefficients from CFD simulations of forced oscillations around the surge, heave and pitch natural periods. The engineering tool with modified QTFs and added mass and damping coefficients is then validated against the free decay motions in surge, heave, and pitch (from both CFD simulations and experiments), and responses in irregular waves (from experiments). Furthermore, the consequences of the modifications on the estimation of short-term extreme response statistics and damage equivalent loads of mooring lines and tower base are investigated.

The organization of this paper is as follows. Section 2 describes the experimental setups. The modifications of QTFs and added mass and damping coefficients are presented in Section 3 together with the introduction of engineering model and the methodology for analyzing the results. The surge, heave and pitch decay are examined in Section 4.1, while the dynamic responses and damage equivalent loads under irregular waves are analyzed in Section 4.2. Conclusions are drawn in Section 5.

2. Experiment setup

In the present work, in order to validate the engineering model with modified nonlinear hydrodynamics from CFD and investigate

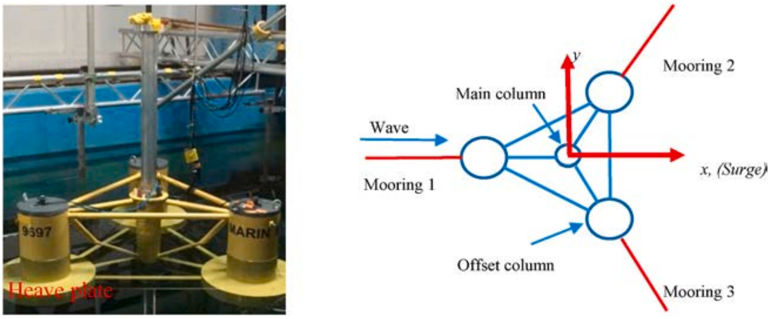

Fig. 1. DeepCwind semi-submersible FWT (left: Geometry of FWT [26], right: Mooring system).

the resulting dynamic responses due to nonlinear hydrodynamic loads, two sets of experimental data are considered. In Phase I of the Offshore Code Comparison Collaboration, Continued, with Correlation, and unCertainty (OC6), the semi-submersible was subjected to wave loads in a narrow towing tank. A linear mooring system was applied, and tower base loads were not measured. In Phase II of the Offshore Code Comparison Collaboration, Continued, with Correlation (OC5) project, the same floater geometry (left subplot of Fig. 1) was tested in an ocean basin, with a catenary mooring system, and with an instrumented flexible tower. Both sets of experiments were conducted at the Maritime Research Institute Netherlands (MARIN) for the same OC5-DeepCwind semi-submersible floater [7] at 1:50 scale. A summary of floater geometry is given in Table 1. The right-handed coordinate system used here originates at the center of the floater at the still water line, with positive y towards the starboard column, and z upward. All data and results are given at full scale in this paper, except when explicitly mentioned.

For the configuration of OC6 project shown in the right subplot of Fig. 1, the wind turbine was removed, but the inertial properties of the floater with tower correspond to the total inertial properties of system in the OC5 Project. Considering the limitation of basin width (Table 2), the mooring system in the OC6 project consisted of 3 taut-spring-lines to reproduce the equivalent linear stiffness of the catenary system in the OC5 project. Robertson et al. [7,26] provide the dimensions and structural properties of the system in the OC5 and OC6 projects. The global motions, such as surge (x-displacement), heave (z-displacement) and pitch (y-rotation), the mooring line tensions, and tower base loads were measured. Table 2 also compares the water depth and the parameters of the selected irregular wave following the JONSWAP wave spectrum in the OC5 and OC6 projects which are nearly identical.

3. Methodology

The CFD simulations to estimate the difference-frequency QTFs (section 3.2) and frequency-dependent added mass and damping (section 3.3) were performed with the open-source CFD toolbox OpenFoam [27] where the two-phase incompressible Navier-Stokes equations were solved. The Volume-Of-Fluid method [28] was used to capture the free surface and a six-degree of freedom solver was coupled to solved the flow-dependent motions [22]. The $k-\omega$ SST turbulence model was applied. See previous works [29,30] for additional details.

3.1. Time-domain analysis

The time-domain analysis is performed using the engineering model SIMA (SIMO-RIFLEX) [31,32] which is developed by SINTEF Ocean. The floater and the rotor-nacelle-assembly (RNA) are modelled as rigid bodies, while the mooring lines and tower are represented as nonlinear bar or beam elements, respectively. The first-order wave-excitation forces and second-order sum-frequency wave forces on the floater are estimated based on the potential flow theory [33]. However, the added mass, damping and second-order difference-frequency wave forces are modified based on the CFD simulations. In addition, viscous effects are considered by applying drag forces of Morison's equation to the columns and cross braces. A constant drag coefficient in the normal direction (0.774, based on towing tests [26]) is applied for each part of the floater and a drag coefficient in the axial direction (2.48, based on previous comparisons of a similar engineering tool with experimental data from the DeepCwind test campaign [6]) is applied for the heave plates of the floater.

The added mass and damping are applied as radiation forces in time domain using the convolution technique [34], and the motions of the floater can be represented as:

$$[\mathbf{M}+\mathbf{A}(\infty)]\ddot{\mathbf{x}}(\mathrm{t})+\int_{-\infty}^{\infty}K(t-\tau)\dot{\mathbf{x}}(\tau)d\tau+\mathbf{C}\mathbf{x}(t)=\mathbf{F}^{(1)}+\mathbf{F}^{(2)}+\mathbf{F}^{(\mathrm{D})}+\mathbf{F}^{(\mathrm{R})} \tag{1}$$

where M is the mass of the floater, $A(\infty)$ is the infinite-frequency added mass, $\ddot{x}, \dot{x}$, and $\mathbf{x}$ are the acceleration, velocity and displacement of the floater, respectively. $K(t-\tau)$ is the retardation function which represents the fluid memory and is calculated from the frequency-dependent damping. $\mathbf{C}$ is the hydrostatic restoring, $\mathbf{F}^{(1)}$ is the first-order wave excitation force, $\mathbf{F}^{(2)}$ is the second-order mean, rapidly varying and slowly varying wave drift force, $\mathbf{F}^{(\mathrm{D})}$ is Morison drag force and $\mathbf{F}^{(\mathrm{R})}$ are the forces from RIFLEX elements, such as mooring lines and tower.

Different combinations of modifications based on CFD are considered in the SIMA simulations, ranging from none (SIMA-W) to all (SIMA-C), as summarized in Table 3. All SIMA models include automatically added linear damping to ensure that cutting-off the retardation function does not result in negative damping. In addition, extra linear damping (Table 3) which is determined by matching the calculated free decay motions of the floater from the CFD simulations is included in SIMA-WL. When comparing with experimental

Table 1
OC5-DeepCwind semi-submersible floater geometry.

Total draft	20.0 m
Diameter of main column	6.5 m
Diameter of offset (upper) column	12.0 m
Diameter of heave plate	24.0 m
Center-center distance between two offset columns	50.0 m

Table 2
Water depth, basin width and irregular wave conditions from the OC5 and OC6 projects.

	OC5 project	OC6 project
Water depth (m)	200.0	180.0
Basin width (m)	36.0	4.0
Significant wave height (m)	7.1	7.4
Peak period (s)	12.1	12.0
Peak enhancement factor (−)	2.2	3.3

results, for all SIMA models, the wave is obtained by filtering the experimentally measured wave elevation at the origin by a high-pass filter with a 0.005 Hz cut-off frequency. All irregular wave components are treated as linear, and assumed to travel in the positive x-direction. In addition, a series of irregular waves with significant wave height $H_s = 7.1$ m, peak period $T_p = 12.1$ s and different wave seeds are selected to predict the short-term extreme values. These irregular waves are generated in SIMA based on the JONSWAP spectrum with the peak enhancement factor equal to 3.3.

3.2. Hydrodynamic added mass and damping with CFD simulations

To estimate the hydrodynamic added mass and damping near the resonance frequencies, several forced oscillations around the surge, heave and pitch natural periods were performed using CFD model [29]. The first harmonic component of the hydrodynamic wave load was extracted and decomposed into in-phase and out-of-phase components to find the added mass and linearized damping. The pitch moment from forced oscillations in surge and the surge force from forced oscillations in pitch are used to calculate cross terms (pitch-surge/surge-pitch).

The first-order radiation solution is used to calculate the added mass and damping in potential flow theory. However, the assumption of inviscid flow requires the potential flow solutions to be augmented with viscous effects by including Morison-type drag. In WAMIT [33], the results include the frequency-dependent added mass and damping from the columns, the frequency-independent added mass of the braces calculated by applying the inertial term of Morison's equation (the added mass coefficient is 1.0) and linearized damping of the columns and braces obtained from the drag term of Morison's equation applying the Fourier-averaged approach.

Because Morison drag forces on the columns and braces are calculated separately in the time domain analysis, the linearized damping from Morison-type drag should be deducted from the damping of CFD simulations when modifying the damping from WAMIT. The added mass and damping near the resonance frequencies are replaced with CFD results. To obtain coefficients for frequencies without CFD results available, for the regions below the resonance frequencies, the gradient remains constant. When the frequency is larger than the resonance frequencies, the gradient varies to ensure a smooth transition from CFD results to WAMIT results (dashed line in Fig. 2). Because the pitch-surge results are equal to the surge-pitch results, only surge (11), heave (33), pitch (55) and pitch-surge (51) added mass (A) and damping (B) are presented in Fig. 2. The other terms are calculated in WAMIT and not shown in this paper. In SIMA, the retardation function is obtained based on the modified frequency-dependent damping. The infinite-frequency added mass is then modified to give the best match between the added mass calculated from the retardation function and the input (modified) frequency-dependent added mass.

The results in Fig. 2 show that the potential flow theory underestimates the amplitude of the added mass at low frequencies by over 10%. A possible explanation is that flow separation and the formation of eddies at the edge of the heave plates change the phase of the pressure relative to the floater motion. Based on the comparisons of damping, the quadratic damping from Morison drag force underestimates the nonlinear viscous damping. The difference depends on the selected drag coefficient (See Sec. 3.1).

3.3. Difference-frequency quadratic transfer functions with CFD simulations

In previous work, CFD simulations were used to calculate the difference-frequency wave loads on a restrained semi-submersible FWT subjected to 24 pairs of bichromatic waves [30]. The bichromatic waves were generated by adding together two regular waves with different wave frequencies. The first order components of bichromatic waves were close to the peak periods of the irregular wave while the difference frequency aligned with either the surge or pitch natural frequency of the FWT where the largest wave-induced responses can be excited in irregular waves [35]. The wave amplitudes (around 1.75 m) of wave component were determined by making the calculated maximum wave height when two waves are added linearly close to the wave height of the

Table 3
Overview of different settings for time-domain simulations in SIMA.

Label	Difference-frequency QTF	Added mass and damping	Additional linear damping
SIMA-W	Potential flow theory	Potential flow theory	x
SIMA-WL	Potential flow theory	Potential flow theory	√
SIMA-CA	Potential flow theory	CFD (forced oscillations)	x
SIMA-CQ	CFD (bichromatic waves)	Potential flow theory	x
SIMA-C	CFD (bichromatic waves)	CFD (forced oscillations)	x

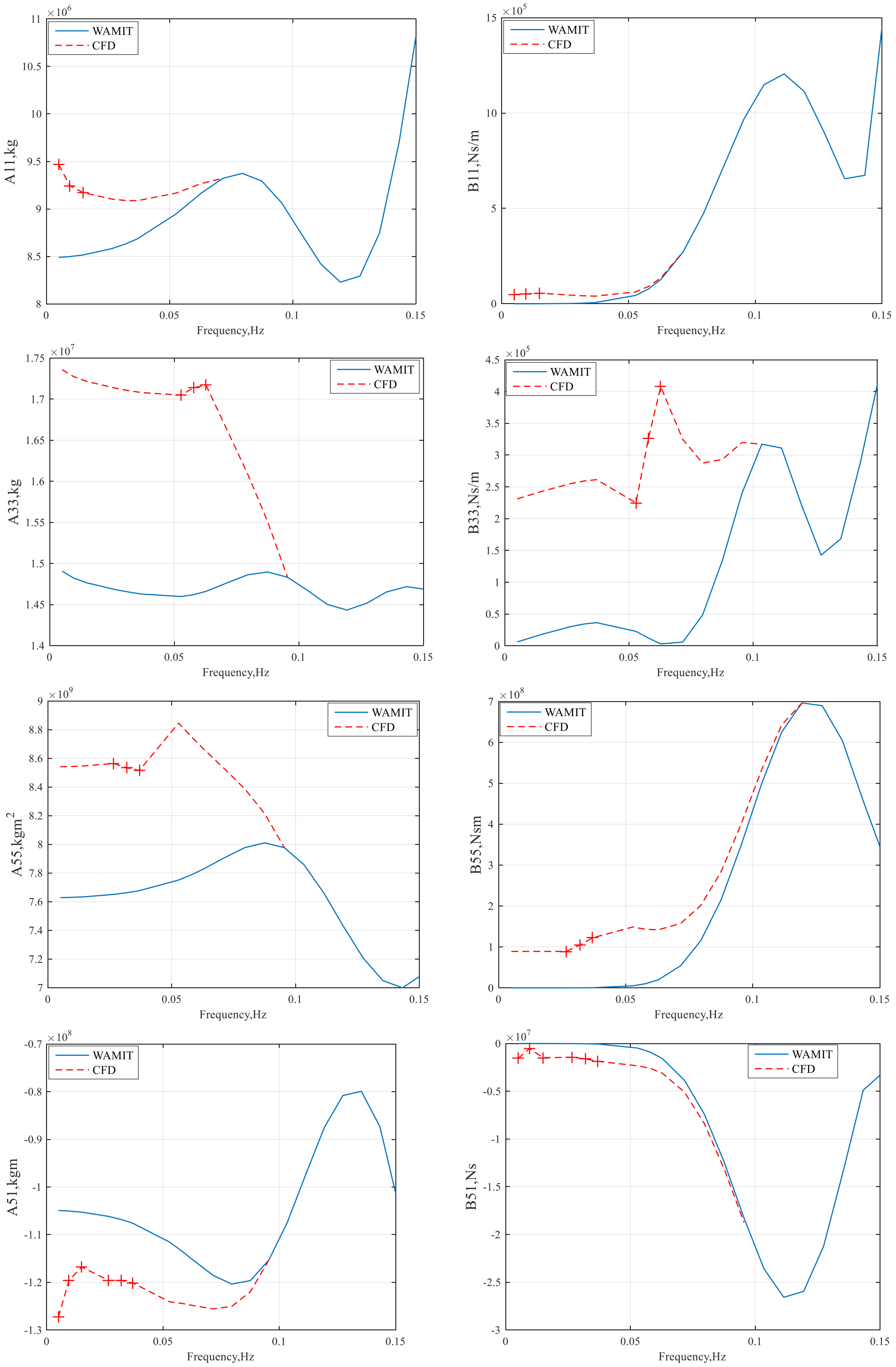

Fig. 2. Comparisons of the added mass and damping between CFD and WAMIT ("+" represents the CFD results from forced oscillation simulations).

irregular-wave (7.1 m) [35]. However, wave amplitudes decreased for shorter wave periods due to the occurrence of significant wave damping in the CFD simulations. The amplitudes and phases of difference-frequency wave loads and each harmonic component of the bichromatic waves were calculated by fitting a second order expansion model to the steady-state part of the numerical time signal with a least squares procedure. Then the values of the QTFs for each of the 24 frequency combinations were calculated by comparing the amplitudes and phases between difference-frequency wave loads and incident waves.

The second-order potential flow theory approximates the nonlinear free-surface boundary condition and wave-body interaction, including the quadratic interaction of first-order quantities. Hence, the second-order wave loads are computed by sum of quadratic contributions from the first-order solution, as well as contributions given by the solution of the second-order velocity potential. See Pinkster [36] for details. WAMIT [33] can completely calculate the second-order velocity potential by including the contributions of incoming wave, diffracted and radiated wave and is used in the current research.

In the CFD simulations, the floater was restrained. The QTFs for the fixed condition ($\text{QTF}_{\text{CFD,fixed}}$) were estimated by subtracting the contributions of the Morison drag and the difference-frequency wave components. However, the contributions due to the first-order motions were not included in the CFD results. Because the first-order motion is predicted well by the first-order potential flow solution, it is assumed that the contribution due to the first-order motion can be accurately estimated by the difference of QTFs for the fixed and floating floater in WAMIT. Hence, the QTF values based on CFD simulations for the floating condition are expressed as:

$$QTF_{CFD,floating} = QTF_{CFD,fixed} + \left(QTF_{WAMIT,floating} - QTF_{WAMIT,fixed}\right). \tag{2}$$

Taking advantage of symmetry relations, we consider the upper-left-half ($f_2 \geq f_1$ in the left subplot of Fig. 3) when discussing how the QTF from potential flow is modified. The diagonal of the difference-frequency QTF matrix ($f_2 = f_1$) represents the mean drift force, which only depends on first order information and is not modified. The amplitudes and phases of QTFs from WAMIT along the surge and pitch natural frequencies are replaced with the available results from CFD simulations. To propagate the correction to other parts of the QTFs, the WAMIT magnitudes or phases with the same f_2 are extracted and corrected based on the results from CFD model. There are two different cases: in case (1), regions with only one value from CFD model, the gradient is maintained to be the same before and after modification; in case (2), regions with two values from CFD model or one value from CFD and one value from WAMIT, the gradient varies linearly between CFD values or CFD and WAMIT values. An example is shown in the right subplot of Fig. 3. The modified QTF is referred to as 'New QTF'. 'Old QTF' is the QTF estimated in WAMIT. Additional details regarding the bichromatic wave simulations and modification procedure for the fixed structure can be found in the previous publication [30].

The magnitudes and phases of the old and new surge force QTF for the floating semi-submersible are presented in Fig. 4. Close to the surge natural frequency, the magnitudes of the new QTF are close to the magnitudes of the old QTF for lower wave frequencies (0.05–0.09 Hz). At higher wave frequencies, the new QTF has higher magnitudes, especially around the pitch natural frequency. The phases of the new QTF follow a similar patten as the old QTF, but differ in value.

The new and old pitch moment QTFs are compared in Fig. 5. Compared to the QTF from potential flow theory, the new magnitudes have similar pattern and values except for the larger moments at the higher wave frequencies. The phase of the new QTF is similar to the old QTF, but big differences occur at the lower wave frequencies between surge and pitch natural frequency.

3.4. Damage equivalent loads

Engineering global analysis models can be used to obtain time series of loads in certain FWT components, such as the tower or mooring lines [37,38]. When comparing against experimental results in irregular waves, the damage equivalent loads can provide a useful metric for comparing results. For a given time series of loads from experiments or simulations, the total damage (D) can be determined based on Miner's rule by linearly accumulating the damage from each stress or tension level:

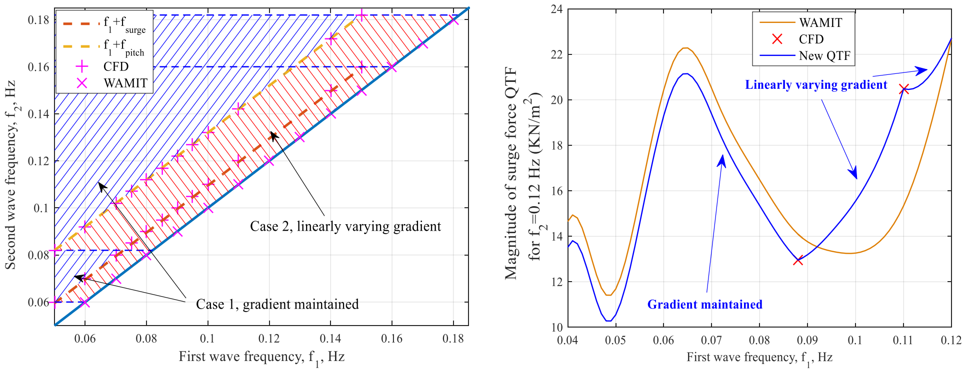

Fig. 3. Different regions of the QTF for modification.

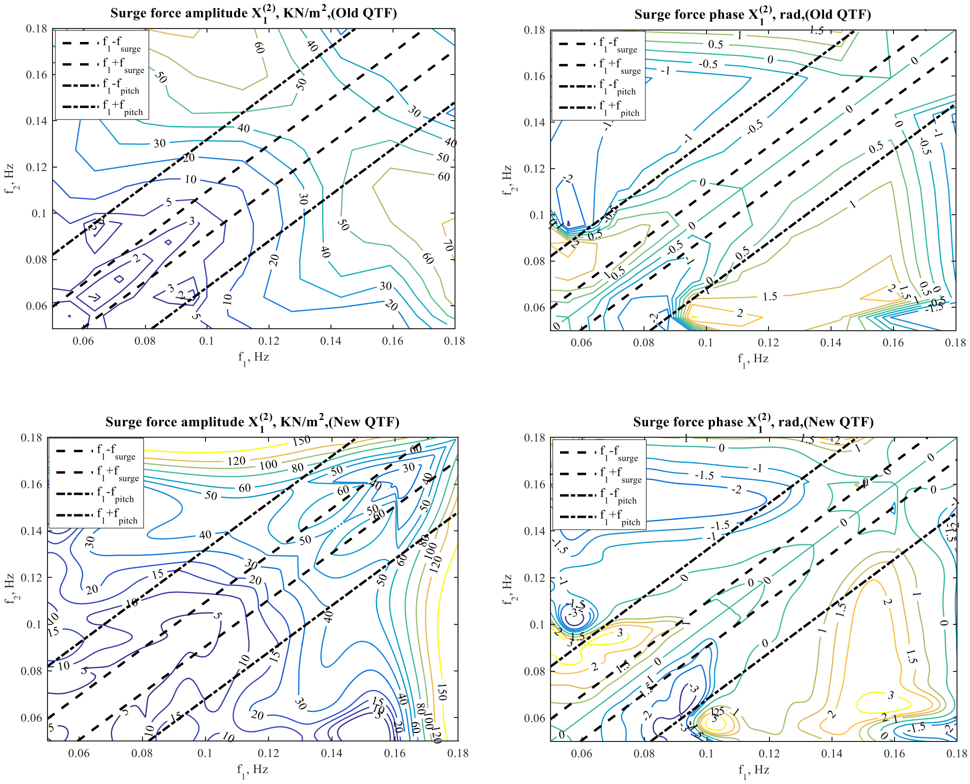

Fig. 4. Magnitudes and phases of surge force QTF.

$$D = \sum_i \frac{n_i}{N_i} \tag{3}$$

where n_i is the number of cycles at the ith stress or tension range in the time series and N_i is the number of cycles to failure at the same stress or tension range according to the S–N curve. In the present work, damage equivalent loads, calculated using a Matlab-based tool (MLife [39]) are used as a metric to quantify the damage. The S–N curve is given as

$$N_i = \left(\frac{\sigma^{ult} - |\sigma^{MF}|}{1/2\sigma_i} \right)^m \tag{4}$$

where σ_i is the ith stress or tension range. σ^{ult} is the ultimate design stress or tension of the material, σ^{MF} is the fixed mean stress or tension value in the time series and m is the Wöhler exponent. The rainflow counting method [40] is applied to count the cycles. The damage equivalent load σ^E is a constant-amplitude damage-load at a fixed frequency that produces equivalent damage as the variable loads.

$$D = \frac{n^E}{N^E} \tag{5}$$

$$n^E = f^E \cdot T \tag{6}$$

$$N^E = \left(\frac{\sigma^{ult} - |\sigma^{MF}|}{1/2\sigma^E} \right)^m \tag{7}$$

where n^E is the total equivalent damage counts in the time series, f^E is the frequency of the damage equivalent load, T is the elapsed time of time series and σ^E is found by forcing Eq. (5) to be equal to Eq. (3).

The damage equivalent load of mooring line is estimated based on the tension and the damage equivalent load at the tower base is calculated based on the axial stress. The frequency f^E is taken as 1 Hz and a Wöhler exponent $m = 3$ is used. The tower base coordinate system is illustrated in Fig. 6. Since the wave propagates along x-axis in this paper, it is sufficient to take the point B as an example for

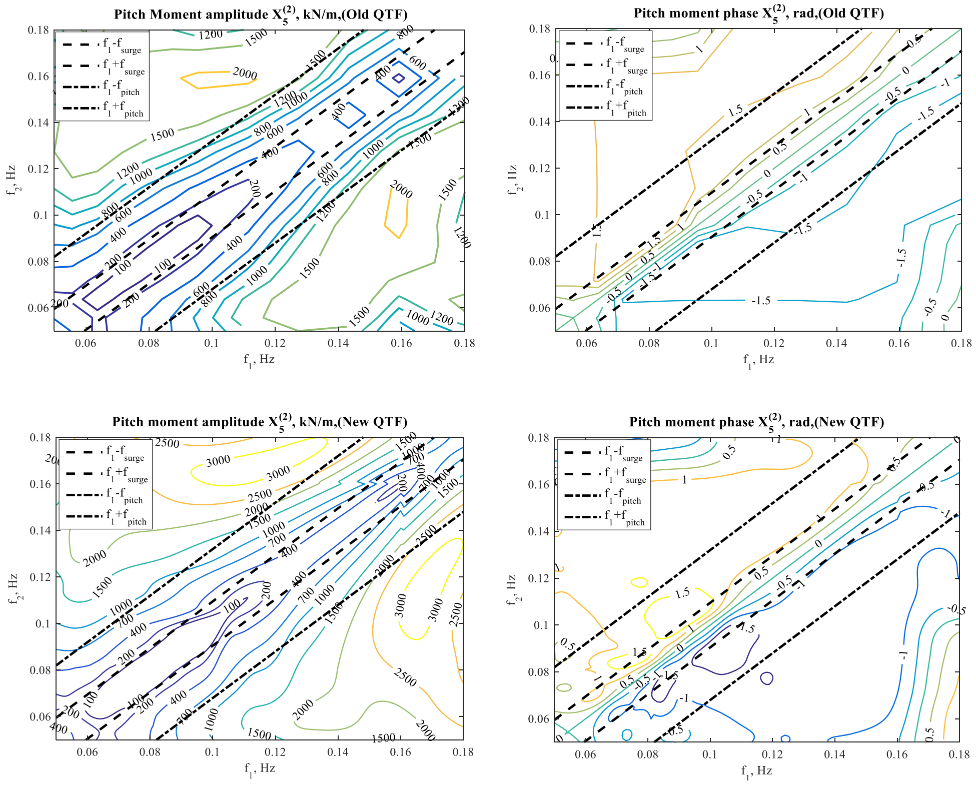

Fig. 5. Magnitudes and phases of pitch moment QTF.

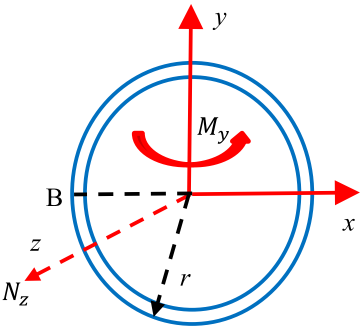

Fig. 6. Coordinate system of tower base (top view).

the damage analysis. Ignoring the cross-section deformation after the loads are exerted, the axial stress is equal to the nominal axial stress:

$$\sigma_B = \frac{N_z}{A} + \frac{M_y \cdot r}{I_y} \tag{8}$$

where N_z is the axial force, A is the nominal cross-sectional area, M_y, I_y are the moments and sectional moments of the area about the local y-axis, respectively, and r is the cross section radius.

3.5. Short-term extreme value prediction

The extreme value of a random stochastic process *X(t)* within a given time duration is defined as the maximum value from a sequence of individual local maxima and minima.

$$X_e = \max\left\{X_{\max 1}, X_{\max 2}, \ldots, X_{\max n,} |X_{\min 1}|, |X_{\min 2}|, \ldots, |X_{\min n}|\right\} \tag{9}$$

where X_e represents the extreme value and X_{maxi}, X_{mini} are the individual local maxima and minima, respectively. Based on the assumption that all individual local maxima and minima are independent and identically distributed with a common distribution function $F_X(x)$, the distribution of X_e can be expressed as:

$$F_{X_e}(x) = \mathrm{Prob}\{X_e \le x\} = [F_X(x)]^{2n} \tag{10}$$

When the number of samples $2n$ is large enough, the extreme value distribution (Eq. (10)) will converge towards one of three types of distributions: Gumbel, Fréchet and Weibull distributions. Among them, the Gumbel distribution is the most recommended model for marine structures subjected to wave loads [41] and implemented in the current research. The cumulative distribution probability F_{X_e} can be written as:

$$F_{X_e} = \exp(-\exp(-\alpha(x-\mu))) \tag{11}$$

where α is the scale parameter and μ is the location parameter.

4. Results and discussions

In this section, the results of the dynamic simulations are presented and discussed for free decay tests and freely floating motions under the irregular waves. The variations in the SIMA model are used to separate the effects of the modifications of the difference-frequency QTFs and added mass and damping.

4.1. Free decay tests

Free decay tests in still water are carried out to establish the natural periods and damping of the rigid body modes of motions. Free decay tests in surge, heave and pitch (Table 1) were carried out experimentally in the OC6 project and using all variations of the engineering model (Table 3) as well as CFD [29].

Damped natural periods are determined as the mean duration between two consecutive peaks or troughs of motion. Damping values are presented as a function of the amplitude of motion. The damping ratio (ξ^*) relative to the critical damping is calculated based on the logarithmic decrement (δ) for each cycle:

$$\delta = \ln \frac{x_n}{x_{n+1}} \tag{12}$$

where x_n and x_{n+1} are two consecutive peaks or troughs. The damping ratio is then computed as:

$$\zeta^* = \frac{1}{\sqrt{1 + \left(\frac{2\pi}{\delta}\right)^2}} \tag{13}$$

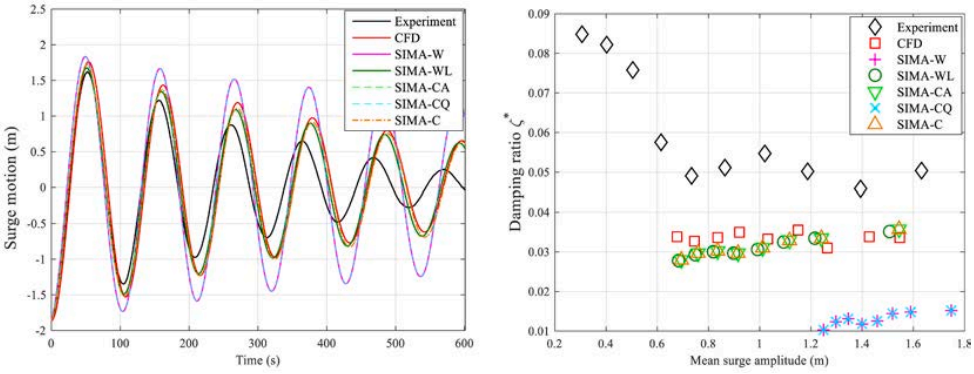

Fig. 7. Surge decay (left: decaying surge motion, right: surge damping ratio).

Both linear (given by the intercept) and quadratic (given by the slope) damping coefficients of the FWT can be estimated in this way. However, in some cases, especially for small motion amplitudes, there are large variations in the damping level.

4.1.1. Surge decay

The surge decay motions are compared in Fig. 7. All numerical models underestimate the damping compared to the experiment. However, the underestimation in the damping ratio in the CFD model is around 30%, while the original potential flow theory model (SIMA-W) underpredicts by approximately 70%. The upturning tail at small surge amplitudes in the experiment is likely due to mechanical friction [26]. This friction leads to a constant Coulomb-friction-type damping. In addition, the hydrodynamic linear damping (given by the intercept) dominates over the quadratic (given by the slope) in the experiment and all numerical models.

The modified difference-frequency surge force QTF has no effect on the free-decay surge motion (SIMA-W vs. SIMA-CQ, or SIMA-CA vs. SIMA-C). When the modified damping is used, the predicted damping in the engineering tool (SIMA-CA, SIMA-C) increases sharply and is quite close to the results in the CFD model. Similarly, after adding additional linear damping, SIMA-WL also shows similar damping as the CFD model.

All numerical models overestimate the surge natural period by around 4% compared to the experiment, as shown in Table 4. One possible reason is related to the uncertainty of mooring stiffness (about 10%) in the experiment [42] which reduces the surge natural period to around 105 s based on the analytical solution. However, the mooring stiffness has little influence on the damping [43]. The larger added mass in the modified model slightly increases the natural period (SIMA-W vs. SIMA-CA), as does the increased linear damping (SIMA-W vs SIMA-WL), but these effects are minor.

4.1.2. Heave decay

Fig. 8 shows the free decay in heave. The difference-frequency heave force QTF is not modified in the current research, only the added mass and damping are adjusted in SIMA-C. The motion amplitudes between experiment and all numerical models are in close proximity of each other, except the original potential flow theory model (SIMA-W). Compared to the experiment, the CFD model captures more linear damping (given by the intercept) and less quadratic damping (given by the slope). The original potential flow theory model (SIMA-W) severely underestimates the damping compared to the experiment and CFD model. However, due to the implementation of Morison-type drag, SIMA-W has similar quadratic damping (given by the slope) as the CFD model, and the difference between them comes from the linear damping. Hence, when adding linear damping, SIMA-WL captures similar damping as the CFD model. Because the frequency-dependent damping is modified based on the calculated linearized damping in the CFD simulations, the predicted damping in SIMA-C is close to the result in SIMA-WL.

Despite the difference in damping, all numerical models agree well with the experiment regarding the heave natural period (within 0.81%) as presented in Table 4.

4.1.3. Pitch decay

For the pitch decay, interaction between pitch and surge motions was observed in the experimental measurement due to the initial condition in the decay test. No such interaction was found in the CFD simulation. Hence, motions at the surge natural frequency are removed from the experimental signal by a high-pass filter with a 0.015 Hz cut-off frequency. The filtered experimental pitch motion is presented in Fig. 9 together with the results in all numerical models. All numerical models capture the damping well except for the underestimation in the SIMA-W and SIMA-CQ. Linear damping dominates the pitch damping, although the overall damping level in the experiment shows large variations.

As for the surge decay motion, the modified difference-frequency pitch moment QTF has no effect on the free-decay. When the modified damping (SIMA-CA, SIMA-C) or the added linear damping (SIMA-WL) is implemented, the predicted damping ratio in the engineering tools increases by around 75%.

Compared to the experiment, all numerical models slightly underpredict the pitch natural periods by up to 2.01% (Table 4). As in the analysis of the surge and heave natural periods, the larger added mass and damping in the CFD and modified SIMA models (SIMA-WL, SIMA-CA and SIMA-C) increase the pitch natural period, but the influence is quite small.

In conclusion, through modifying the added mass and damping based on the forced oscillations in CFD simulations, the engineering tools can capture similar damping as the CFD model in the free decay. Despite the difference in added mass and damping, the differences of predicted natural periods among the experiments and all numerical models are quite small.

Table 4
Natural periods obtained from experiments and numerical simulations.

	Surge (s)	Difference (%)	Heave (s)	Difference (%)	Pitch (s)	Difference (%)
Experiment	104.1	0	17.32	0	31.29	0
CFD	108.4	4.13	17.39	0.40	31.07	0.70
SIMA-W	108.1	3.84	17.18	0.81	30.66	2.01
SIMA-WL	108.2	3.94	17.19	0.75	30.67	1.98
SIMA-CA	109.1	4.80	N/A	N/A	30.96	1.05
SIMA-CQ	108.1	3.84	N/A	N/A	30.66	2.01
SIMA-C	109.1	4.80	17.33	0.058	30.96	1.05

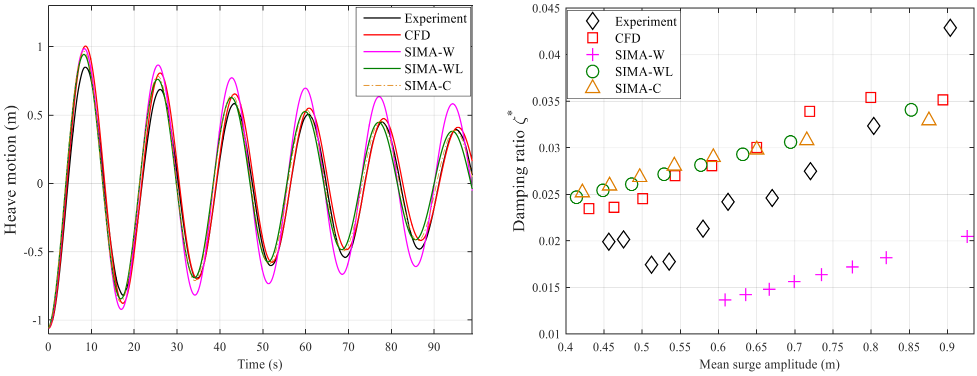

Fig. 8. Heave decay (left: decaying heave motion, right: heave damping ratio).

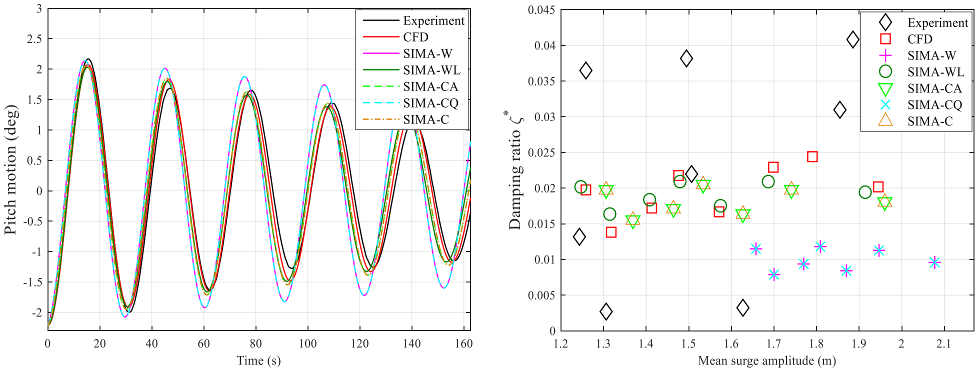

Fig. 9. Pitch decay (left: decaying pitch motion, Experiment: high-pass filtered results, right: pitch damping ratio).

4.2. Irregular wave cases

In order to assess the performance of the engineering model with modified hydrodynamics based on CFD simulations, numerical results in irregular waves are compared against experimental measurements (Table 2). All SIMA simulations are carried out for at least 12,600 s and the transient phase during the first 1800 s is eliminated to obtain a 3-h simulation. A response metric (referred to as ‘PSD sum’ [26]) is adopted to measure the dynamic responses both within and outside the wave frequency range. The power-spectral density (PSD) sum is an integration of the one-sided, discrete power density functions of the response in the frequency range of interest. The frequency ranges are shown in Table 5. These are determined based on the ranges over which the wave spectra were defined and natural frequencies in surge, pitch and heave motions.

The numerically calculated irregular waves in all SIMA models are compared to the experimentally measured irregular waves in the OC6 project in Fig. 10 and Table 6. There is good agreement between the numerical model and experiment except for small differences in the distribution of the largest wave elevations (>6 m) and the mean value. The PSD sums in low-frequency ranges are less than 1% of the energy from the wave frequency range.

Only one realization was generated in the experiment. Meanwhile, 20 different random seeds of irregular waves were simulated numerically. The corresponding probability distribution for the 3-h maximum wave elevation based on these 20 numerical simulations is shown in Fig. 11. Most simulations have similar maximum wave elevation ranging from 7 m to 7.5 m, while two of them predict larger maxima.

Table 5
Frequency limits for PSD sum.

	The lowest frequency (Hz)	The highest frequency (Hz)
Surge natural frequency	0.006	0.012
Pitch natural frequency	0.029	0.035
Heave natural frequency	0.054	0.060
Wave frequency	0.072	0.092

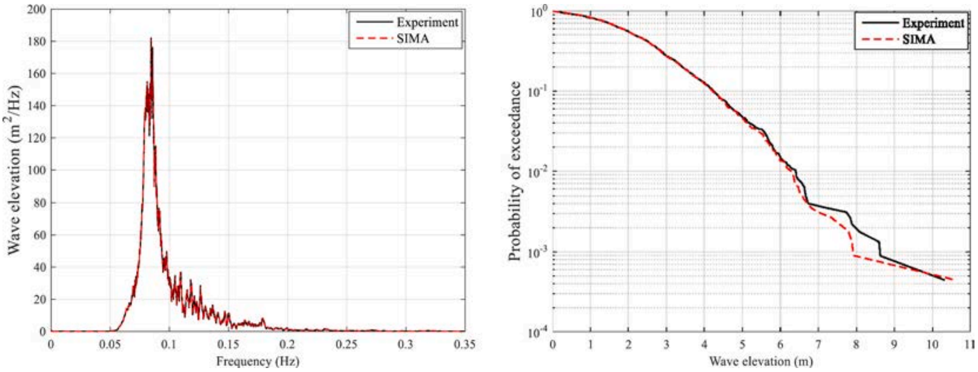

Fig. 10. Irregular wave in the OC6 project (left: PSD, right: probability of exceedance of all local maxima and minima).

Table 6
Statistical results and PSD sums for irregular wave elevation in the OC6 project.

	Mean (m)	Standard deviation (m)	Wave PSD sum (m^2)
Experiment	−1.50E-3	1.908	2.015
SIMA	8.75E-4	1.907	2.011

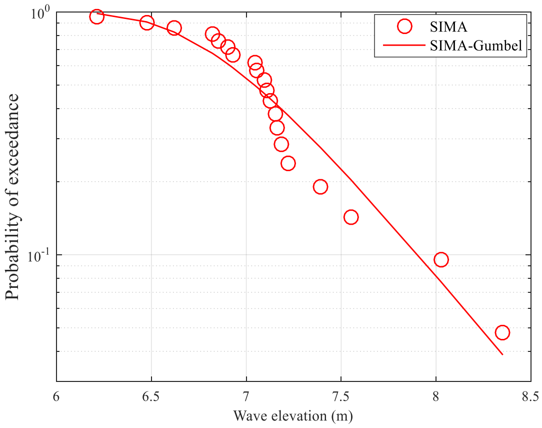

Fig. 11. Three-hour maximum irregular wave elevation ($H_s = 7.1\ m,\ T_p = 12.1\ s$).

4.2.1. *Floater motions*

Due to the symmetry of the model, and the fact that the waves travel along an axis of symmetry (Fig. 1), sway, roll and yaw motions are negligible. Therefore, the floater motions in surge, heave and pitch are selected as critical responses.

The numerically estimated surge motions are compared against the experimental data in Fig. 12 and Table 7. Surge resonance dominates surge motion with very little contribution from wave frequency response (Surge PSD sum vs Wave PSD sum in Table 7). Therefore, only the responses around the surge natural frequency are compared (left subplot in Fig. 11). The surge natural frequency is outside the linear wave-excitation range, and must be excited by some nonlinear force. Compared with potential flow theory, CFD can more accurately calculate the difference-frequency wave forces: the modified difference-frequency surge force QTF greatly increases the response (SIMA-CQ, SIMA-C). The maxima and standard deviation of surge motion increase by about 15% and 20% respectively in SIMA-CQ and SIMA-C. The modified frequency-dependent damping (SIMA-CA) or the additional linear damping (SIMA-WL) reduce the surge resonance. However, the effect of different low-frequency damping on the local maxima and standard deviation of surge motion is minor (SIMA-W vs SIMA-WL vs SIMA-CA). The mean value and the wave PSD sum are related to the first-order potential flow solution, and a slight difference (within 10%) is observed in all SIMA models compared to the experimental measurements. The best correspondence with the experiment is found in SIMA-C model with the modified surge force QTF and added mass and damping with CFD simulations.

Applying the modified models with numerically generated realizations of the same sea state results in the 3-h maxima distribution

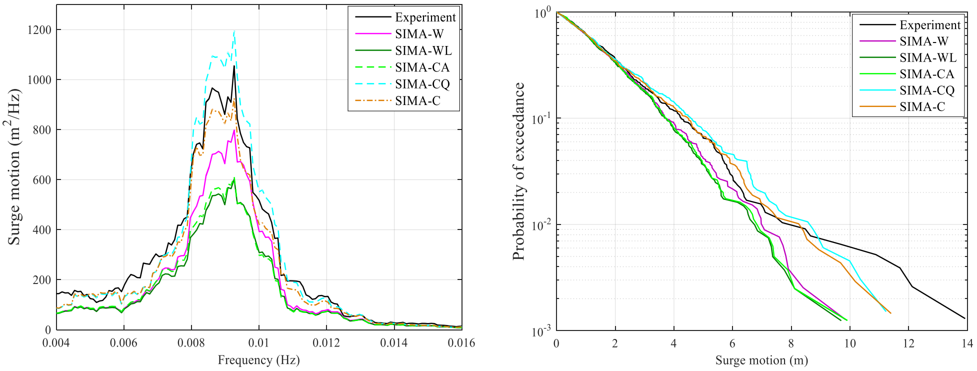

Fig. 12. Surge motion in the OC6 project (left: PSD, right: probability of exceedance of all local maxima and minima).

Table 7
Statistical results and PSD sums for surge motion in the OC6 project.

	Mean (m)	Diff. (%)	Standard deviation (m)	Diff. (%)	Surge PSD sum (m^2)	Diff. (%)	Wave PSD sum (m^2)	Diff. (%)
Experiment	1.397	0	2.156	0	2.75	0	0.763	0
SIMA-W	1.329	4.87	1.858	13.82	1.995	27.45	0.686	10.09
SIMA-WL	1.323	5.30	1.745	19.06	1.605	41.64	0.686	10.09
SIMA-CA	1.326	5.08	1.768	18.00	1.655	39.82	0.699	8.39
SIMA-CQ	1.472	5.34	2.138	0.83	2.922	6.25	0.695	8.91
SIMA-C	1.468	5.08	2.019	6.35	2.419	12.04	0.708	7.21

for the surge motion in Fig. 13. The solid line shows a fitted Gumbel distribution while the maxima from each simulation with different wave seeds are shown as markers. For all SIMA models, the numerical data are well-described by the Gumbel function. Generally, the predicted maxima for an exceedance level of 90% in the model with modified surge force QTF increases by 9.3% compared to the result from potential flow solutions, while the modified damping reduces the predicted maxima by up to 3.5%.

Fig. 14 and Table 8 compare the heave motions between the experiment and all SIMA models. Like heave decay, in SIMA-C model, the difference-frequency heave force QTF is not modified, considering the minor effect on the motions and relatively high heave resonance frequency (which is likely to be excited by first-order waves). Heave resonance contributes equally as the wave frequency component to the total heave motion. Better agreement between the experimental and numerical results occurs in the wave-frequency region. The potential flow solution (SIMA-W) significantly overestimates the heave resonance due to the lack of low-frequency damping. The overestimation of heave resonance reduces by almost 50% with consideration of the additional linear damping (SIMA-WL) or the modified frequency-dependent damping (SIMA-C). However, the low-frequency damping has minor influence on the local maxima and standard deviation of heave motion (within 6%). Additionally, the heave resonance frequencies in the numerical results slightly deviate from the measured frequency, and the frequency in SIMA-C with larger added mass shifts towards the

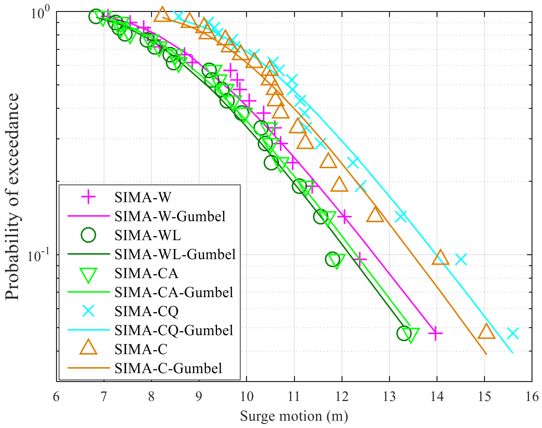

Fig. 13. Three-hour maximum surge motion in the OC6 project.

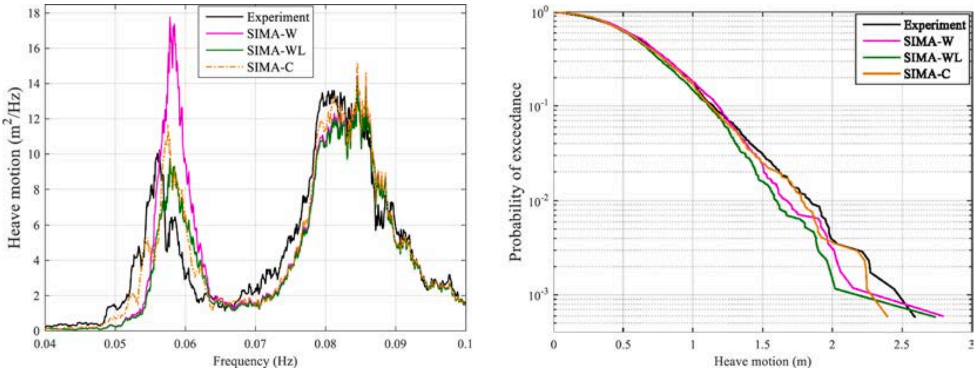

Fig. 14. Heave motion in the OC6 project (left: PSD, right: probability of exceedance of all local maxima and minima).

Table 8
Statistical results and PSD sums for heave motion in the OC6 project.

	Mean (m)	Diff. (%)	Standard deviation (m)	Diff. (%)	Heave PSD sum (m^2)	Diff. (%)	Wave PSD sum (m^2)	Diff. (%)
Experiment	0.035	0	0.543	0	0.040	0	0.171	0
SIMA-W	0.046	23.91	0.541	0.37	0.060	50.0	0.156	8.77
SIMA-WL	0.046	23.91	0.510	6.08	0.036	10.0	0.153	10.53
SIMA-C	0.031	11.42	0.531	2.21	0.043	7.5	0.163	4.68

experimental result. There are two possible explanations: one is the uncertainty of mooring stiffness (about 10%) in the experiment [42], another is the underestimation of the added mass in the numerical models. The mean heave motions are close to zero, which leads to a large apparent relative variation among different numerical models. Among all numerical models, SIMA-C performs best in simulating the heave motions both in the heave resonant frequency and wave frequency range.

Fig. 15 compare the 3-h maximum heave motions in different SIMA models. Due to the lack of low-frequency damping, SIMA-W predicts the largest maxima for a given exceedance probability, while the predicted maxima in SIMA-WL and SIMA-C are close to each other. The Gumbel function fits well for most of the original maximum values, but differs in larger values due to the outliers over 2.8 m. These outliers are related to the same large wave events as in Fig. 11.

The pitch motions are compared in Fig. 16 and Table 9. The main contribution to pitch motions comes from the pitch resonance, shown in the left subplot of Fig. 16. The wave-frequency response is relatively small. There is also a small response around the surge natural frequency due to coupling between pitch and surge motions, which is also compared in the PSD sums of Table 9.

The numerically estimated pitch resonant frequency is overpredicted by about 6% compared to the measured frequency. The uncertainty in the vertical center of mass (0.21 m) [42] contributes significantly to the uncertainty of the pitch resonance frequency (about 3%). The response at the pitch resonance frequency is mainly affected by the difference-frequency pitch moment QTF, which increases when modified based on CFD simulations. There is a corresponding increase in the maxima and in the standard deviation of pitch motion in SIMA-CQ and SIMA-C.

Fig. 16 shows that the SIMA-CQ and SIMA-C models each have one very large extreme value (close to 9 deg), which corresponds to a particularly large wave event at around 3230 s, as shown in Fig. 17. The reason for this overprediction may be related to the highly nonlinear wave elevation (left subplot of Fig. 17), which is treated as a linear input in SIMA. The modification of the QTF results in a changes in the phase of the second order force. For this event, the difference-frequency pitch excitation has an additive phasing effect for the modified QTF, while the original QTF results in a subtractive phasing effect.

The nearly identical pitch resonant frequency in the numerical results illustrates that the effect of changed added mass on the pitch resonant frequency is negligible. The larger damping in SIMA-CA or SIMA-WL reduces the pitch resonance and standard deviation of pitch motion, but has limited influence on the maxima. The mean value and wave frequency responses can be captured well in all SIMA models. The combination of the modified pitch moment QTF and added mass and damping gives the best agreement with the experiment for the low-frequency pitch motion.

The 3-h maximum pitch motions are compared in Fig. 18. The maxima of pitch motion over an exceedance level of 90% increases by over 35% with the modified difference-frequency pitch moment QTF. The effect of low-frequency damping is less significant. In addition, all maxima in the models with modified QTFs (SIMA-CQ, SIMA-C) fit with Gumbel function well, while larger differences can be found in the other three SIMA models due to the outliers (around 6.5 deg) which correspond to the realizations with largest maximum wave elevation (8.35 m in Fig. 11).

4.2.2. Mooring line tension

Considering symmetry, the mooring line tension on the starboard side (Mooring line 2, right subplot of Fig. 1) should be equal to the

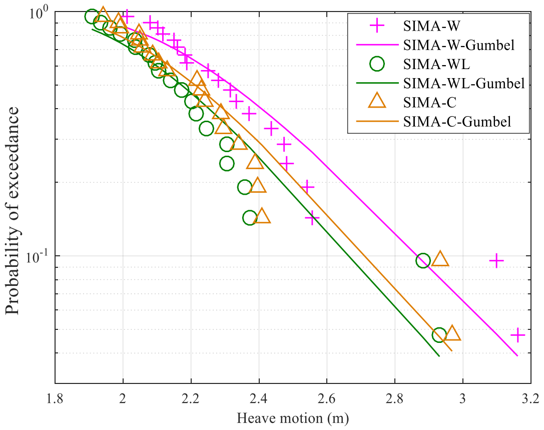

Fig. 15. Three-hour maximum heave motion in the OC6 project.

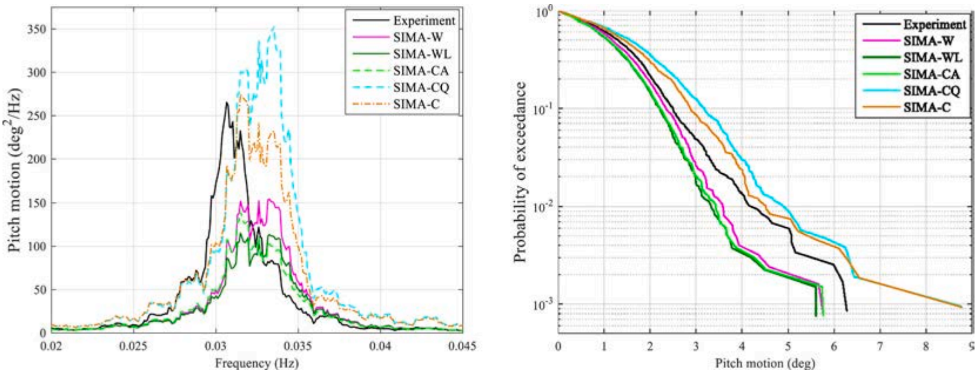

Fig. 16. Pitch motion in the OC6 project (left: wave spectra, right: probability of exceedance of all local maxima and minima).

Table 9
Statistical results and PSD sums for pitch motion in the OC6 project.

	Mean (deg)	Diff. (%)	Standard deviation (deg)	Diff. (%)	Surge PSD sum (deg^2)	Diff. (%)	Pitch PSD sum (deg^2)	Diff. (%)	Wave PSD sum (deg^2)	Diff. (%)
Experiment	0.060	0	1.22	0	0.020	0	0.768	0	0.251	0
SIMA-W	0.057	5.0	1.11	9.02	0.004	80.0	0.595	22.53	0.237	5.58
SIMA-WL	0.057	5.0	1.04	14.75	0.004	80.0	0.460	40.10	0.237	5.58
SIMA-CA	0.056	6.67	1.05	13.93	0.005	75.0	0.487	36.59	0.238	5.18
SIMA-CQ	0.062	3.33	1.49	22.13	0.015	25.0	1.281	66.80	0.225	10.36
SIMA-C	0.061	1.67	1.38	13.11	0.016	20.0	1.026	33.59	0.227	9.56

tension on the port side (Mooring line 3, right subplot of Fig. 1). Therefore, only the tension of mooring line 1 and 2 (ML1 and ML2) are presented in this section. In addition, the pretension is subtracted from presented results. The mooring line tension is compared for the linear mooring system with 3 taut-spring-lines that was used in the OC6 project.

The upwind mooring line (ML1) tension is shown in Fig. 19 and Table 10. The largest contribution to the ML1 tension comes from the surge natural frequency (as shown in the left subplot of Fig. 19), while two smaller peaks are observed at the pitch natural frequency and wave frequency. Similar to surge motion, the tension around the surge natural frequency increases by about 45% in the models with the modified difference-frequency QTFs (SIMA-CQ, SIMA-C) and decreases in the model with the modified damping (SIMA-CA) or the additional damping (SIMA-WL). The effects of modifying the added mass are not significant. The maximum tension increases by around 15% when the modified QTFs are used, but no obvious difference is found for different levels of damping. All numerical models overestimate the wave-frequency responses by over 20%. The uncertainty of wave-frequency PSD sum is about 20% due to the uncertainty of mooring line axial stiffness (10%) in the experiment [42]. From the comparisons, SIMA-C with modified QTFs

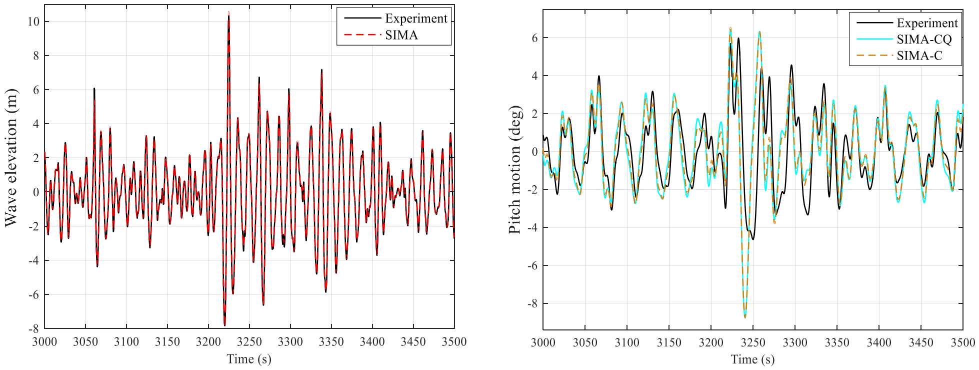

Fig. 17. Time series of wave elevation (left) and pitch motion (right) in the OC6 project.

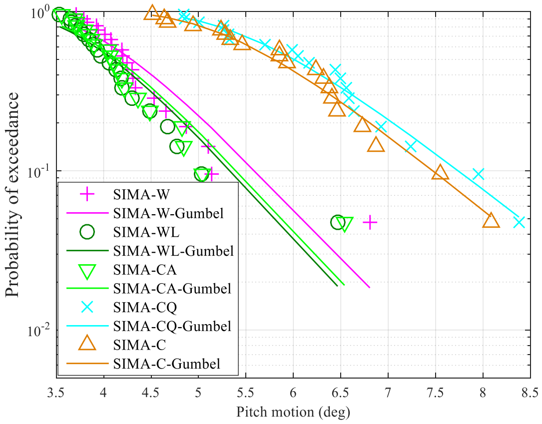

Fig. 18. Three-hour maximum pitch motion in the OC6 project.

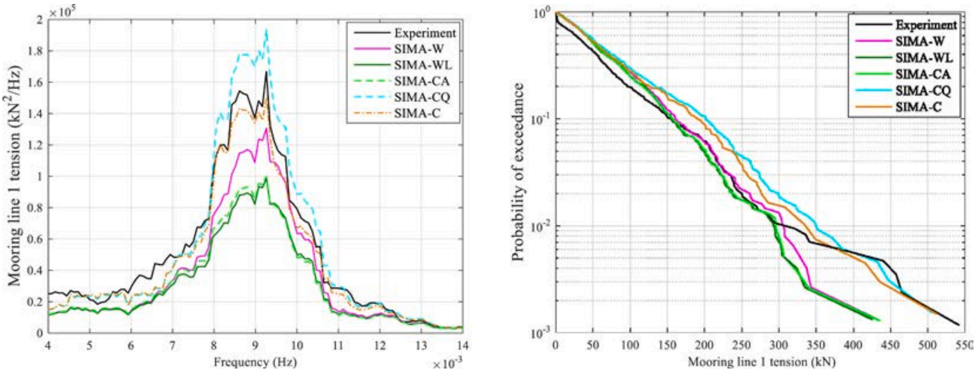

Fig. 19. Mooring line tension for ML1 in the OC6 project (left: PSD, right: probability of exceedance of all local maxima and minima).

and added mass and damping captures the upwind mooring line tension best.

The 3-h maximum tensions of the upwind mooring line (ML1) are shown in Fig. 20. As for surge, the Gumbel function fits with the numerical data well in all SIMA models. The model with modified QTFs predicts about 15% larger maxima than the model with potential flow solutions for an exceedance level of 90%, while the modified damping has a smaller influence on the predicted maxima.

Similar to the upwind mooring line (ML1), the tensions of mooring line on the starboard side (ML2) are dominated by responses

Table 10
Statistical results and PSD sums for mooring line tension of ML1 in the OC6 project (after subtracting pretension).

	Mean (kN)	Diff. (%)	Standard deviation (kN)	Diff. (%)	Surge PSD sum (kN^2)	Diff. (%)	Pitch PSD sum (kN^2)	Diff. (%)	Wave PSD sum (kN^2)	Diff. (%)
Experiment	55.51	0	84.87	0	4338	0	221.1	0	824.5	0
SIMA-W	56.57	1.91	76.74	9.58	3267	24.69	184.5	16.55	1024	24.20
SIMA-WL	56.20	1.24	71.62	15.61	2637	39.21	145.4	34.24	995.5	20.74
SIMA-CA	56.34	1.50	72.61	14.44	2712	37.48	156.4	29.26	1020	23.71
SIMA-CQ	62.58	12.74	88.27	4.01	4738	9.22	311.2	40.75	1024	24.20
SIMA-C	62.24	12.12	82.83	2.40	3923	9.57	246.0	11.23	1019	23.59

around the surge natural frequency which are shown in Fig. 21. A difference is that there is a smaller response around the heave natural frequency besides the pitch natural frequency and wave frequency, all of which are shown in Table 11. The modified QTFs and added mass and damping have the same effect on the tension of ML2 as on ML1, and SIMA-C is also the best model to capture the tension of ML2 compared to the experiment measurements. Due to the positive mean surge motion, the mean value of the dynamic tension of ML2 is negative. It can be noted that the 3-h maximum tension of ML2 (Fig. 22) has similar variation in different SIMA models as tension of ML1 (Fig. 20).

The damage equivalent loads for the mooring lines are shown in Fig. 23. The percentage on each bar represents the difference compared to the experimental results. The potential flow solution (SIMA-W) underestimates the damage equivalent load, and the additional damping in SIMA-WL increases this underestimation. It can be seen the damage equivalent loads are fairly consistent for models with similar damping (SIMA-WL vs SIMA-CA). The modified difference-frequency QTFs (SIMA-CQ) increase the damage equivalent load, resulting in an overestimation (4.74%). The overestimation is reduced and the best agreement with the experimental results is achieved when the QTFs, added mass and damping are modified (SIMA-C) together.

4.2.3. Tower base load

In this section, the experimental data are from the OC5 project. The tower bending natural frequency is about 0.32 Hz [4], which is larger than the wave frequency (0.0826 Hz) of irregular wave and can be excited by the sum-frequency wave loads. Meanwhile, the low-frequency wave loads also contribute to the tower base load for a semi-submersible FWT [4]. An example of tower base fore-aft moment (M_y in Fig. 6) is shown in Fig. 24. The PSD of fore-aft moment shows three distinct frequencies: the pitch natural frequency at 0.03 Hz, the linear wave excitation around 0.14 Hz and the tower-bending natural frequency about 0.32 Hz. The motion of floater related to the irregular wave creates a larger response around 0.14 Hz occurring away from the wave peak frequency. SIMA with either sum-frequency (‘SF’ in Fig. 24) or difference-frequency (‘DF’ in Fig. 24) QTFs underestimates the low-frequency or high-frequency responses, respectively. Therefore, all SIMA models presented in this section consider both QTFs. An example (SIMA-C) is shown in Fig. 24 where both low-frequency and high-frequency responses are captured well.

The largest contribution to the stress on the leading edge of tower base (Point B in Fig. 6) comes from the fore-aft moment which is considered in Fig. 25 and Table 12. The sum-frequency QTFs from potential flow solution are implemented for all numerical models. The other settings in different SIMA models follow the descriptions in Table 3. The ranges of frequency for calculating the PSD sum are shown in Fig. 24. The wave-frequency responses are underpredicted by more than 12% (Table 12). However, all SIMA models overpredict the responses around tower-bending natural frequency by over 60% which not only depend on the potential flow solution, but also relate to the motions which are compared in Fig. 26. A larger overprediction up to 101% is seen when the difference-frequency QTF from potential flow solutions (SIMA-W, SIMA-WL, SIMA-CA) is applied. In addition, the modified difference-frequency QTFs (SIMA-CQ, SIMA-C) reduce the underprediction of low-frequency responses in the potential flow solutions (left subplot of Fig. 25) and predict larger bending moments (by about 6%) down to the probability of 0.5% (right subplot of Fig. 25). For even smaller probabilities, the models with potential flow solution (SIMA-W, SIMA-WL,SIMA-CA) predict larger moments, which depend on the high frequency responses (right subplot of Fig. 27). However, these larger values disappear in the short-term extreme value analysis (Fig. 28) when using numerically generated irregular waves. Additionally, the time when the maxima occurs (around 2940 s) in the model with potential flow solution (SIMA-W) does not cohere with the experimental data (around 710 s). Hence, it is not fair to declare that the potential flow solution has a better performance in predicting the maximum fore-aft moment, as shown in the right subplot of Fig. 25. Furthermore, the effect of low-frequency damping on the maxima is negligible.

Table 11
Statistical results and PSD sums for mooring line tension of ML2 in the OC6 project (after subtracting pretension).

	Mean (kN)	Diff (%)	Standard deviation (kN)	Diff. (%)	Surge PSD sum (kN^2)	Diff. (%)	Pitch PSD sum (kN^2)	Diff. (%)	Heave PSD sum (kN^2)	Diff. (%)	Wave PSD sum (kN^2)	Diff. (%)
Experiment	−27.06	0	41.90	0	1032	0	52.12	0	26.48	0	254.9	0
SIMA-W	−24.06	11.1	37.17	11.3	735.8	28.7	56.62	8.64	32.44	22.5	273.5	7.30
SIMA-WL	−24.07	11.0	34.88	16.8	592.2	42.6	43.06	17.4	17.17	35.2	283.5	11.2
SIMA-CA	−27.09	1.11	35.41	15.5	609.1	41.0	46.01	11.7	18.14	31.5	293.3	15.1
SIMA-CQ	−26.81	0.92	42.64	1.77	1052	1.94	88.32	69.5	38.76	46.4	287.1	12.6
SIMA-C	−26.89	0.63	40.21	4.03	866.5	16.0	70.51	35.3	23.34	11.9	307.4	20.6

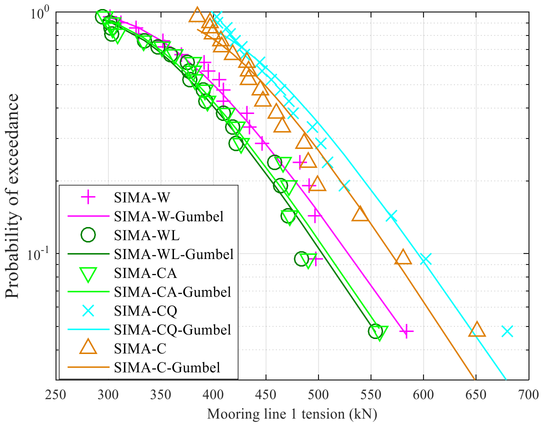

Fig. 20. Three-hour maximum mooring line tension of ML1 in the OC6 project.

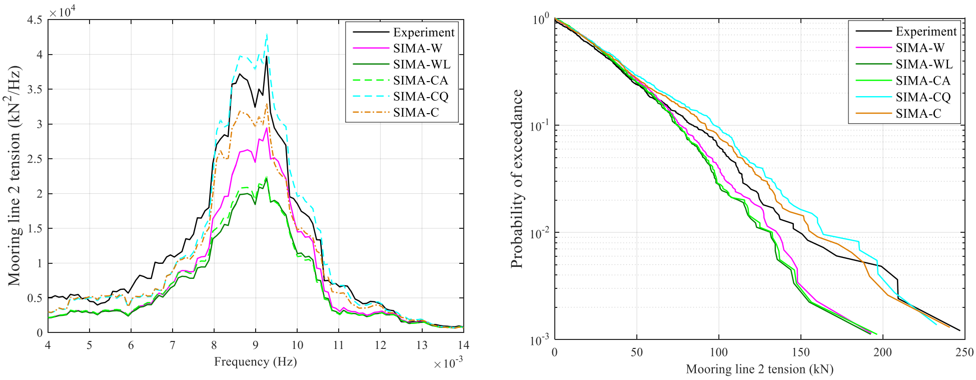

Fig. 21. Mooring line tension for ML2 in the OC6 project (left: PSD, right: probability of exceedance of all local maxima and minima).

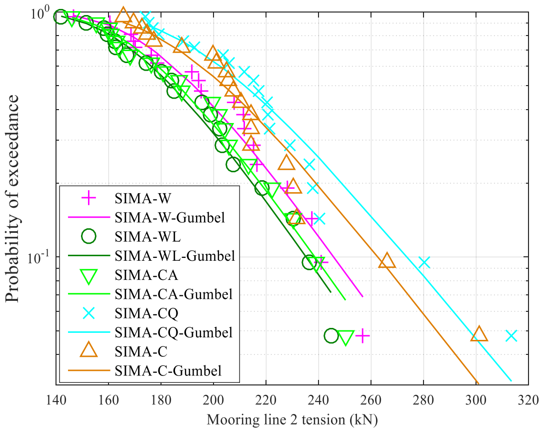

Fig. 22. Three-hour maximum mooring line tension of ML2 in the OC6 project.

The 3-h maxima for the tower base fore-aft bending moment are compared in Fig. 26. The effect of modified difference-frequency QTFs is dominant and increases the maxima over an exceedance level of 90% by 8.5%. The modified damping has minor influence. The damage equivalent loads for the tower base are shown in Fig. 29 with the difference compared to the experimental results.

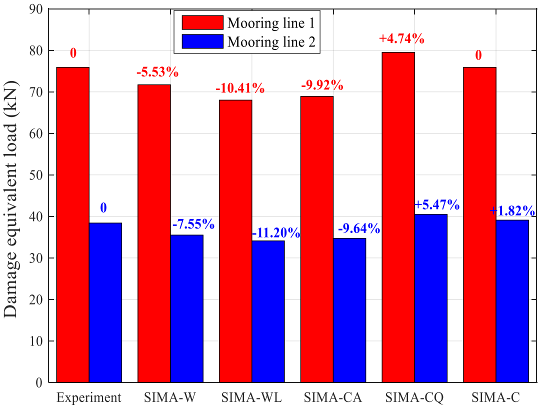

Fig. 23. Damage equivalent loads for mooring line 1 and 2 in the OC6 project.

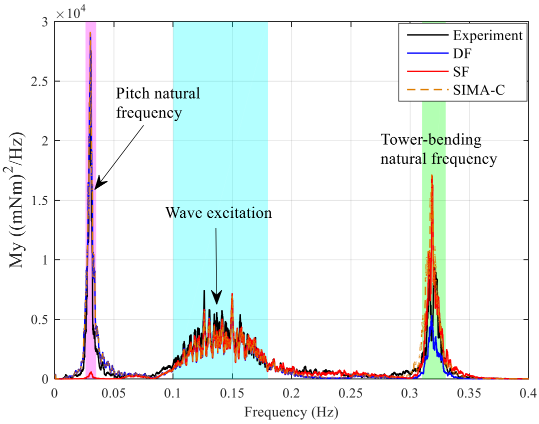

Fig. 24. PSD of the tower base fore-aft moment in the OC5 project.

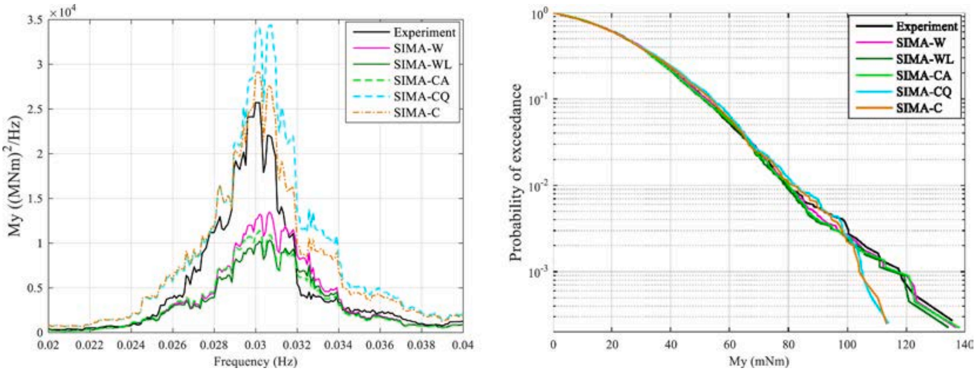

Fig. 25. Tower base fore-aft moment in the OC5 project (left: PSD, right: probability of exceedance of all local maxima and minima).

Table 12
Statistical results and PSD sums for tower base fore-aft moment in the OC5 project.

	Mean (kNm)	Diff. (%)	Standard deviation (kNm)	Diff. (%)	Pitch PSD sum (mNm^2)	Diff. (%)	Wave PSD sum (mNm^2)	Diff. (%)	Tower bending PSD sum (mNm^2)	Diff. (%)
Experiment	−495.1	0	2345	0	81.29	0	246.0	0	89.04	0
SIMA-W	−415.3	16.1	2354	0.38	53.17	52.9	216.0	12.19	179.1	101
SIMA-WL	−415.3	16.1	2310	1.49	43.28	46.8	215.7	12.32	170.5	90.9
SIMA-CA	−423.2	14.5	2326	0.81	45.99	43.4	214.8	12.68	175.8	97.4
SIMA-CQ	−489.2	1.19	2490	6.18	118.2	42.4	211.6	13.98	146.8	64.9
SIMA-C	−496.0	0.18	2443	4.18	101.6	24.9	210.6	14.39	145.0	62.8

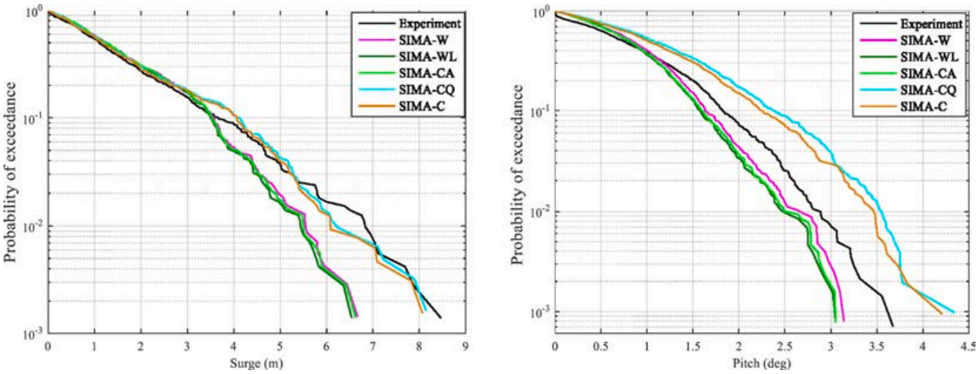

Fig. 26. Probability of exceedance for surge (left) and pitch (right) motions in the OC5 project.

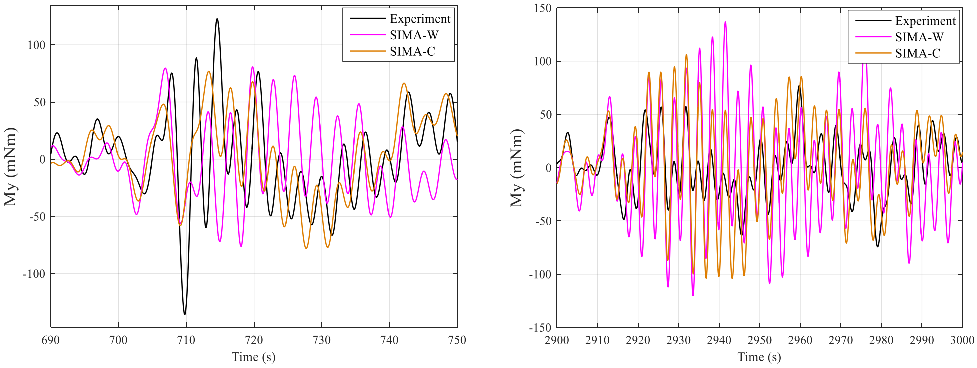

Fig. 27. Different time series of tower base fore-aft moment in the OC5 project.

Different SIMA models predict similar wave-frequency responses, but differ in estimating the low- and high-frequency responses. Considering the longer period for the low-frequency responses, the effect on the fatigue is limited. Even so, the more low-frequency responses the model can capture, the better agreement the estimated damage equivalent load is with the experimental data. This is consistent with the finding in the OC5 project that the tower base loads around pitch natural frequency have an significant effect on the damage-equivalent load [4].

5. Conclusions

This study investigates the dynamic responses of a semi-submersible FWT based on modifying the difference-frequency QTF and frequency-dependent added mass and damping from potential flow theory using CFD simulations. Decay tests in still water and irregular wave tests are considered to compare the numerically estimated results against experimentally measured data.

The QTF values estimated by the difference-frequency forces on a restrained FWT in the CFD simulations have been corrected for the floating condition based on the assumption that the contributions of the first-order motion can be accurately estimated in the potential flow theory. The modified QTFs have larger magnitudes, especially at higher wave frequencies. The frequency-dependent

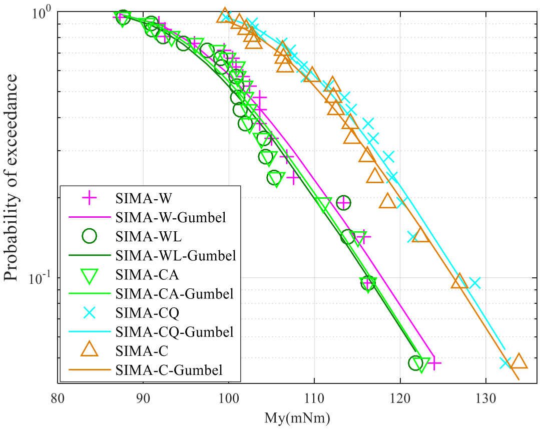

Fig. 28. Three-hour maxiamum tower base fore-aft moment in the OC5 project.

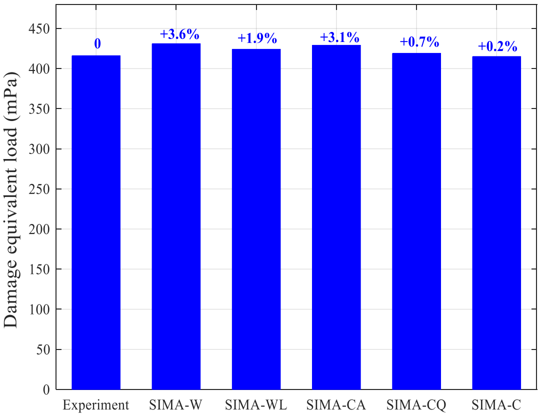

Fig. 29. Damage equivalent load for the leading edge (Point B in Fig. 5) of tower base in the OC5 project.

added mass and damping are modified by the estimated added mass and linearized damping from forced oscillation tests in the CFD simulations. The potential flow theory underestimates the amplitude of added mass by over 10%. The quadratic damping in Morison drag force also underestimates the nonlinear viscous damping. This depends on the selected drag coefficients.

In the free decay tests, there is no effect of modified difference-frequency QTFs. After modifying the frequency-dependent added mass and damping based on the CFD forced oscillation simulations, the underestimation of damping in the potential flow solution reduces and the engineering tool can capture similar damping as the CFD model. Although there are differences in the added mass and damping, the predicted natural periods in all numerical models are close to the experimental results (within 5%).

The natural frequencies of the floater motions are outside the linear wave-excitation range, and must be excited by some nonlinear forces. The largest contribution to the motions comes from the resonant frequency, except for the heave motion with equal contributions from the resonant and wave frequencies. The difference-frequency QTFs from the potential flow theory result in underestimation of the responses at resonant frequencies. The additional linear damping for matching calculated free decay motions from the CFD simulations increases this underestimation. However, when the difference-frequency QTFs are modified based on CFD simulations with a restrained floater, the motions are overestimated compared to the experimental data. The overestimation can be reduced by adjusting the frequency-dependent damping at the same time. There is a good agreement between experiment and engineering tools with modified QTFs and added mass and damping. The same trend is also valid for the exceedance probability distribution, standard deviation and extreme values of motions.

Considering symmetry, only the tensions of upwind mooring line and mooring line on the starboard side are investigated. The tension is mainly influenced by the surge resonance. Therefore, the difference-frequency QTFs and added mass and damping influence the tension in the same way as the surge motion. The damage-equivalent tension in the mooring line increases when more difference-frequency wave loads are captured and decreases with increasing damping.

For the tower base fore-aft moment, there are three significant contributions: the pitch natural frequency, wave frequency and tower bending natural frequency. The modified hydrodynamics from the CFD simulations influence the responses around pitch natural frequency and tower bending natural frequency. Although the low-frequency moments have a longer period, the more low-frequency responses the model can capture, the better agreement the estimated damage equivalent load of tower base is with the experimental data.

In conclusion, more accurate estimation of nonlinear hydrodynamics on the floater in the CFD simulations reduces the under-prediction of the low-frequency dynamic responses of a semi-submersible FWT in the potential flow solutions and show the best agreement with the experimental measurements.

Declaration of competing interest

The authors declare that they have no known competing financial interests or personal relationships that could have appeared to influence the work reported in this paper.

Acknowledgements

The author Haoran Li gratefully acknowledges the financial support from China Scholarship Council (CSC, 201706230219). Computing time on Vilje is granted by the Norwegian Research Council (Program for Supercomputing, under project nn9676k). The support of Centre for Autonomous Marine Operations and Systems (NTNU-AMOS, NFR project 223254) is gratefully acknowledged by the author Erin. E. Bachynski-Polić.

References

[1] Cordle A, Jonkman J. National renewable energy lab. (NREL), golden, CO (United States). State of the art in floating wind turbine design tools 2011.
[2] Coulling AJ, et al. Importance of second-order difference-frequency wave-diffraction forces in the validation of a FAST semi-submersible floating wind turbine model. No. NREL/CP-5000-57697. ASME 2013 32nd International Conference on Ocean, Offshore and Arctic Engineering 2013 [American Society of Mechanical Engineers Digital Collection].
[3] Mercier JA, Leverette SJ, Bliault AL. Evaluation of Hutton TLP response to environmental loads. Offshore technology conference 1982 [Offshore Technology Conference].
[4] Robertson AN, et al. OC5 project phase II: validation of global loads of the DeepCwind floating semisubmersible wind turbine. Energy Procedia 2017;137:38–57.
[5] Wei Y-f, Yang J-m, Chen X. A Review of the hydrodynamic Performance of heave damping Plates on spar platform [J]. China Offshore Platform 2010:6.
[6] Robertson A, et al. National renewable energy lab. (NREL), golden, CO (United States). Definition of the semisubmersible floating system for phase II of OC4. No. NREL/TP-5000-60601 2014.
[7] Robertson A, et al. Technical report NREL. Definition of the OC5 DeepCwind semisubmersible floating system 2016.
[8] Bayati I, et al. The effects of second-order hydrodynamics on a semisubmersible floating offshore wind turbine. J Phys Conf 2014 [IOP Publishing].
[9] Cao Q, et al. Second-order responses of a conceptual semi-submersible 10 MW wind turbine using full quadratic transfer functions. Renew Energy 2020;153: 653–68.
[10] Gueydon S, Duarte T, Jonkman J. Comparison of second-order loads on a semisubmersible floating wind turbine. Int Conf Offshore Mech Arctic Eng 2014 [American Society of Mechanical Engineers].
[11] Kvittem MI, Bachynski EE, Moan T. Effects of hydrodynamic modelling in fully coupled simulations of a semi-submersible wind turbine. Energy Procedia 2012; 24:351–62.
[12] Zhang L, et al. Second-order hydrodynamic effects on the response of three semisubmersible floating offshore wind turbines. Ocean Eng 2020;207:107371.
[13] Xu K, Gao Z, Moan T. Effect of hydrodynamic load modelling on the response of floating wind turbines and its mooring system in small water depths. J Phys Conf 2018 [IOP Publishing].
[14] Luan C, Gao Z, Moan T. Design and analysis of a braceless steel 5-MW semi-submersible wind turbine. ASME 2016 35th International Conference on Ocean, Offshore and Arctic Engineering 2016 [American Society of Mechanical Engineers Digital Collection].
[15] Wang L, et al. Uncertainty assessment of CFD investigation of the nonlinear difference-frequency wave loads on a semisubmersible FOWT platform. Sustainability 2021;13(1):64.
[16] Benitz MA, et al. Comparison of hydrodynamic load predictions between reduced order engineering models and computational fluid dynamics for the OC4-DeepCwind semi-submersible. No. NREL/CP-5000-61157. ASME 2014 33rd International Conference on Ocean, Offshore and Arctic Engineering 2014 [American Society of Mechanical Engineers Digital Collection].
[17] Benitz MA, et al. Validation of hydrodynamic load models using CFD for the OC4-DeepCwind semisubmersible. No. NREL/CP-5000-63751. ASME 2015 34th International Conference on Ocean, Offshore and Arctic Engineering 2015 [American Society of Mechanical Engineers Digital Collection].
[18] Lopez-Pavon C, Souto-Iglesias A. Hydrodynamic coefficients and pressure loads on heave plates for semi-submersible floating offshore wind turbines: a comparative analysis using large scale models. Renew Energy 2015;81:864–81.
[19] Bozonnet P, Emery A. International society of offshore and polar engineers. CFD simulations for the design of offshore floating wind platforms encompassing heave plates. in The Twenty-fifth International Ocean and Polar Engineering Conference 2015.
[20] Burmester S, et al. Investigation of a semi-submersible floating wind turbine in surge decay using CFD. Ship Technol Res 2020;67(1):2–14.
[21] Wang Y, et al. CFD simulation of semi-submersible floating offshore wind turbine under pitch decay motion. Int Conf Offshore Mech Arctic Eng 2019 [American Society of Mechanical Engineers].
[22] Bruinsma N, Paulsen B, Jacobsen N. Validation and application of a fully nonlinear numerical wave tank for simulating floating offshore wind turbines. Ocean Eng 2018;147:647–58.
[23] Rivera-Arreba I, et al. Modeling of a semisubmersible floating offshore wind platform in severe waves. J Offshore Mech Arctic Eng 2019;141:6.
[24] Tran TT, Kim D-H. The coupled dynamic response computation for a semi-submersible platform of floating offshore wind turbine. Journal of wind engineering and industrial aerodynamics 2015;147:104–19.
[25] Wang Y, et al. CFD simulation of semi-submersible floating offshore wind turbine under regular waves. The 30th International Ocean and Polar Engineering Conference 2020 [International Society of Offshore and Polar Engineers].
[26] Robertson A, et al. OC6 Phase I: investigating the underprediction of low-frequency hydrodynamic loads and responses of a floating wind turbine. TORQUE 2020;2020.
[27] Weller HG, et al. *A tensorial approach to computational continuum mechanics using object-oriented techniques.* Computers in physics 1998;12(6):620–31.
[28] Hirt CW, Nichols BD. Volume of fluid (VOF) method for the dynamics of free boundaries. Journal of computational physics 1981;39(1):201–25.
[29] Li H, Bachynski-Polić EE. Experimental and numerically obtained low-frequency radiation characteristics of the OC5-DeepCwind semisubmersible. Ocean Eng 2021;232:109130.

[30] Li H. Analysis of difference-frequency wave loads and quadratic transfer functions on a restrained semi-submersible floating wind turbine. Ocean Eng 2021;232: 109165.
[31] Marintek, Simo—Theory Manual Version 4.0. Marintek trondheim, Norway. 2012.
[32] Ormberg H, Passano E. *RIFLEX theory manual.* Marintek. Trondheim 2012.
[33] Lee C-H. Massachusetts Institute of technology, department of ocean engineering. WAMIT theory manual 1995.
[34] Cummins W. The impulse response function and ship motions. 1962 [David Taylor Model Basin Washington DC].
[35] Tom N, et al. Bichromatic wave selection for validation of the difference-frequency transfer function for the OC6 validation campaign. Int Conf Offshore Mech Arctic Eng 2019 [American Society of Mechanical Engineers].
[36] Pinkster JA. Low frequency second order wave exciting forces on floating structures. 1980.
[37] Kvittem MI, Moan T. Time domain analysis procedures for fatigue assessment of a semi-submersible wind turbine. Mar Struct 2015;40:38–59.
[38] Li H, et al. Short-term fatigue analysis for tower base of a spar-type wind turbine under stochastic wind-wave loads. International Journal of Naval Architecture and Ocean Engineering 2018;10(1):9–20.
[39] Hayman G. National renewable energy laboratory (NREL). 2012.
[40] Matsuishi M, Endo T. Fatigue of metals subjected to varying stress. Japan Society of Mechanical Engineers. Fukuoka, Japan 1968;68(2):37–40.
[41] Naess A, Moan T. Stochastic dynamics of marine structures. Cambridge University Press; 2013.
[42] Robertson A, et al. Total experimental uncertainty in hydrodynamic testing of a semisubmersible wind turbine, considering numerical propagation of systematic uncertainty. Ocean Eng 2020;195:106605.
[43] Robertson AN. Uncertainty analysis of OC5-DeepCwind floating semisubmersible offshore wind test campaign. NREL/CP-5000-68035. National Renewable Energy Lab. (NREL), Golden, CO (United States) 2017.

Appendix C

List of previous PhD theses at Dept. of Marine Tech.

Previous PhD theses published at the Department of Marine Technology (earlier: Faculty of Marine Technology)
NORWEGIAN UNIVERSITY OF SCIENCE AND TECHNOLOGY

Report No.	Author	Title
	Kavlie, Dag	Optimization of Plane Elastic Grillages, 1967
	Hansen, Hans R.	Man-Machine Communication and Data-Storage Methods in Ship Structural Design, 1971
	Gisvold, Kaare M.	A Method for non-linear mixed -integer programming and its Application to Design Problems, 1971
	Lund, Sverre	Tanker Frame Optimalization by means of SUMT-Transformation and Behaviour Models, 1971
	Vinje, Tor	On Vibration of Spherical Shells Interacting with Fluid, 1972
	Lorentz, Jan D.	Tank Arrangement for Crude Oil Carriers in Accordance with the new Anti-Pollution Regulations, 1975
	Carlsen, Carl A.	Computer-Aided Design of Tanker Structures, 1975
	Larsen, Carl M.	Static and Dynamic Analysis of Offshore Pipelines during Installation, 1976
UR-79-01	Brigt Hatlestad, MK	The finite element method used in a fatigue evaluation of fixed offshore platforms. (Dr.Ing. Thesis)
UR-79-02	Erik Pettersen, MK	Analysis and design of cellular structures. (Dr.Ing. Thesis)
UR-79-03	Sverre Valsgård, MK	Finite difference and finite element methods applied to nonlinear analysis of plated structures. (Dr.Ing. Thesis)
UR-79-04	Nils T. Nordsve, MK	Finite element collapse analysis of structural members considering imperfections and stresses due to fabrication. (Dr.Ing. Thesis)
UR-79-05	Ivar J. Fylling, MK	Analysis of towline forces in ocean towing systems. (Dr.Ing. Thesis)
UR-80-06	Nils Sandsmark, MM	Analysis of Stationary and Transient Heat Conduction by the Use of the Finite Element Method. (Dr.Ing. Thesis)
UR-80-09	Sverre Haver, MK	Analysis of uncertainties related to the stochastic modeling of ocean waves. (Dr.Ing. Thesis)
UR-81-15	Odland, Jonas	On the Strength of welded Ring stiffened cylindrical Shells primarily subjected to axial Compression
UR-82-17	Engesvik, Knut	Analysis of Uncertainties in the fatigue Capacity of

		Welded Joints
UR-82-18	Rye, Henrik	Ocean wave groups
UR-83-30	Eide, Oddvar Inge	On Cumulative Fatigue Damage in Steel Welded Joints
UR-83-33	Mo, Olav	Stochastic Time Domain Analysis of Slender Offshore Structures
UR-83-34	Amdahl, Jørgen	Energy absorption in Ship-platform impacts
UR-84-37	Mørch, Morten	Motions and mooring forces of semi submersibles as determined by full-scale measurements and theoretical analysis
UR-84-38	Soares, C. Guedes	Probabilistic models for load effects in ship structures
UR-84-39	Aarsnes, Jan V.	Current forces on ships
UR-84-40	Czujko, Jerzy	Collapse Analysis of Plates subjected to Biaxial Compression and Lateral Load
UR-85-46	Alf G. Engseth, MK	Finite element collapse analysis of tubular steel offshore structures. (Dr.Ing. Thesis)
UR-86-47	Dengody Sheshappa, MP	A Computer Design Model for Optimizing Fishing Vessel Designs Based on Techno-Economic Analysis. (Dr.Ing. Thesis)
UR-86-48	Vidar Aanesland, MH	A Theoretical and Numerical Study of Ship Wave Resistance. (Dr.Ing. Thesis)
UR-86-49	Heinz-Joachim Wessel, MK	Fracture Mechanics Analysis of Crack Growth in Plate Girders. (Dr.Ing. Thesis)
UR-86-50	Jon Taby, MK	Ultimate and Post-ultimate Strength of Dented Tubular Members. (Dr.Ing. Thesis)
UR-86-51	Walter Lian, MH	A Numerical Study of Two-Dimensional Separated Flow Past Bluff Bodies at Moderate KC-Numbers. (Dr.Ing. Thesis)
UR-86-52	Bjørn Sortland, MH	Force Measurements in Oscillating Flow on Ship Sections and Circular Cylinders in a U-Tube Water Tank. (Dr.Ing. Thesis)
UR-86-53	Kurt Strand, MM	A System Dynamic Approach to One-dimensional Fluid Flow. (Dr.Ing. Thesis)
UR-86-54	Arne Edvin Løken, MH	Three Dimensional Second Order Hydrodynamic Effects on Ocean Structures in Waves. (Dr.Ing. Thesis)
UR-86-55	Sigurd Falch, MH	A Numerical Study of Slamming of Two-Dimensional Bodies. (Dr.Ing. Thesis)
UR-87-56	Arne Braathen, MH	Application of a Vortex Tracking Method to the Prediction of Roll Damping of a Two-Dimension Floating Body. (Dr.Ing. Thesis)

UR-87-57	Bernt Leira, MK	Gaussian Vector Processes for Reliability Analysis involving Wave-Induced Load Effects. (Dr.Ing. Thesis)
UR-87-58	Magnus Småvik, MM	Thermal Load and Process Characteristics in a Two-Stroke Diesel Engine with Thermal Barriers (in Norwegian). (Dr.Ing. Thesis)
MTA-88-59	Bernt Arild Bremdal, MP	An Investigation of Marine Installation Processes – A Knowledge - Based Planning Approach. (Dr.Ing. Thesis)
MTA-88-60	Xu Jun, MK	Non-linear Dynamic Analysis of Space-framed Offshore Structures. (Dr.Ing. Thesis)
MTA-89-61	Gang Miao, MH	Hydrodynamic Forces and Dynamic Responses of Circular Cylinders in Wave Zones. (Dr.Ing. Thesis)
MTA-89-62	Martin Greenhow, MH	Linear and Non-Linear Studies of Waves and Floating Bodies. Part I and Part II. (Dr.Techn. Thesis)
MTA-89-63	Chang Li, MH	Force Coefficients of Spheres and Cubes in Oscillatory Flow with and without Current. (Dr.Ing. Thesis
MTA-89-64	Hu Ying, MP	A Study of Marketing and Design in Development of Marine Transport Systems. (Dr.Ing. Thesis)
MTA-89-65	Arild Jæger, MH	Seakeeping, Dynamic Stability and Performance of a Wedge Shaped Planing Hull. (Dr.Ing. Thesis)
MTA-89-66	Chan Siu Hung, MM	The dynamic characteristics of tilting-pad bearings
MTA-89-67	Kim Wikstrøm, MP	Analysis av projekteringen for ett offshore projekt. (Licenciat-avhandling)
MTA-89-68	Jiao Guoyang, MK	Reliability Analysis of Crack Growth under Random Loading, considering Model Updating. (Dr.Ing. Thesis)
MTA-89-69	Arnt Olufsen, MK	Uncertainty and Reliability Analysis of Fixed Offshore Structures. (Dr.Ing. Thesis)
MTA-89-70	Wu Yu-Lin, MR	System Reliability Analyses of Offshore Structures using improved Truss and Beam Models. (Dr.Ing. Thesis)
MTA-90-71	Jan Roger Hoff, MH	Three-dimensional Green function of a vessel with forward speed in waves. (Dr.Ing. Thesis)
MTA-90-72	Rong Zhao, MH	Slow-Drift Motions of a Moored Two-Dimensional Body in Irregular Waves. (Dr.Ing. Thesis)
MTA-90-73	Atle Minsaas, MP	Economical Risk Analysis. (Dr.Ing. Thesis)
MTA-90-74	Knut-Aril Farnes, MK	Long-term Statistics of Response in Non-linear Marine Structures. (Dr.Ing. Thesis)
MTA-90-75	Torbjørn Sotberg, MK	Application of Reliability Methods for Safety Assessment of Submarine Pipelines. (Dr.Ing.

		Thesis)
MTA-90-76	Zeuthen, Steffen, MP	SEAMAID. A computational model of the design process in a constraint-based logic programming environment. An example from the offshore domain. (Dr.Ing. Thesis)
MTA-91-77	Haagensen, Sven, MM	Fuel Dependant Cyclic Variability in a Spark Ignition Engine - An Optical Approach. (Dr.Ing. Thesis)
MTA-91-78	Løland, Geir, MH	Current forces on and flow through fish farms. (Dr.Ing. Thesis)
MTA-91-79	Hoen, Christopher, MK	System Identification of Structures Excited by Stochastic Load Processes. (Dr.Ing. Thesis)
MTA-91-80	Haugen, Stein, MK	Probabilistic Evaluation of Frequency of Collision between Ships and Offshore Platforms. (Dr.Ing. Thesis)
MTA-91-81	Sødahl, Nils, MK	Methods for Design and Analysis of Flexible Risers. (Dr.Ing. Thesis)
MTA-91-82	Ormberg, Harald, MK	Non-linear Response Analysis of Floating Fish Farm Systems. (Dr.Ing. Thesis)
MTA-91-83	Marley, Mark J., MK	Time Variant Reliability under Fatigue Degradation. (Dr.Ing. Thesis)
MTA-91-84	Krokstad, Jørgen R., MH	Second-order Loads in Multidirectional Seas. (Dr.Ing. Thesis)
MTA-91-85	Molteberg, Gunnar A., MM	The Application of System Identification Techniques to Performance Monitoring of Four Stroke Turbocharged Diesel Engines. (Dr.Ing. Thesis)
MTA-92-86	Mørch, Hans Jørgen Bjelke, MH	Aspects of Hydrofoil Design: with Emphasis on Hydrofoil Interaction in Calm Water. (Dr.Ing. Thesis)
MTA-92-87	Chan Siu Hung, MM	Nonlinear Analysis of Rotordynamic Instabilities in Highspeed Turbomachinery. (Dr.Ing. Thesis)
MTA-92-88	Bessason, Bjarni, MK	Assessment of Earthquake Loading and Response of Seismically Isolated Bridges. (Dr.Ing. Thesis)
MTA-92-89	Langli, Geir, MP	Improving Operational Safety through exploitation of Design Knowledge - an investigation of offshore platform safety. (Dr.Ing. Thesis)
MTA-92-90	Sævik, Svein, MK	On Stresses and Fatigue in Flexible Pipes. (Dr.Ing. Thesis)
MTA-92-91	Ask, Tor Ø., MM	Ignition and Flame Growth in Lean Gas-Air Mixtures. An Experimental Study with a Schlieren System. (Dr.Ing. Thesis)
MTA-86-92	Hessen, Gunnar, MK	Fracture Mechanics Analysis of Stiffened Tubular Members. (Dr.Ing. Thesis)

MTA-93-93	Steinebach, Christian, MM	Knowledge Based Systems for Diagnosis of Rotating Machinery. (Dr.Ing. Thesis)
MTA-93-94	Dalane, Jan Inge, MK	System Reliability in Design and Maintenance of Fixed Offshore Structures. (Dr.Ing. Thesis)
MTA-93-95	Steen, Sverre, MH	Cobblestone Effect on SES. (Dr.Ing. Thesis)
MTA-93-96	Karunakaran, Daniel, MK	Nonlinear Dynamic Response and Reliability Analysis of Drag-dominated Offshore Platforms. (Dr.Ing. Thesis)
MTA-93-97	Hagen, Arnulf, MP	The Framework of a Design Process Language. (Dr.Ing. Thesis)
MTA-93-98	Nordrik, Rune, MM	Investigation of Spark Ignition and Autoignition in Methane and Air Using Computational Fluid Dynamics and Chemical Reaction Kinetics. A Numerical Study of Ignition Processes in Internal Combustion Engines. (Dr.Ing. Thesis)
MTA-94-99	Passano, Elizabeth, MK	Efficient Analysis of Nonlinear Slender Marine Structures. (Dr.Ing. Thesis)
MTA-94-100	Kvålsvold, Jan, MH	Hydroelastic Modelling of Wetdeck Slamming on Multihull Vessels. (Dr.Ing. Thesis)
MTA-94-102	Bech, Sidsel M., MK	Experimental and Numerical Determination of Stiffness and Strength of GRP/PVC Sandwich Structures. (Dr.Ing. Thesis)
MTA-95-103	Paulsen, Hallvard, MM	A Study of Transient Jet and Spray using a Schlieren Method and Digital Image Processing. (Dr.Ing. Thesis)
MTA-95-104	Hovde, Geir Olav, MK	Fatigue and Overload Reliability of Offshore Structural Systems, Considering the Effect of Inspection and Repair. (Dr.Ing. Thesis)
MTA-95-105	Wang, Xiaozhi, MK	Reliability Analysis of Production Ships with Emphasis on Load Combination and Ultimate Strength. (Dr.Ing. Thesis)
MTA-95-106	Ulstein, Tore, MH	Nonlinear Effects of a Flexible Stern Seal Bag on Cobblestone Oscillations of an SES. (Dr.Ing. Thesis)
MTA-95-107	Solaas, Frøydis, MH	Analytical and Numerical Studies of Sloshing in Tanks. (Dr.Ing. Thesis)
MTA-95-108	Hellan, Øyvind, MK	Nonlinear Pushover and Cyclic Analyses in Ultimate Limit State Design and Reassessment of Tubular Steel Offshore Structures. (Dr.Ing. Thesis)
MTA-95-109	Hermundstad, Ole A., MK	Theoretical and Experimental Hydroelastic Analysis of High Speed Vessels. (Dr.Ing. Thesis)
MTA-96-110	Bratland, Anne K., MH	Wave-Current Interaction Effects on Large-Volume Bodies in Water of Finite Depth. (Dr.Ing. Thesis)
MTA-96-111	Herfjord, Kjell, MH	A Study of Two-dimensional Separated Flow by a Combination of the Finite Element Method and

		Navier-Stokes Equations. (Dr.Ing. Thesis)
MTA-96-112	Æsøy, Vilmar, MM	Hot Surface Assisted Compression Ignition in a Direct Injection Natural Gas Engine. (Dr.Ing. Thesis)
MTA-96-113	Eknes, Monika L., MK	Escalation Scenarios Initiated by Gas Explosions on Offshore Installations. (Dr.Ing. Thesis)
MTA-96-114	Erikstad, Stein O., MP	A Decision Support Model for Preliminary Ship Design. (Dr.Ing. Thesis)
MTA-96-115	Pedersen, Egil, MH	A Nautical Study of Towed Marine Seismic Streamer Cable Configurations. (Dr.Ing. Thesis)
MTA-97-116	Moksnes, Paul O., MM	Modelling Two-Phase Thermo-Fluid Systems Using Bond Graphs. (Dr.Ing. Thesis)
MTA-97-117	Halse, Karl H., MK	On Vortex Shedding and Prediction of Vortex-Induced Vibrations of Circular Cylinders. (Dr.Ing. Thesis)
MTA-97-118	Igland, Ragnar T., MK	Reliability Analysis of Pipelines during Laying, considering Ultimate Strength under Combined Loads. (Dr.Ing. Thesis)
MTA-97-119	Pedersen, Hans-P., MP	Levendefiskteknologi for fiskefartøy. (Dr.Ing. Thesis)
MTA-98-120	Vikestad, Kyrre, MK	Multi-Frequency Response of a Cylinder Subjected to Vortex Shedding and Support Motions. (Dr.Ing. Thesis)
MTA-98-121	Azadi, Mohammad R. E., MK	Analysis of Static and Dynamic Pile-Soil-Jacket Behaviour. (Dr.Ing. Thesis)
MTA-98-122	Ulltang, Terje, MP	A Communication Model for Product Information. (Dr.Ing. Thesis)
MTA-98-123	Torbergsen, Erik, MM	Impeller/Diffuser Interaction Forces in Centrifugal Pumps. (Dr.Ing. Thesis)
MTA-98-124	Hansen, Edmond, MH	A Discrete Element Model to Study Marginal Ice Zone Dynamics and the Behaviour of Vessels Moored in Broken Ice. (Dr.Ing. Thesis)
MTA-98-125	Videiro, Paulo M., MK	Reliability Based Design of Marine Structures. (Dr.Ing. Thesis)
MTA-99-126	Mainçon, Philippe, MK	Fatigue Reliability of Long Welds Application to Titanium Risers. (Dr.Ing. Thesis)
MTA-99-127	Haugen, Elin M., MH	Hydroelastic Analysis of Slamming on Stiffened Plates with Application to Catamaran Wetdecks. (Dr.Ing. Thesis)
MTA-99-128	Langhelle, Nina K., MK	Experimental Validation and Calibration of Nonlinear Finite Element Models for Use in Design of Aluminium Structures Exposed to Fire. (Dr.Ing. Thesis)
MTA-99-	Berstad, Are J., MK	Calculation of Fatigue Damage in Ship Structures.

129		(Dr.Ing. Thesis)
MTA-99-130	Andersen, Trond M., MM	Short Term Maintenance Planning. (Dr.Ing. Thesis)
MTA-99-131	Tveiten, Bård Wathne, MK	Fatigue Assessment of Welded Aluminium Ship Details. (Dr.Ing. Thesis)
MTA-99-132	Søreide, Fredrik, MP	Applications of underwater technology in deep water archaeology. Principles and practice. (Dr.Ing. Thesis)
MTA-99-133	Tønnessen, Rune, MH	A Finite Element Method Applied to Unsteady Viscous Flow Around 2D Blunt Bodies With Sharp Corners. (Dr.Ing. Thesis)
MTA-99-134	Elvekrok, Dag R., MP	Engineering Integration in Field Development Projects in the Norwegian Oil and Gas Industry. The Supplier Management of Norne. (Dr.Ing. Thesis)
MTA-99-135	Fagerholt, Kjetil, MP	Optimeringsbaserte Metoder for Ruteplanlegging innen skipsfart. (Dr.Ing. Thesis)
MTA-99-136	Bysveen, Marie, MM	Visualization in Two Directions on a Dynamic Combustion Rig for Studies of Fuel Quality. (Dr.Ing. Thesis)
MTA-2000-137	Storteig, Eskild, MM	Dynamic characteristics and leakage performance of liquid annular seals in centrifugal pumps. (Dr.Ing. Thesis)
MTA-2000-138	Sagli, Gro, MK	Model uncertainty and simplified estimates of long term extremes of hull girder loads in ships. (Dr.Ing. Thesis)
MTA-2000-139	Tronstad, Harald, MK	Nonlinear analysis and design of cable net structures like fishing gear based on the finite element method. (Dr.Ing. Thesis)
MTA-2000-140	Kroneberg, André, MP	Innovation in shipping by using scenarios. (Dr.Ing. Thesis)
MTA-2000-141	Haslum, Herbjørn Alf, MH	Simplified methods applied to nonlinear motion of spar platforms. (Dr.Ing. Thesis)
MTA-2001-142	Samdal, Ole Johan, MM	Modelling of Degradation Mechanisms and Stressor Interaction on Static Mechanical Equipment Residual Lifetime. (Dr.Ing. Thesis)
MTA-2001-143	Baarholm, Rolf Jarle, MH	Theoretical and experimental studies of wave impact underneath decks of offshore platforms. (Dr.Ing. Thesis)
MTA-2001-144	Wang, Lihua, MK	Probabilistic Analysis of Nonlinear Wave-induced Loads on Ships. (Dr.Ing. Thesis)
MTA-2001-145	Kristensen, Odd H. Holt, MK	Ultimate Capacity of Aluminium Plates under Multiple Loads, Considering HAZ Properties. (Dr.Ing. Thesis)
MTA-2001-146	Greco, Marilena, MH	A Two-Dimensional Study of Green-Water

		Loading. (Dr.Ing. Thesis)
MTA-2001-147	Heggelund, Svein E., MK	Calculation of Global Design Loads and Load Effects in Large High Speed Catamarans. (Dr.Ing. Thesis)
MTA-2001-148	Babalola, Olusegun T., MK	Fatigue Strength of Titanium Risers – Defect Sensitivity. (Dr.Ing. Thesis)
MTA-2001-149	Mohammed, Abuu K., MK	Nonlinear Shell Finite Elements for Ultimate Strength and Collapse Analysis of Ship Structures. (Dr.Ing. Thesis)
MTA-2002-150	Holmedal, Lars E., MH	Wave-current interactions in the vicinity of the sea bed. (Dr.Ing. Thesis)
MTA-2002-151	Rognebakke, Olav F., MH	Sloshing in rectangular tanks and interaction with ship motions. (Dr.Ing. Thesis)
MTA-2002-152	Lader, Pål Furset, MH	Geometry and Kinematics of Breaking Waves. (Dr.Ing. Thesis)
MTA-2002-153	Yang, Qinzheng, MH	Wash and wave resistance of ships in finite water depth. (Dr.Ing. Thesis)
MTA-2002-154	Melhus, Øyvin, MM	Utilization of VOC in Diesel Engines. Ignition and combustion of VOC released by crude oil tankers. (Dr.Ing. Thesis)
MTA-2002-155	Ronæss, Marit, MH	Wave Induced Motions of Two Ships Advancing on Parallel Course. (Dr.Ing. Thesis)
MTA-2002-156	Økland, Ole D., MK	Numerical and experimental investigation of whipping in twin hull vessels exposed to severe wet deck slamming. (Dr.Ing. Thesis)
MTA-2002-157	Ge, Chunhua, MK	Global Hydroelastic Response of Catamarans due to Wet Deck Slamming. (Dr.Ing. Thesis)
MTA-2002-158	Byklum, Eirik, MK	Nonlinear Shell Finite Elements for Ultimate Strength and Collapse Analysis of Ship Structures. (Dr.Ing. Thesis)
IMT-2003-1	Chen, Haibo, MK	Probabilistic Evaluation of FPSO-Tanker Collision in Tandem Offloading Operation. (Dr.Ing. Thesis)
IMT-2003-2	Skaugset, Kjetil Bjørn, MK	On the Suppression of Vortex Induced Vibrations of Circular Cylinders by Radial Water Jets. (Dr.Ing. Thesis)
IMT-2003-3	Chezhian, Muthu	Three-Dimensional Analysis of Slamming. (Dr.Ing. Thesis)
IMT-2003-4	Buhaug, Øyvind	Deposit Formation on Cylinder Liner Surfaces in Medium Speed Engines. (Dr.Ing. Thesis)
IMT-2003-5	Tregde, Vidar	Aspects of Ship Design: Optimization of Aft Hull with Inverse Geometry Design. (Dr.Ing. Thesis)
IMT-	Wist, Hanne Therese	Statistical Properties of Successive Ocean Wave

2003-6		Parameters. (Dr.Ing. Thesis)
IMT-2004-7	Ransau, Samuel	Numerical Methods for Flows with Evolving Interfaces. (Dr.Ing. Thesis)
IMT-2004-8	Soma, Torkel	Blue-Chip or Sub-Standard. A data interrogation approach of identity safety characteristics of shipping organization. (Dr.Ing. Thesis)
IMT-2004-9	Ersdal, Svein	An experimental study of hydrodynamic forces on cylinders and cables in near axial flow. (Dr.Ing. Thesis)
IMT-2005-10	Brodtkorb, Per Andreas	The Probability of Occurrence of Dangerous Wave Situations at Sea. (Dr.Ing. Thesis)
IMT-2005-11	Yttervik, Rune	Ocean current variability in relation to offshore engineering. (Dr.Ing. Thesis)
IMT-2005-12	Fredheim, Arne	Current Forces on Net-Structures. (Dr.Ing. Thesis)
IMT-2005-13	Heggernes, Kjetil	Flow around marine structures. (Dr.Ing. Thesis
IMT-2005-14	Fouques, Sebastien	Lagrangian Modelling of Ocean Surface Waves and Synthetic Aperture Radar Wave Measurements. (Dr.Ing. Thesis)
IMT-2006-15	Holm, Håvard	Numerical calculation of viscous free surface flow around marine structures. (Dr.Ing. Thesis)
IMT-2006-16	Bjørheim, Lars G.	Failure Assessment of Long Through Thickness Fatigue Cracks in Ship Hulls. (Dr.Ing. Thesis)
IMT-2006-17	Hansson, Lisbeth	Safety Management for Prevention of Occupational Accidents. (Dr.Ing. Thesis)
IMT-2006-18	Zhu, Xinying	Application of the CIP Method to Strongly Nonlinear Wave-Body Interaction Problems. (Dr.Ing. Thesis)
IMT-2006-19	Reite, Karl Johan	Modelling and Control of Trawl Systems. (Dr.Ing. Thesis)
IMT-2006-20	Smogeli, Øyvind Notland	Control of Marine Propellers. From Normal to Extreme Conditions. (Dr.Ing. Thesis)
IMT-2007-21	Storhaug, Gaute	Experimental Investigation of Wave Induced Vibrations and Their Effect on the Fatigue Loading of Ships. (Dr.Ing. Thesis)
IMT-2007-22	Sun, Hui	A Boundary Element Method Applied to Strongly Nonlinear Wave-Body Interaction Problems. (PhD Thesis, CeSOS)
IMT-2007-23	Rustad, Anne Marthine	Modelling and Control of Top Tensioned Risers. (PhD Thesis, CeSOS)
IMT-2007-24	Johansen, Vegar	Modelling flexible slender system for real-time simulations and control applications
IMT-2007-25	Wroldsen, Anders Sunde	Modelling and control of tensegrity structures.

		(PhD Thesis, CeSOS)
IMT-2007-26	Aronsen, Kristoffer Høye	An experimental investigation of in-line and combined inline and cross flow vortex induced vibrations. (Dr. avhandling, IMT)
IMT-2007-27	Gao, Zhen	Stochastic Response Analysis of Mooring Systems with Emphasis on Frequency-domain Analysis of Fatigue due to Wide-band Response Processes (PhD Thesis, CeSOS)
IMT-2007-28	Thorstensen, Tom Anders	Lifetime Profit Modelling of Ageing Systems Utilizing Information about Technical Condition. (Dr.ing. thesis, IMT)
IMT-2008-29	Refsnes, Jon Erling Gorset	Nonlinear Model-Based Control of Slender Body AUVs (PhD Thesis, IMT)
IMT-2008-30	Berntsen, Per Ivar B.	Structural Reliability Based Position Mooring. (PhD-Thesis, IMT)
IMT-2008-31	Ye, Naiquan	Fatigue Assessment of Aluminium Welded Box-stiffener Joints in Ships (Dr.ing. thesis, IMT)
IMT-2008-32	Radan, Damir	Integrated Control of Marine Electrical Power Systems. (PhD-Thesis, IMT)
IMT-2008-33	Thomassen, Paul	Methods for Dynamic Response Analysis and Fatigue Life Estimation of Floating Fish Cages. (Dr.ing. thesis, IMT)
IMT-2008-34	Pákozdi, Csaba	A Smoothed Particle Hydrodynamics Study of Two-dimensional Nonlinear Sloshing in Rectangular Tanks. (Dr.ing.thesis, IMT/ CeSOS)
IMT-2007-35	Grytøyr, Guttorm	A Higher-Order Boundary Element Method and Applications to Marine Hydrodynamics. (Dr.ing.thesis, IMT)
IMT-2008-36	Drummen, Ingo	Experimental and Numerical Investigation of Nonlinear Wave-Induced Load Effects in Containerships considering Hydroelasticity. (PhD thesis, CeSOS)
IMT-2008-37	Skejic, Renato	Maneuvering and Seakeeping of a Singel Ship and of Two Ships in Interaction. (PhD-Thesis, CeSOS)
IMT-2008-38	Harlem, Alf	An Age-Based Replacement Model for Repairable Systems with Attention to High-Speed Marine Diesel Engines. (PhD-Thesis, IMT)
IMT-2008-39	Alsos, Hagbart S.	Ship Grounding. Analysis of Ductile Fracture, Bottom Damage and Hull Girder Response. (PhD-thesis, IMT)
IMT-2008-40	Graczyk, Mateusz	Experimental Investigation of Sloshing Loading and Load Effects in Membrane LNG Tanks Subjected to Random Excitation. (PhD-thesis, CeSOS)
IMT-2008-41	Taghipour, Reza	Efficient Prediction of Dynamic Response for Flexible amd Multi-body Marine Structures. (PhD-

		thesis, CeSOS)
IMT-2008-42	Ruth, Eivind	Propulsion control and thrust allocation on marine vessels. (PhD thesis, CeSOS)
IMT-2008-43	Nystad, Bent Helge	Technical Condition Indexes and Remaining Useful Life of Aggregated Systems. PhD thesis, IMT
IMT-2008-44	Soni, Prashant Kumar	Hydrodynamic Coefficients for Vortex Induced Vibrations of Flexible Beams, PhD thesis, CeSOS
IMT-2009-45	Amlashi, Hadi K.K.	Ultimate Strength and Reliability-based Design of Ship Hulls with Emphasis on Combined Global and Local Loads. PhD Thesis, IMT
IMT-2009-46	Pedersen, Tom Arne	Bond Graph Modelling of Marine Power Systems. PhD Thesis, IMT
IMT-2009-47	Kristiansen, Trygve	Two-Dimensional Numerical and Experimental Studies of Piston-Mode Resonance. PhD-Thesis, CeSOS
IMT-2009-48	Ong, Muk Chen	Applications of a Standard High Reynolds Number Model and a Stochastic Scour Prediction Model for Marine Structures. PhD-thesis, IMT
IMT-2009-49	Hong, Lin	Simplified Analysis and Design of Ships subjected to Collision and Grounding. PhD-thesis, IMT
IMT-2009-50	Koushan, Kamran	Vortex Induced Vibrations of Free Span Pipelines, PhD thesis, IMT
IMT-2009-51	Korsvik, Jarl Eirik	Heuristic Methods for Ship Routing and Scheduling. PhD-thesis, IMT
IMT-2009-52	Lee, Jihoon	Experimental Investigation and Numerical in Analyzing the Ocean Current Displacement of Longlines. Ph.d.-Thesis, IMT.
IMT-2009-53	Vestbøstad, Tone Gran	A Numerical Study of Wave-in-Deck Impact usin a Two-Dimensional Constrained Interpolation Profile Method, Ph.d.thesis, CeSOS.
IMT-2009-54	Bruun, Kristine	Bond Graph Modelling of Fuel Cells for Marine Power Plants. Ph.d.-thesis, IMT
IMT 2009-55	Holstad, Anders	Numerical Investigation of Turbulence in a Sekwed Three-Dimensional Channel Flow, Ph.d.-thesis, IMT.
IMT 2009-56	Ayala-Uraga, Efren	Reliability-Based Assessment of Deteriorating Ship-shaped Offshore Structures, Ph.d.-thesis, IMT
IMT 2009-57	Kong, Xiangjun	A Numerical Study of a Damaged Ship in Beam Sea Waves. Ph.d.-thesis, IMT/CeSOS.
IMT 2010-58	Kristiansen, David	Wave Induced Effects on Floaters of Aquaculture Plants, Ph.d.-thesis, CeSOS.

IMT 2010-59	Ludvigsen, Martin	An ROV-Toolbox for Optical and Acoustic Scientific Seabed Investigation. Ph.d.-thesis IMT.
IMT 2010-60	Hals, Jørgen	Modelling and Phase Control of Wave-Energy Converters. Ph.d.thesis, CeSOS.
IMT 2010- 61	Shu, Zhi	Uncertainty Assessment of Wave Loads and Ultimate Strength of Tankers and Bulk Carriers in a Reliability Framework. Ph.d. Thesis, IMT/ CeSOS
IMT 2010-62	Shao, Yanlin	Numerical Potential-Flow Studies on Weakly-Nonlinear Wave-Body Interactions with/without Small Forward Speed, Ph.d.thesis,CeSOS.
IMT 2010-63	Califano, Andrea	Dynamic Loads on Marine Propellers due to Intermittent Ventilation. Ph.d.thesis, IMT.
IMT 2010-64	El Khoury, George	Numerical Simulations of Massively Separated Turbulent Flows, Ph.d.-thesis, IMT
IMT 2010-65	Seim, Knut Sponheim	Mixing Process in Dense Overflows with Emphasis on the Faroe Bank Channel Overflow. Ph.d.thesis, IMT
IMT 2010-66	Jia, Huirong	Structural Analysis of Intect and Damaged Ships in a Collission Risk Analysis Perspective. Ph.d.thesis CeSoS.
IMT 2010-67	Jiao, Linlin	Wave-Induced Effects on a Pontoon-type Very Large Floating Structures (VLFS). Ph.D.-thesis, CeSOS.
IMT 2010-68	Abrahamsen, Bjørn Christian	Sloshing Induced Tank Roof with Entrapped Air Pocket. Ph.d.thesis, CeSOS.
IMT 2011-69	Karimirad, Madjid	Stochastic Dynamic Response Analysis of Spar-Type Wind Turbines with Catenary or Taut Mooring Systems. Ph.d.-thesis, CeSOS.
IMT - 2011-70	Erlend Meland	Condition Monitoring of Safety Critical Valves. Ph.d.-thesis, IMT.
IMT – 2011-71	Yang, Limin	Stochastic Dynamic System Analysis of Wave Energy Converter with Hydraulic Power Take-Off, with Particular Reference to Wear Damage Analysis, Ph.d. Thesis, CeSOS.
IMT – 2011-72	Visscher, Jan	Application of Particla Image Velocimetry on Turbulent Marine Flows, Ph.d.Thesis, IMT.
IMT – 2011-73	Su, Biao	Numerical Predictions of Global and Local Ice Loads on Ships. Ph.d.Thesis, CeSOS.
IMT – 2011-74	Liu, Zhenhui	Analytical and Numerical Analysis of Iceberg Collision with Ship Structures. Ph.d.Thesis, IMT.
IMT – 2011-75	Aarsæther, Karl Gunnar	Modeling and Analysis of Ship Traffic by Observation and Numerical Simulation. Ph.d.Thesis, IMT.

Imt – 2011-76	Wu, Jie	Hydrodynamic Force Identification from Stochastic Vortex Induced Vibration Experiments with Slender Beams. Ph.d.Thesis, IMT.
Imt – 2011-77	Amini, Hamid	Azimuth Propulsors in Off-design Conditions. Ph.d.Thesis, IMT.
IMT – 2011-78	Nguyen, Tan-Hoi	Toward a System of Real-Time Prediction and Monitoring of Bottom Damage Conditions During Ship Grounding. Ph.d.thesis, IMT.
IMT-2011-79	Tavakoli, Mohammad T.	Assessment of Oil Spill in Ship Collision and Grounding, Ph.d.thesis, IMT.
IMT-2011-80	Guo, Bingjie	Numerical and Experimental Investigation of Added Resistance in Waves. Ph.d.Thesis, IMT.
IMT-2011-81	Chen, Qiaofeng	Ultimate Strength of Aluminium Panels, considering HAZ Effects, IMT
IMT-2012-82	Kota, Ravikiran S.	Wave Loads on Decks of Offshore Structures in Random Seas, CeSOS.
IMT-2012-83	Sten, Ronny	Dynamic Simulation of Deep Water Drilling Risers with Heave Compensating System, IMT.
IMT-2012-84	Berle, Øyvind	Risk and resilience in global maritime supply chains, IMT.
IMT-2012-85	Fang, Shaoji	Fault Tolerant Position Mooring Control Based on Structural Reliability, CeSOS.
IMT-2012-86	You, Jikun	Numerical studies on wave forces and moored ship motions in intermediate and shallow water, CeSOS.
IMT-2012-87	Xiang ,Xu	Maneuvering of two interacting ships in waves, CeSOS
IMT-2012-88	Dong, Wenbin	Time-domain fatigue response and reliability analysis of offshore wind turbines with emphasis on welded tubular joints and gear components, CeSOS
IMT-2012-89	Zhu, Suji	Investigation of Wave-Induced Nonlinear Load Effects in Open Ships considering Hull Girder Vibrations in Bending and Torsion, CeSOS
IMT-2012-90	Zhou, Li	Numerical and Experimental Investigation of Station-keeping in Level Ice, CeSOS
IMT-2012-91	Ushakov, Sergey	Particulate matter emission characteristics from diesel enignes operating on conventional and alternative marine fuels, IMT
IMT-2013-1	Yin, Decao	Experimental and Numerical Analysis of Combined In-line and Cross-flow Vortex Induced Vibrations, CeSOS

IMT-2013-2	Kurniawan, Adi	Modelling and geometry optimisation of wave energy converters, CeSOS
IMT-2013-3	Al Ryati, Nabil	Technical condition indexes doe auxiliary marine diesel engines, IMT
IMT-2013-4	Firoozkoohi, Reza	Experimental, numerical and analytical investigation of the effect of screens on sloshing, CeSOS
IMT-2013-5	Ommani, Babak	Potential-Flow Predictions of a Semi-Displacement Vessel Including Applications to Calm Water Broaching, CeSOS
IMT-2013-6	Xing, Yihan	Modelling and analysis of the gearbox in a floating spar-type wind turbine, CeSOS
IMT-7-2013	Balland, Océane	Optimization models for reducing air emissions from ships, IMT
IMT-8-2013	Yang, Dan	Transitional wake flow behind an inclined flat plate-----Computation and analysis, IMT
IMT-9-2013	Abdillah, Suyuthi	Prediction of Extreme Loads and Fatigue Damage for a Ship Hull due to Ice Action, IMT
IMT-10-2013	Ramìrez, Pedro Agustìn Pèrez	Ageing management and life extension of technical systems- Concepts and methods applied to oil and gas facilities, IMT
IMT-11-2013	Chuang, Zhenju	Experimental and Numerical Investigation of Speed Loss due to Seakeeping and Maneuvering. IMT
IMT-12-2013	Etemaddar, Mahmoud	Load and Response Analysis of Wind Turbines under Atmospheric Icing and Controller System Faults with Emphasis on Spar Type Floating Wind Turbines, IMT
IMT-13-2013	Lindstad, Haakon	Strategies and measures for reducing maritime CO2 emissons, IMT
IMT-14-2013	Haris, Sabril	Damage interaction analysis of ship collisions, IMT
IMT-15-2013	Shainee, Mohamed	Conceptual Design, Numerical and Experimental Investigation of a SPM Cage Concept for Offshore Mariculture, IMT
IMT-16-2013	Gansel, Lars	Flow past porous cylinders and effects of biofouling and fish behavior on the flow in and around Atlantic salmon net cages, IMT
IMT-17-2013	Gaspar, Henrique	Handling Aspects of Complexity in Conceptual Ship Design, IMT
IMT-18-2013	Thys, Maxime	Theoretical and Experimental Investigation of a Free Running Fishing Vessel at Small Frequency of Encounter, CeSOS
IMT-19-2013	Aglen, Ida	VIV in Free Spanning Pipelines, CeSOS

IMT-1-2014	Song, An	Theoretical and experimental studies of wave diffraction and radiation loads on a horizontally submerged perforated plate, CeSOS
IMT-2-2014	Rogne, Øyvind Ygre	Numerical and Experimental Investigation of a Hinged 5-body Wave Energy Converter, CeSOS
IMT-3-2014	Dai, Lijuan	Safe and efficient operation and maintenance of offshore wind farms ,IMT
IMT-4-2014	Bachynski, Erin Elizabeth	Design and Dynamic Analysis of Tension Leg Platform Wind Turbines, CeSOS
IMT-5-2014	Wang, Jingbo	Water Entry of Freefall Wedged – Wedge motions and Cavity Dynamics, CeSOS
IMT-6-2014	Kim, Ekaterina	Experimental and numerical studies related to the coupled behavior of ice mass and steel structures during accidental collisions, IMT
IMT-7-2014	Tan, Xiang	Numerical investigation of ship's continuous- mode icebreaking in leverl ice, CeSOS
IMT-8-2014	Muliawan, Made Jaya	Design and Analysis of Combined Floating Wave and Wind Power Facilities, with Emphasis on Extreme Load Effects of the Mooring System, CeSOS
IMT-9-2014	Jiang, Zhiyu	Long-term response analysis of wind turbines with an emphasis on fault and shutdown conditions, IMT
IMT-10-2014	Dukan, Fredrik	ROV Motion Control Systems, IMT
IMT-11-2014	Grimsmo, Nils I.	Dynamic simulations of hydraulic cylinder for heave compensation of deep water drilling risers, IMT
IMT-12-2014	Kvittem, Marit I.	Modelling and response analysis for fatigue design of a semisubmersible wind turbine, CeSOS
IMT-13-2014	Akhtar, Juned	The Effects of Human Fatigue on Risk at Sea, IMT
IMT-14-2014	Syahroni, Nur	Fatigue Assessment of Welded Joints Taking into Account Effects of Residual Stress, IMT
IMT-1-2015	Bøckmann, Eirik	Wave Propulsion of ships, IMT
IMT-2-2015	Wang, Kai	Modelling and dynamic analysis of a semi-submersible floating vertical axis wind turbine, CeSOS
IMT-3-2015	Fredriksen, Arnt Gunvald	A numerical and experimental study of a two-dimensional body with moonpool in waves and current, CeSOS
IMT-4-2015	Jose Patricio Gallardo Canabes	Numerical studies of viscous flow around bluff bodies, IMT

IMT-5-2015	Vegard Longva	Formulation and application of finite element techniques for slender marine structures subjected to contact interactions, IMT
IMT-6-2015	Jacobus De Vaal	Aerodynamic modelling of floating wind turbines, CeSOS
IMT-7-2015	Fachri Nasution	Fatigue Performance of Copper Power Conductors, IMT
IMT-8-2015	Oleh I Karpa	Development of bivariate extreme value distributions for applications in marine technology,CeSOS
IMT-9-2015	Daniel de Almeida Fernandes	An output feedback motion control system for ROVs, AMOS
IMT-10-2015	Bo Zhao	Particle Filter for Fault Diagnosis: Application to Dynamic Positioning Vessel and Underwater Robotics, CeSOS
IMT-11-2015	Wenting Zhu	Impact of emission allocation in maritime transportation, IMT
IMT-12-2015	Amir Rasekhi Nejad	Dynamic Analysis and Design of Gearboxes in Offshore Wind Turbines in a Structural Reliability Perspective, CeSOS
IMT-13-2015	Arturo Jesùs Ortega Malca	Dynamic Response of Flexibles Risers due to Unsteady Slug Flow, CeSOS
IMT-14-2015	Dagfinn Husjord	Guidance and decision-support system for safe navigation of ships operating in close proximity, IMT
IMT-15-2015	Anirban Bhattacharyya	Ducted Propellers: Behaviour in Waves and Scale Effects, IMT
IMT-16-2015	Qin Zhang	Image Processing for Ice Parameter Identification in Ice Management, IMT
IMT-1-2016	Vincentius Rumawas	Human Factors in Ship Design and Operation: An Experiential Learning, IMT
IMT-2-2016	Martin Storheim	Structural response in ship-platform and ship-ice collisions, IMT
IMT-3-2016	Mia Abrahamsen Prsic	Numerical Simulations of the Flow around single and Tandem Circular Cylinders Close to a Plane Wall, IMT
IMT-4-2016	Tufan Arslan	Large-eddy simulations of cross-flow around ship sections, IMT

IMT-5-2016	Pierre Yves-Henry	Parametrisation of aquatic vegetation in hydraulic and coastal research,IMT
IMT-6-2016	Lin Li	Dynamic Analysis of the Instalation of Monopiles for Offshore Wind Turbines, CeSOS
IMT-7-2016	Øivind Kåre Kjerstad	Dynamic Positioning of Marine Vessels in Ice, IMT
IMT-8-2016	Xiaopeng Wu	Numerical Analysis of Anchor Handling and Fish Trawling Operations in a Safety Perspective, CeSOS
IMT-9-2016	Zhengshun Cheng	Integrated Dynamic Analysis of Floating Vertical Axis Wind Turbines, CeSOS
IMT-10-2016	Ling Wan	Experimental and Numerical Study of a Combined Offshore Wind and Wave Energy Converter Concept
IMT-11-2016	Wei Chai	Stochastic dynamic analysis and reliability evaluation of the roll motion for ships in random seas, CeSOS
IMT-12-2016	Øyvind Selnes Patricksson	Decision support for conceptual ship design with focus on a changing life cycle and future uncertainty, IMT
IMT-13-2016	Mats Jørgen Thorsen	Time domain analysis of vortex-induced vibrations, IMT
IMT-14-2016	Edgar McGuinness	Safety in the Norwegian Fishing Fleet – Analysis and measures for improvement, IMT
IMT-15-2016	Sepideh Jafarzadeh	Energy effiency and emission abatement in the fishing fleet, IMT
IMT-16-2016	Wilson Ivan Guachamin Acero	Assessment of marine operations for offshore wind turbine installation with emphasis on response-based operational limits, IMT
IMT-17-2016	Mauro Candeloro	Tools and Methods for Autonomous Operations on Seabed and Water Coumn using Underwater Vehicles, IMT
IMT-18-2016	Valentin Chabaud	Real-Time Hybrid Model Testing of Floating Wind Tubines, IMT
IMT-1-2017	Mohammad Saud Afzal	Three-dimensional streaming in a sea bed boundary layer
IMT-2-2017	Peng Li	A Theoretical and Experimental Study of Wave-induced Hydroelastic Response of a Circular Floating Collar
IMT-3-2017	Martin Bergström	A simulation-based design method for arctic maritime transport systems

IMT-4-2017	Bhushan Taskar	The effect of waves on marine propellers and propulsion
IMT-5-2017	Mohsen Bardestani	A two-dimensional numerical and experimental study of a floater with net and sinker tube in waves and current
IMT-6-2017	Fatemeh Hoseini Dadmarzi	Direct Numerical Simualtion of turbulent wakes behind different plate configurations
IMT-7-2017	Michel R. Miyazaki	Modeling and control of hybrid marine power plants
IMT-8-2017	Giri Rajasekhar Gunnu	Safety and effiency enhancement of anchor handling operations with particular emphasis on the stability of anchor handling vessels
IMT-9-2017	Kevin Koosup Yum	Transient Performance and Emissions of a Turbocharged Diesel Engine for Marine Power Plants
IMT-10-2017	Zhaolong Yu	Hydrodynamic and structural aspects of ship collisions
IMT-11-2017	Martin Hassel	Risk Analysis and Modelling of Allisions between Passing Vessels and Offshore Installations
IMT-12-2017	Astrid H. Brodtkorb	Hybrid Control of Marine Vessels – Dynamic Positioning in Varying Conditions
IMT-13-2017	Kjersti Bruserud	Simultaneous stochastic model of waves and current for prediction of structural design loads
IMT-14-2017	Finn-Idar Grøtta Giske	Long-Term Extreme Response Analysis of Marine Structures Using Inverse Reliability Methods
IMT-15-2017	Stian Skjong	Modeling and Simulation of Maritime Systems and Operations for Virtual Prototyping using co-Simulations
IMT-1-2018	Yingguang Chu	Virtual Prototyping for Marine Crane Design and Operations
IMT-2-2018	Sergey Gavrilin	Validation of ship manoeuvring simulation models
IMT-3-2018	Jeevith Hegde	Tools and methods to manage risk in autonomous subsea inspection,maintenance and repair operations
IMT-4-2018	Ida M. Strand	Sea Loads on Closed Flexible Fish Cages
IMT-5-2018	Erlend Kvinge Jørgensen	Navigation and Control of Underwater Robotic Vehicles

IMT-6-2018	Bård Stovner	Aided Intertial Navigation of Underwater Vehicles
IMT-7-2018	Erlend Liavåg Grotle	Thermodynamic Response Enhanced by Sloshing in Marine LNG Fuel Tanks
IMT-8-2018	Børge Rokseth	Safety and Verification of Advanced Maritime Vessels
IMT-9-2018	Jan Vidar Ulveseter	Advances in Semi-Empirical Time Domain Modelling of Vortex-Induced Vibrations
IMT-10-2018	Chenyu Luan	Design and analysis for a steel braceless semi-submersible hull for supporting a 5-MW horizontal axis wind turbine
IMT-11-2018	Carl Fredrik Rehn	Ship Design under Uncertainty
IMT-12-2018	Øyvind Ødegård	Towards Autonomous Operations and Systems in Marine Archaeology
IMT-13-2018	Stein Melvær Nornes	Guidance and Control of Marine Robotics for Ocean Mapping and Monitoring
IMT-14-2018	Petter Norgren	Autonomous Underwater Vehicles in Arctic Marine Operations: Arctic marine research and ice monitoring
IMT-15-2018	Minjoo Choi	Modular Adaptable Ship Design for Handling Uncertainty in the Future Operating Context
MT-16-2018	Ole Alexander Eidsvik	Dynamics of Remotely Operated Underwater Vehicle Systems
IMT-17-2018	Mahdi Ghane	Fault Diagnosis of Floating Wind Turbine Drivetrain- Methodologies and Applications
IMT-18-2018	Christoph Alexander Thieme	Risk Analysis and Modelling of Autonomous Marine Systems
IMT-19-2018	Yugao Shen	Operational limits for floating-collar fish farms in waves and current, without and with well-boat presence
IMT-20-2018	Tianjiao Dai	Investigations of Shear Interaction and Stresses in Flexible Pipes and Umbilicals
IMT-21-2018	Sigurd Solheim Pettersen	Resilience by Latent Capabilities in Marine Systems
IMT-22-2018	Thomas Sauder	Fidelity of Cyber-physical Empirical Methods. Application to the Active Truncation of Slender Marine Structures
IMT-23-2018	Jan-Tore Horn	Statistical and Modelling Uncertainties in the Design of Offshore Wind Turbines

IMT-24-2018	Anna Swider	Data Mining Methods for the Analysis of Power Systems of Vessels
IMT-1-2019	Zhao He	Hydrodynamic study of a moored fish farming cage with fish influence
IMT-2-2019	Isar Ghamari	Numerical and Experimental Study on the Ship Parametric Roll Resonance and the Effect of Anti-Roll Tank
IMT-3-2019	Håkon Strandenes	Turbulent Flow Simulations at Higher Reynolds Numbers
IMT-4-2019	Siri Mariane Holen	Safety in Norwegian Fish Farming – Concepts and Methods for Improvement
IMT-5-2019	Ping Fu	Reliability Analysis of Wake-Induced Riser Collision
IMT-6-2019	Vladimir Krivopolianskii	Experimental Investigation of Injection and Combustion Processes in Marine Gas Engines using Constant Volume Rig
IMT-7-2019	Anna Maria Kozlowska	Hydrodynamic Loads on Marine Propellers Subject to Ventilation and out of Water Condition.
IMT-8-2019	Hans-Martin Heyn	Motion Sensing on Vessels Operating in Sea Ice: A Local Ice Monitoring System for Transit and Stationkeeping Operations under the Influence of Sea Ice
IMT-9-2019|	Stefan Vilsen	Method for Real-Time Hybrid Model Testing of Ocean Structures – Case on Slender Marine Systems
IMT-10-2019	Finn-Christian W. Hanssen	Non-Linear Wave-Body Interaction in Severe Waves
IMT-11-2019	Trygve Olav Fossum	Adaptive Sampling for Marine Robotics
IMT-12-2019	Jørgen Bremnes Nielsen	Modeling and Simulation for Design Evaluation
IMT-13-2019	Yuna Zhao	Numerical modelling and dyncamic analysis of offshore wind turbine blade installation
IMT-14-2019	Daniela Myland	Experimental and Theoretical Investigations on the Ship Resistance in Level Ice
IMT-15-2019	Zhengru Ren	Advanced control algorithms to support automated offshore wind turbine installation
IMT-16-2019	Drazen Polic	Ice-propeller impact analysis using an inverse propulsion machinery simulation approach
IMT-17-2019	Endre Sandvik	Sea passage scenario simulation for ship system performance evaluation

IMT-18-2019	Loup Suja-Thauvin	Response of Monopile Wind Turbines to Higher Order Wave Loads
IMT-19-2019	Emil Smilden	Structural control of offshore wind turbines – Increasing the role of control design in offshore wind farm development
IMT-20-2019	Aleksandar-Sasa Milakovic	On equivalent ice thickness and machine learning in ship ice transit simulations
IMT-1-2020	Amrit Shankar Verma	Modelling, Analysis and Response-based Operability Assessment of Offshore Wind Turbine Blade Installation with Emphasis on Impact Damages
IMT-2-2020	Bent Oddvar Arnesen Haugaløkken	Autonomous Technology for Inspection, Maintenance and Repair Operations in the Norwegian Aquaculture
IMT-3-2020	Seongpil Cho	Model-based fault detection and diagnosis of a blade pitch system in floating wind turbines
IMT-4-2020	Jose Jorge Garcia Agis	Effectiveness in Decision-Making in Ship Design under Uncertainty
IMT-5-2020	Thomas H. Viuff	Uncertainty Assessment of Wave-and Current-induced Global Response of Floating Bridges
IMT-6-2020	Fredrik Mentzoni	Hydrodynamic Loads on Complex Structures in the Wave Zone
IMT-7-2020	Senthuran Ravinthrakumar	Numerical and Experimental Studies of Resonant Flow in Moonpools in Operational Conditions
IMT-8-2020	Stian Skaalvik Sandøy	Acoustic-based Probabilistic Localization and Mapping using Unmanned Underwater Vehicles for Aquaculture Operations
IMT-9-2020	Kun Xu	Design and Analysis of Mooring System for Semi-submersible Floating Wind Turbine in Shallow Water
IMT-10-2020	Jianxun Zhu	Cavity Flows and Wake Behind an Elliptic Cylinder Translating Above the Wall
IMT-11-2020	Sandra Hogenboom	Decision-making within Dynamic Positioning Operations in the Offshore Industry – A Human Factors based Approach
IMT-12-2020	Woongshik Nam	Structural Resistance of Ship and Offshore Structures Exposed to the Risk of Brittle Failure
IMT-13-2020	Svenn Are Tutturen Værnø	Transient Performance in Dynamic Positioning of Ships: Investigation of Residual Load Models and Control Methods for Effective Compensation
IMT-14-2020	Mohd Atif Siddiqui	Experimental and Numerical Hydrodynamic Analysis of a Damaged Ship in Waves
IMT-15-2020	John Marius Hegseth	Efficient Modelling and Design Optimization of Large Floating Wind Turbines

IMT-16-2020	Asle Natskår	Reliability-based Assessment of Marine Operations with Emphasis on Sea Transport on Barges
IMT-17-2020	Shi Deng	Experimental and Numerical Study of Hydrodynamic Responses of a Twin-Tube Submerged Floating Tunnel Considering Vortex-Induced Vibration
IMT-18-2020	Jone Torsvik	Dynamic Analysis in Design and Operation of Large Floating Offshore Wind Turbine Drivetrains
IMT-1-2021	Ali Ebrahimi	Handling Complexity to Improve Ship Design Competitiveness
IMT-2-2021	Davide Proserpio	Isogeometric Phase-Field Methods for Modeling Fracture in Shell Structures
IMT-3-2021	Cai Tian	Numerical Studies of Viscous Flow Around Step Cylinders
IMT-4-2021	Farid Khazaeli Moghadam	Vibration-based Condition Monitoring of Large Offshore Wind Turbines in a Digital Twin Perspective
IMT-5-2021	Shuaishuai Wang	Design and Dynamic Analysis of a 10-MW Medium-Speed Drivetrain in Offshore Wind Turbines
IMT-6-2021	Sadi Tavakoli	Ship Propulsion Dynamics and Emissions
IMT-7-2021	Haoran Li	Nonlinear wave loads, and resulting global response statistics of a semi-submersible wind turbine platform with heave plates